ALEX(02)-TR-76-01-PART A

SOURCE STUDIES IN THE NEAR- AND FAR-FIELD

SEMI-ANNUAL TECHNICAL REPORT NO. 6 - PART A
1 NOVEMBER 1975 TO 31 MAY 1976

Prepared by
David Sun

TEXAS INSTRUMENTS INCORPORATED
Equipment Group
Post Office Box 6015
Dallas, Texas 75222

Contract No. F44620-73-C-0055
Amount of Contract: $294,749
Beginning 23 April 1973
Ending 30 June 1976

Prepared for

AIR FORCE OFFICE OF SCIENTIFIC RESEARCH

Sponsored by

ADVANCED RESEARCH PROJECTS AGENCY
Nuclear Monitoring Research Office
ARPA Program Code No. F10
ARPA Order No. 1827

31 May 1976

Acknowledgment: This research was supported by the Advanced Research Projects Agency, Nuclear Monitoring Research Office, under Project VELA-UNIFORM, and accomplished under the direction of the Air Force Office of Scientific Research under Contract Number F44620-73-C-0055.

AIR FORCE OFFICE OF SCIENTIFIC RESEARCH (AFSC)
NOTICE OF TRANSMITTAL TO DDC
This technical report has been reviewed and is approved for public release IAW AFR 190-12 (7b).
Distribution is unlimited.
A. D. BLOSE
Technical Information Officer

ALEX(02)-TR-76-01-PART A

SOURCE STUDIES IN THE NEAR- AND FAR-FIELD

SEMI-ANNUAL TECHNICAL REPORT NO. 6 - PART A
1 NOVEMBER 1975 TO 31 MAY 1976

Prepared by
David Sun

TEXAS INSTRUMENTS INCORPORATED
Equipment Group
Post Office Box 6015
Dallas, Texas 75222

Contract No. F44620-73-C-0055
Amount of Contract: $294,749
Beginning 23 April 1973
Ending 30 June 1976

Prepared for

AIR FORCE OFFICE OF SCIENTIFIC RESEARCH

Sponsored by

ADVANCED RESEARCH PROJECTS AGENCY
Nuclear Monitoring Research Office
ARPA Program Code No. F10
ARPA Order No. 1827

31 May 1976

Acknowledgment: This research was supported by the Advanced Research Projects Agency, Nuclear Monitoring Research Office, under Project VELA-UNIFORM, and accomplished under the direction of the Air Force Office of Scientific Research under Contract Number F44620-73-C-0055.

UNCLASSIFIED

SECURITY CLASSIFICATION OF THIS PAGE (When Data Entered)

(19) REPORT DOCUMENTATION PAGE

READ INSTRUCTIONS BEFORE COMPLETING FORM

(18) 1. REPORT NUMBER: AFOSR - TR - 76 - 1260

2. GOVT ACCESSION NO.

3. RECIPIENT'S CATALOG NUMBER

(6) 4. TITLE (and Subtitle): SOURCE STUDIES IN THE NEAR- AND FAR-FIELD.

5. TYPE OF REPORT & PERIOD COVERED: Semi-Annual Technical 11/01/75 to 05/31/76

(14) 6. PERFORMING ORG. REPORT NUMBER: TI - ALEX(02)-TR-76-01-Part-A

7. AUTHOR(s)

(10) David Sun

(15) 8. CONTRACT OR GRANT NUMBER(s): F44620-73-C-0055; ARPA Order-1827

9. PERFORMING ORGANIZATION NAME AND ADDRESS
Texas Instruments Incorporated
Equipment Group
Dallas, Texas 75222

10. PROGRAM ELEMENT, PROJECT, TASK AREA & WORK UNIT NUMBERS
ARPA Program Code No. F10

11. CONTROLLING OFFICE NAME AND ADDRESS
Advanced Research Projects Agency
Nuclear Monitoring Research Office
Arlington, Virginia 22209

(11) 12. REPORT DATE: 31 May 76

13. NUMBER OF PAGES: 175

14. MONITORING AGENCY NAME & ADDRESS (if different from Controlling Office)
Air Force Office of Scientific Research
Bolling Air Force Base, Bldg. 410
Washington, D. C. 20332

(12) 177 p.

15. SECURITY CLASS. (of this report): UNCLASSIFIED

15a. DECLASSIFICATION/DOWNGRADING SCHEDULE

16. DISTRIBUTION STATEMENT (of this Report)

APPROVED FOR PUBLIC RELEASE, DISTRIBUTION UNLIMITED

(9) Semi-annual technical rept. no. 6

17. DISTRIBUTION STATEMENT (of the abstract entered in Block 20, if different from Report)

(Part A), 1 Nov 75 - 31 May 76

18. SUPPLEMENTARY NOTES

ARPA Order No. 1827

19. KEY WORDS (Continue on reverse side if necessary and identify by block number)

Seismology
Surface Waves
Spectral Fitting
Spectral Ratios
Effective Attenuation
Travel Path

20. ABSTRACT (Continue on reverse side if necessary and identify by block number)

Far-field solutions (source mechanism and focal depth) have been obtained for nineteen events in the Sinkiang, China, earthquake swarm of August 1974. Both spectral and ratio-of-events fitting methods were employed. The solutions indicated two kinds of source mechanisms in this swarm: vertical strike-slip and dip-slip with a dip angle of fourty degrees. The results suggested that these events occurred at shallow depths with the estimated source depth varying between 4 km and 14 km.

next page

DD FORM 1 JAN 73 1473 EDITION OF 1 NOV 65 IS OBSOLETE

UNCLASSIFIED

SECURITY CLASSIFICATION OF THIS PAGE (When Data Entered)

405 076

20. continued

cont.

The effective Rayleigh wave attenuation coefficients along several specific travel paths have been determined for the periods of 10 seconds to 50 seconds. The two-station method was applied to two sets of observed data: the 1974 Sinkiang earthquake swarm and earthquakes used in the previous M_s - m_b study (Turnbull, et al., 1975). This yielded results for the travel paths KON-OGD, KON-ALQ, KON-TLO, and TLO-ZLP (where KON, OGD, TLO, and ZLP are VLPE stations).

The original and a modified version of the Tryggvason's isotropic-source method for the determination of the surface wave attenuation has been formulated and implemented. They were employed to calculate the average Rayleigh wave attenuation coefficients along the travel paths between eastern Kazakh and three array stations ~~(ALPA, LASA, and NORSAR),~~ and those between the U.S. Nevada test site (NTS) and the three array stations. All available surface wave data of 1975 EKZ and NTS events were used. The results indicated that the attenuation across the Eurasian continent was much higher than that across the North American continent for the period between 20 and 50 seconds. The general trend of the attenuation curve obtained here and that of Tryggvason's is quite similar; although the former shows a slightly higher attenuation.

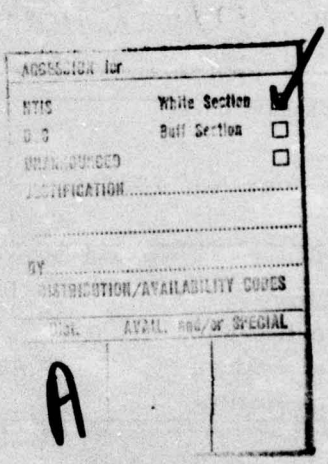

ABSTRACT

Far-field solutions (source mechanism and focal depth) have been obtained for nineteen events in the Sinkiang, China, earthquake swarm of August 1974. Both spectral and ratio-of-events fitting methods were employed. The solutions indicated two kinds of source mechanisms in this swarm: vertical strike-slip and dip-slip with a dip angle of forty degrees. The results suggested that these events occurred at shallow depths with the estimated source depth varying between 4 km and 14 km.

The effective Rayleigh wave attenuation coefficients along several specific travel paths have been determined for the periods of 10 seconds to 50 seconds. The two-station method was applied to two sets of observed data: the 1974 Sinkiang earthquake swarm and earthquakes used in the previous M_s-m_b study (Turnbull et al., 1975). This study yielded results for the travel paths KON-OGD, KON-ALQ, KON-TLO, and TLO-ZLP (where KON, OGD, TLO, and ZLP are VLPE stations).

The original and a modified version of the Tryggvason isotropic-source method for the determination of the surface wave attenuation has been formulated and implemented. They were employed to calculate the average Rayleigh wave attenuation coefficients along the travel paths between the eastern Kazakh and three array stations (ALPA, LASA, and NORSAR), and those between the U. S. Nevada test site (NTS) and the three array stations. All available surface wave data of 1975 EKZ and NTS events were used. The results indicated that the attenuation across the Eurasian continent was much higher than that across the North American continent for the period between

20 and 50 seconds. The general trend of the attenuation curve obtained here and that of Tryggvason's is quite similar, although the former shows a slightly higher attenuation.

ACKNOWLEDGMENTS

Mr. Alan C. Strauss provided the processed signals which were used in the analysis of Section II.

Mrs. Cherylann B. Saunders prepared the tables and captioned the figures.

Mrs. Mary E. Palmer edited and typed the manuscript.

Dr. Lawrence S. Turnbull, Jr., made helpful suggestions and reviewed the manuscript.

TABLE OF CONTENTS

LIST OF FIGURES

LIST OF FIGURES
(continued)

LIST OF FIGURES
(continued)

LIST OF FIGURES
(continued)

LIST OF FIGURES
(continued)

LIST OF FIGURES
(continued)

LIST OF FIGURES
(continued)

LIST OF TABLES

LIST OF TABLES
(continued)

SECTION I
INTRODUCTION

During this report period, several investigations of the seismic source from far-field surface wave data have been continued. For the source mechanism study, the surface waves of nineteen events in the Sinkiang, China, earthquake swarm of August 1974 are analyzed, and the results are discussed in Section II. In Section III, travel path effects are examined where several approaches to determine the surface wave energy attenuation are presented. Using the surface wave data of earthquakes (1974 Sinkiang earthquake swarm and earthquakes used in previous M_s-m_b studies) and presumed underground nuclear explosions in 1975 from the East Kazakh and the Nevada test site, Rayleigh wave energy attenuation coefficients are calculated for various travel paths of interest.

SECTION II

ANALYSIS OF THE SINKIANG, CHINA, EARTHQUAKE SWARM OF AUGUST 1974

A. INTRODUCTION

Several Eurasian earthquakes were analyzed and discussed in previous reports (Turnbull et al., 1973, 1974). These events took place in Central Eurasia near the Chinese-Russian border and were quite widely separated in terms of their locations and dates. This separation gave us the chance to model several different source region structures and to study the source mechanisms in them.

During most of the month of August and the early part of September 1974, a major earthquake swarm of over 300 recorded events occurred in Sinkiang, China. The geographic location of the swarm is shown in Figure II-1, with the travel paths encountered to the VLPE stations: ALPA, NORSAR, and LASA. Its location is shown again by the boxed area in Figure II-2, but this time in relation to the major geologic features. A study of this earthquake swarm offered the following advantages:

- The opportunity to analyze a large number of events from a small region, investigating the repeatability of source mechanism from event to event.
- The possibility of using a master event or events with spectral ratios to eliminate the travel path effects, which usually are complicated and not well understood; and the station instrument response corrections, which sometimes are not too reliable (especially those of VLPE stations), for a better estimation of the source parameters.

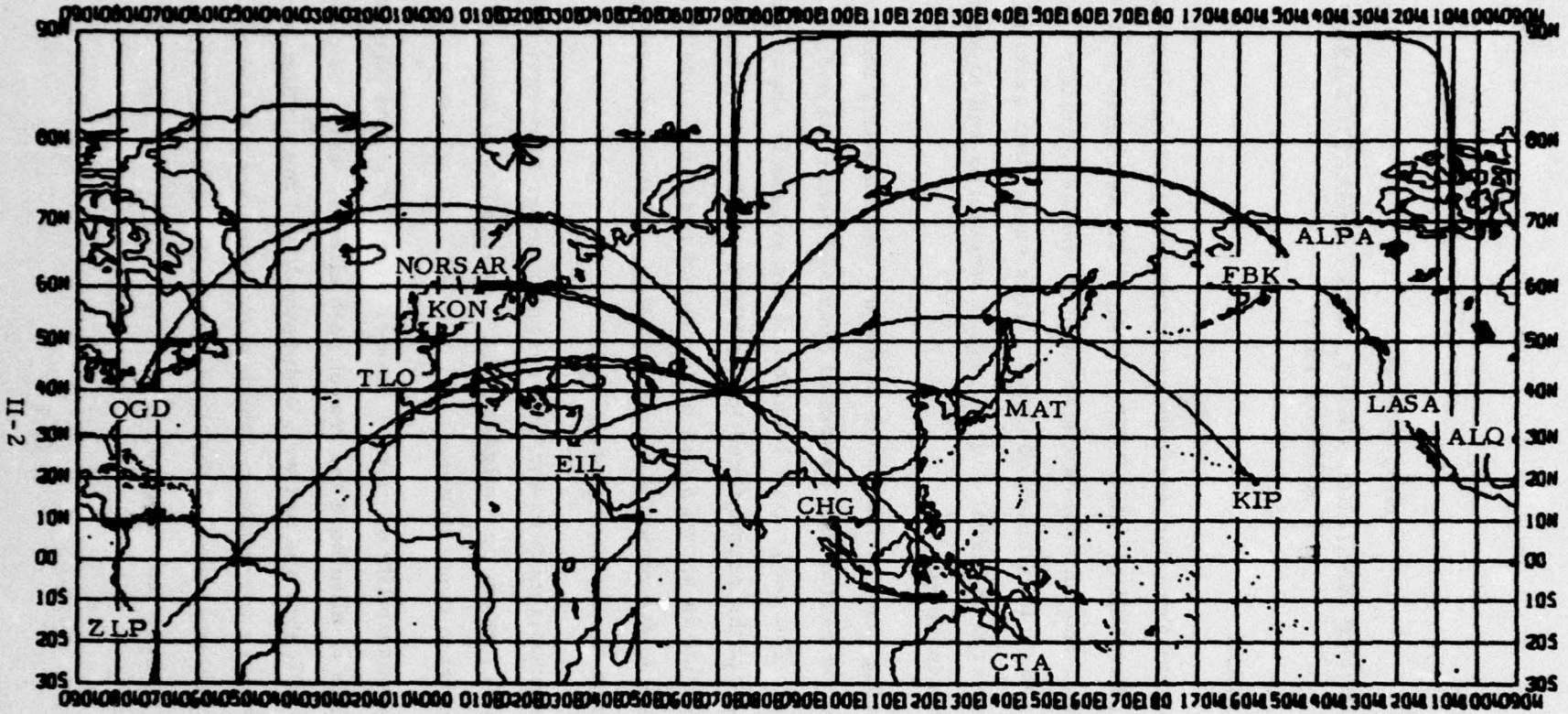

MILLER MODIFIED MERCATOR PROJECTION
MAP SCALE: 0.02500 INCHES/DEGREE LONGITUDE

FIGURE II-1

LOCATION OF 1974 SINKIANG CHINA EARTHQUAKE SWARM
RELATIVE TO THE OBSERVATION STATIONS

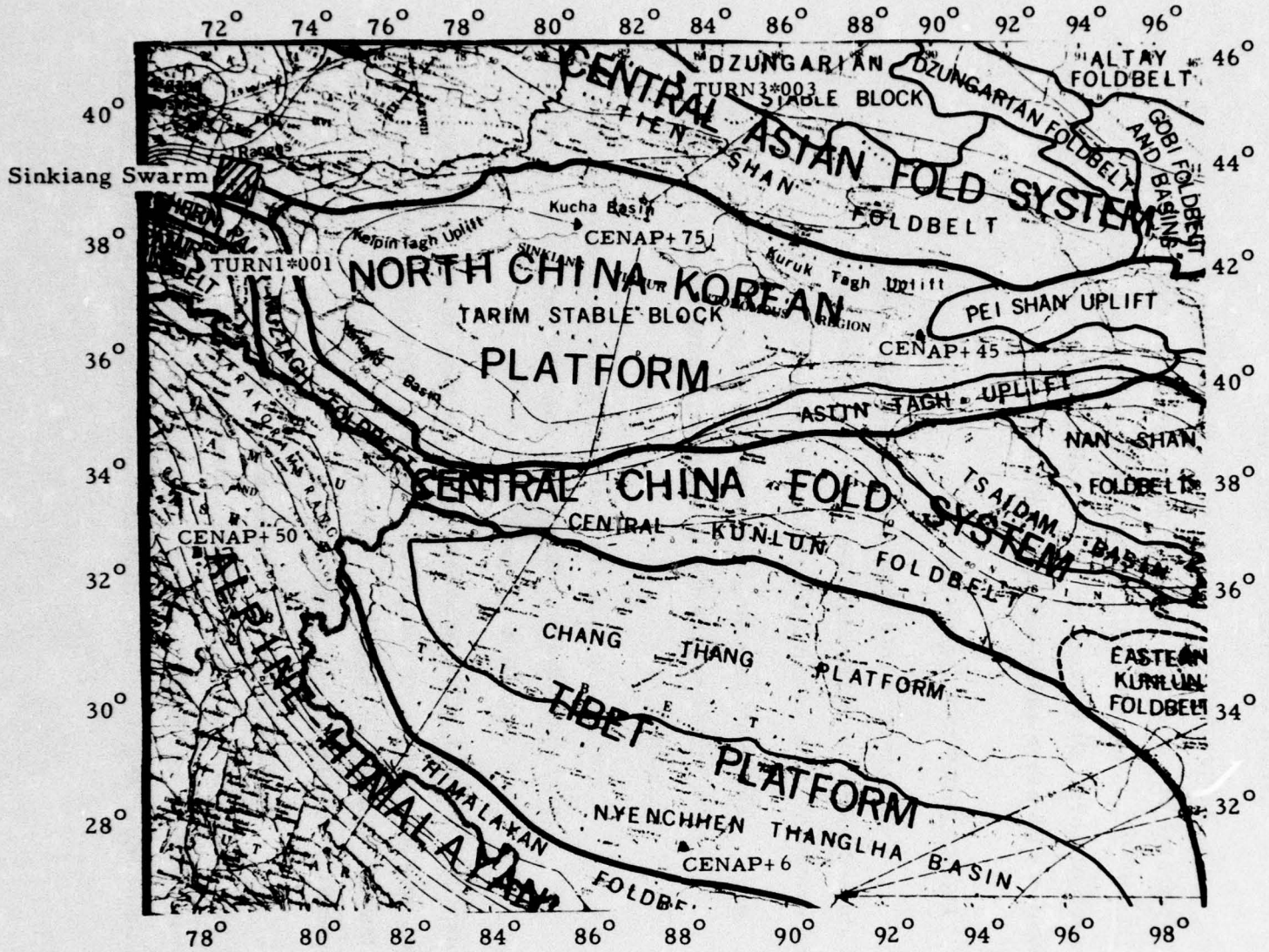

FIGURE II-2

LOCATION OF 1974 SINKIANG CHINA EARTHQUAKE SWARM

- The opportunity to determine the effective surface wave attenuation along some specific travel paths, using the two-station method with more than one event.

In this section are presented discussions and results on the source parameter estimation for the chosen events in this swarm. The travel path attenuation using the available data from the swarm will be given in the next section where all discussions and results are devoted to the travel path attenuation with other additional data and methods.

B. PROCEDURE OF ANALYSIS

Nineteen events from this earthquake swarm have been chosen to be studied here. In selecting these nineteen events out of about sixty processed events for this swarm, the following criteria were used:

- The event is a single event at all recording stations; that is, the mixed events due to the overlapping signal time gates are excluded.
- The observed data are available at three or more stations with good data quality. Hopefully, these stations are distributed in two consecutive quadrants.

Data quality is judged by the appearances of the time traces, the dispersion curves, and the uncorrected amplitude spectra. The typical Rayleigh wave time traces, dispersion curves, and uncorrected amplitude spectra are given in Appendix A for the event LX+SINK+S018.

To show their relative locations, Figure II-3 displays the detailed locations of these events. Their locations, dates, origin times, body-wave magnitudes, and PDE depths (if available) are given in Table II-1. Information concerning the observation stations is given in Table II-2 for each event.

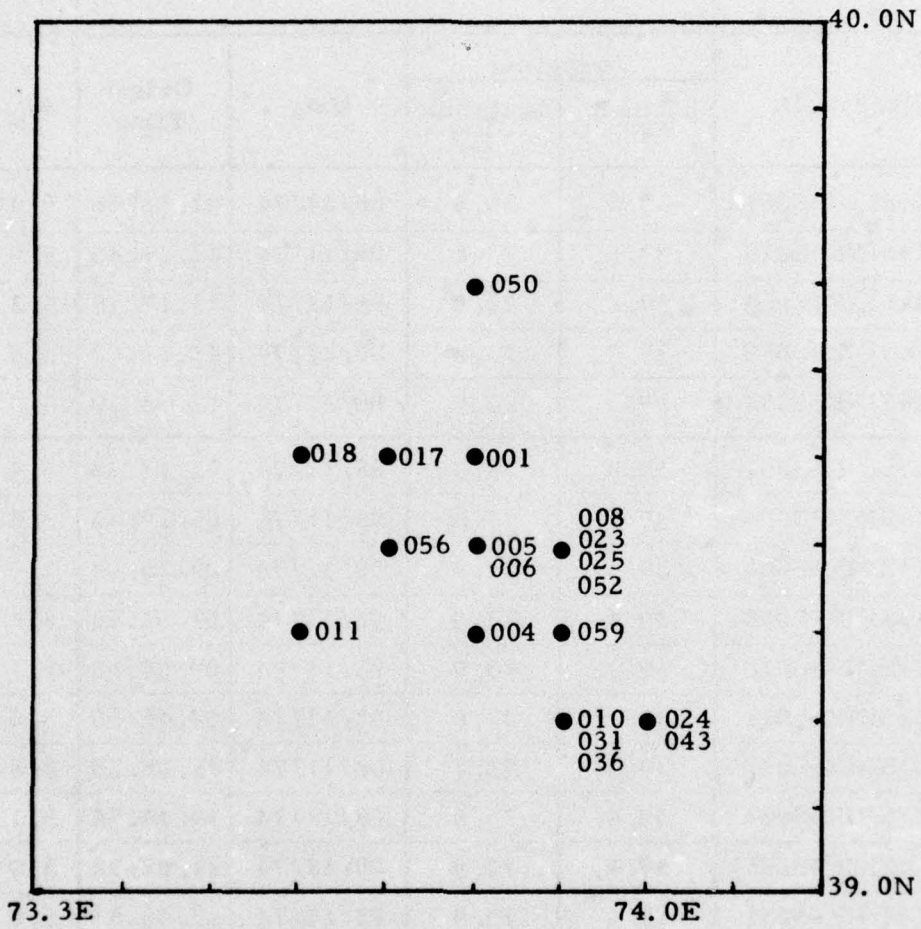

FIGURE II-3

DETAILED LOCATIONS OF THE EVENTS

TABLE II-1

1974 SINKIANG EARTHQUAKE SWARM

	Event I. D.	Location		Date	Origin Time	m_b	PDE Depth (km)
		Latitude °N	Longitude °E				
I	LX+SINK+S001	39.5	73.8	08/11/74	01.13.56	6.4	9
	LX+SINK+S018	39.5	73.6	08/11/74	21.21.40	5.9	9
	LX+SINK+S024	39.2	74.0	08/12/74	21.17.48	5.2	27
	LX+SINK+S050	39.7	73.8	08/27/74	12.56.03	5.8	--
	LX+SINK+S052	39.4	73.9	08/27/74	17.33.39	5.3	--
II	LX+SINK+S004	39.3	73.8	08/11/74	05.12.33	5.4	--
	LX+SINK+S005	39.4	73.8	08/11/74	05.19.33	5.2	--
	LX+SINK+S006	39.4	73.8	08/11/74	05.23.52	5.6	27
	LX+SINK+S008	39.4	73.9	08/11/74	07.02.08	5.2	--
	LX+SINK+S010	39.2	73.9	08/11/74	09.08.58	5.1	12
	LX+SINK+S011	39.3	73.6	08/11/74	12.45.39	5.0	--
	LX+SINK+S017	39.5	73.7	08/11/74	20.05.30	5.8	--
	LX+SINK+S023	39.4	73.9	08/12/74	14.14.54	5.1	--
	LX+SINK+S025	39.4	73.9	08/12/74	21.57.18	5.0	--
	LX+SINK+S031	39.4	73.9	08/14/74	22.06.53	5.0	--
	LX+SINK+S036	39.2	73.9	08/17/74	23.50.59	5.0	--
	LX+SINK+S043	39.2	74.0	08/21/74	18.45.17	5.0	--
	LX+SINK+S056	39.4	73.7	09/03/74	19.41.20	5.4	--
	LX+SINK+S059	39.3	73.9	09/07/74	15.46.31	4.9	--

TABLE II-2

OBSERVATION STATIONS FOR 1974 SINKIANG EARTHQUAKE SWARM
(PAGE 1 OF 2)

	Event I. D.	*	Station I. D.								
			4 TLO	6 KON	8 KIP	9 ALQ	10 ZLP	11 MAT	ALPA	LASA	NORSAR
I	LX+SINK+S001	AZ	-62.4	-	48.4	-	-65.8	-	17.2	0.0	-39.2
		Δ	57.9	-	102.3	-	139.7	-	70.5	94.0	43.5
	LX+SINK+S018	AZ	-62.5	-	48.3	-	-66.0	-	17.1	-0.1	-39.2
		Δ	57.8	-	102.5	-	139.6	-	70.6	94.0	43.4
	LX+SINK+S024	AZ	-62.2	-	48.6	0.4	-65.9	-	17.2	0.2	-39.0
		Δ	58.2	-	102.4	106.0	140.0	-	70.8	94.3	43.8
	LX+SINK+S050	AZ	-62.6	-41.1	48.4	0.2	-	71.9	17.2	0.0	-39.4
		Δ	57.8	44.0	102.2	105.5	-	49.7	70.4	93.8	43.3
	LX+SINK+S052	AZ	-62.3	-40.8	48.5	0.3	-	71.7	17.2	0.1	-39.2
		Δ	58.0	44.3	102.3	105.8	-	49.7	70.6	94.1	43.6
II	LX+SINK+S004	AZ	-62.3	-	48.5	-	-	-	17.2	-	-39.1
		Δ	58.0	-	102.5	-	-	-	70.7	-	43.6
	LX+SINK+S005	AZ	-62.4	-	48.4	-	-	-	17.2	-	-39.2
		Δ	57.9	-	102.4	-	-	-	70.6	-	43.5
	LX+SINK+S006	AZ	-62.4	-	48.4	-	-	-	17.2	-	-39.2
		Δ	57.9	-	102.4	-	-	-	70.6	-	43.5
	LX+SINK+S008	AZ	-	-	48.5	-	-66.0	-	17.2	-	-39.0
		Δ	-	-	102.5	-	139.9	-	70.8	-	43.7
	LX+SINK+S010	AZ	-62.2	-	48.5	-	-	-	17.2	0.1	-39.0
		Δ	58.1	-	102.5	-	-	-	70.8	94.3	43.7

* AZ = Azimuth at source (+ for NE) Δ = Distance to source in degrees.

TABLE II-2

OBSERVATION STATIONS FOR 1974 SINKIANG EARTHQUAKE SWARM
(PAGE 2 OF 2)

	Event I. D.	*	Station I. D.								
			4 TLO	6 KON	8 KIP	9 ALQ	10 ZLP	11 MAT	ALPA	LASA	NORSAR
II	LX+SINK+S011	AZ	-	-	-	-	-	-	17.2	-0.1	-39.1
		Δ	-	-	-	-	-	-	70.8	94.2	43.5
	LX+SINK+S017	AZ	-62.5	-	48.3	-	-65.9	-	17.1	-	-39.2
		Δ	57.8	-	102.4	-	139.7	-	70.6	-	43.4
	LX+SINK+S023	AZ	-	-	-	-	-	-	17.2	0.1	-39.2
		Δ	-	-	-	-	-	-	70.6	94.1	43.6
	LX+SINK+S025	AZ	-62.3	-	-	-	-	71.7	17.2	0.1	-39.2
		Δ	58.0	-	-	-	-	49.7	70.6	94.1	43.6
	LX+SINK+S031	AZ	-62.2	-	-	-	-	-	17.2	0.1	-39.0
		Δ	58.1	-	-	-	-	-	70.8	94.3	43.7
	LX+SINK+S036	AZ	-62.2	-	48.5	-	-	-	17.2	-	-39.0
		Δ	58.1	-	102.5	-	-	-	70.8	-	43.7
	LX+SINK+S043	AZ	-	-	-	-	-	-	17.2	0.2	-39.0
		Δ	-	-	-	-	-	-	70.8	94.3	43.8
	LX+SINK+S056	AZ	-62.4	-40.9	48.4	0.1	-	-	-	-	-
		Δ	57.9	44.2	102.5	105.8	-	-	-	-	-
	LX+SINK+S059	AZ	-62.3	-	-	0.3	-	-	17.2	-	-39.1
		Δ	58.1	-	-	105.9	-	-	70.7	-	43.7

* AZ = Azimuth at source (+ for NE) Δ = Distance to source in degrees.

These nineteen events are discussed in two groups, as indicated in both Tables II-1 and II-2. The first group consists of five events for which both Rayleigh and Love wave data are available. The number of observation stations is betweeen six and eight for this group. The remaining fourteen events constitute the second group. It is noticed that observation stations are distributed in the NE and the NW quadrants for all nineteen events. The procedure used in the analysis of the events is as follows:

- Choice of source region earth model - The layered earth model is determined by comparing the source region earth structure profiles with the known earth models (as discussed by Turnbull et al., 1974). The Harkrider's medium response solutions are calculated for the selected earth model in order to produce the theoretical amplitude spectra. For this swarm, it has been found that the normal Gutenberg-Bullen earth model is most appropriate.

- Data handling - Applying a series of narrowband filters (as discussed by Turnbull et al., 1974), each component is analyzed for evidence of multipathing. At each period, group velocities are determined for each multipath, and then compared to the standard group velocity curves for the type of travel path encountered (see example in Appendix A). Estimating the correct multipath from this comparison, the amplitude spectra is obtained and then corrected for attenuation, geometric spreading, and instrument response.

- Source parameter determination - Spectral fitting procedures (Turnbull et al., 1973) are then applied to the corrected spectra, using a theoretical source model placed in the selected layer earth model. Source parameters are estimated by first using simple spectral fitting. A master (or reference) event

(or events) is picked based on the information obtained from the spectral fitting. Then the ratio-of-events fitting is applied to the rest of the events in the same group using the selected master event (or events) as reference.

C. FAR-FIELD SOLUTION

1. Group-I

For this group, observed surface wave data are available for both Rayleigh and Love waves at most of the stations. The observation stations include all three array stations: ALPA, LASA, and NORSAR. In general, data quality is better at the array station than at the VLPE. Here, we first apply the spectral fitting method using all available Rayleigh and Love wave data. For the five events in this group, the estimations of the source parameters based on the minimum-residual criterion are listed in Table II-3, and those based on the distribution-of-minimum-residual criterion are listed in Table II-4. The distributions of minimum residuals of each parameter of each event are shown in Figures II-4 through II-8 with their spectral fits.

Referring to those figures of the spectral fits, it is noticed that the spectral fits for the Love wave in general are poor in both spectral level and in shape, except for the events LX+SINK+S050 and S052. This is probably caused by the poor quality of the observed Love wave spectra. To determine whether the estimation of the source parameters will be significantly affected by these poor Love wave data, we next apply the spectral fitting method using Rayleigh wave data only. The results from this fitting are given in Tables II-5 and II-6 and in Figures II-9 through II-13.

Comparing the results obtained from two spectral fittings (see Tables II-3 and II-5), using both Rayleigh and Love wave and using Rayleigh wave only, no significant differences in the source parameter estimations have been observed, except the dip and slip angles for events LX+SINK+S001

TABLE II-3

ESTIMATIONS OF SOURCE PARAMETERS OBTAINED BY AMPLITUDE SPECTRAL FITTING BASED ON MINIMUM-RESIDUAL CRITERION: ALL AVAILABLE LR AND LQ DATA

Event I. D.	Optimal Solution				
	Depth h (km)	Dip Angle δ^{o}	Slip Angle λ^{o}	Strike $N\phi^{o}E$	Moment 10^{25} dyne-cm
LX+SINK+S001	6	40 50	± 90	75	0.123×10^{2}
LX+SINK+S018	6	60	60	80	0.161×10^{1}
LX+SINK+S024	6	40	-60	130	0.193
LX+SINK+S050	4	40 50	± 90	35	0.797
LX+SINK+S052	4	40 50	± 90	60	0.827×10^{-1}

TABLE II-4

ESTIMATIONS OF SOURCE PARAMETERS OBTAINED BY AMPLITUDE SPECTRAL FITTING BASED ON DISTRIBUTION-OF-MINIMUM-RESIDUAL CRITERION: ALL AVAILABLE LR AND LQ DATA

Event I. D.	Source Parameters							
	Depth h (km)		Dip Angle δ^o		Slip Angle λ^o		Strike Nϕ^oE	
	Probable Range	% Confidence	Probable Range	% Confidence	Probable Range	% Confidence	Probable Range	% Confidence
LX+SINK+S001	2-8	92	40-70	77	$\pm$30 $\pm$90	31 33	-	-
LX+SINK+S018	4-10	90	30-60	79	$\pm$30 $\pm$60	30 41	55-80 120-150	25 31
LX+SINK+S024	2-8	96	40-60	69	$\pm$30 $\pm$60	32 41	100-155	66
LX+SINK+S050	2-8	80	40-70	70	-30, 0, 30 $\pm$90	57 22	25-85	65
LX+SINK+S052	2-6	90	30-60	82	$\pm$60 $\pm$90	35 33	15-75	75

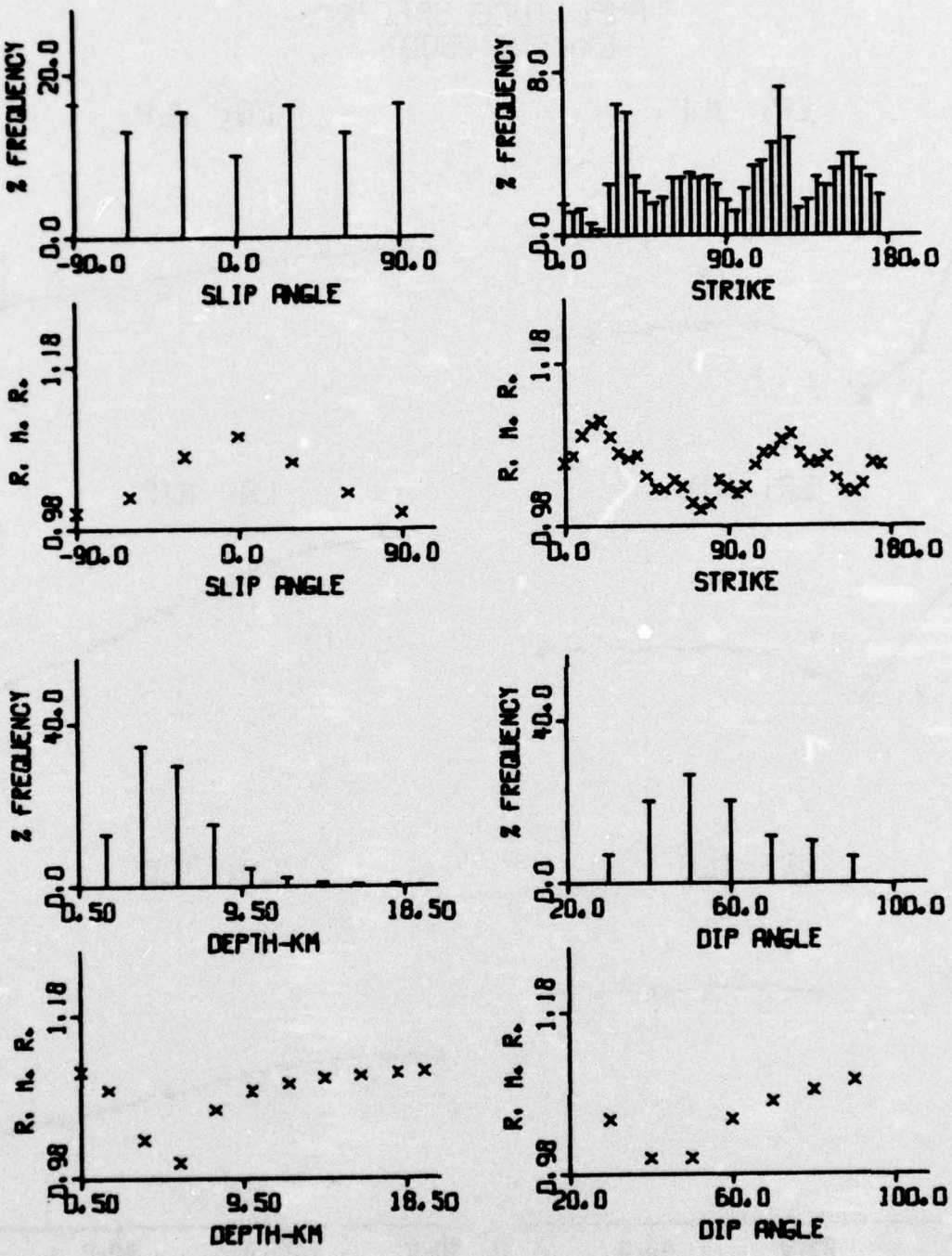

FIGURE II-4a

SOURCE PARAMETER DISTRIBUTIONS:
LX+SINK+S001 - BOTH LR AND LQ
(PAGE 1 OF 3)

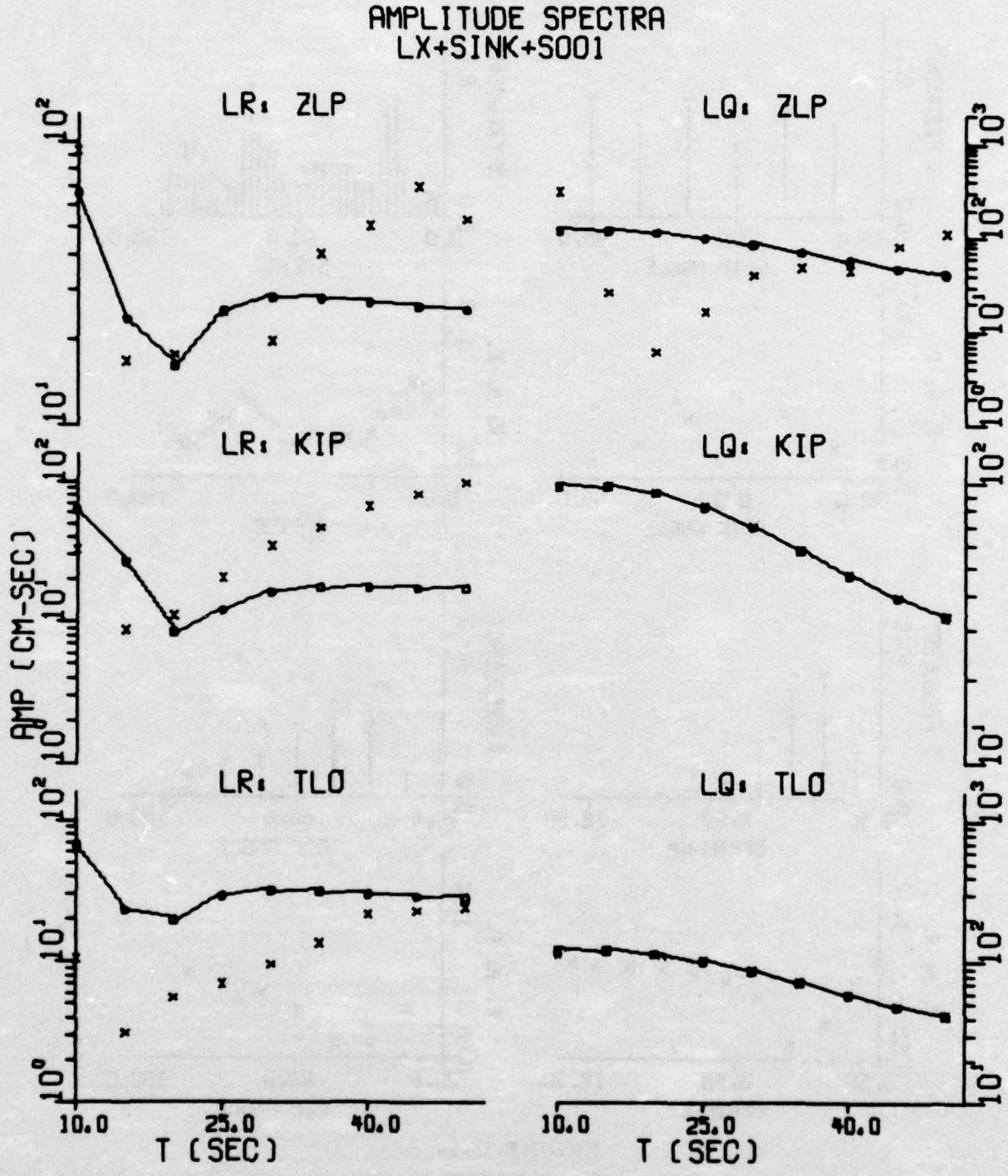

FIGURE II-4b

SPECTRAL FIT: LX+SINK+S001 - BOTH LR AND LQ
(PAGE 2 OF 3)

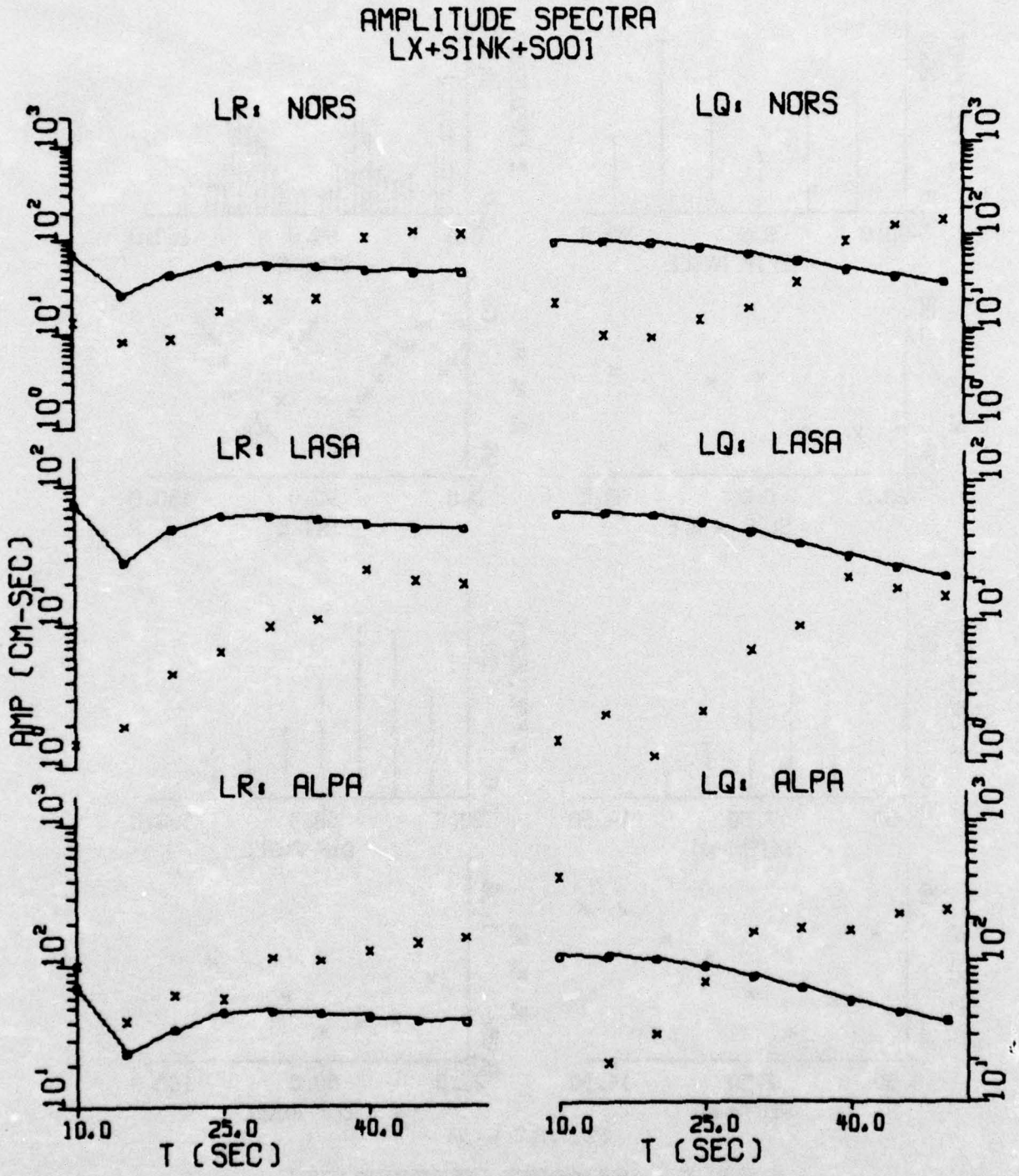

FIGURE II-4b

SPECTRAL FIT: LX+SINK+S001 - BOTH LR AND LQ
(PAGE 3 OF 3)

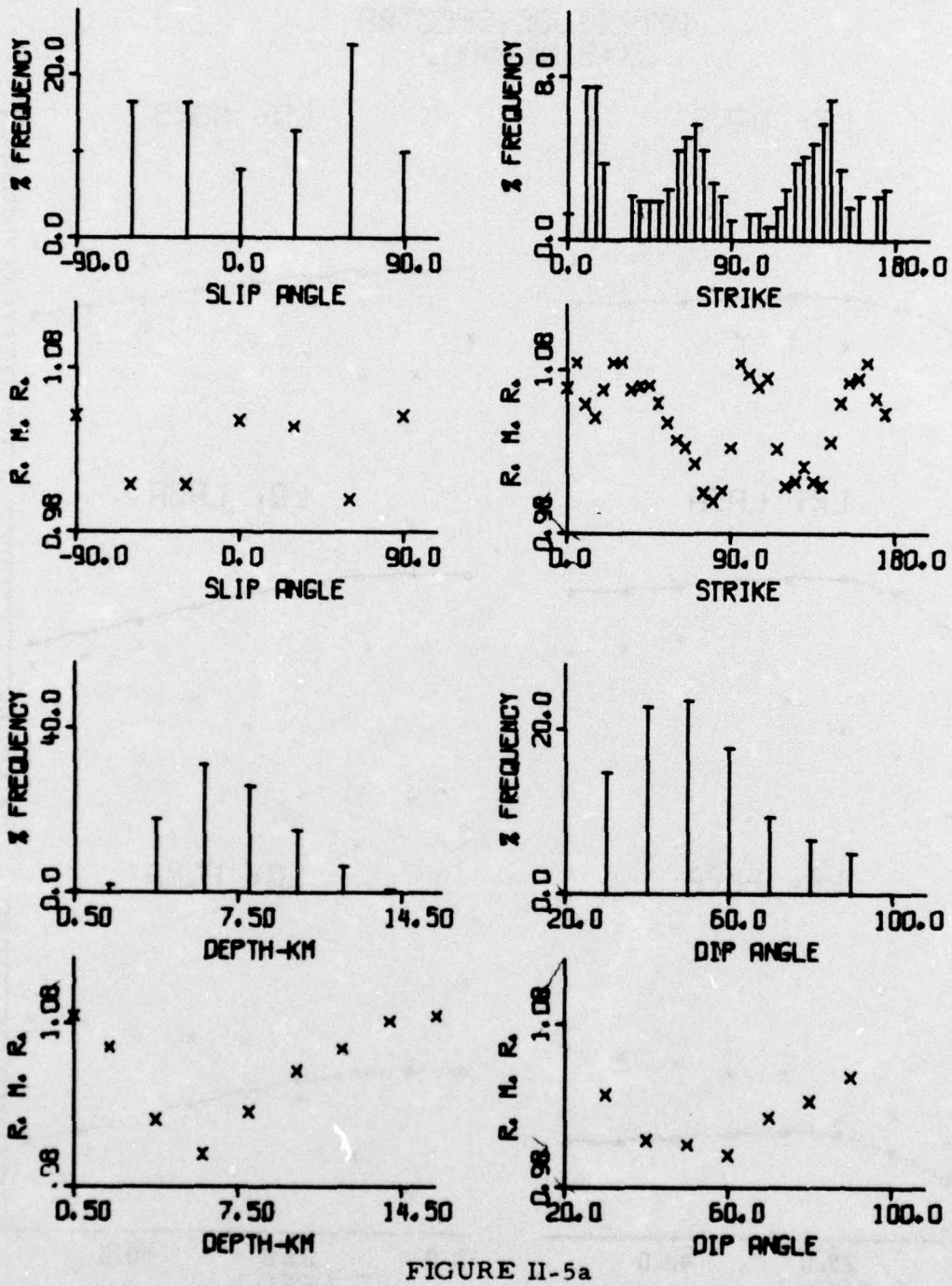

FIGURE II-5a

SOURCE PARAMETER DISTRIBUTIONS:
LX+SINK+S018 - BOTH LR AND LQ
(PAGE 1 OF 3)

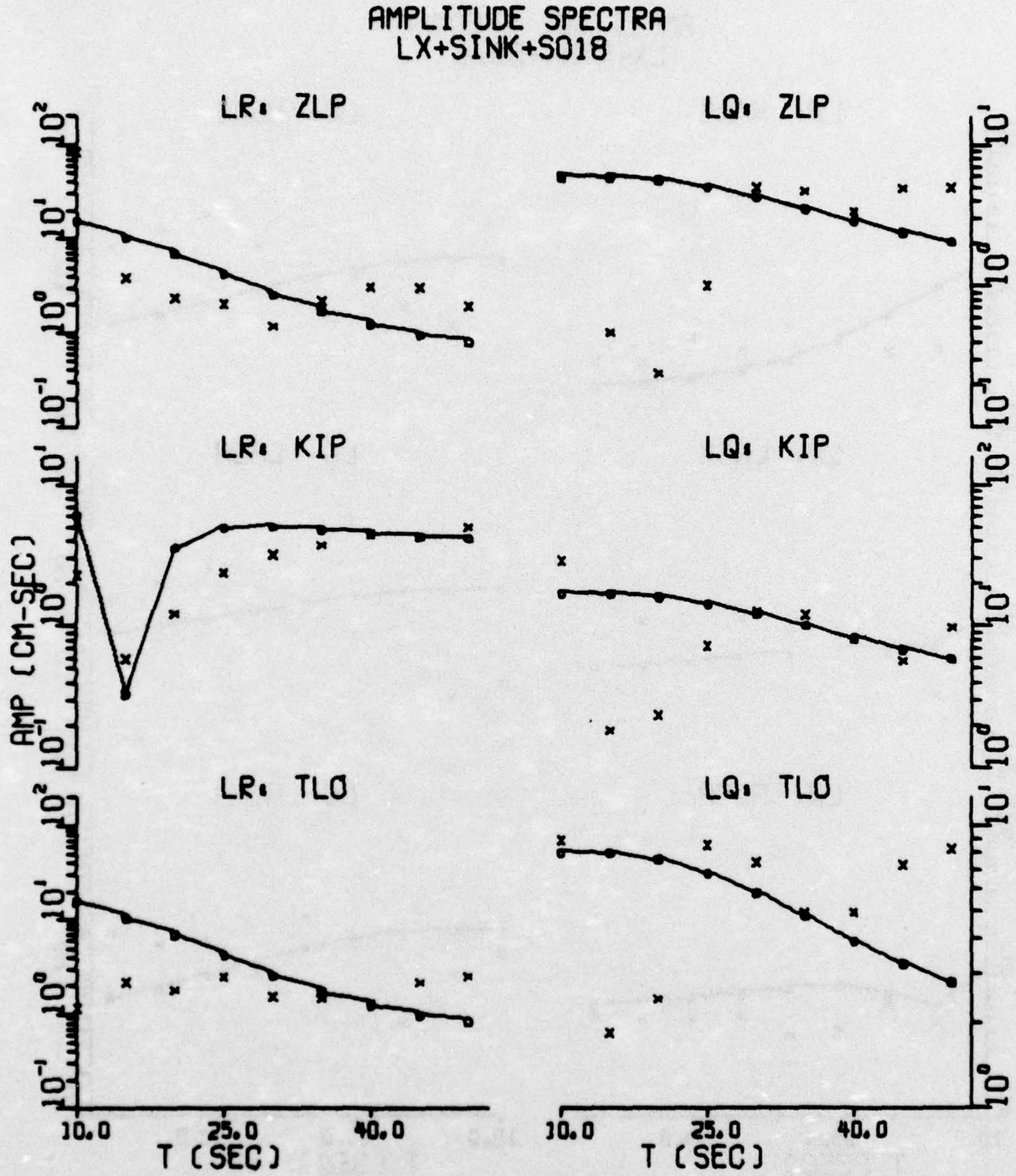

FIGURE II-5b

SPECTRAL FIT: LX+SINK+S018 - BOTH LR AND LQ
(PAGE 2 OF 3)

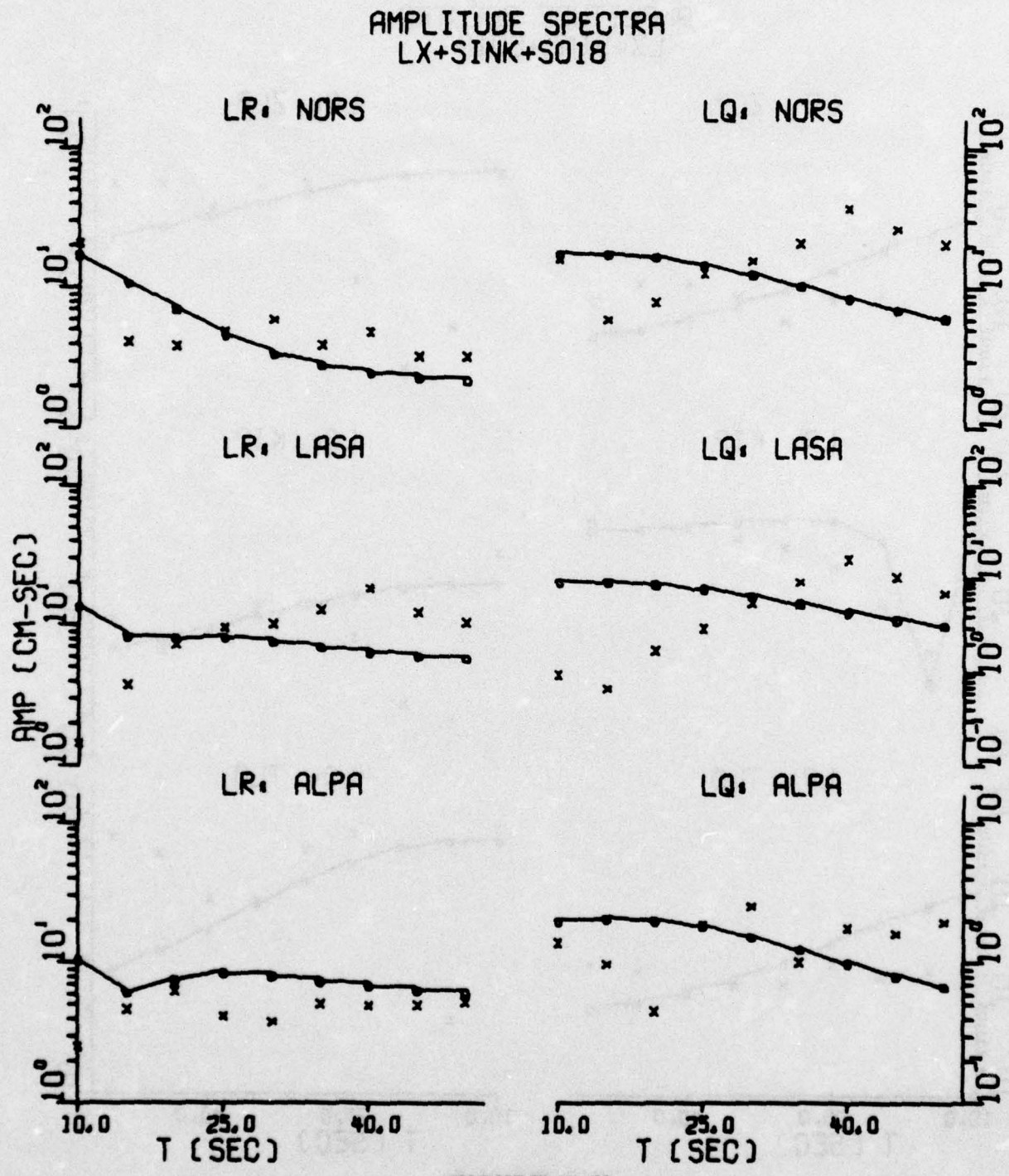

FIGURE II-5b

SPECTRAL FIT: LX+SINK+S018 - BOTH LR AND LQ
(PAGE 3 OF 3)

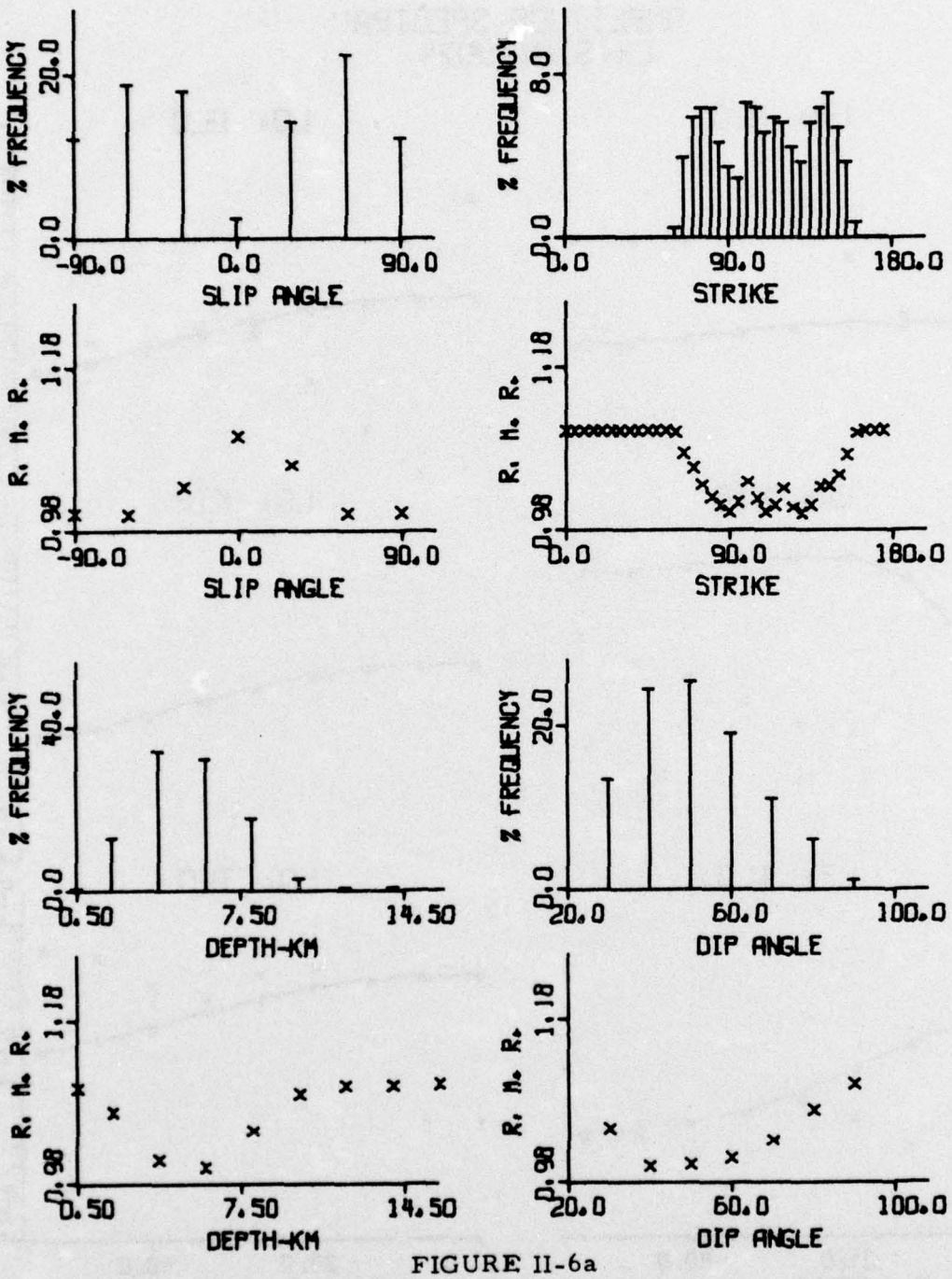

FIGURE II-6a

SOURCE PARAMETER DISTRIBUTIONS:
LX+SINK+S024 - BOTH LR AND LQ
(PAGE 1 OF 3)

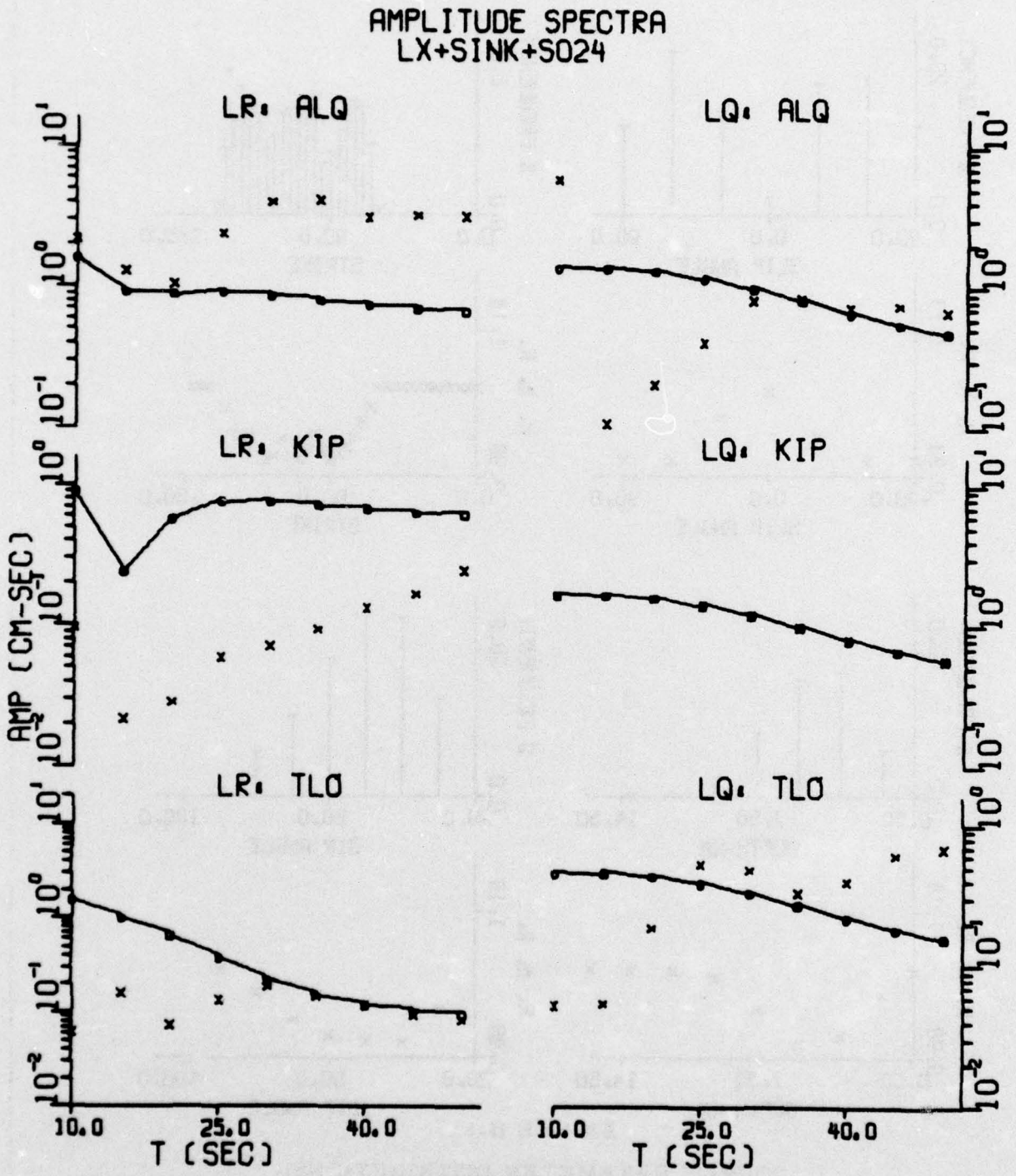

FIGURE II-6b

SPECTRAL FIT: LX+SINK+S024 - BOTH LR AND LQ
(PAGE 2 OF 3)

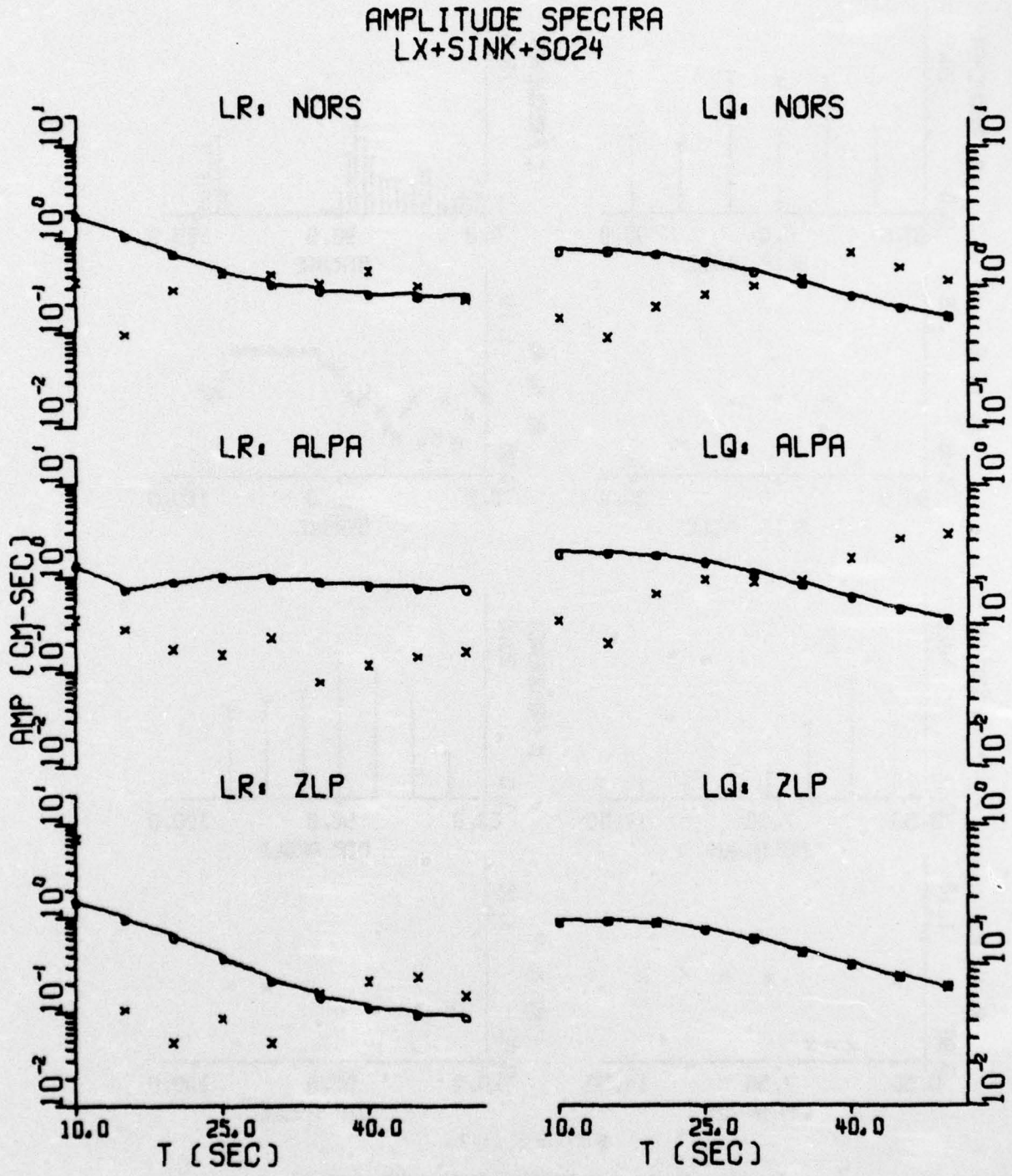

FIGURE II-6b

SPECTRAL FIT: LX+SINK+S024 - BOTH LR AND LQ
(PAGE 3 OF 3)

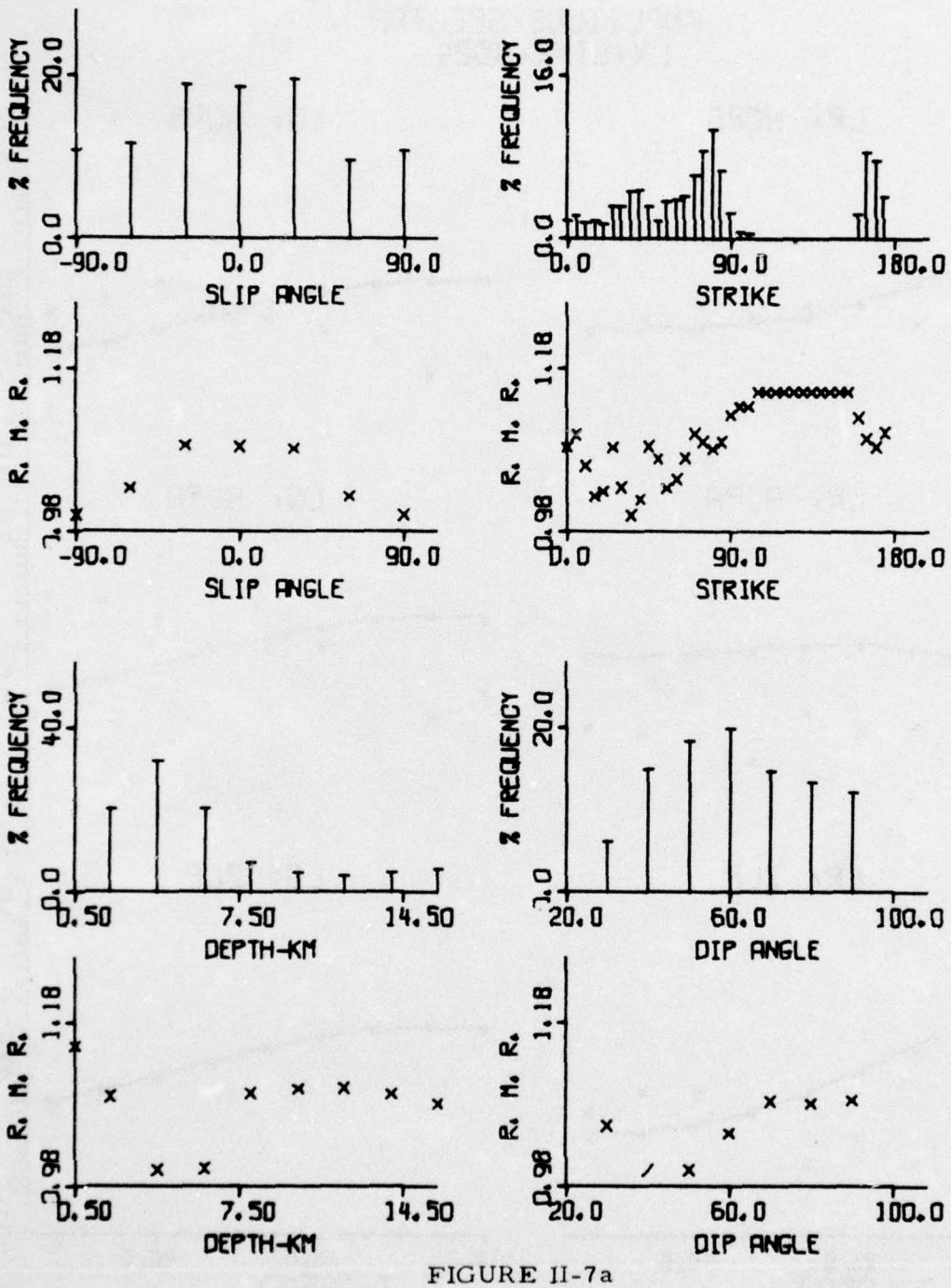

FIGURE II-7a

SOURCE PARAMETER DISTRIBUTIONS:
LX+SINK+S050 - BOTH LR AND LQ
(PAGE 1 OF 3)

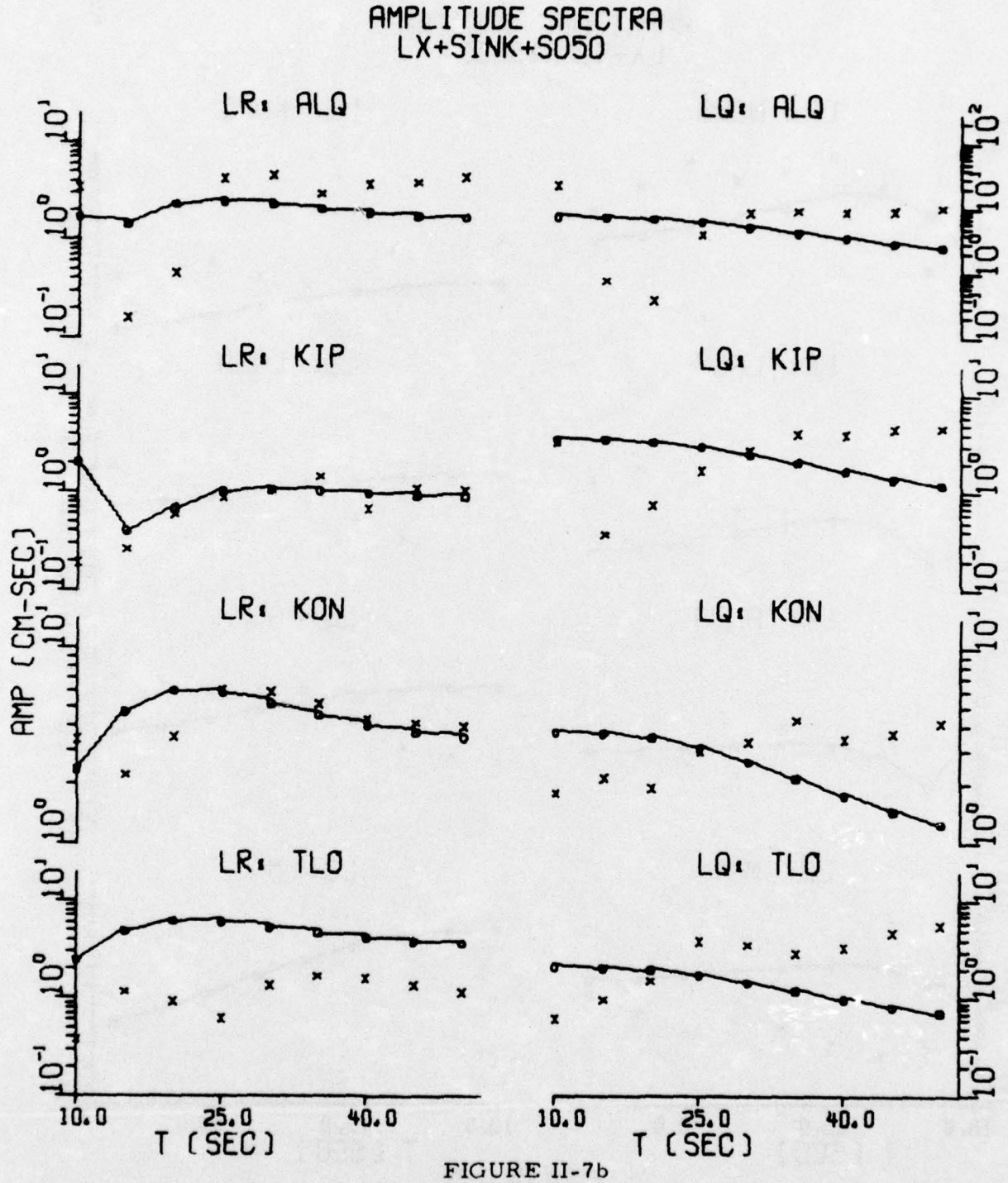

FIGURE II-7b

SPECTRAL FIT: LX+SINK+S050 - BOTH LR AND LQ
(PAGE 2 OF 3)

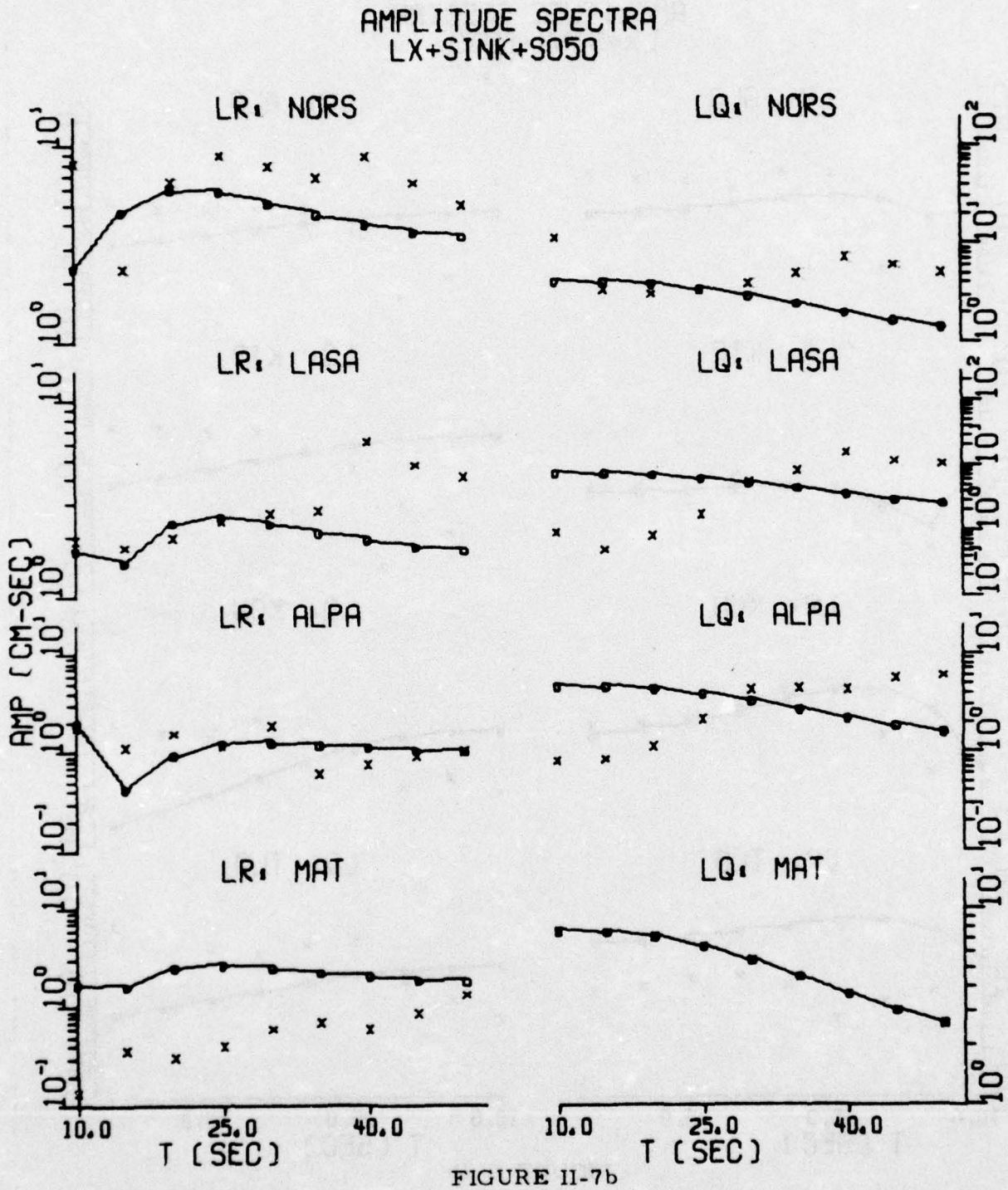

FIGURE II-7b

SPECTRAL FIT: LX+SINK+S050 - BOTH LR AND LQ
(PAGE 3 OF 3)

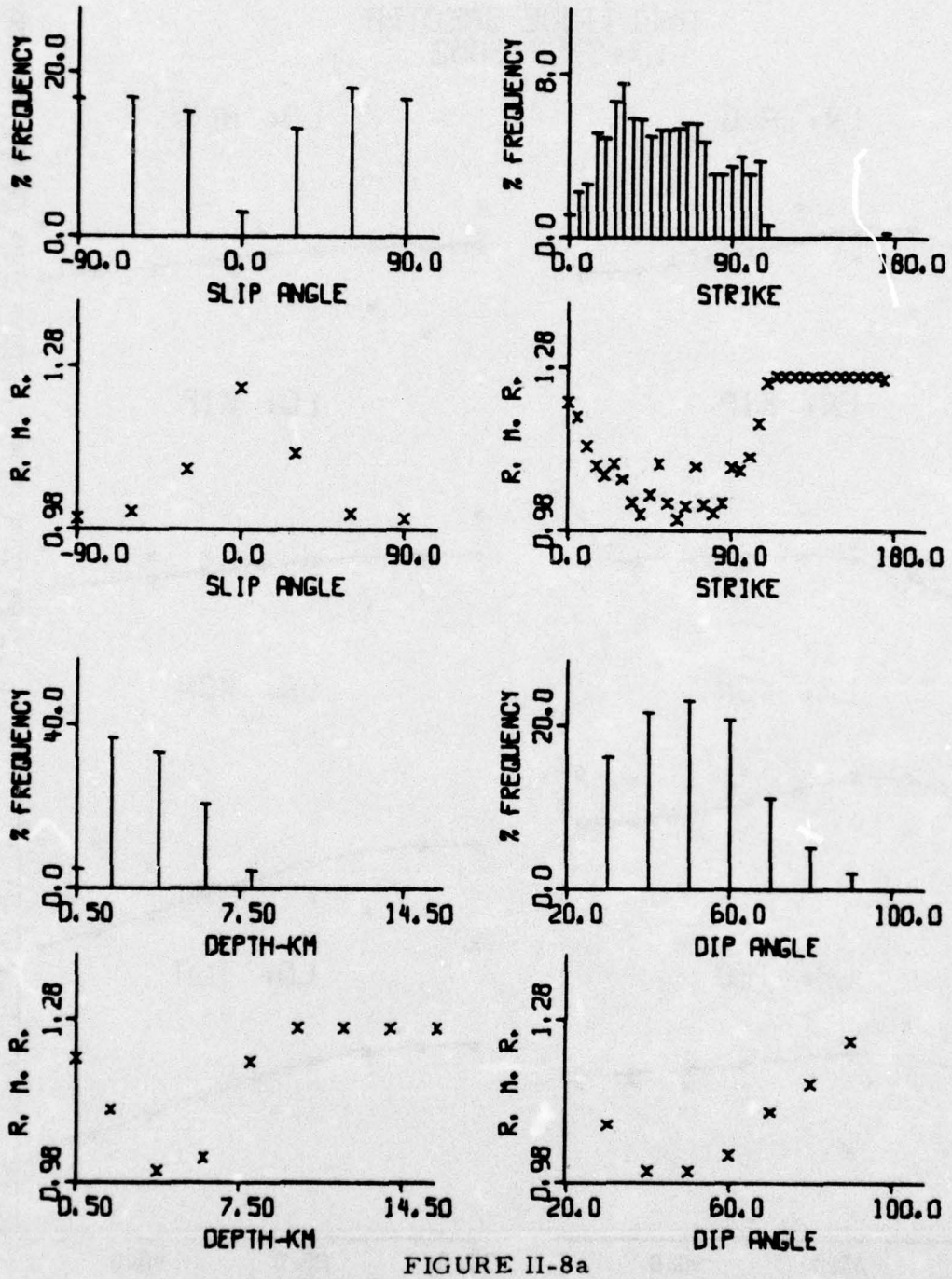

FIGURE II-8a

SOURCE PARAMETER DISTRIBUTIONS:
LX+SINK+S052 - BOTH LR AND LQ
(PAGE 1 OF 3)

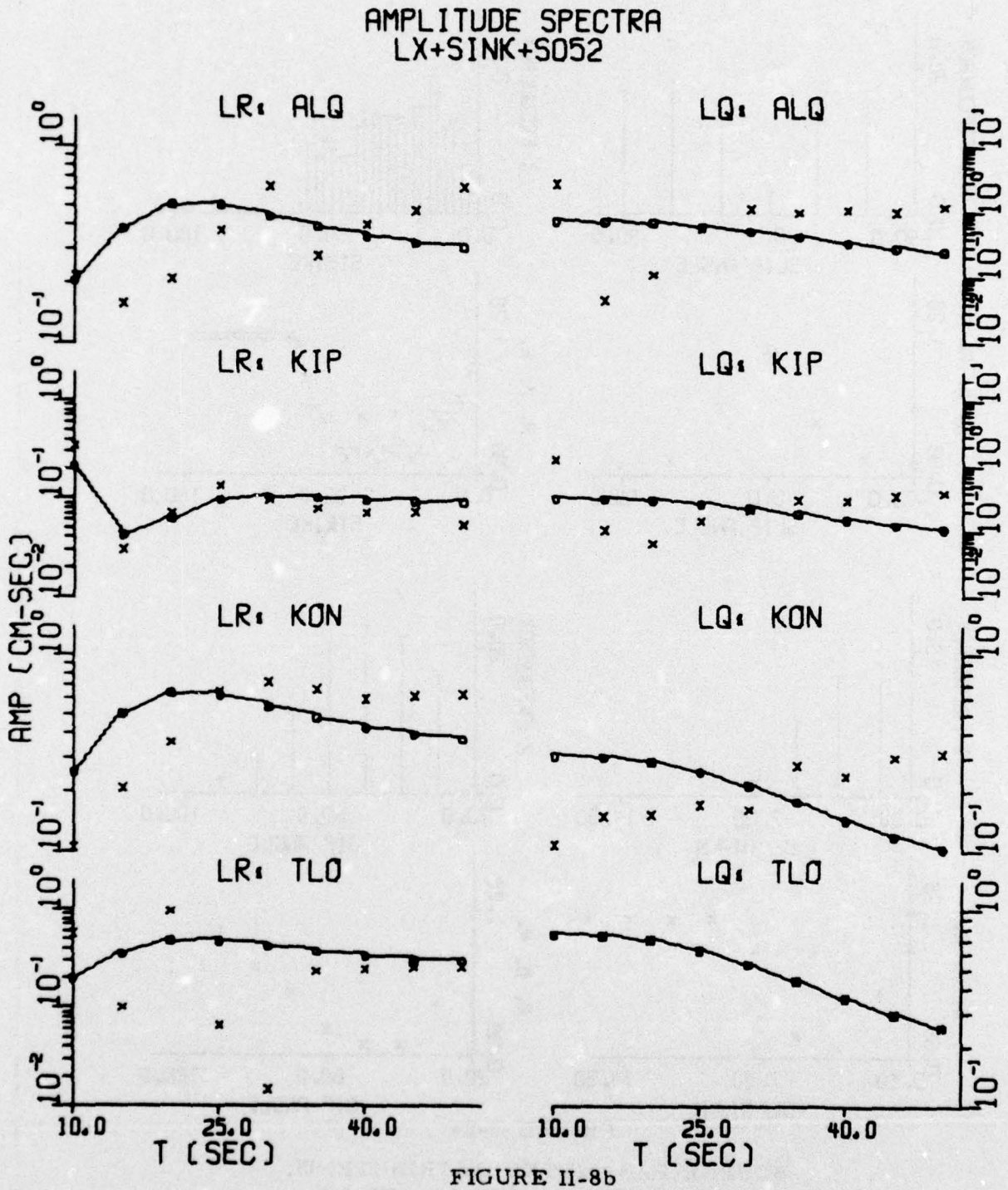

FIGURE II-8b

SPECTRAL FIT: LX+SINK+S052 - BOTH LR AND LQ
(PAGE 2 OF 3)

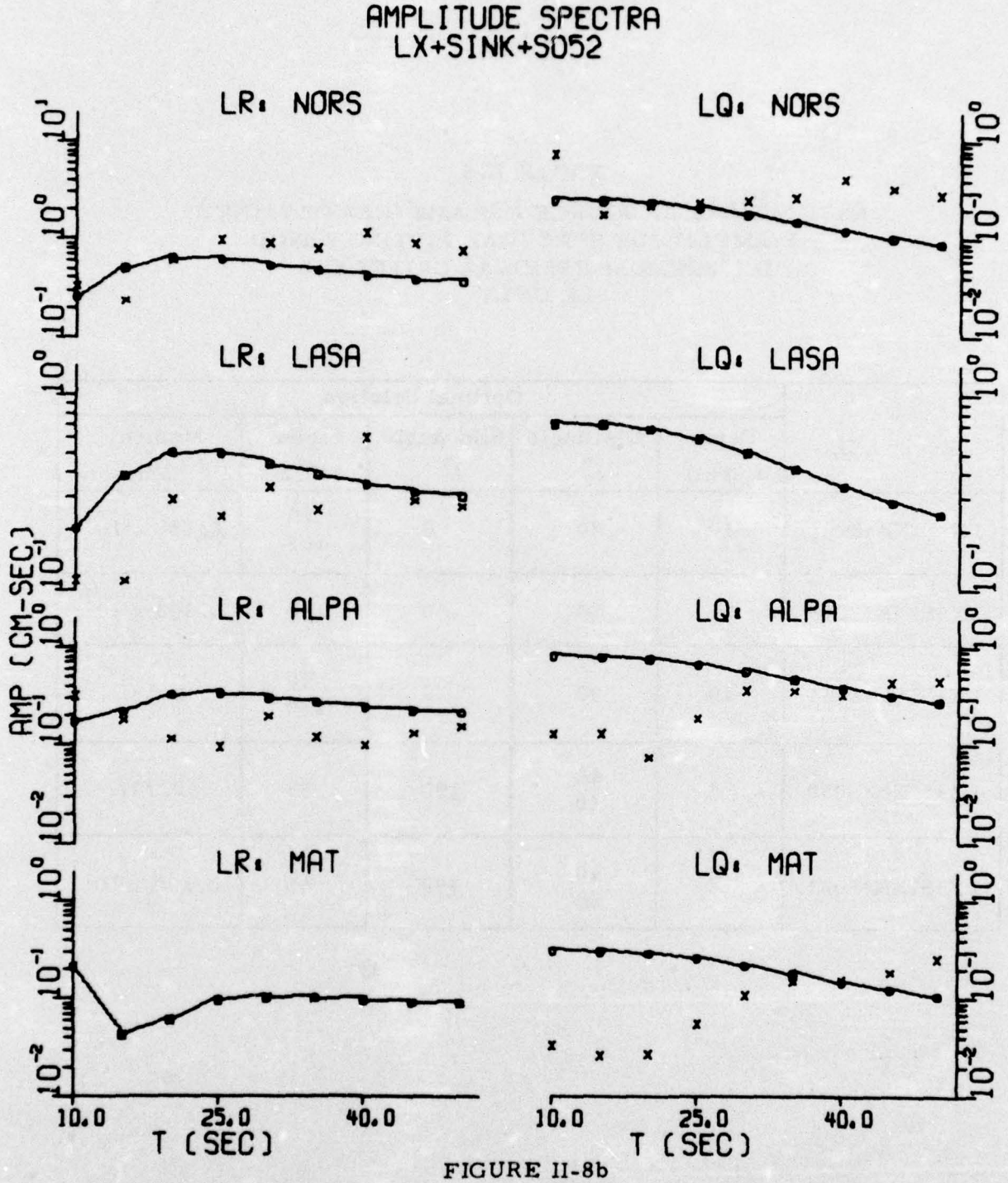

FIGURE II-8b

SPECTRAL FIT: LX+SINK+S052 - BOTH LR AND LQ
(PAGE 3 OF 3)

TABLE II-5

ESTIMATIONS OF SOURCE PARAMETERS OBTAINED
BY AMPLITUDE SPECTRAL FITTING BASED
ON MINIMUM-RESIDUAL CRITERION:
LR ONLY

Event I. D.	Optimal Solution				
	Depth h (km)	Dip Angle δ°	Slip Angle λ°	Strike $N\phi^{\circ}E$	Moment 10^{25} dyne-cm
LX+SINK+S001	10	90	0	75 165	0.188×10^{2}
LX+SINK+S018	6	50	-30	120	0.198×10^{1}
LX+SINK+S024	10	90	0	40 130	0.597
LX+SINK+S050	4	40 50	± 90	55	0.707
LX+SINK+S052	4	40 50	± 90	55	0.890×10^{-1}

TABLE II-6

ESTIMATIONS OF SOURCE PARAMETERS OBTAINED BY AMPLITUDE SPECTRAL FITTING BASED ON DISTRIBUTION-OF-MINIMUM-RESIDUAL CRITERION: LR ONLY

Event I. D.	Source Parameters							
	Depth h (km)		Dip Angle δ°		Slip Angle λ°		Strike Nϕ°E	
	Probable Range	% Confidence	Probable Range	% Confidence	Probable Range	% Confidence	Probable Range	% Confidence
LX+SINK+S001	4-12	88	40-50 80-90	45 44	±90 0	44 48	-	-
LX+SINK+S018	4-8	87	50-90	78	-60-60	87	15-50 105-140	40 33
LX+SINK+S024	4-12	92	40-50 80-90	34 42	±30 0	23 41	35-50 120-140	25 31
LX+SINK+S050	2-6	76	30-60	78	±60 ±90	34 38	15-85	79
LX+SINK+S052	2-6	92	30-60	81	±60 ±90	36 39	15-85	78

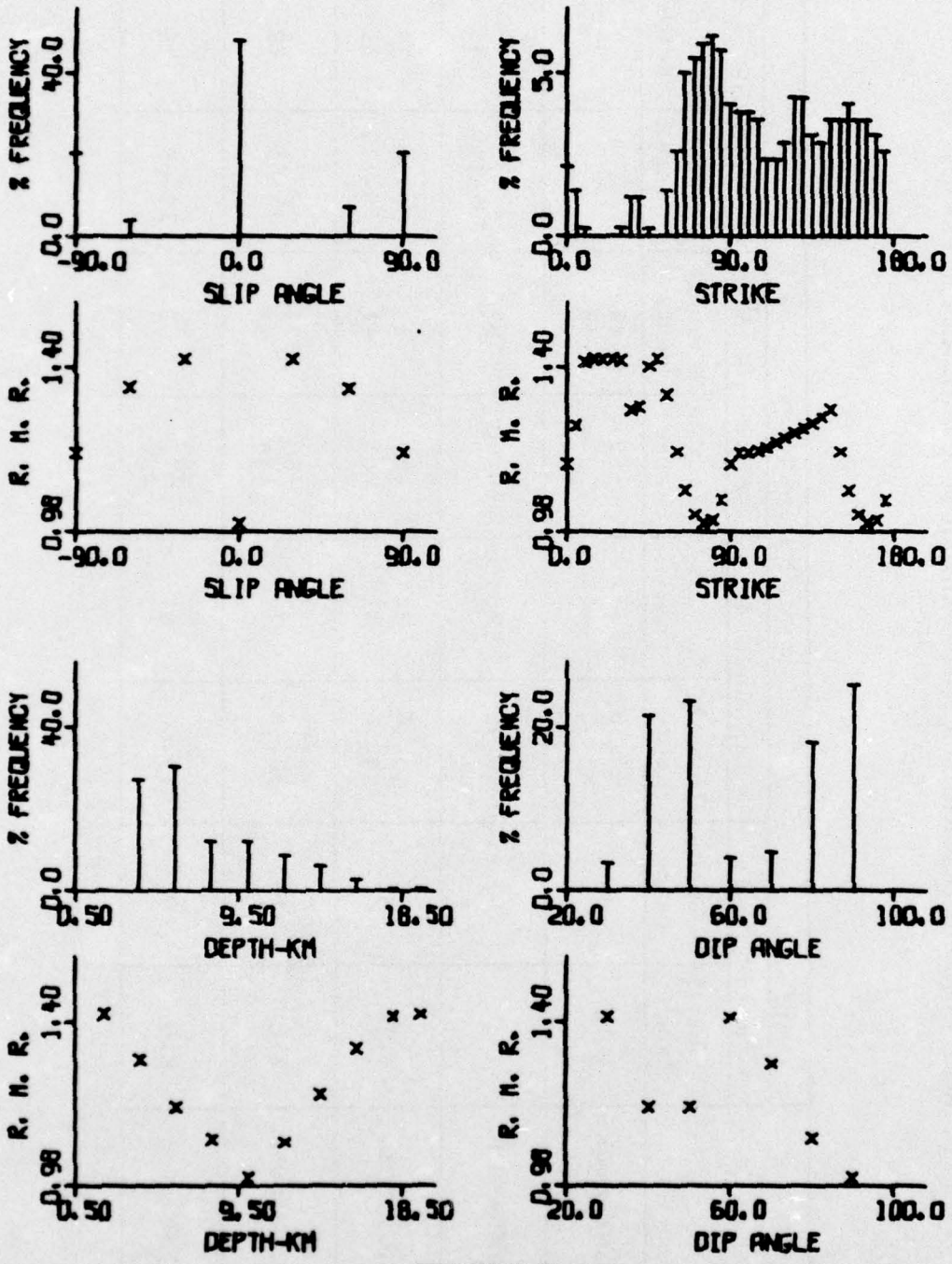

FIGURE II-9a

SOURCE PARAMETER DISTRIBUTIONS:
LX+SINK+S001 - LR ONLY
(PAGE 1 OF 3)

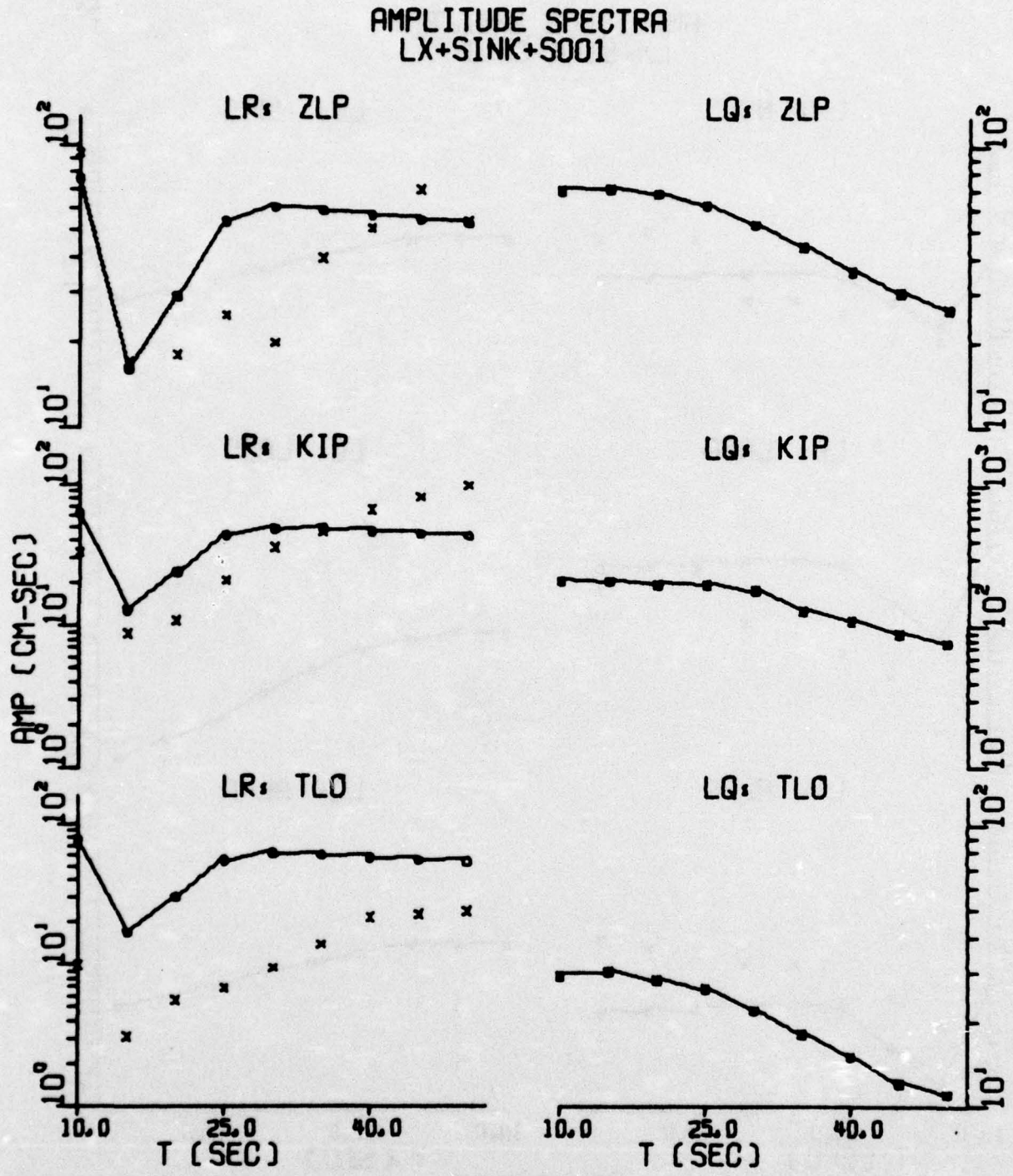

FIGURE II-9b

SPECTRAL FIT: LX+SINK+S001 - LR ONLY
(PAGE 2 OF 3)

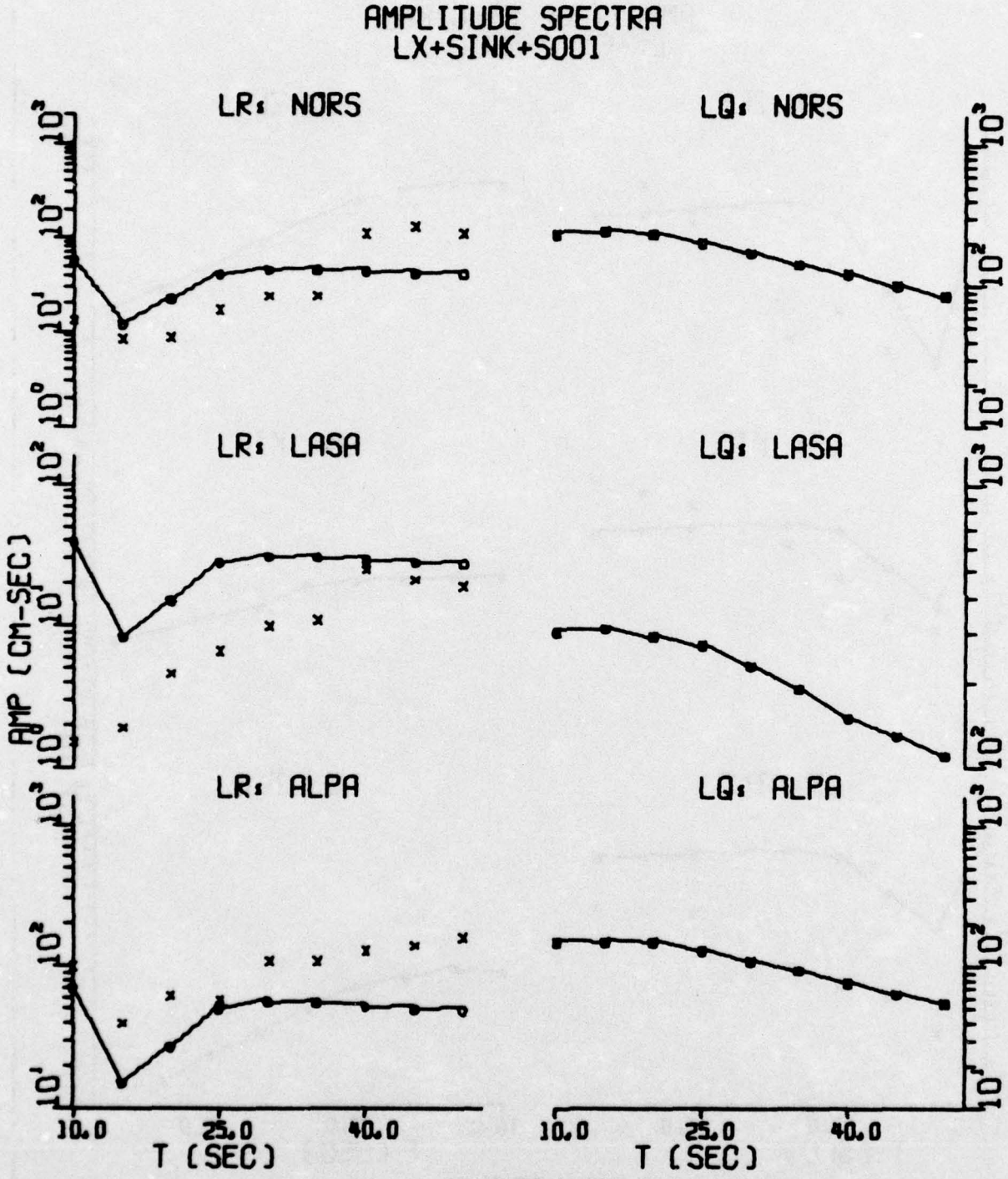

FIGURE II-9b

SPECTRAL FIT: LX+SINK+S001 - LR ONLY
(PAGE 3 OF 3)

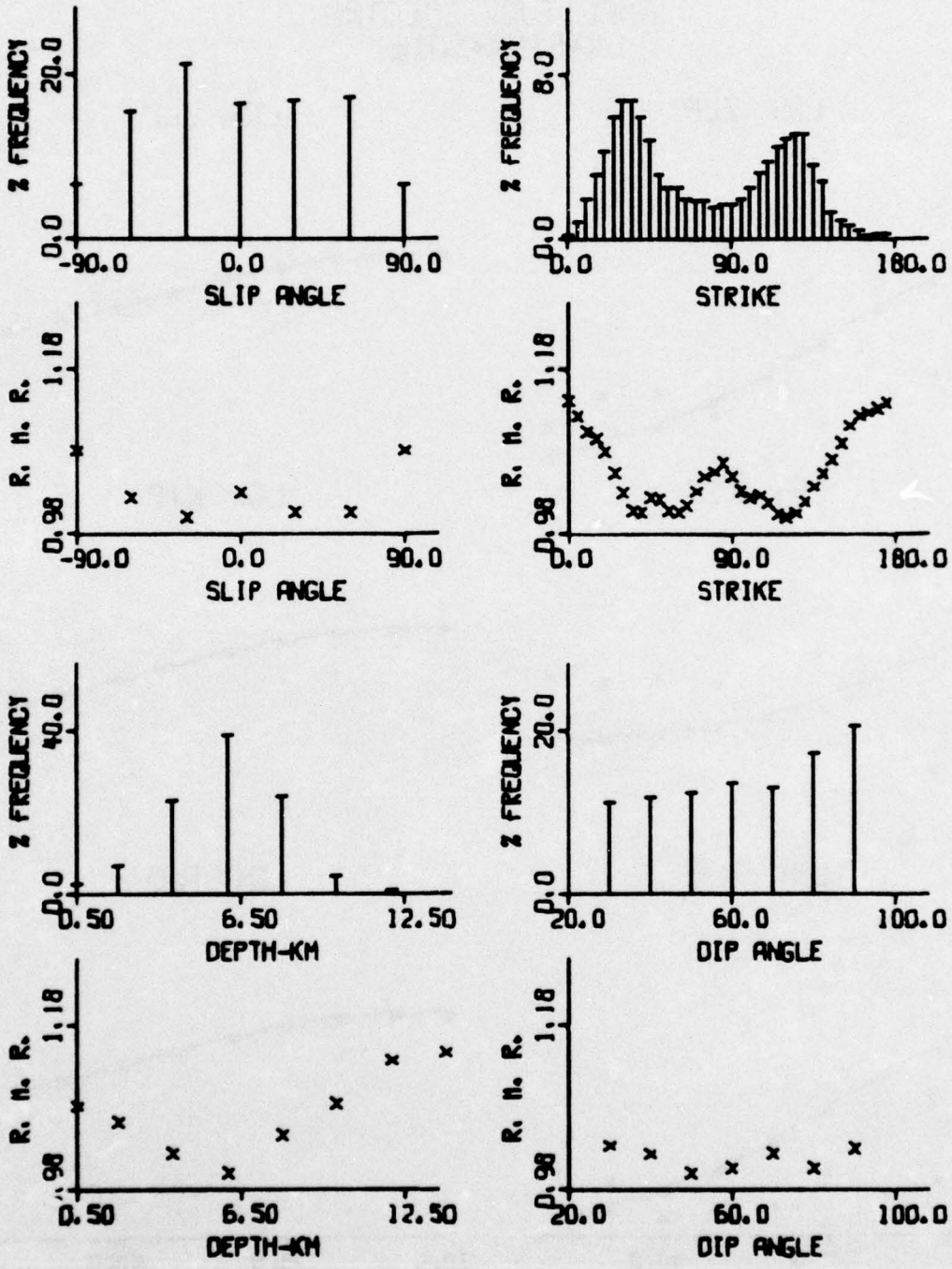

FIGURE II-10a

SOURCE PARAMETER DISTRIBUTIONS:
LX+SINK+S018 - LR ONLY
(PAGE 1 OF 3)

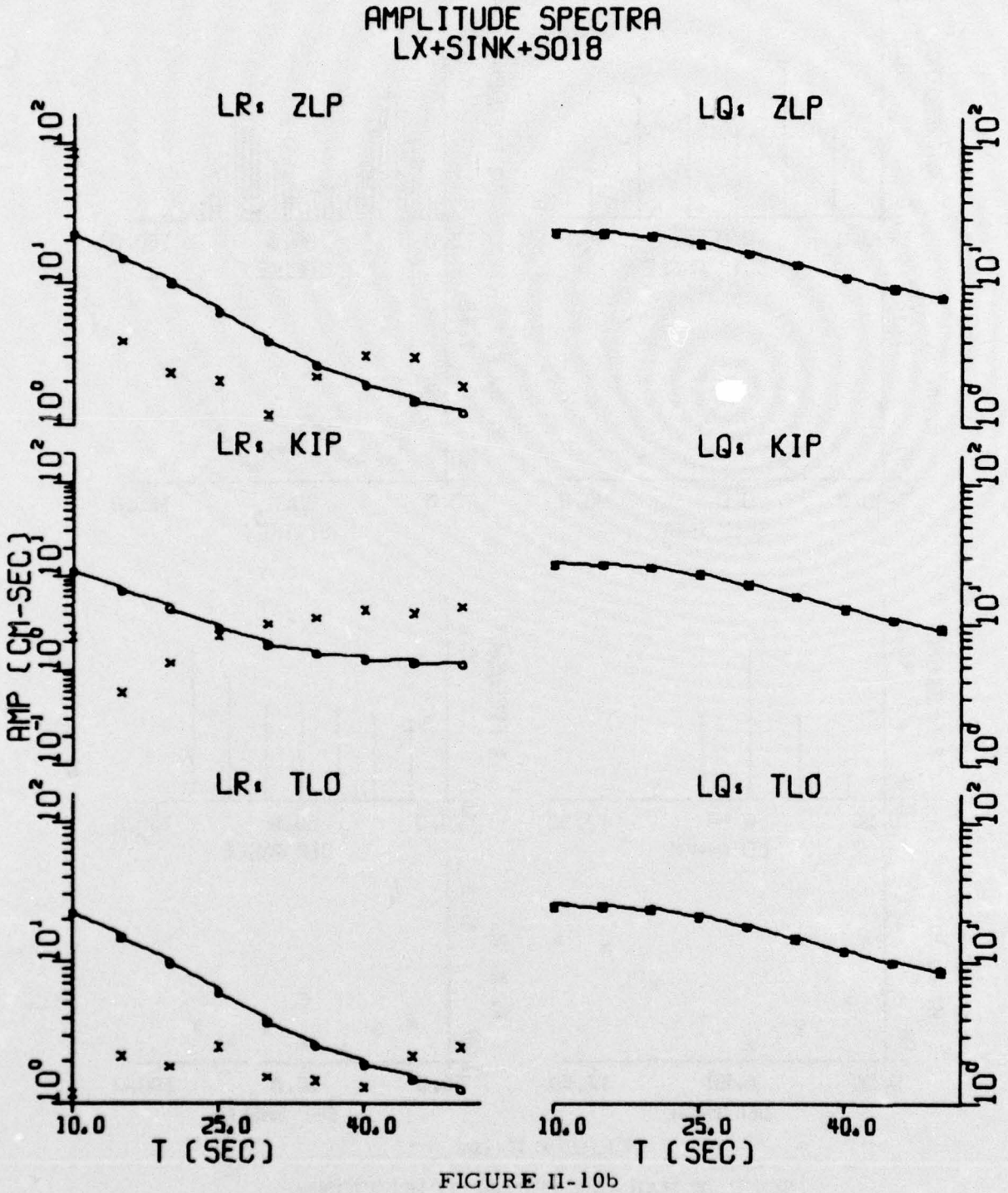

FIGURE II-10b

SPECTRAL FIT: LX+SINK+S018 - LR ONLY
(PAGE 2 OF 3)

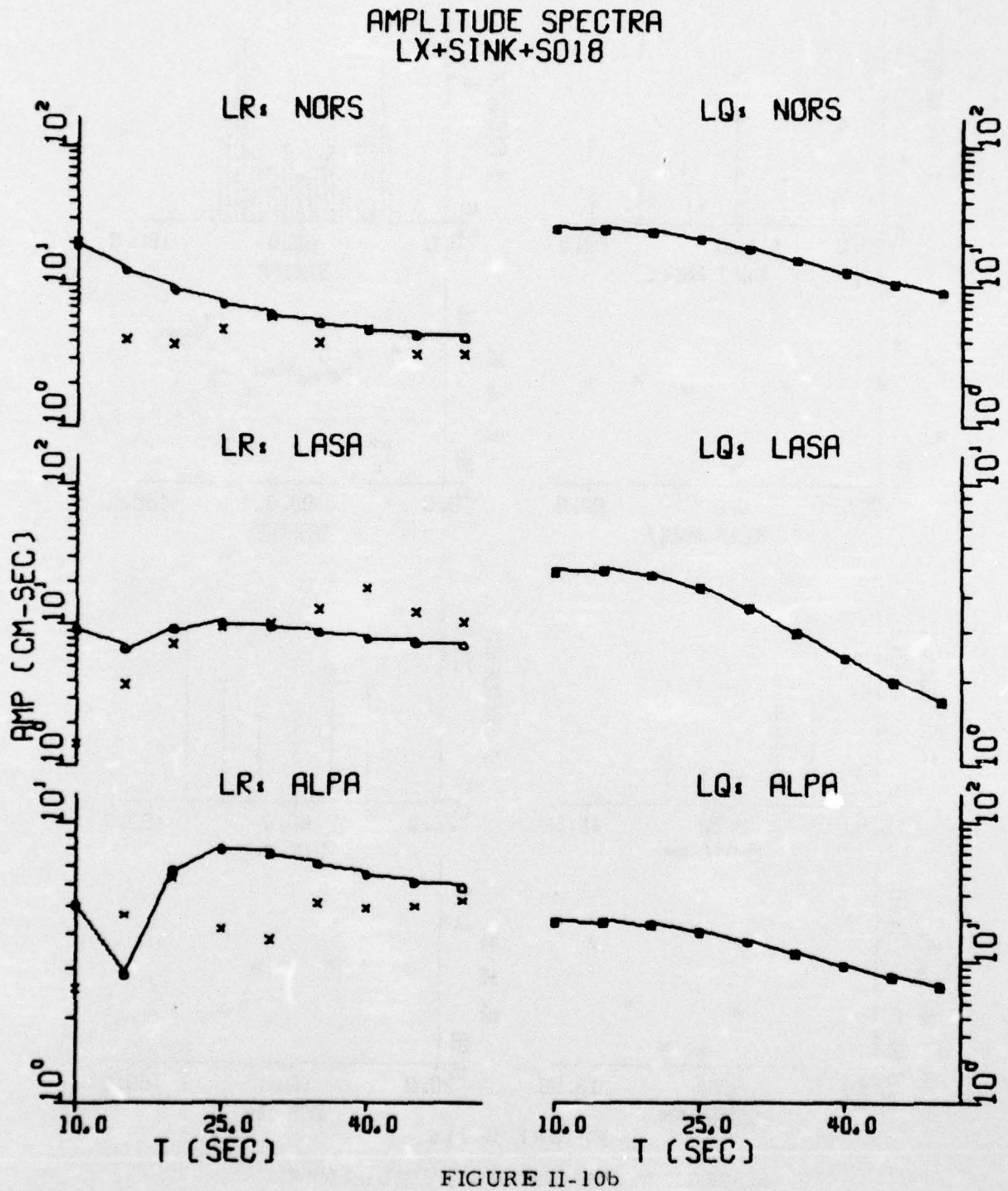

FIGURE II-10b

SPECTRAL FIT: LX+SINK+S018 - LR ONLY
(PAGE 3 OF 3)

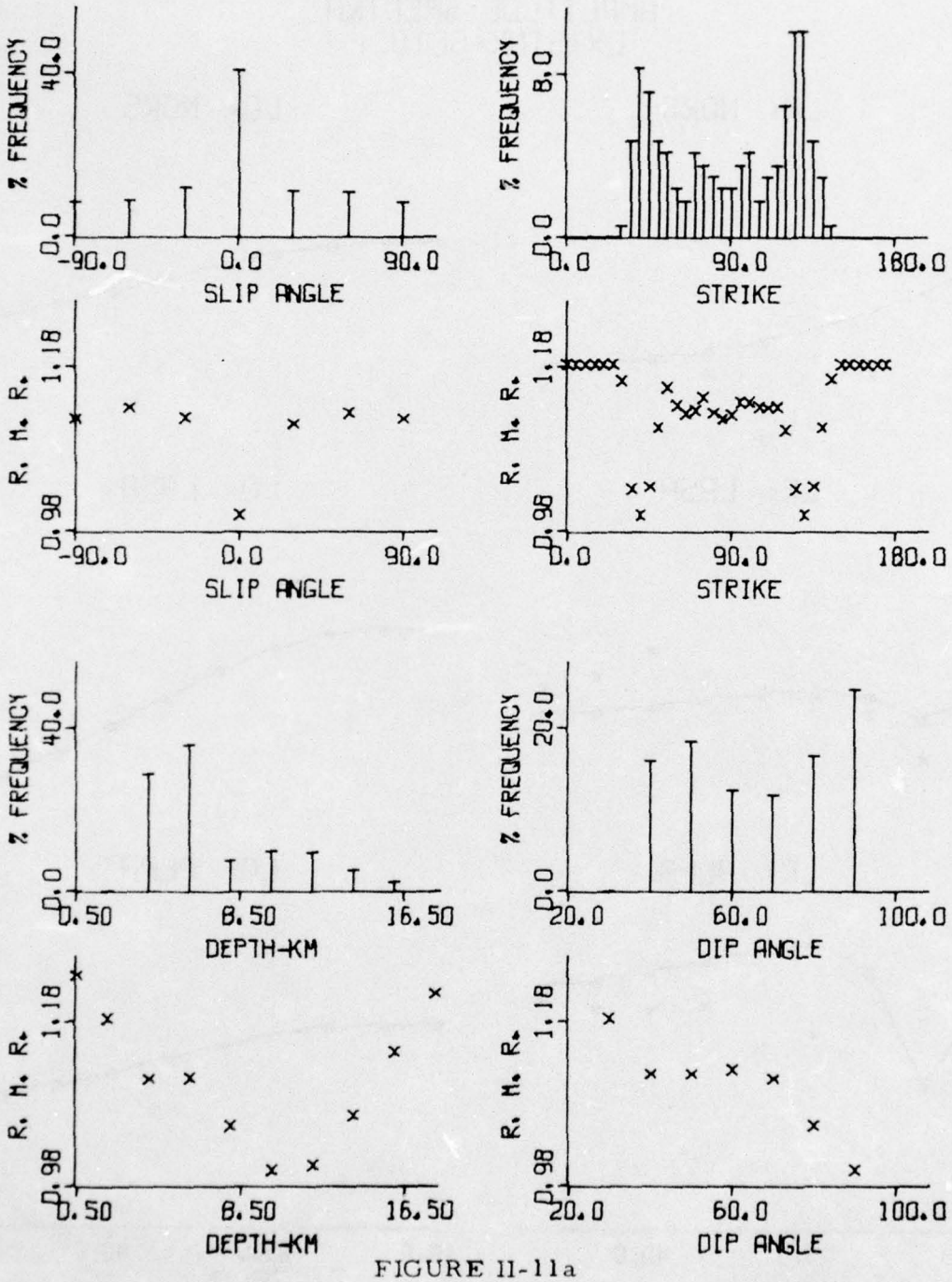

FIGURE II-11a

SOURCE PARAMETER DISTRIBUTIONS:
LX+SINK+S024 - LR ONLY
(PAGE 1 OF 3)

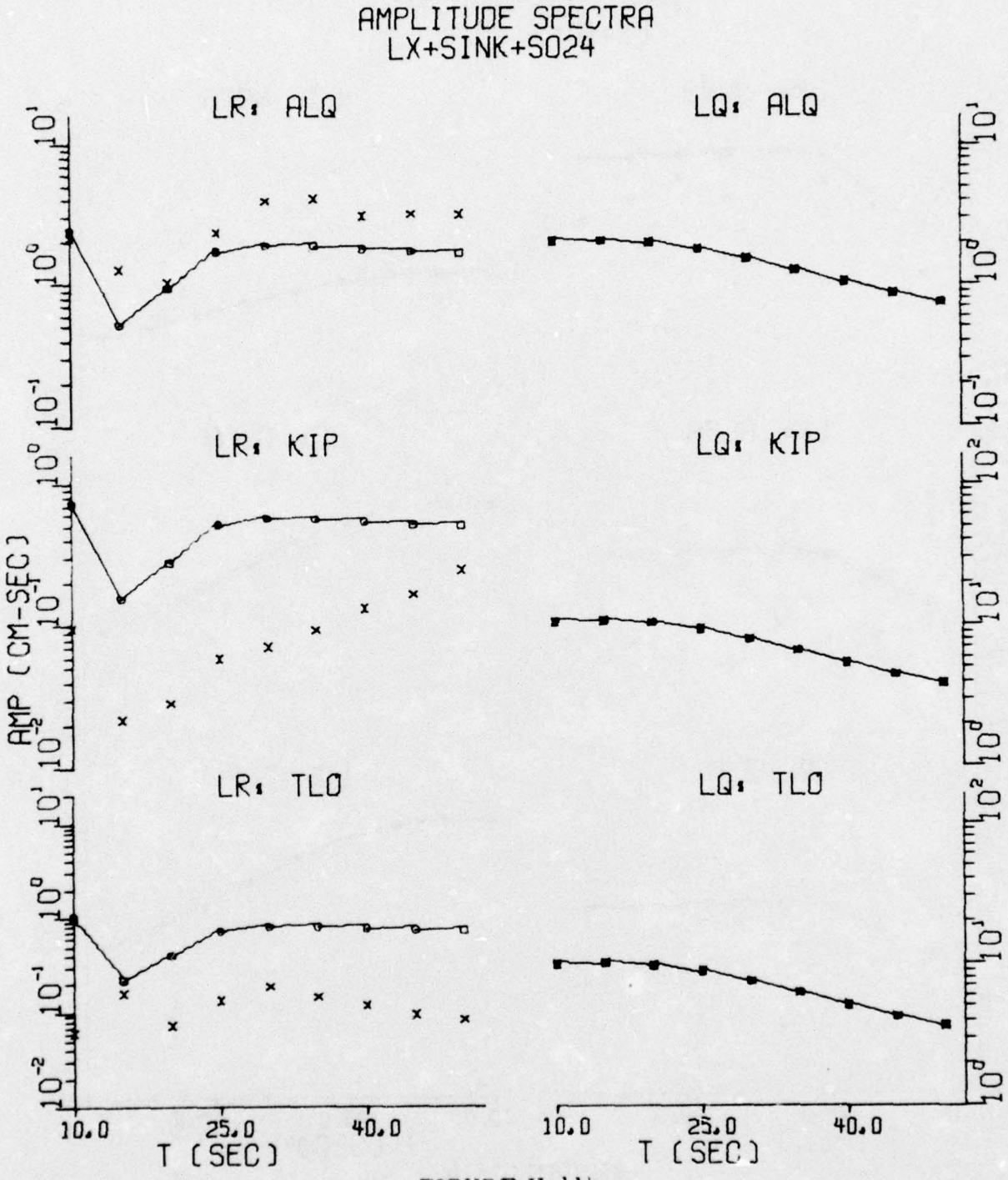

FIGURE II-11b

SPECTRAL FIT: LX+SINK+S024 - LR ONLY
(PAGE 2 OF 3)

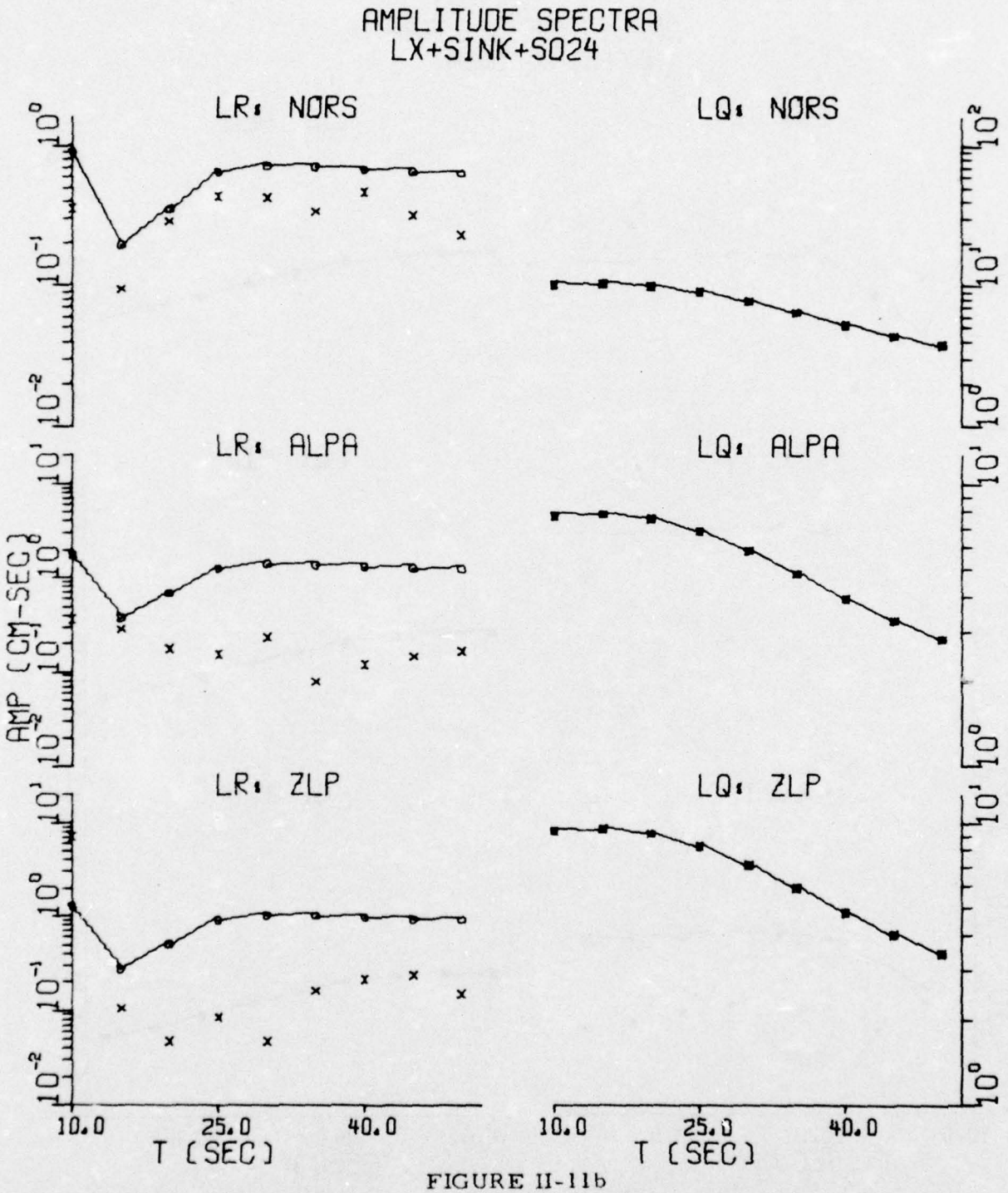

FIGURE II-11b

SPECTRAL FIT: LX+SINK+S024 - LR ONLY
(PAGE 3 OF 3)

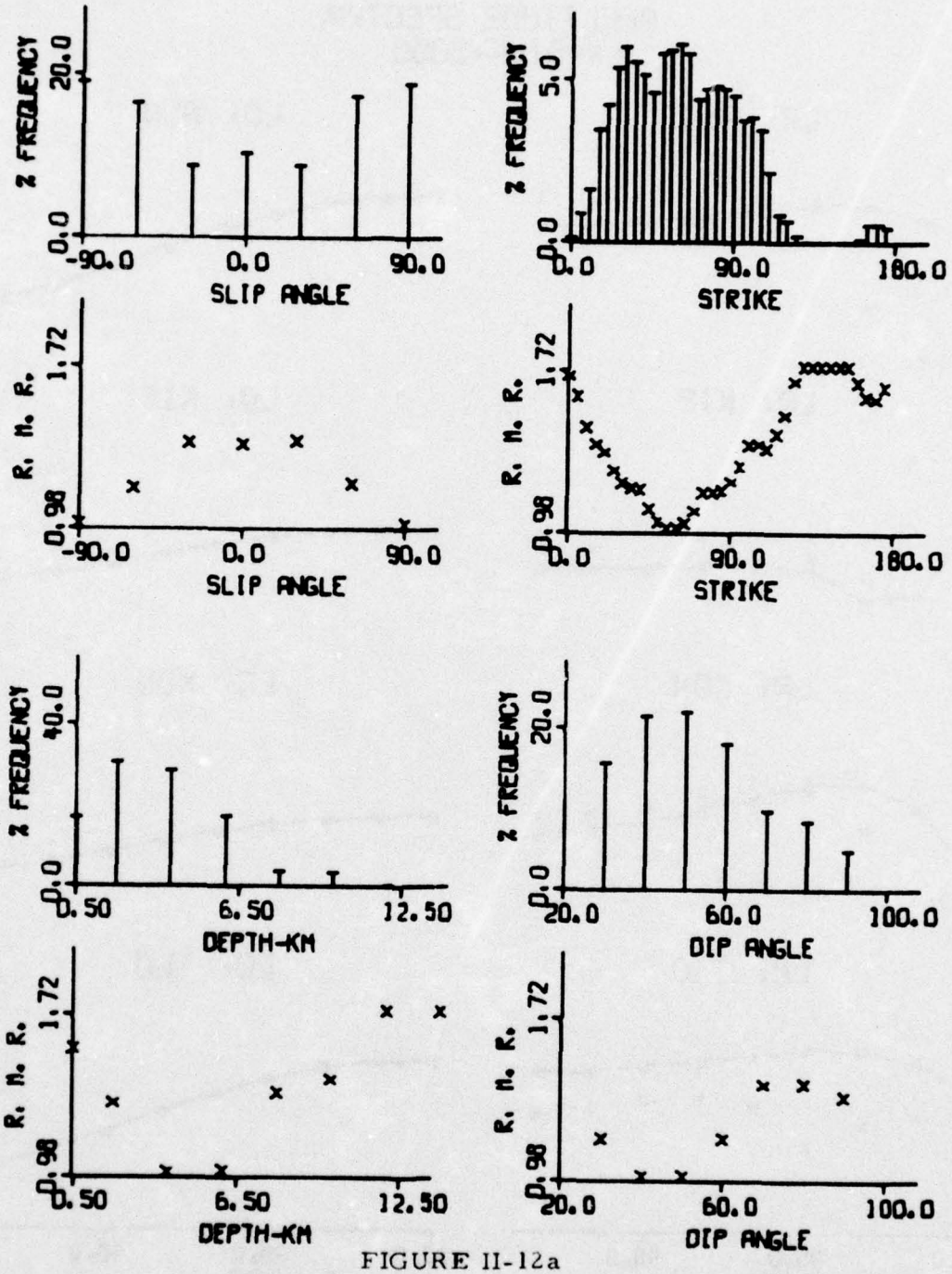

FIGURE II-12a

SOURCE PARAMETER DISTRIBUTIONS:
LX+SINK+S050 - LR ONLY
(PAGE 1 OF 3)

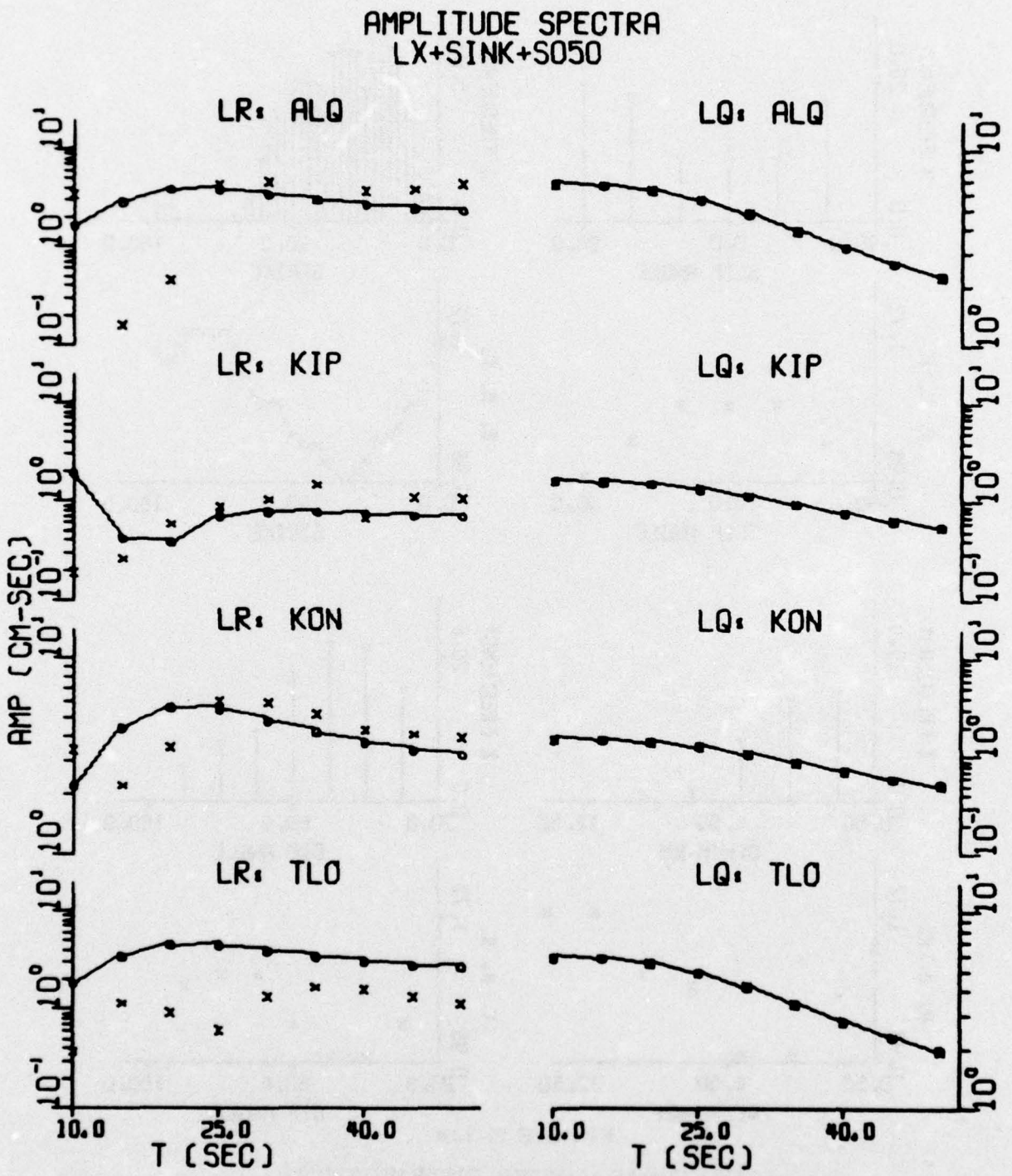

FIGURE II-12b

SPECTRAL FIT: LX+SINK+S050 - LR ONLY
(PAGE 2 OF 3)

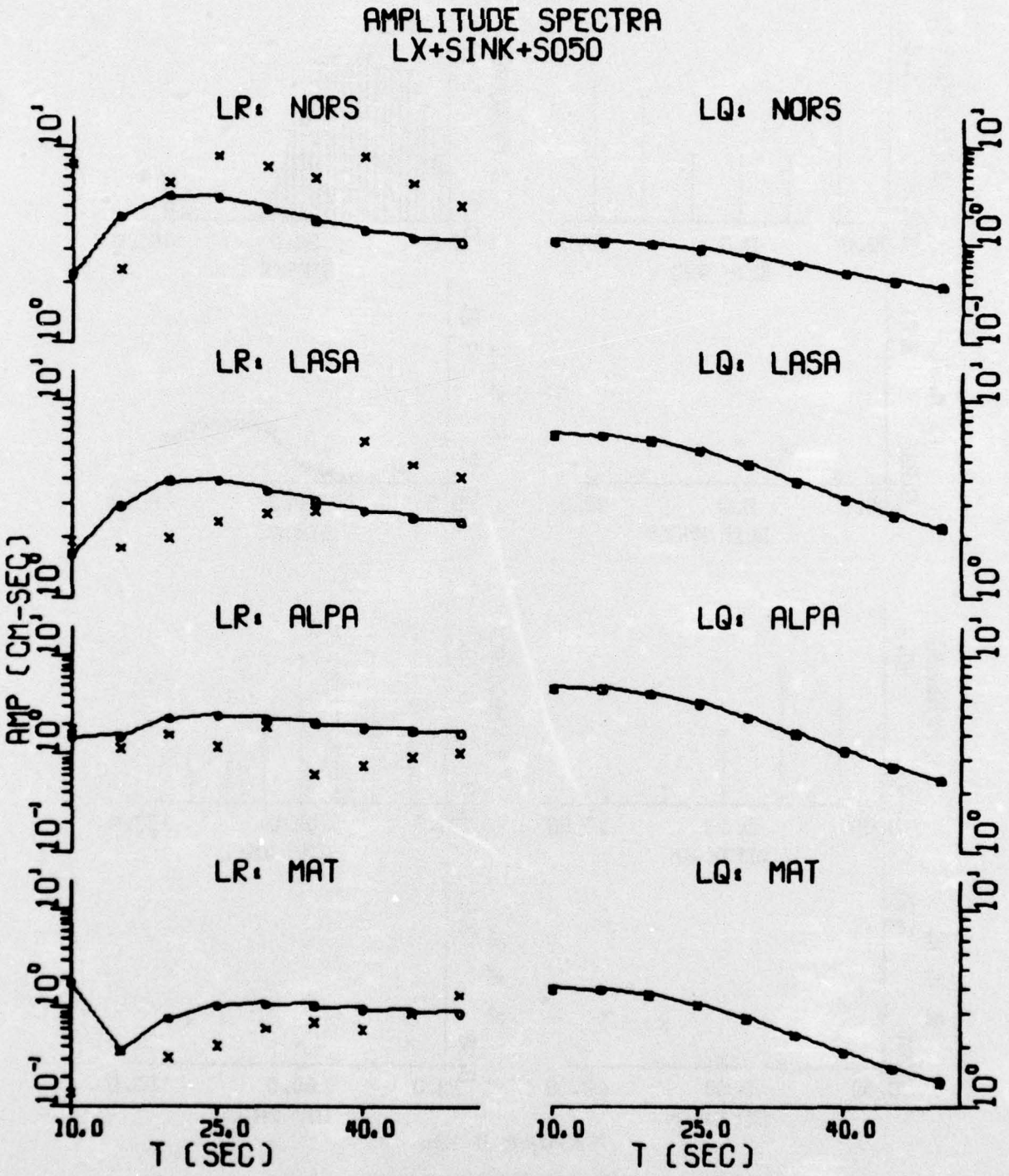

FIGURE II-12b

SPECTRAL FIT: LX+SINK+S050 - LR ONLY
(PAGE 3 OF 3)

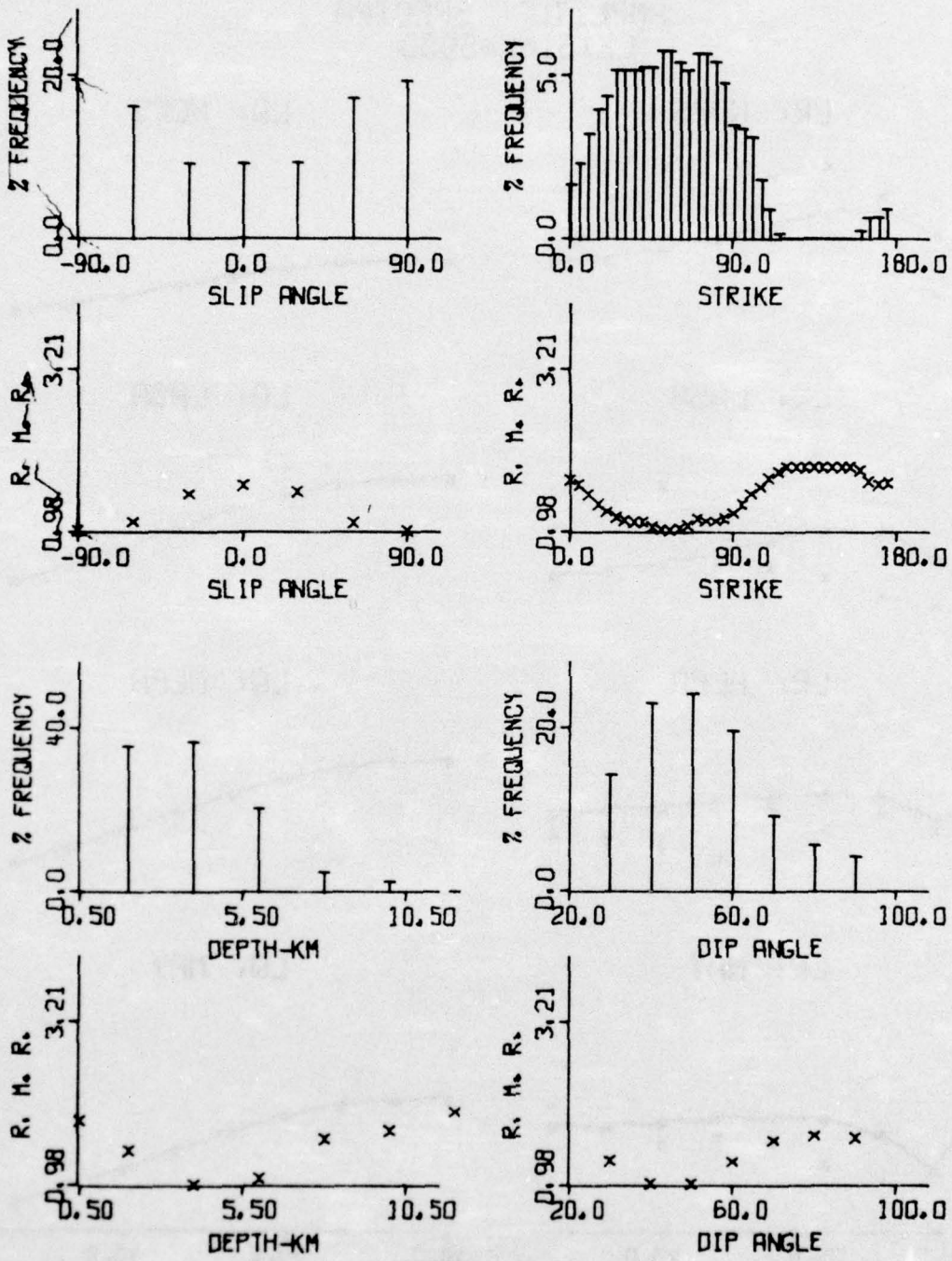

FIGURE II-13a

SOURCE PARAMETER DISTRIBUTIONS:
LX+SINK+S052 - LR ONLY
(PAGE 1 OF 3)

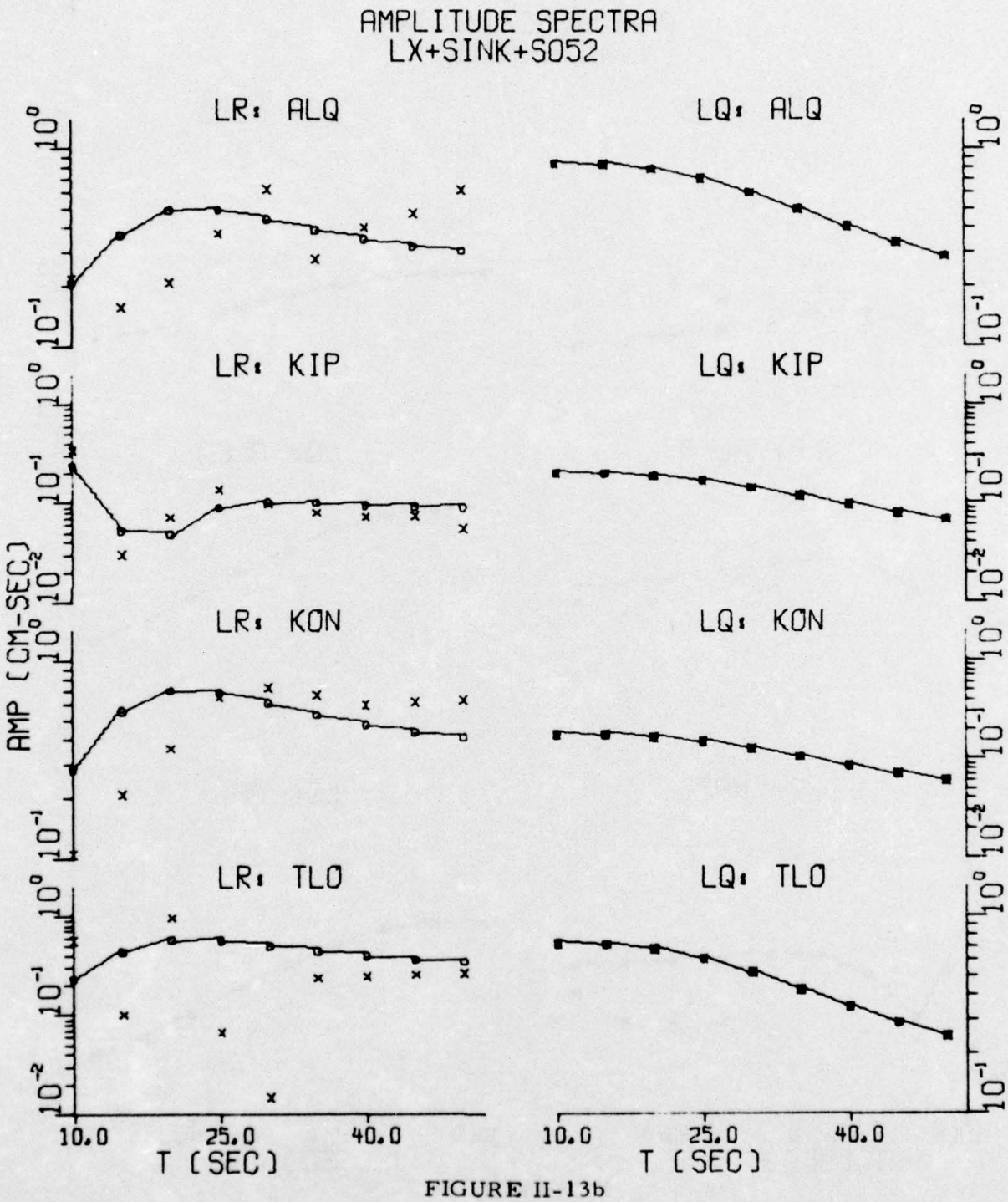

FIGURE II-13b

SPECTRAL FIT: LX+SINK+S052 - LR ONLY

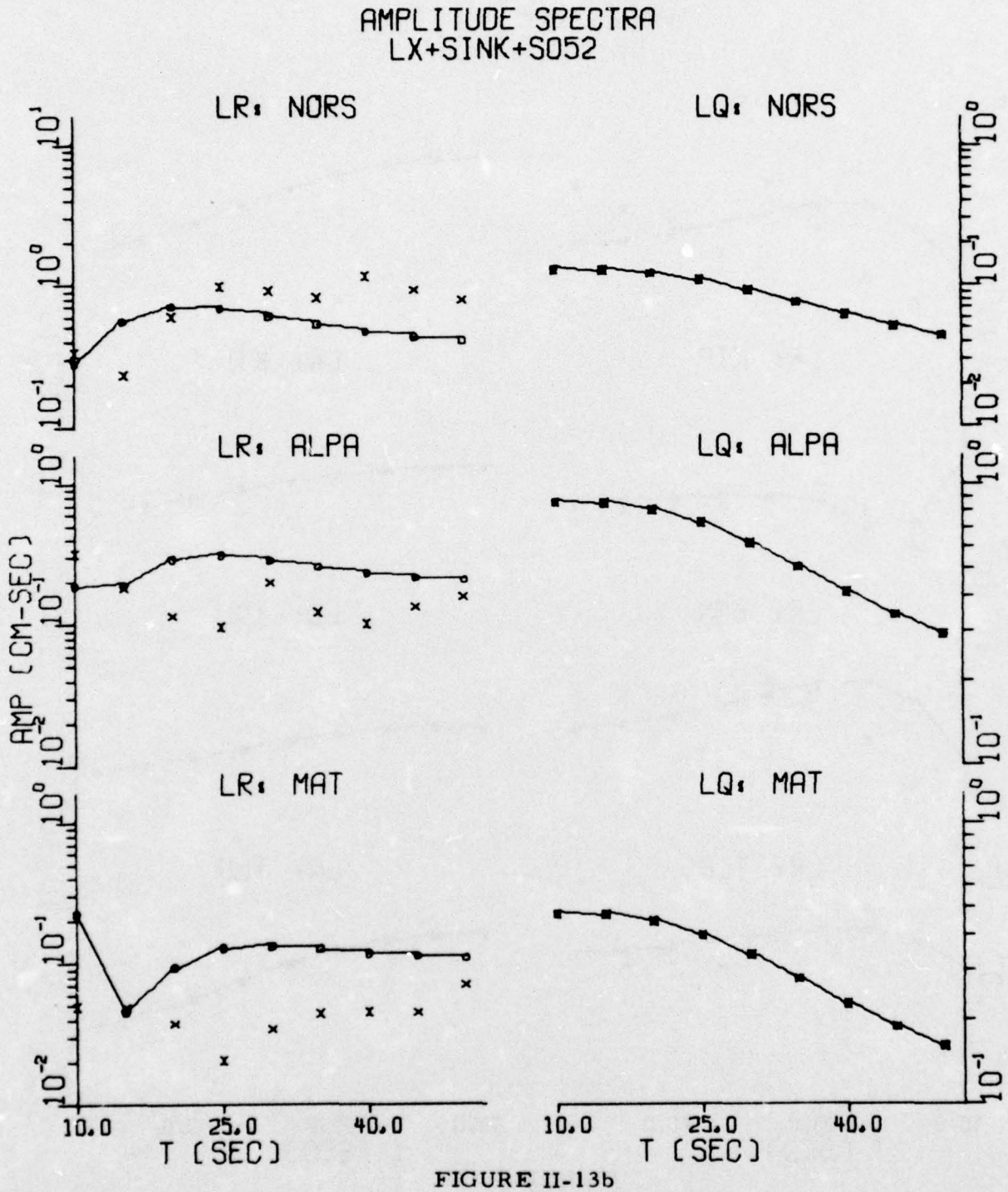

FIGURE II-13b

SPECTRAL FIT: LX+SINK+S052 - LR ONLY
(PAGE 3 OF 3)

and S024. In fact, for events LX+SINK+S050 and S052, the Love wave fits of which are compatible with their Rayleigh wave fits, two spectral fittings have yielded practically the same source parameter estimation. For events LX+SINK+S001 and S024, the Love wave fits of which are poor, the spectral fitting using Rayleigh wave only has changed the source mechanism solution from dip-slip to vertical strike-slip. This difference can be reasonably explained based on the observed fact that the theoretical Rayleigh wave amplitude spectra of the pure dip-slip (slip angle of 90^{o}) and the vertical strike-slip fault are very similar in shape, and the addition of the poor Love wave data in the spectral fitting does not help in resolving this similarity. Although based on the minimum-residual criterion, two spectral fittings have resulted in quite different source mechanisms for two events in this group. Based on the distribution-of-minimum-residual criterion, these fittings give more or less the same probable ranges in the source parameter estimation.

Among these five events, events LX+SINK+S018 and S052 are chosen to be used as the reference event in the ratio-of-events fitting, based on the observation that the spatial fitting solutions for these two events seem to be more stable and yield a better spectral fit. The ratio-of-events fitting method is applied to the event LX+SINK+S001 using LX+SINK+S018 as a reference and to events LX+SINK+S024 and S050 using LX+SINK+S052 as a reference. Referring to Table II-2, these pairs of events are picked such that two events in the same pair have the maximum number of common observation stations. Estimations of the source parameters obtained by the ratio-of-events fitting are presented in Tables II-7 through II-9, with the distributions of minimum-residuals shown in Figures II-14 through II-16. For the event LX+SINK+S050, the ratio-of-events fitting has yielded an estimation of the same source parameter as the spectral fitting. For the event LX+SINK+S001, the source parameter estimation by the ratio-of-events fitting favors the strike-slip fault, while for the event LX+SINK+S024, the estimation favors the dip-slip fault.

TABLE II-7

ESTIMATIONS OF SOURCE PARAMETERS
OBTAINED BY RATIO-OF-EVENTS FITTING

Reference Event : LX+SINK+S018

Solutions for Event: LX+SINK+S001 (SK+01/R-18)

A. Solution by Minimum-Residual Criterion

Event I. D.	Optimal Solution				
	Depth h (km)	Dip Angle δ^{o}	Slip Angle λ^{o}	Strike $N\phi^{o}E$	Moment 10^{25} dyne-cm
LX+SINK+S001	8	80	-30	30	0.148×10^{2}

B. Solution by Distribution-Of-Minimum-Residual Criterion

Event I. D. : LX+SINK+S001		
Source Parameters	Probable Range	% Confidence
h	6-10	84
δ	70-90	79
λ	-30, 0, +30	93
ϕ	25-40 115-130	23 38

TABLE II-8

ESTIMATIONS OF SOURCE PARAMETERS
OBTAINED BY RATIO-OF-EVENTS FITTING

Reference Event : LX+SINK+S052

Solutions for Event: LX+SINK+S024 (SK+24/R-52)

A. Solution by Minimum-Residual Criterion

Event I. D.	Optimal Solution				
	Depth h (km)	Dip Angle δ^o	Slip Angle λ^o	Strike $N\phi^oE$	Moment 10^{25} dyne-cm
LX+SINK+S024	4	40 50	± 90	65	0.179

B. Solution by Distribution-Of-Minimum-Residual Criterion

Event I. D. : LX+SINK+S024		
Source Parameters	Probable Range	% Confidence
h	0.5-4	90
δ	30-60	60
λ	-	-
ϕ	-	-

TABLE II-9

ESTIMATIONS OF SOURCE PARAMETERS
OBTAINED BY RATIO-OF-EVENTS FITTING

Reference Event : LX+SINK+S052

Solutions for Event: LX+SINK+S050 (SK+50/R-52)

A. Solution by Minimum-Residual Criterion

Event I. D.	Optimal Solution				
	Depth h (km)	Dip Angle δ°	Slip Angle λ°	Strike $N\phi^\circ E$	Moment 10^{25} dyne-cm
LX+SINK+S050	4	40 50	$\pm$90	65	0.828

B. Solution by Distribution-Of-Minimum-Residual Criterion

Event I. D. : LX+SINK+S050		
Source Parameters	Probable Range	% Confidence
h	0.5-6	84
δ	30-60	82
λ	$\pm$60 $\pm$90	30 42
ϕ	30-90	66

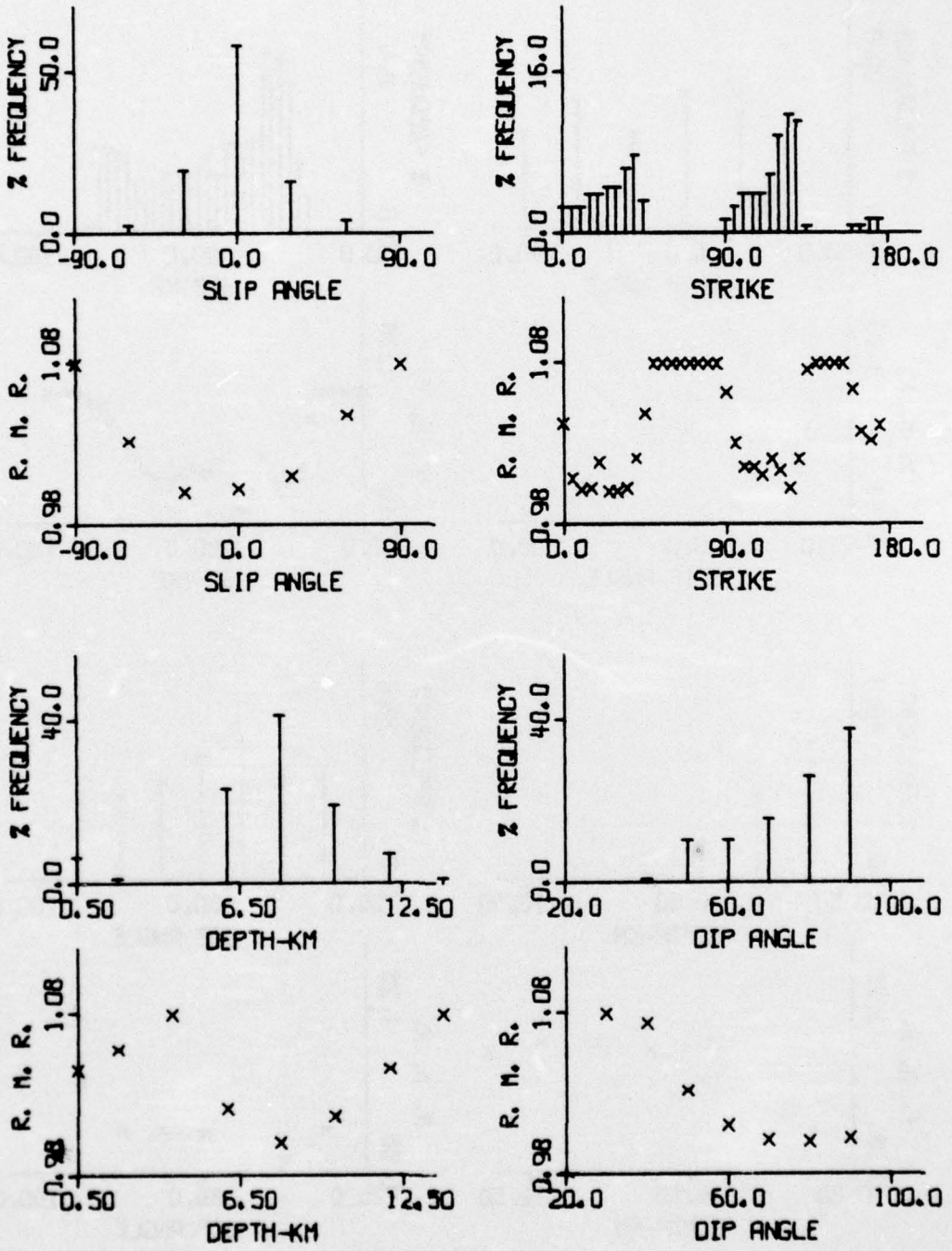

FIGURE II-14

SOURCE PARAMETER DISTRIBUTIONS BY RATIO-OF-EVENTS:
LX+SINK+S001

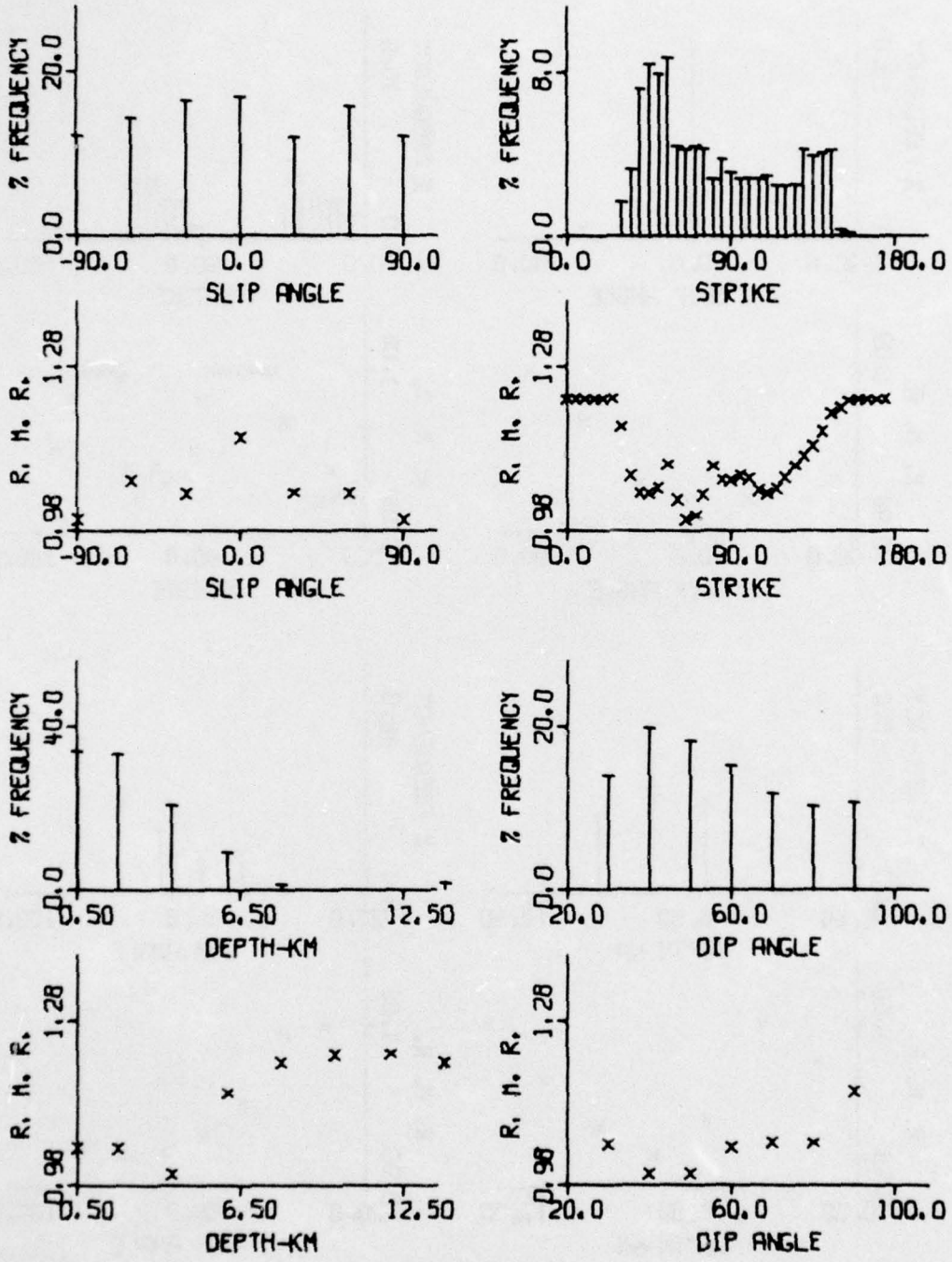

FIGURE II-15

SOURCE PARAMETER DISTRIBUTIONS BY RATIO-OF-EVENTS:
LX+SINK+S024

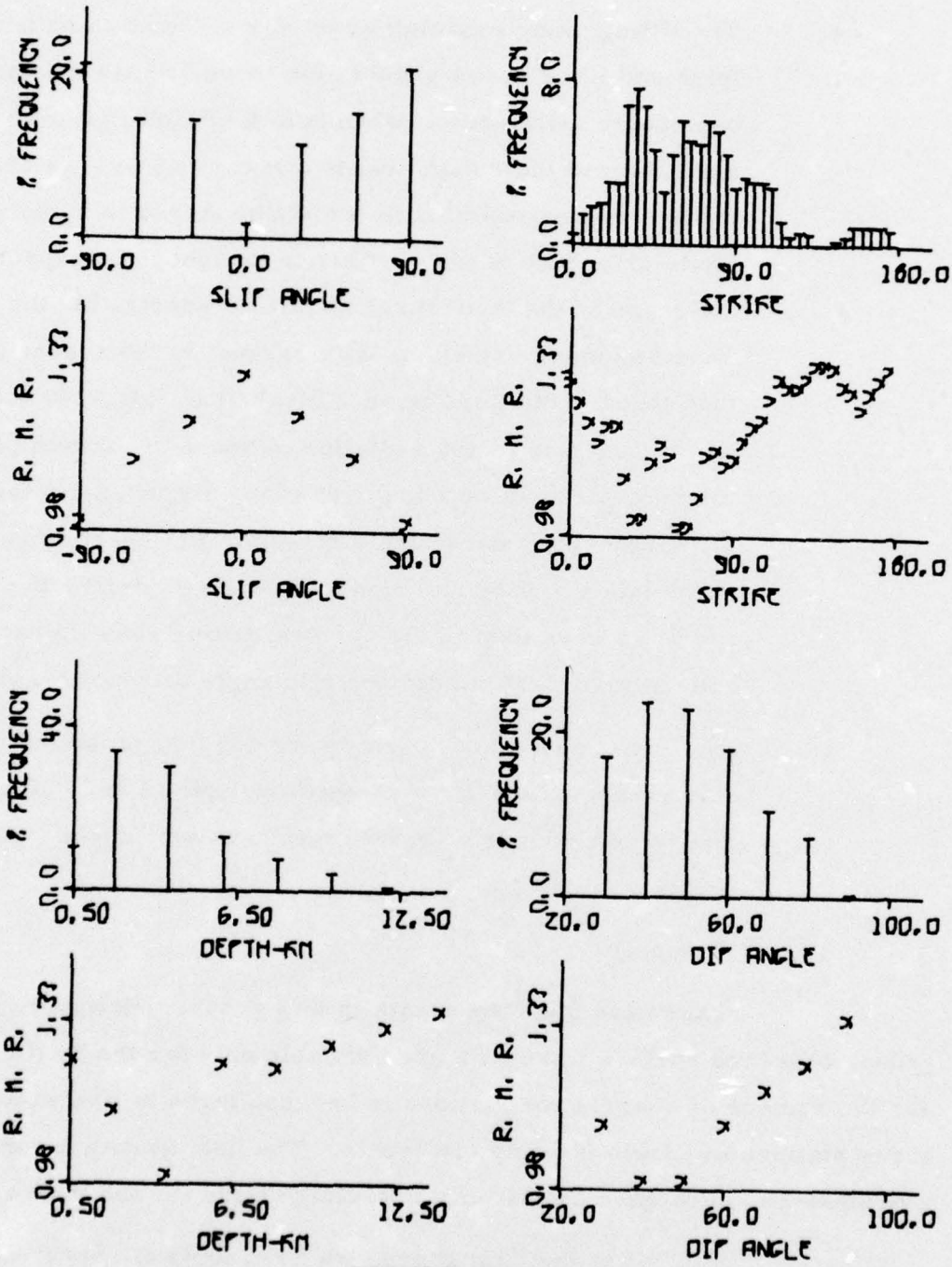

FIGURE II-16

SOURCE PARAMETER DISTRIBUTIONS BY RATIO-OF-EVENTS:
LX+SINK+S050

The major results from the analysis of this group are as follows:

- The fitting using Rayleigh wave only and that using both Rayleigh and Love waves should give more or less the same source parameter estimation. When both Rayleigh and Love wave data are good and their data quality are compatible, we can expect to have more resolution in the strike direction by using both Rayleigh and Love wave. This is thought to be expected, since the shape of the theoretical amplitude spectra for the Rayleigh wave has more variations with respect to the source parameters than that for the Love wave (Turnbull et al., 1973), and the theoretical Love wave radiation patterns of various periods of interest (10 to 50 seconds) and have sharper nodes for the better diagnosis of the strike direction. However, when the Love wave data are poor as compared to the Rayleigh, the addition of the Love wave data in the spectral fitting sometimes will change the estimation of the dip and slip angle very noticeably.

- The estimated source parameters for this group indicate that five events all occurred at shallow depth (4 km - 10 km) with two possible kinds of source mechanisms: dip-slip and vertical strike-slip faults.

2. Group-II

There are fourteen events in this group. However, for this group, observed surface wave data are available only for the Rayleigh wave, and the number of observation stations is between three to five with all three array stations available for only six events. The data quality for this group, nevertheless, is as good as that of the Rayleigh wave for the first group.

Similar to the first group, we first apply the spectral fitting method to each event. The estimations of the source parameters based on

the minimum-residual criterion are listed in Table II-10, and those based on the distribution-of-minimum-residual criterion are listed in Table II-11. The distributions of minimum residuals of each parameter of each event are given in Appendix B. These results again indicate that for this group there are two kinds of source mechanisms --dip-slip and vertical strike-slip fault -- and the focal depths of these events are all shallow, ranging between 4 km and 14 km.

We also apply the ratio-of-events fitting method to these events using the event LX+SINK+S010 as a reference. The event LX+SINK+S010 is chosen to be the reference because: (1) this event has better spectral fits, especially for three array stations; (2) the estimation of the focal depth from the spectral fitting agrees quite well with the PDE depth; and (3) all other events in this group have the largest number of common observation stations with this event. The results obtained from the ratio-of-events fitting method are presented in Tables II-12 and II-13.

Referring to Tables II-10 and II-12, which are based on the minimum-residual criterion, there is good agreement between the focal depth estimation from the spectral fitting and that from the ratio-of-events fitting. Although for several events two fittings have yielded quite different estimations of the dip and the slip angle based on the minimum-residual criterion, the probable ranges of the dip and the slip angle estimations (see Tables II-11 and II-13) obtained from the fitting are very similar. This is the same situation that was observed and discussed in the first group.

In Figure II-17, we have plotted the estimated seismic moment (m_o) versus bodywave magnitude (m_b) for each event, in both the first and the second group, in relation to the ω^2-model determined by Tsai (1972). We see that there is close agreement.

TABLE II-10

ESTIMATIONS OF SOURCE PARAMETERS OBTAINED
BY AMPLITUDE SPECTRAL FITTING BASED
ON MINIMUM-RESIDUAL CRITERION
(PAGE 1 OF 2)

Event I. D.	Optimal Solution				
	Depth h (km)	Dip Angle δ^o	Slip Angle λ^o	Strike $N\phi^oE$	Moment 10^{25} dyne-cm
LX+SINK+S004	10	90	0	30 120	0.391
LX+SINK+S005	4	40	-60	100	0.117
LX+SINK+S006	12	90	0	30 120	0.496
LX+SINK+S008	6	40	-60	95	0.224
LX+SINK+S010	10	90	0	30 120	0.195
LX+SINK+S011	10	90	0	25 115	0.265×10^{-1}
LX+SINK+S017	10	90	0	30 120	0.171×10^{1}

TABLE II-10

ESTIMATIONS OF SOURCE PARAMETERS OBTAINED
BY AMPLITUDE SPECTRAL FITTING BASED
ON MINIMUM-RESIDUAL CRITERION
(PAGE 2 OF 2)

Event I. D.	Optimal Solution				
	Depth h (km)	Dip Angle δ°	Slip Angle λ°	Strike $N\phi^\circ E$	Moment 10^{25} dyne-cm
LX+SINK+S023	8	80	0	125	0.967×10^{-1}
LX+SINK+S025	4	40 50	± 90	70	0.254×10^{-1}
LX+SINK+S031	8	90	0	30 120	0.571×10^{-1}
LX+SINK+S036	4	40 50	± 90	65	0.475×10^{-1}
LX+SINK+S043	10	80	0	120	0.423×10^{-1}
LX+SINK+S056	14	90	0	40 130	0.387
LX+SINK+S059	14	90	0	30 120	0.147

TABLE II-11

ESTIMATIONS OF SOURCE PARAMETERS OBTAINED BY AMPLITUDE SPECTRAL FITTING BASED ON DISTRIBUTION-OF-MINIMUM-RESIDUAL CRITERION
(PAGE 1 OF 2)

Event I. D.	Source Parameters							
	Depth h (km)		Dip Angle δ^o		Slip Angle λ^o		Strike $N\phi^oE$	
	Probable Range	% Confidence	Probable Range	% Confidence	Probable Range	% Confidence	Probable Range	% Confidence
LX+SINK+S004	6-12	85	80-90	76	0	76	-	-
LX+SINK+S005	2-8	90	40-60	58	±60, ±90 0	64 20	40-105	71
LX+SINK+S006	6 10-14	33 58	40-50 80-90	26 64	±90 0	25 67	0-30 85-120	31 47
LX+SINK+S008	4-12	95	-	-	±90 0	33 23	-	-
LX+SINK+S010	6-10	79	40-50 80-90	47 53	±90 0	47 53	20-40 60-90 110-130	20 47 33
LX+SINK+S011	6-12	95	40-50 80-90	39 39	-30, 0, 30	62	25-50 105-125	31 37
LX+SINK+S017	6-10	82	40-50 90	46 46	±90 0	45 55	30-35 75-90 120-125	14 45 20

TABLE II-11

ESTIMATIONS OF SOURCE PARAMETERS OBTAINED BY AMPLITUDE SPECTRAL FITTING BASED ON DISTRIBUTION-OF-MINIMUM-RESIDUAL CRITERION
(PAGE 2 OF 2)

Event I. D.	Source Parameters							
	Depth h (km)		Dip Angle δ°		Slip Angle λ°		Strike Nϕ°E	
	Probable Range	% Confidence	Probable Range	% Confidence	Probable Range	% Confidence	Probable Range	% Confidence
LX+SINK+S023	4-8	90	40-80	90	±30 0	28 31	115-130	28
LX+SINK+S025	0-6	98	30-60	83	±60 ±90	35 43	40-100	75
LX+SINK+S031	4-10	95	40-50 80-90	45 35	±90 0	29 37	-	-
LX+SINK+S036	0-4	88	30-60	70	±60 ±90	27 40	30-100	88
LX+SINK+S043	6-12	88	40-60 80	59 13	±90 0	33 24	-	-
LX+SINK+S056	4-6 12-16	28 48	80-90	77	0	68	30-50 120-140	68
LX+SINK+S059	12-16	57	80-90	78	0	76	20-40 110-130	84

TABLE II-12

ESTIMATIONS OF SOURCE PARAMETERS OBTAINED
BY RATIO-OF-EVENT FITTING BASED ON
MINIMUM-RESIDUAL CRITERION
(PAGE 1 OF 2)

Reference: LX+SINK+S010 h = 10km, $\delta = 90$, $\lambda = 0$, $\phi = 30$, M = 0.195

Event I. D.	Optimal Solution				
	Depth h (km)	Dip Angle δ^{o}	Slip Angle λ^{o}	Strike $N\phi^{o}E$	Moment 10^{25} dyne-cm
LX+SINK+S004	10	90	0	30 120	0.426
LX+SINK+S005	4	40 50	±90	105	0.893×10^{-1}
LX+SINK+S006	10	90	0	25 115	0.675
LX+SINK+S008	8	80	0	85	0.262
LX+SINK+S011	6	40 50	±90	60	0.133×10^{-1}
LX+SINK+S017	10	90	0	30 120	0.194×10^{1}

TABLE II-12

ESTIMATIONS OF SOURCE PARAMETERS OBTAINED
BY RATIO-OF-EVENTS FITTING BASED ON
MINIMUM-RESIDUAL CRITERION
(PAGE 2 OF 2)

Reference: LX+SINK+S010 h = 10km, $\delta = 90$, $\lambda = 0$, $\phi = 30$, M = 0.195

Event I. D.	Optimal Solution				
	Depth h (km)	Dip Angle δ°	Slip Angle λ°	Strike $N\phi^\circ E$	Moment 10^{25} dyne-cm
LX+SINK+S023	6	80	0	35	0.676×10^{-1}
LX+SINK+S025	6	90	0	30 120	0.451×10^{-1}
LX+SINK+S031	6	80	0	30	0.318×10^{-1}
LX+SINK+S036	8	90	0	25	0.177
LX+SINK+S043	6	40 50	± 90	60	0.258×10^{-1}
LX+SINK+S059	6	90	0	25 115	0.454×10^{-1}

TABLE II-13

ESTIMATIONS OF SOURCE PARAMETERS OBTAINED BY RATIO-OF-EVENT FITTING BASED ON DISTRIBUTION-OF-MINIMUM-RESIDUAL CRITERION
(PAGE 1 OF 2)

Reference: LX+SINK+S010 h = 10km, $\delta = 90, \lambda = 0, \Phi = 30, M = 0.195$

Event I. D.	Source Parameters							
	Depth h (km)		Dip Angle δ°		Slip Angle λ°		Strike $N\Phi^\circ E$	
	Probable Range	% Confidence	Probable Range	% Confidence	Probable Range	% Confidence	Probable Range	% Confidence
LX+SINK+S004	4-10	82	70-90	80	0	65	25-30 115-120	67
LX+SINK+S005	2-8	88	30-70	77	$\pm 60, \pm 90$ 0	59 21	25-30 95-135	17 54
LX+SINK+S006	6-12	70	80-90	77	0	71	25-30 115-120	53 35
LX+SINK+S008	4-8	89	40-60 80-90	51 39	± 90 0	39 39	-	-
LX+SINK+S011	0-6	85	40-50 80-90	46 40	± 90 0	40 37	-	-
LX+SINK+S017	6-10	87	90	75	0	100	25-30 115-120	62 38

TABLE II-13

ESTIMATIONS OF SOURCE PARAMETERS OBTAINED BY RATIO-OF-EVENT FITTING BASED ON DISTRIBUTION-OF-MINIMUM-RESIDUAL CRITERION
(PAGE 2 OF 2)

Reference: LX+SINK+S010 h = 10km, $\delta = 90, \lambda = 0, \phi = 30, M = 0.195$

Event I. D.	Source Parameters							
	Depth h (km)		Dip Angle δ°		Slip Angle λ°		Strike Nϕ°E	
	Probable Range	% Confidence	Probable Range	% Confidence	Probable Range	% Confidence	Probable Range	% Confidence
LX+SINK+S023	0-6	95	60-90	62	±30 0	31 28	30-55 75-100 115-140	31 23 31
LX+SINK+S025	0-6	87	80-90	70	0	70	25-30 115-120	52 45
LX+SINK+S031	0-6	87	70-90	60	±30, 0	70	20-35 105-125	39 36
LX+SINK+S036	0-6	90	30-50 80-90	42 35	-30-+30 ±90	57 31	20-30 105-125	23 50
LX+SINK+S043	6-10	84	40-60 80	76 10	±90 0	57 14	50-95	45
LX+SINK+S059	0-6	87	40-50 80-90	23 58	±30, 0	79	25-30 115-120	43 32

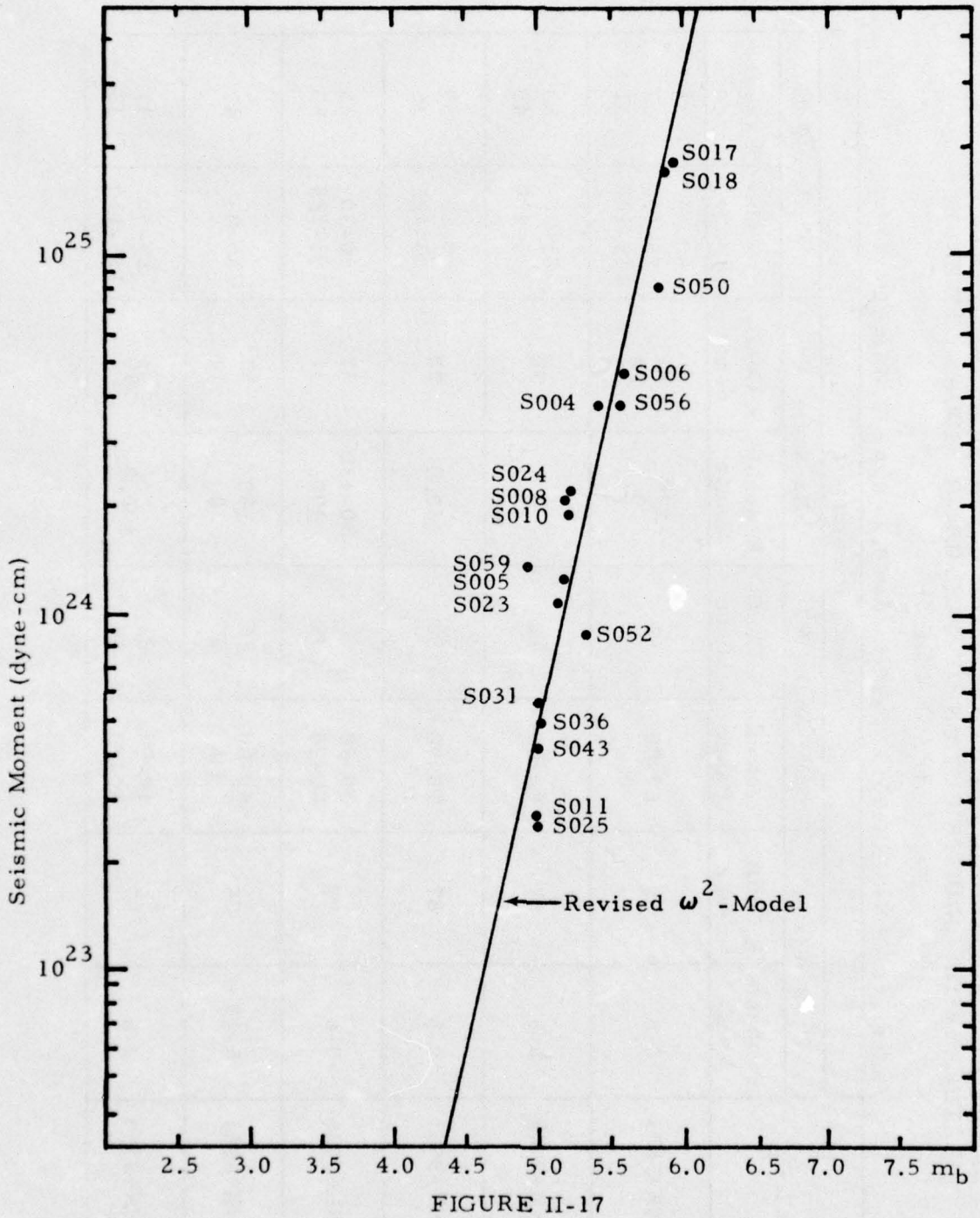

FIGURE II-17

SEISMIC MOMENT ESTIMATIONS OF 1974 SINKIANG, CHINA EARTHQUAKE SWARM IN RELATION TO THE ω^2-MODEL

D. CONCLUSIONS

Analysis of the far-field surface wave spectra of the nineteen events in the 1974 Sinkiang, China, earthquake swarm has yielded consistently shallow focal depth estimations ranging from 4 km to 14 km for these events. This agrees quite well with the PDE depth which is available for five events (see Table II-1). Also, from the distributions of the minimum-residuals for the focal depth estimations obtained, it is believed that the shallow-focal depth estimations should be quite reliable. For the estimations of the dip and the slip angles, the results suggest that there were two possible kinds of source mechanisms involved in this earthquake swarm: The dip-slip fault probably was responsible for six events and the other thirteen events had vertical strike-slip faults. It is conjectured, however, that the vertical strike-slip fault is the more probable source mechanism for events in this earthquake swarm based on the following observed facts:

- The source parameter estimations have resulted in the vertical strike-slip fault for the majority of the events (thirteen out of nineteen) being analyzed for this earthquake swarm. Moreover, for these events with the dip-slip fault, the distributions of the minimum-residuals indicate that the strike-slip fault is also possible.
- The theoretical amplitude spectra of the vertical strike-slip fault and those of the normal dip-slip fault (i.e., slip angle of $\pm 90^{\circ}$) are very similar in shape.
- The previously-analyzed earthquakes in this region seem to favor the strike-slip fault (Tsai and Shen, 1972; Turnbull et al., 1973, 1974).

The estimation of the strike direction for the events with vertical strike-slip faults is about $N40^{\circ}\sim 50^{\circ}W$ (or $N50^{\circ}\sim 40^{\circ}E$). This is quite consistent from event to event.

SECTION III
TRAVEL PATH ATTENUATION

A. INTRODUCTION

There are several factors which can affect the spectral level and shape of the observed far-field surface wave amplitude spectra of a given seismic event. These factors can be conveniently lumped into three groups: the source mechanism, the travel path effect, and the instrument response of the observation station. Therefore, in order to estimate the seismic source parameters using the observed far-field surface wave spectra, some appropriate corrections to the observed spectra must be made. The corrections for the instrument response and the geometric spreading, which are considered part of the travel path effect here, are trivial; while the correction for the energy attenuation, which is the other part of the travel path effect, generally is not well known due to the limited knowledge of the surface wave energy dissipation.

The travel path attenuation correction is important in the estimation of the seismic source parameters by the spectral fitting method using observed far-field surface wave data. The level of the attenuation curve as the function of frequency can affect the estimation of the seismic moment, and the general shape of the curve will affect the estimation of the focal depth and source mechanism. So far, when no reliable knowledge of energy attenuation along the travel paths of interest is available, the Tryggvason's energy attenuation curve for the normal continental path (Tryggvason, 1965) has been used. The general shape of the Tryggvason curve is believed to be reasonable while the level of the curve seems too low (Tryggvason, 1965; Anderson, 1964). It

is the purpose of this section to obtain the surface wave attenuation curves for several travel paths of interest.

Several methods to determine the surface wave attenuation coefficient will be derived and discussed in Subsection B. In Subsection C, these methods are applied to several groups of observed surface wave data, and Rayleigh wave energy attenuation curves are obtained for several travel paths of interest.

B. METHODS

The term 'energy dissipation' or 'energy attenuation' used throughout this section is chosen to indicate all energy lost along the travel path including absorption, reflected energy, and scattered energy.

In the following derivation, it is assumed that there is no energy transferred from one frequency to the other along the travel path and that the observed amplitude spectrum has been corrected for the station instrument response. Two methods will be described below: the two-station method which can be employed by the earthquake data, and the isotropic-source method which is suitable for the explosion data.

1. Two-Station Method

The observed surface wave amplitude spectra of a given seismic event recorded at two stations can be related as follows:

$$\frac{A_1(f)}{A_2(f)} = R(O_1, O_2, f) \left(\frac{\sin\Delta_2}{\sin\Delta_1}\right)^{1/2} e^{-k_{A1}(f)D_1 + k_{A2}(f)D_2} \qquad \text{(III-1)}$$

where

$A_i(f)$ is the observed amplitude spectrum for frequency f at station i,

$k_{Ai}(f)$ is the amplitude attenuation coefficient for frequency f along the travel path i (great circle path between the seismic event and station i),

D_i is the epicenter distance in km to station i ,

Δ_i is the epicenter distance in degrees to station i ,

O_i is the source azimuthal angle to station i , and

$R(O_1, O_2, f)$ is the ratio of the source excitation in O_1 to that in O_2 for frequency f .

In equation (III-1) the term $R(O_1, O_2, f)$ accounts for the non-circular radiation pattern of the source. For an isotropic source, $R(O_1, O_2, f)$ is one. For an anisotropic source, such as an earthquake, in general, $R(O_1, O_2, f)$ is different from one. However, $R(O_1, O_2, f)$ will be one if O_1 is equal to O_2 , regardless of source type. That is, when two observation stations are on the same great circle path between the seismic event and the station and have the same azimuthal angle, equation (III-1) can be reduced as follows:

$$\frac{A_1(f)}{A_2(f)} = \left(\frac{\sin\Delta_2}{\sin\Delta_1}\right)^{1/2} e^{-k_A(f)(D_1 - D_2)} \qquad \text{(III-2)}$$

where $k_A(f)$ now is the amplitude attenuation coefficient for frequency f along the travel path between stations 1 and 2. Therefore, equation (III-2) can be applied to the appropriate earthquake data to calculate the travel path attenuation as follows:

$$k_E(f) = 2k_A(f) = \frac{2\ell n\left[\frac{A_1(f)}{A_2(f)}\right] + \ell n\left(\frac{\sin\Delta_1}{\sin\Delta_2}\right)}{D_2 - D_1} \qquad \text{(III-3)}$$

where $k_E(f)$ is the energy attenuation coefficient for frequency f .

2. Isotropic Source Method

Tryggvason's approach assumes that radiation is isotropic and that attenuation is the same along all event-station travel paths. Then the energy attenuation coefficient can be estimated from the following equation by using the far-field observed surface wave spectra at several observation stations for one explosion (Tryggvason, 1965):

$$2\ell nA_i(f) + \ell n \sin\Delta_i = C_2(f) - D_i k_E(f) \qquad i = 1, NSITE \qquad \text{(III-4)}$$

where A_i, Δ_i, D_i, and k_E have the same meaning as before. C_2 is a constant depending on frequency and the size of explosion. NSITE is the number of observation stations. In equation (III-4), k_E and C_2 are two unknown parameters to be estimated. Hence, when NSITE is greater than two, k_E and C_2 can be estimated by the least-squares method, i.e., minimizing the following quantity:

$$\epsilon = \sum_{i=1}^{NSITE} \left[(C_2 - D_i k_E) - (2\ell nA_i + \ell n \sin\Delta_i)\right]^2 . \qquad \text{(III-5)}$$

The estimated k_E will be as follows:

$$k_E = \frac{NSITE \sum_i \left[(2\ell nA_i + \ell n \sin\Delta_i)D_i\right] - (\sum_i D_i)\left[\sum_i (2\ell nA_i + \ell n \sin\Delta_i)\right]}{(\sum_i D_i)(\sum_i D_i) - NSITE \sum_i (D_i D_i)} \qquad \text{(III-6)}$$

where $\sum_i$ stands for $\sum_{i=1}^{NSITE}$.

To facilitate the later discussion, this original Tryggvason's approach will be named as ISM-A. It can be easily shown that equation (III-6) will be reduced to equation (III-3) of the two-station method when NSITE is equal to two, as expected.

The ISM-A utilizes only the observed surface wave spectra from one explosion. When there are several explosions taking place in the same area, the best usage of these available data by the ISM-A will be that when k_{Ej} is estimated from equation (III-6) by using the observed spectra of one explosion j, and the final estimate of k_E is obtained by some curve-fitting technique or just by taking the following simple average:

$$k_E = \sum_{j=1}^{NEXP} k_{Ej}/NEXP \ , \qquad \text{(III-7)}$$

where NEXP is the number of available explosions. When there is a sufficiently large number of the observation stations, the variation between k_E's and k_{Ej}'s can be expected to be small. However, when the number of observation stations is too small, say three, large variations among k_{Ej}'s can be expected. For this case, to take the advantage of several available explosives and to best utilize the observed data, we can modify the ISM-A by simultaneously taking all explosions into account in the estimation of k_E as follows.

Modification of equation (III-4) by considering all available explosions at the same time yields the following result:

$$2\ell n A_{ij} + \ell n \sin\Delta_{ij} = C_{2j} - D_{ij}k_E$$

$$i = 1, NSITE \qquad j = 1, NEXP \qquad \text{(III-8)}$$

where now:

A_{ij} is the observed amplitude spectrum for frequency f at station i due to the explosion j,

D_{ij}, Δ_{ij} is the epicenter distance in km and degrees, respectively, between the station i and the explosion j,

C_{2j} is a constant for frequency f and explosion j.

Proceed as in the ISM-A, but this time minimize the following quantity:

$$\epsilon = \sum_{j}^{NEXP} \sum_{i}^{NSITE} \left[(C_{2j} - D_{ij} k_E) - (2 \ell n A_{ij} + \ell n \sin \Delta_{ij}) \right]^2 . \quad \text{(III-9)}$$

The estimated k_E will be as follows:

$$k_E = \frac{NSITE \sum_j \sum_i \left[(2 \ell n A_{ij} + \ell n \sin \Delta_{ij})(D_{ij}) \right] - \sum_j \left[\sum_i (2 \ell n A_{ij} + \ell n \sin \Delta_{ij}) \right] \left(\sum_i D_{ij} \right)}{\sum_j \left[\left(\sum_i D_{ij} \right) \left(\sum_i D_{ij} \right) \right] - NSITE \sum_j \sum_i (D_{ij} D_{ij})}$$

where $\sum_j$ and $\sum_i$ stand for $\sum_{j=1}^{NEXP}$ and $\sum_{i=1}^{NSITE}$, respectively. (III-10)

We will call this modified approach an ISM-B. With ISM-B, as long as NSITE ≥ 2 and NEXP ≥ 2, the energy attenuation coefficient k_E can be estimated; while with ISM-A, NSITE must be greater than two in order to estimate k_E. When NSITE = 2, the ISM-A can offer only the deterministic value of k_E, as does the two-station method. With a small number of available observations stations, therefore, the ISM-B probably will yield a better estimate of k_E, as long as NEXP ≥ 2.

C. RESULTS

To calculate the surface wave energy attenuation for the travel paths of interest, the methods discussed in the previous subsection are applied to two classes of observed data: Rayleigh waves of the earthquake and of the explosion. Here, before the application of these methods, the observed Rayleigh wave data are preprocessed by narrowband filtering to eliminate any possible multipathing, as done in Section II. The observed Rayleigh wave spectra are obtained and then corrected for the station instrument response.

1. Earthquake Data

Two sets of earthquake data -- the 1974 Sinkiang, China, earthquake swarm and earthquakes used in the previous M_s-m_b study (Turnbull et al., 1975) -- were examined to determine which events could be employed by the two-station method. As previously mentioned (see Subsection B-1), with earthquake data, the two-station method can be applied to the events which have two observation stations lying on the same great circle path with the same source azimuth.

For the 1974 Sinkiang swarm, there were five events which approximately satisfy the above requirement. The pertinent information about the events and stations for these five events is given in Table III-1 with the event-station travel paths plotted in Figure III-1. The two stations involved are VLPE stations at Toledo, Spain (TLO), and La Paz, Bolivia (ZLP). It is noticed that, although these two stations are not quite on the same event-station great circle path, their event-station travel paths are fairly close: two source azimuths differing by 3.5 degrees. The calculated energy attenuation coefficients along this travel path (TLO-ZLP) are plotted in Figure III-2, with the variation among events given as a vertical bar and the average values of k_E for various frequencies connected by a solid line.

For earthquakes used in the previous M_s-m_b study (59 events), three events were found suitable for the two-station method. The pertinent information about the events and the stations is listed in Table III-2 with the event-station travel paths plotted in Figure III-3. Three travel paths for which the two-station method can be used to calculate the travel path attenuation are as follows:

- KON (VLPE station at Kongsberg, Norway) to TLO obtainable from the event LX+KURSP+425,
- KON to OGD (VLPE station at Ogdensburg, New Jersey) obtainable from the event LX+CAUCA+124, and

TABLE III-1

INFORMATION OF EVENTS AND STATIONS FOR THE TLO-ZLP PATH

Event I. D.	Date	Location		m_b	Station I. D.					
					TLO (39.9N, 4.02W)			ZLP (16.5S, 68.1W)		
		Latitude °N	Longitude °E		* AZ	** Δ°	Δ km	* AZ	** Δ°	Δ km
LX+SINK+S001	08/11/74	39.5	73.8	6.4	-62.4	57.9	6445.0	-65.8	139.7	15543.5
LX+SINK+S004	08/11/74	39.3	73.8	5.4	-62.3	58.6	6455.3	-65.9	139.8	15556.6
LX+SINK+S017	08/11/74	39.5	73.7	5.8	-62.5	57.8	6437.4	-65.9	139.7	15535.7
LX+SINK+S018	08/11/74	39.5	73.6	5.9	-62.5	57.8	6429.8	-66.0	139.6	15527.9
LX+SINK+S024	08/12/74	39.2	74.0	5.2	-62.2	58.2	6475.8	-65.9	140.0	15572.9

* AZ : Source azimuth + for NE

** Δ : Epicenter distance in degrees and km

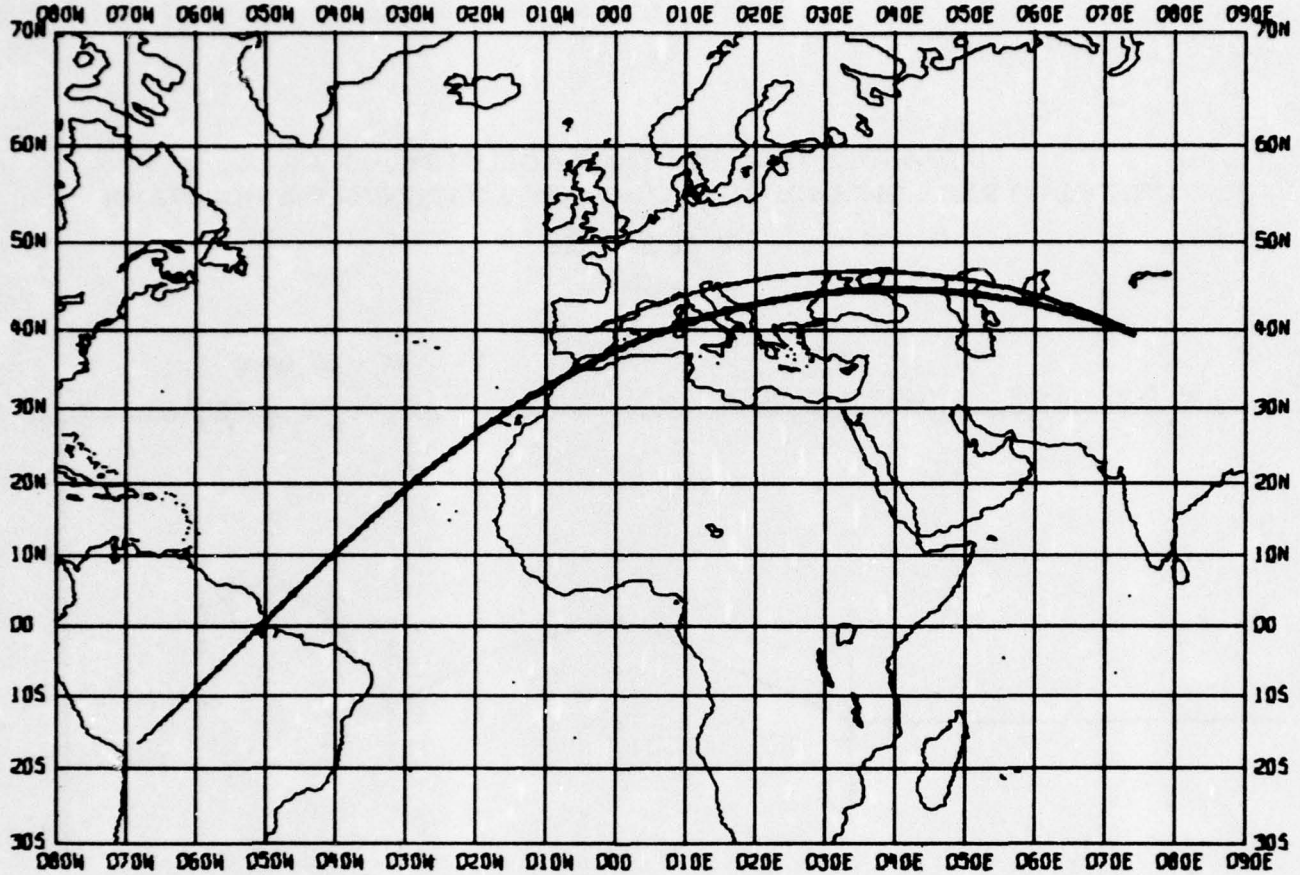

FIGURE III-1

EVENT-STATION TRAVEL PATH: TLO-ZLP

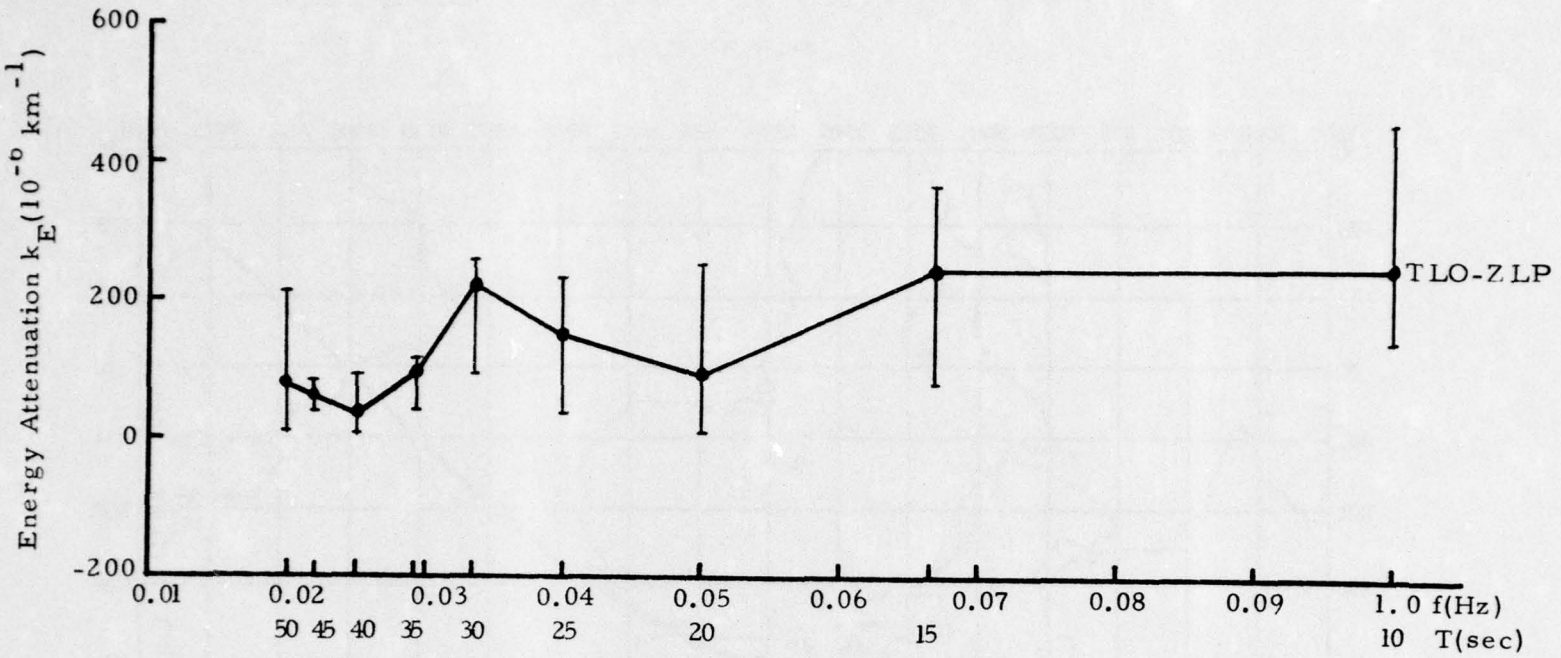

FIGURE III-2

RAYLEIGH WAVE ENERGY ATTENUATION COEFFICIENTS OBTAINED BY TWO-STATION METHOD: TLO-ZLP PATH

TABLE III-2

INFORMATION OF EVENTS AND STATIONS

(a) Path KON-TLO

Event: LX+KURSP+425 ; 04/05/73 ; 43.6N , 147.7E ; m_b= 5.4					
Station	Latitude °N	Longitude °E	AZ *	Δ° **	Δ km
KON	59.7	9.59	-20.9	71.3	7937.9
TLO	39.7	-4.02	-21.3	92.9	10336.2

(b) Path KON-OGD

Event: LX-CAUCA-124 ; 02/03/72 ; 40.0N , 48.4E ; m_b= 5.1					
Station	Latitude °N	Longitude °E	AZ *	Δ° **	Δ km
KON	59.7	9.59	-37.9	31.1	3464.4
OGD	41.1	-74.6	-39.5	84.0	9344.0

(c) Path KON-ALQ

Event: LX+GTURP+134 ; 02/19/73 ; 40.2N , 33.9E ; m_b= 4.9					
Station	Latitude °N	Longitude °E	AZ *	Δ° **	Δ km
KON	59.7	9.59	-30.0	24.7	2747.1
ALQ	34.9	-106.5	-31.7	96.6	10749.7

* AZ: Source azimuth + for NE

** Δ: Epicenter distance in degrees and km

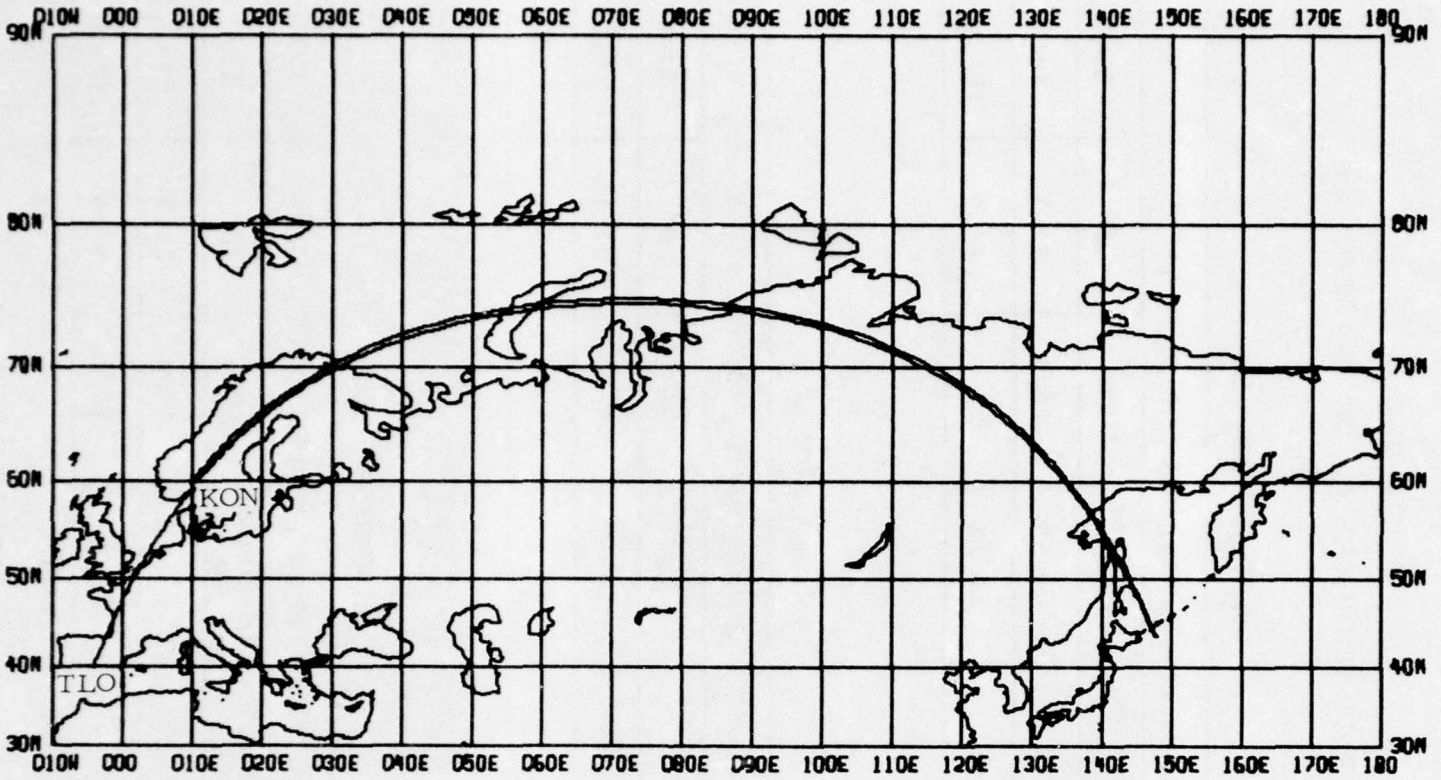

FIGURE III-3a

EVENT-STATION TRAVEL PATH: KON-TLO

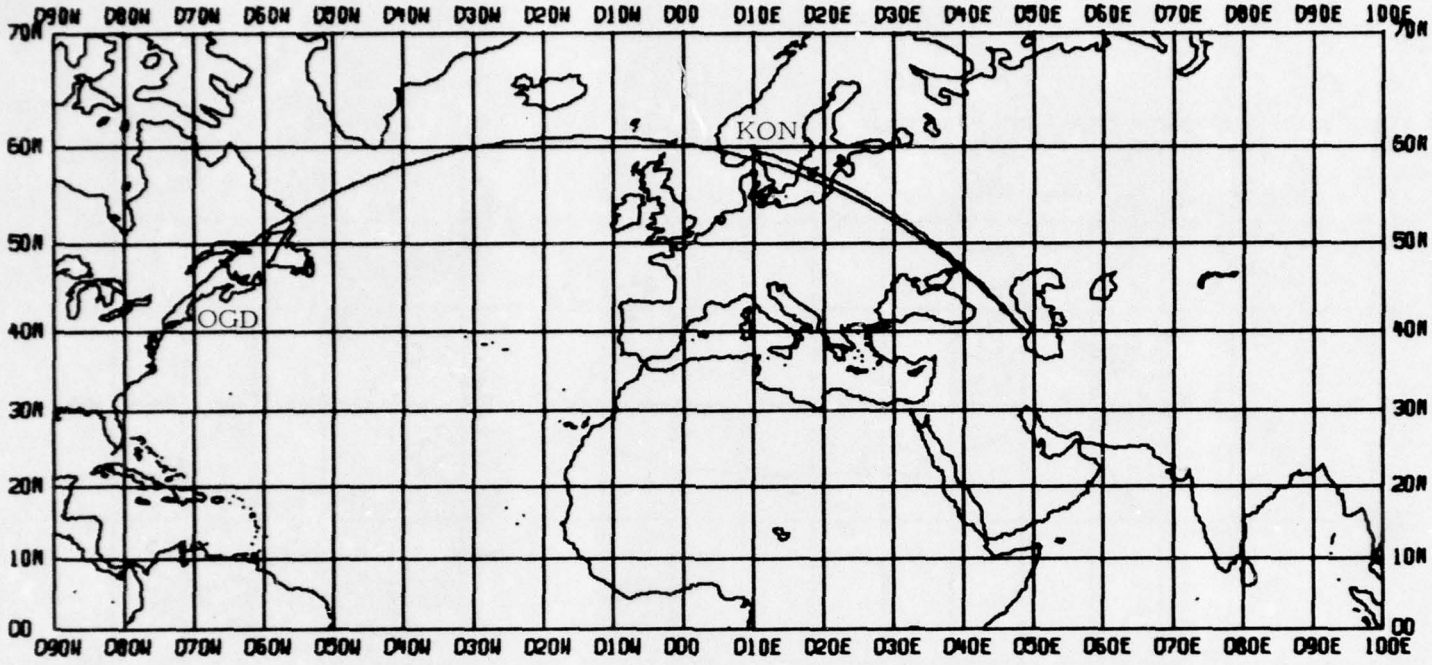

FIGURE III-3b

EVENT-STATION TRAVEL PATH: KON-OGD

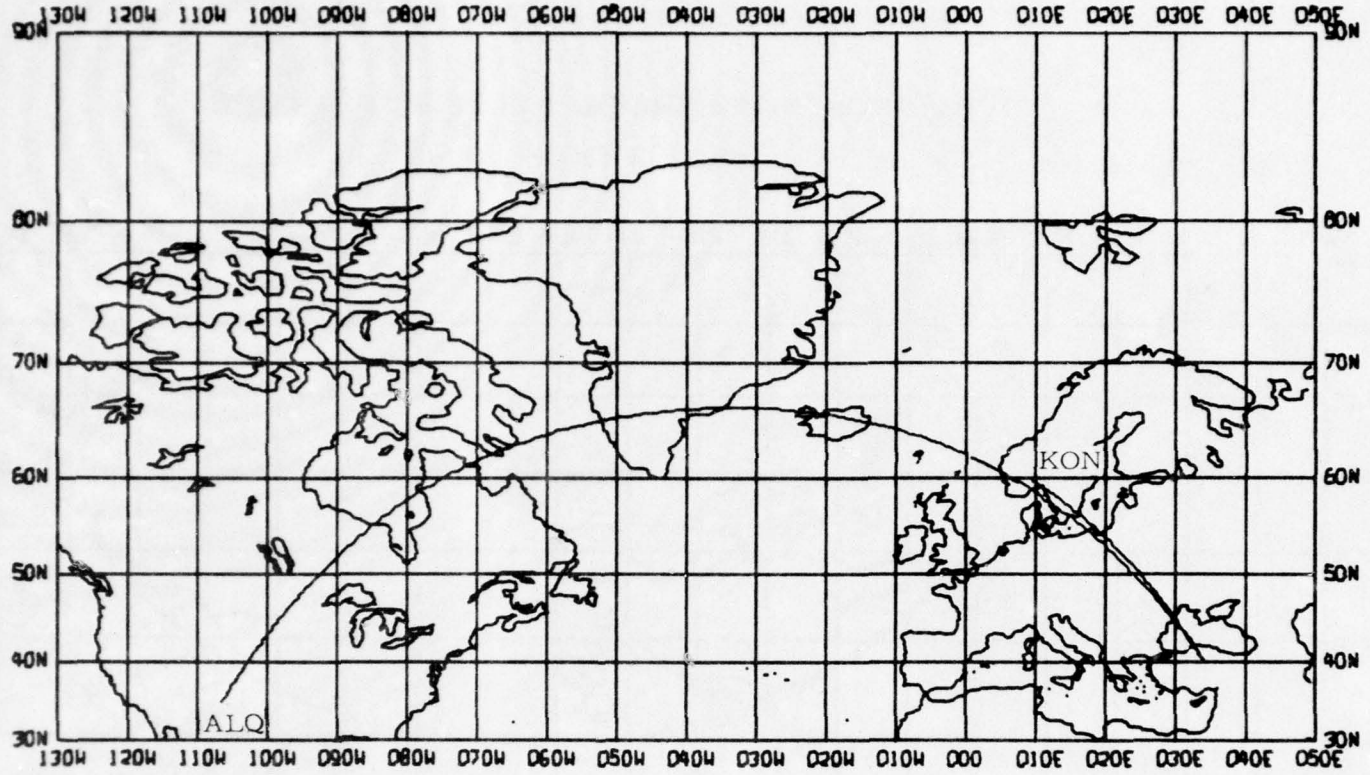

FIGURE III-3c

EVENT-STATION TRAVEL PATH: KON-ALQ

- KON to ALQ (VLPE station at Albuquerque, New Mexico) obtainable from the event LX+GTURP+134.

Again, the two stations involved are not exactly on the same event-station great circle path; however, the difference is small as compared to that in the previous TLO-ZLP path; the source azimuths of the two stations differing by 0.4 degree for KON-TLO path, 1.6 degrees for KON-OGD path, and 1.7 degrees for KON to ALQ path. The calculated energy attenuation coefficients for these three paths are shown in Figure III-4.

Among these four travel paths, the KON-OGD path lies mostly in the Atlantic Ocean; the KON-TLO path lies mostly along the continental shelf of the west coast of Europe; the KON-ALQ and the TLO-ZLP paths are mixed, more continental for the former and more oceanic for the latter. Referring to Figures III-2 and III-4, it is noticed that the calculated attenuation curves are quite irregular and comparison seems hard. However, the calculated attenuation coefficients here seem to be reasonable in the sense that they correspond to the realistic Q values between 100 and 1000, where $Q = 2\pi f/k_E U$ and U is the group velocity at frequency f. One common feature for these four paths is that the attenuation coefficients for the 10-second period here appears to be too low relative to the other periods. This is judged from the existing knowledge that for the continental path the attenuation should increase significantly with decreasing period in the shorter periods (Tryggvason, 1965); and the oceanic path usually has higher attenuation than the continental path, especially for the shorter periods. The exact cause for this relatively low attenuation coefficient at 10 seconds is not known; but may possibly be caused by the improper instrument response correction for the 10-second period, as commonly observed at the VLPE stations and by the fact that the observed 10-second energy was relatively small and the extraction of the 10-second spectrum could not be made accurately.

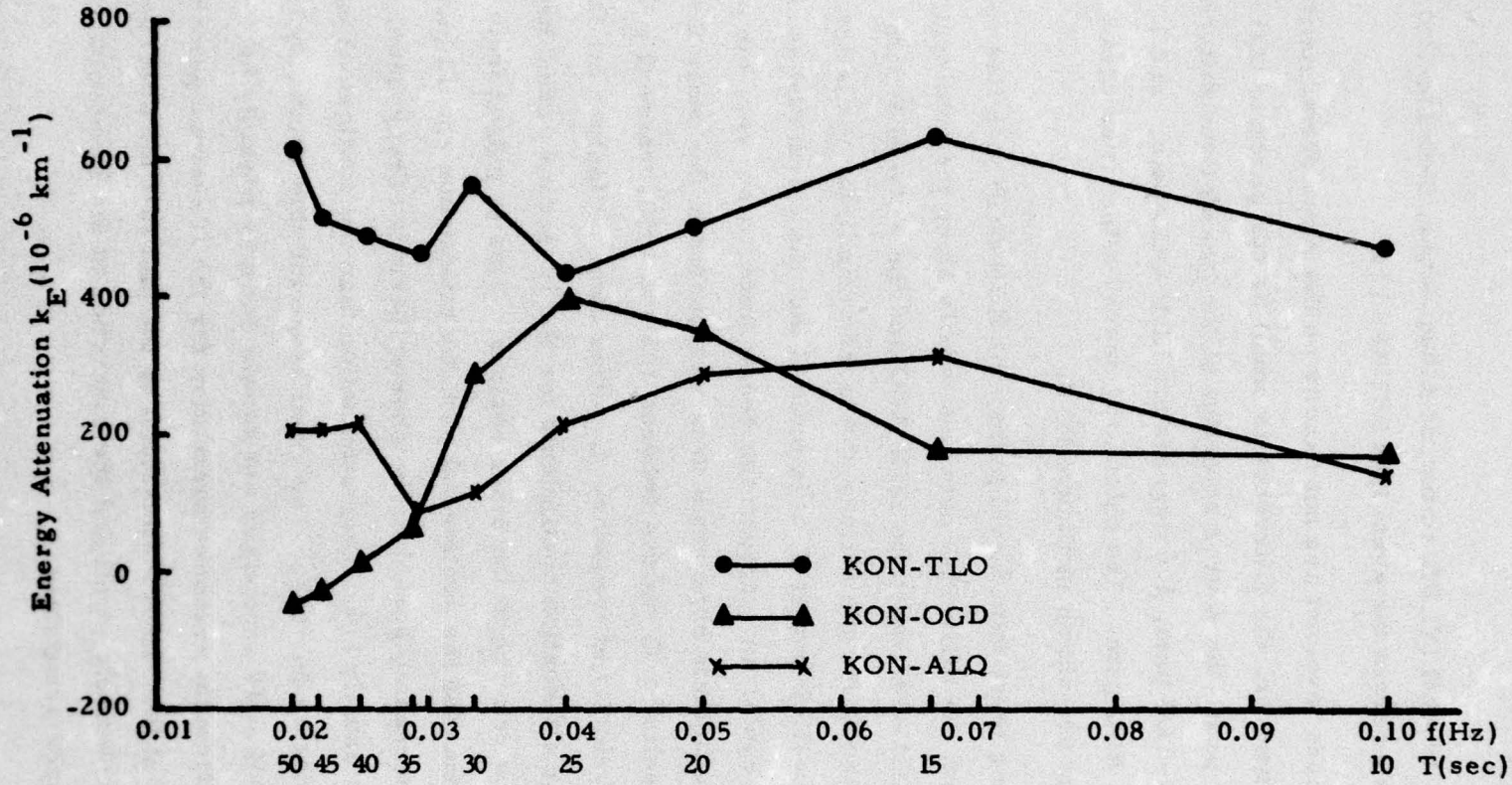

FIGURE III-4

RAYLEIGH WAVE ENERGY ATTENUATION COEFFICIENTS OBTAINED BY TWO-STATION METHOD: KON-TLO, KON-OGD, AND KON-ALQ PATH

For the KON-OGD path, the computed attenuation coefficient at 40 seconds is unreasonably low (only 10^{-5} km^{-1}) and those at 45 and 50 seconds are negative, physically impossible. One possible explanation is that these two stations are not exactly on the same event-station great circle path, the great circle path being very close to the nodal direction of the Rayleigh wave radiation pattern. For the periods between 15 and 35 seconds, the level of the attenuation curve obtained here is compatible with that obtained by Tsai and Aki (1969) for some other oceanic path across the Atlantic Ocean, although the detailed variations are quite different.

For the KON-TLO path, the level of the computed attenuation curve is higher than that obtained for the other three paths here. This seems unusual, since the KON-TLO path is mostly continental while the other three are either entirely oceanic or mixed. This situation, however, will also be observed for the average travel path in the northern part of Eurasia as we apply the isotropic-source method to the explosion data in the following subsection.

2. Explosion Data

Long period Rayleigh waves of presumed underground explosions from the U. S. Nevada test site (NTS) and from the Russian eastern Kazakh (EKZ) taking place during the first six months of 1975 when the recordings at three array stations (ALPA, LASA, and NORSAR) were all readily available on-line to SDAC were examined in order to estimate the average Rayleigh wave attenuation for the travel paths from NTS and EKZ to three array stations. Five NTS and three EKZ events were available and usable for this purpose. For NTS events, the observed Rayleigh wave data were available and good at all three array stations; while for EKZ events, data quality was not as good as that of the NTS and two events did not have LASA recordings.

Table III-3 presents the information of events and stations pertinent to the calculation. The involved event-station great circle paths are

TABLE III-3

INFORMATION OF EVENTS AND STATIONS FOR NTS AND EKZ EVENTS

	Date	Location		m_b	Station I. D.					
					ALPA (65.22N, 147.74W)		LASA (46.69N, 106.22W)		NORSAR (60.84N, 10.89E)	
		Latitude °N	Longitude °E		* AZ	** Δ	* AZ	** Δ	* AZ	** Δ
NTS	04/30/75	37.2	-116.3	5.2	-23.4	33.5 3731.3	35.1	12.0 1339.6	24.0	73.1 8128.5
	05/14/75	38.2	-115.6	6.0	-24.3	32.9 3655.7	36.2	10.9 1216.8	24.4	71.9 8005.1
	06/03/75	37.0	-116.0	5.8	-23.4	33.8 3763.2	33.9	12.1 1346.2	24.1	73.2 8141.1
	06/03/75	37.0	-116.0	5.3	-23.4	33.8 3763.2	33.9	12.1 1346.2	24.1	73.2 8141.1
	06/19/75	37.0	-116.0	5.8	-23.4	33.8 3763.2	33.9	12.1 1346.2	24.1	73.2 8141.1
EKZ	03/11/75	49.8	78.3	5.4	20.5	59.8 6650.9	-	-	-46.9	38.1 4241.3
	04/27/75	50.0	79.0	5.6	20.8	59.4 6612.3	3.6	83.4 9278.9	-47.0	38.3 4262.8
	06/30/75	49.0	80.0	4.9	21.0	60.1 6690.4	-	-	-45.9	39.5 4392.0

* AZ: Source azimuth + for NE

** Δ: Epicenter distance in degrees and km

plotted in Figures III-5 and III-6 for NTS and EKZ events, respectively. It is noticed that these travel paths are mostly continental -- over the northern part of North America for NTS events and over Eurasia for EKZ events. This uniformity among the travel paths is desirable in using the isotropic-source method.

We first applied ISM-A to both NTS and EKZ events. The average energy attenuation coefficients, k_E, for periods from 10 to 50 seconds computed by equations (III-6) and (III-7) are plotted in Figure III-7. Notice that the estimated k_E values from EKZ events are more scattered than those from NTS events. This is thought to be reasonable, since for EKZ events data quality was not as good as that of NTS because the number of observation stations were fewer and the k_E values were averaged over a fewer number of events. We next applied ISM-B to the same events listed in Table III-3. The estimated k_E values are again plotted in Figure III-7. Referring to Figure III-7, it is fair to say that the ISM-A and the ISM-B have yielded compatible results. However, the ISM-B estimated attenuation curves appear to be smoothed and to offer better estimates for the general trend of the attenuation curve in the low frequency range of 20 to 50 seconds. For comparison purposes, the Tryggvason attenuation curve (Tryggvason, 1965) is also shown in Figure III-7.

Again referring to Figure III-7, but this time focusing attention on the attenuation curves obtained from NTS events (NTS curve) and those obtained from EKZ events (EKZ curve), it is not hard to see that the EKZ curve and the NTS curve are quite different in two respects. First, the level of the EKZ curve is much higher than that of the NTS curve in the low frequency range of 20 to 50 seconds. Second, the EKZ curve has a maximum value at 40 seconds and decreases toward both longer and shorter periods (down to 15 seconds); while the NTS curve has a minimum value at 35 seconds and increases toward both longer and shorter periods.

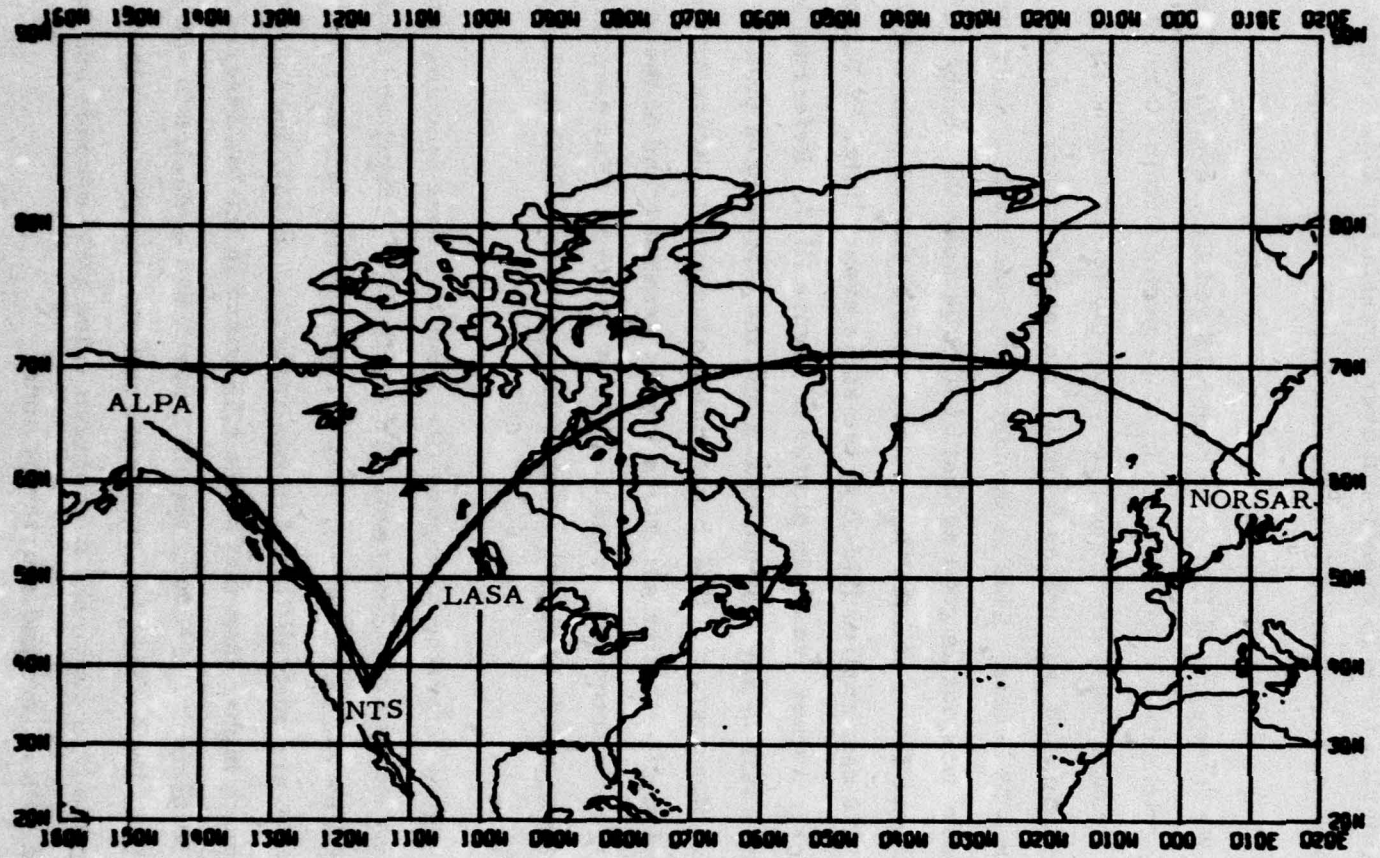

FIGURE III-5

EVENT-STATION TRAVEL PATHS: NTS TO THREE ARRAY STATIONS

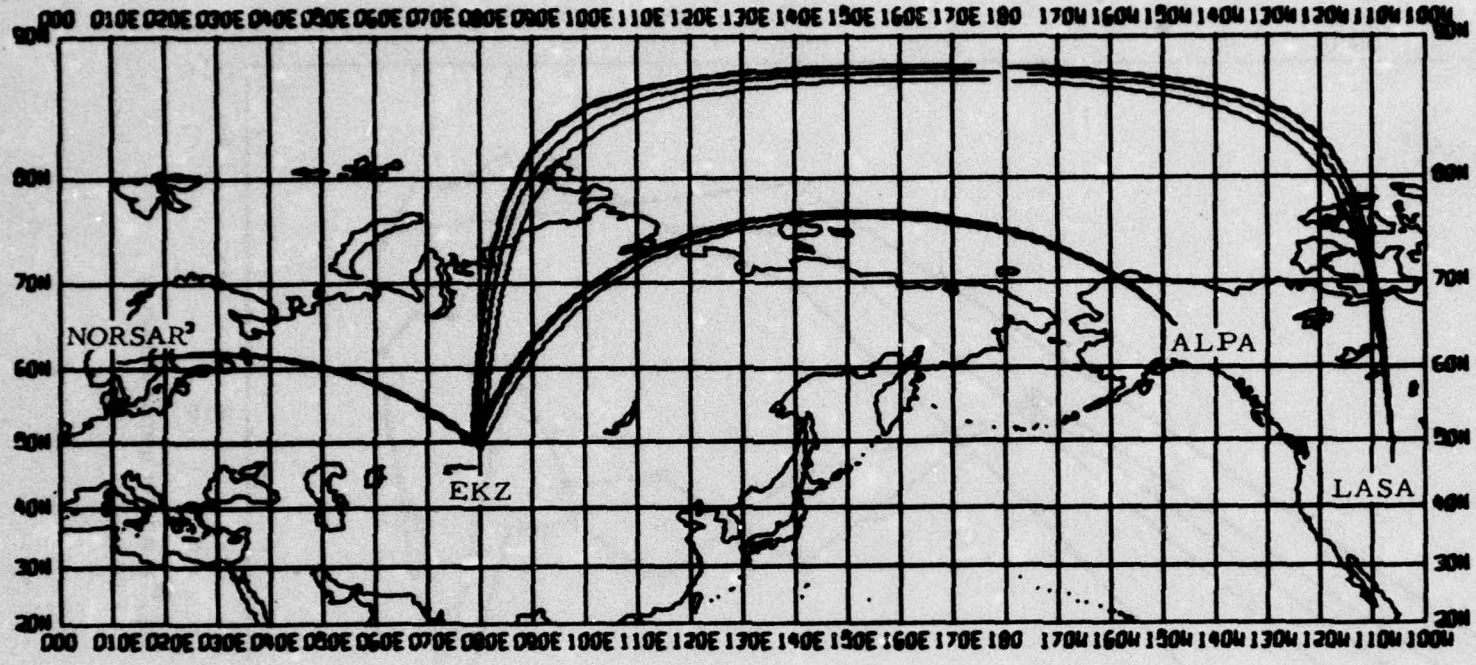

FIGURE III-6

EVENT-STATION TRAVEL PATHS: EKZ TO THREE ARRAY STATIONS

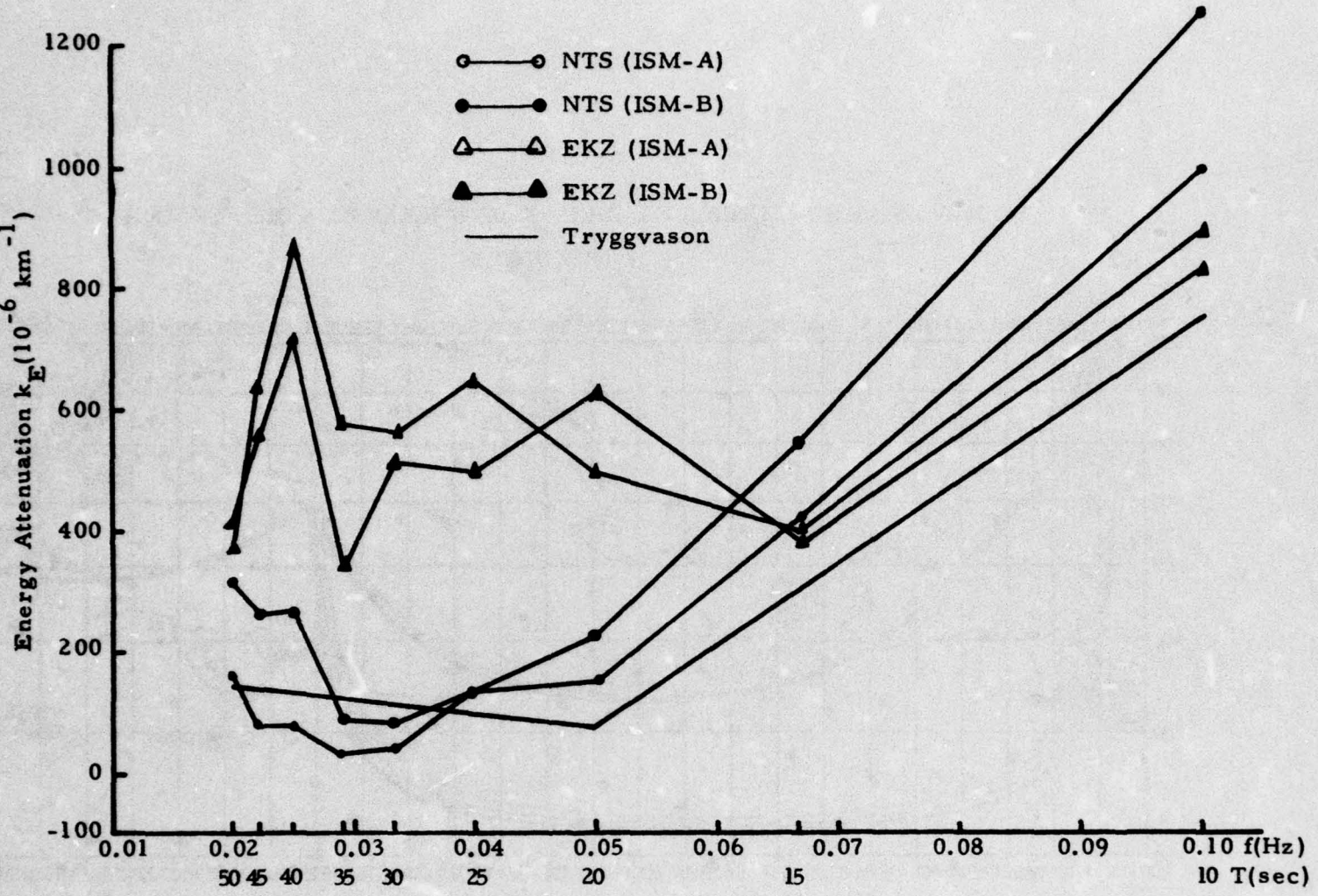

FIGURE III-7

AVERAGE RAYLEIGH WAVE ENERGY ATTENUATION COEFFICIENTS
OBTAINED BY THE ISM-A AND THE ISM-B IN RELATION
TO THE TRYGGVASON'S CURVE

The frequency variation of the EKZ curve may not be reliable and probably is not too significant, since the estimated k_E values from EKZ events are scattered, as discussed earlier, and the attenuation curve here has been obtained by just connecting the k_E values for nine discrete frequencies. However, the large difference between the EKZ curve and the NTS curve in the level of the attenuation curve is thought to be believable, since it merely reflects the large difference between the observed signal amplitudes of EKZ events and those of NTS events, as shown in the following figure. Figure III-8 shows the observed Rayleigh wave traces recorded at NORSAR for 4/30/75 NTS event (NTS/430/75N0) and for 4/27/75 EKZ event (EKZ/427/75N0). Also given in the figure are the values of the bodywave magnitude (m_b), the epicenter distance (Δ), and the maximum recorded amplitude (zero-to-peak) in computer count (CC). It is noticed that EKZ/427/75N0 had a half-magnitude larger m_b and about one-half time smaller Δ than NTS/430/75 (5.6 versus 5.2 and 38^o versus 73^o); yet two events produced almost the same observed signal amplitude (55.2 CC versus 51.5 CC). A simple explanation is that the energy attenuation along the path from EKZ to NORSAR is much larger than that along the path from NTS to NORSAR.

Comparing the NTS curve with the Tryggvason curve, it is found that general trends of two curves are quite similar, especially when a straight line is fitted through the NTS curve from 50 to 20 seconds. The general trend is that the k_E has a local maximum of 50 seconds, decreases slowly toward 20 seconds, and increases linearly from 20 to 10 seconds. Nevertheless, a small difference does exist between the two curves; namely, the NTS curve has a little bit higher value at 20 seconds and increases faster toward 10 seconds.

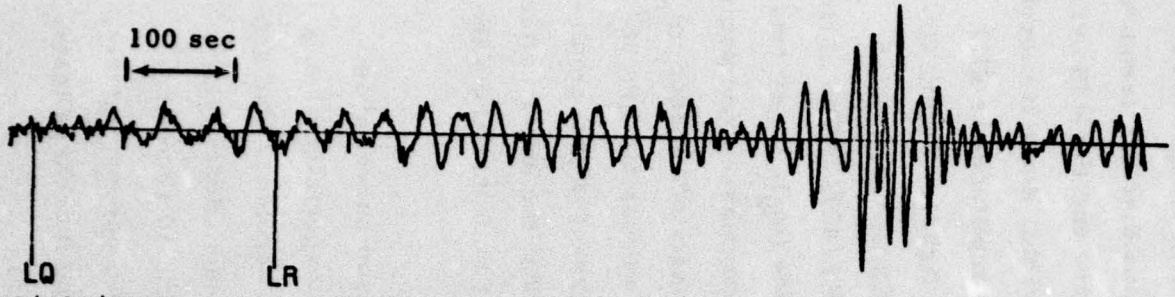

(a) NTS/430/75NO: m_b = 5.2
Δ = 73°
amp = 51.5 computer counts

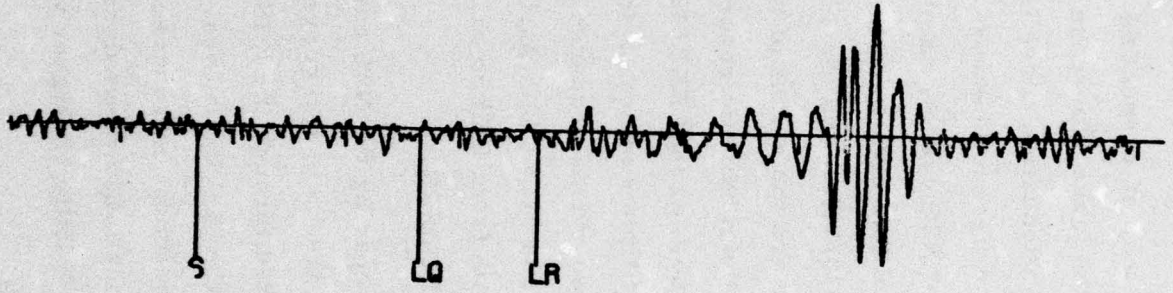

(b) EKZ/427/75NO: m_b = 5.6
Δ = 38°
amp = 55.2 computer counts

FIGURE III-8

NORSAR RECORDED RAYLEIGH WAVES OF 4/30/75 NTS EVENT
AND 4/27/75 EKZ EVENT

D. CONCLUSIONS

Rayleigh wave energy attenuation coefficients in the period range of 10 to 50 seconds have been estimated for several travel paths by applying the two-station method and the isotropic-source method to the earthquake and explosion data. In general, the results are thought to be reasonably realistic. However, no attempt has been made to interpret the obtained attenuation curves in terms of the Q-values of the earth structure. The attenuation coefficients computed here are intended to be used for the travel path attenuation correction in the far-field source parameter estimation and possibly in the calculation of surface wave magnitude. Based on the knowledge gained from the travel path attenuation study presented here, the following remarks can be stated:

- The two-station method is simple; however, its practical application is thought to be limited due to the fact that it is hard to have two stations lie exactly on the same event-station great circle path. Serious error in the computed energy attenuation can be made when the source azimuths of two stations are not exactly the same and are close to the nodal direction of the surface wave radiation pattern.
- A noticeable difference in the frequency variation of the computed attenuation curve can be expected among different travel paths. Hence, it seems that the attenuation coefficients obtained for a specific travel path by the two-station method can, at best, be used along that path.
- The ISM-B applied to a small number of observation stations with many available events can be expected to yield compatible results as the ISM-A applied to a large number of observation stations with one single event. When only the small number of

observation stations with many events is available, the ISM-B can be expected to do better. However, with the ISM-B the data quality should be good and consistent among events; otherwise, the computed k_E values can be negative and physically unrealistic.

- The average Rayleigh wave attenuation coefficients estimated from the NTS events for the travel paths from NTS to three array stations agree quite well with the Tryggvason attenuation curve, although the former has a little bit higher value for the short periods.

- Based on the observed Rayleigh wave data used here, the large energy attenuation coefficients obtained for the path from EKZ to three array stations are believable, although this seems unusual and may not be a general situation.

SECTION IV
REFERENCES

Anderson, D. L., 1964, The Anelasticity of the Earth, J. Geophys. Res., 69, 2071-2084.

Tryggvason, E., 1965, Dissipation of Rayleigh Wave Energy, J. Geophys. Res., 70, 1449-1455.

Tsai, Y. B., 1972, Utility of Tsai's Method for Seismic Discrimination: Semi-Annual Technical Report No. 2, AFOSR Contract Number F44620-71-C-0112, Texas Instruments Incorporated, Dallas, Texas.

Tsai, Y. B., and K. Aki, 1969, Simultaneous Determination of the Seismic Moment and Attenuation of Seismic Surface Waves, Bul. Seismol. Soc. Amer., 59, 275-287.

Tsai, Y. B., and W. W. Shen, 1972, Utility of Tsai's Method for Seismic Discrimination, Final Technical Report, AFOSR Contract Number F44620-71-C-0112, Texas Instruments Incorporated, Dallas, Texas.

Turnbull, L. S., D. F. D. Sun, and J. S. Shaub, 1973, Determination of Seismic Source Parameters from Frequency Dependent Rayleigh and Love Wave Radiation Patterns, Semi-Annual Technical Report No. 1-Part C, Texas Instruments Report No. ALEX(02)-TR-73-01-Part C, AFOSR Contract Number F44620-73-C-0055, Texas Instruments Incorporated, Dallas, Texas.

Turnbull, L. S., D. Sun, and D. G. Black, 1974, Determination of Seismic Source Parameters from Long-Period Teleseismic Waves, Semi-Annual Report No. 2-Part A, Texas Instruments Report No.

ALEX(02)-TR-74-01-Part A, AFOSR Contract Number F44620-73-C-0055, Texas Instruments Incorporated, Dallas, Texas.

Turnbull, L. S., J. C. Battis, D. Sun, and A. C. Strauss, 1975, Source Studies in the Near- and Far-Field, Semi-Annual Technical Report No. 4-Part A, Texas Instruments Report No. ALEX(02)-TR-75-01-Part A, AFOSR Contract Number F44620-73-C-0055, Texas Instruments Incorporated, Dallas, Texas.

APPENDIX A

Observed surface waves for the event LX+SINK+S018 in the 1974 Sinkiang, China,earthquake swarm are shown in the following figures. These figures are thought to be representative for the events in this swarm. In these figures, for each observation station, the recorded surface wave trace is given first, followed by the average group velocity curve for that travel path and the uncorrected amplitude spectrum which are obtained from the narrowband filtering process.

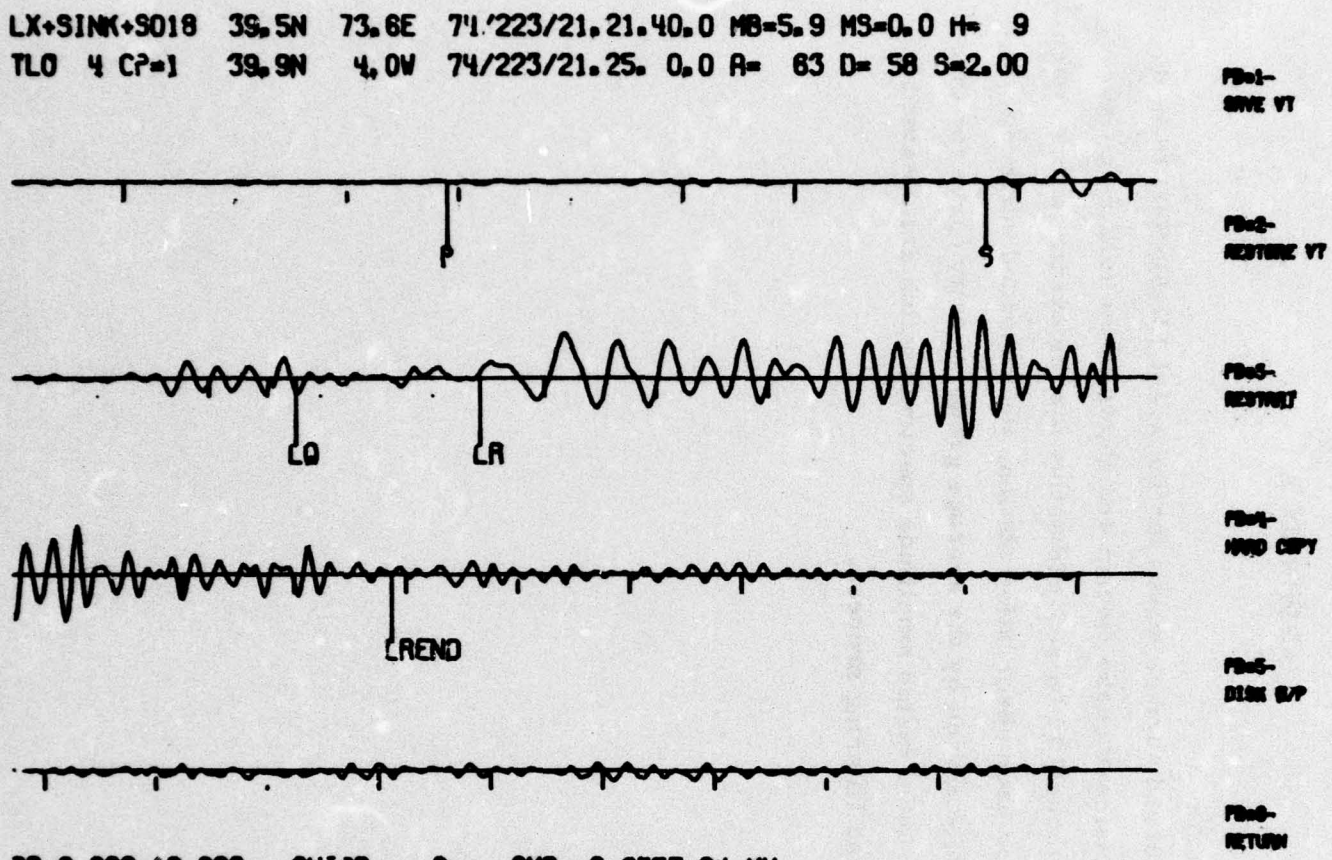

FIGURE A-1a

RAYLEIGH WAVE TRACE: RECORDED AT TLO

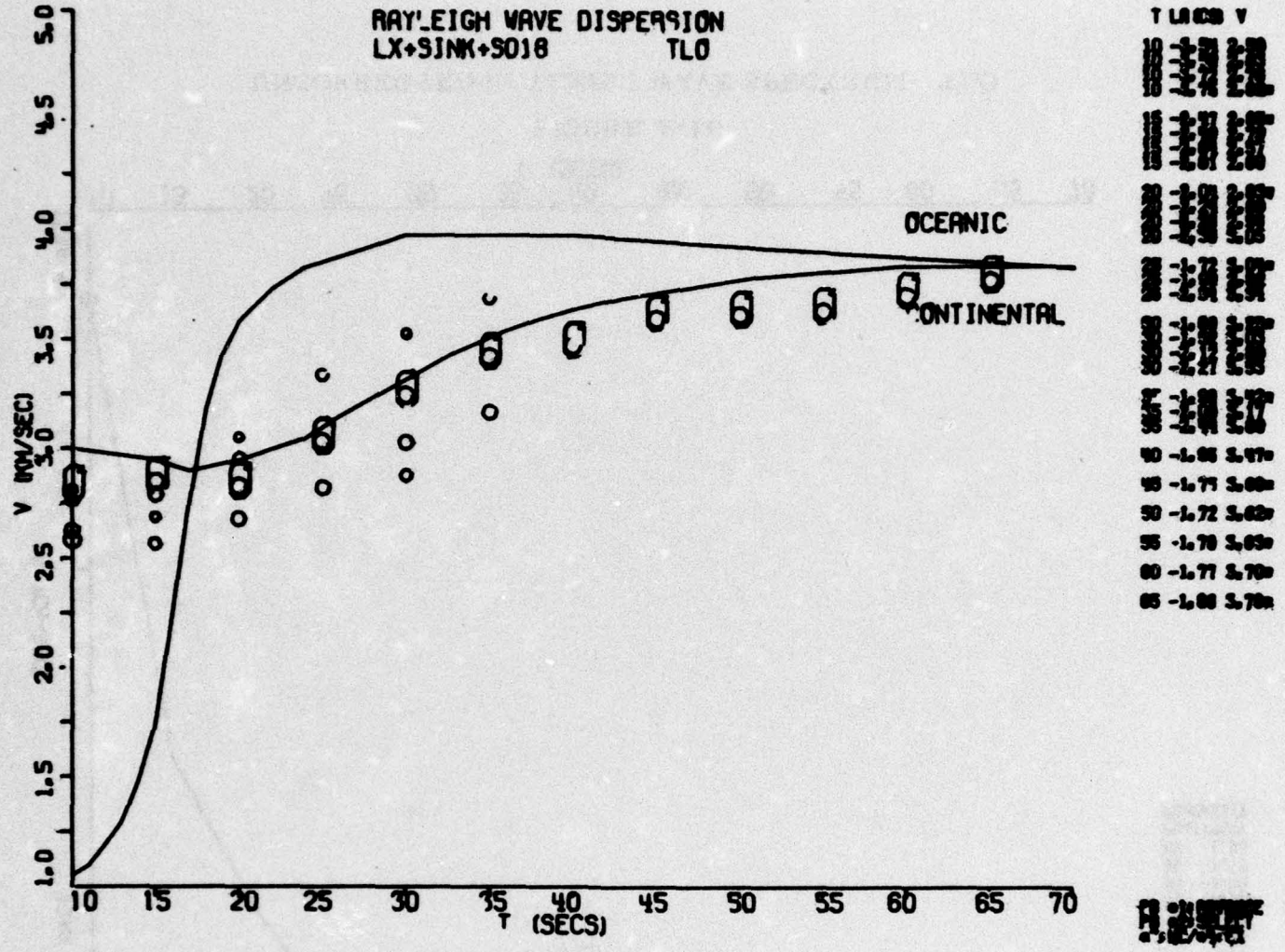

FIGURE A-1b

LR GROUP VELOCITY CURVE ALONG SINKIANG-TLO PATH

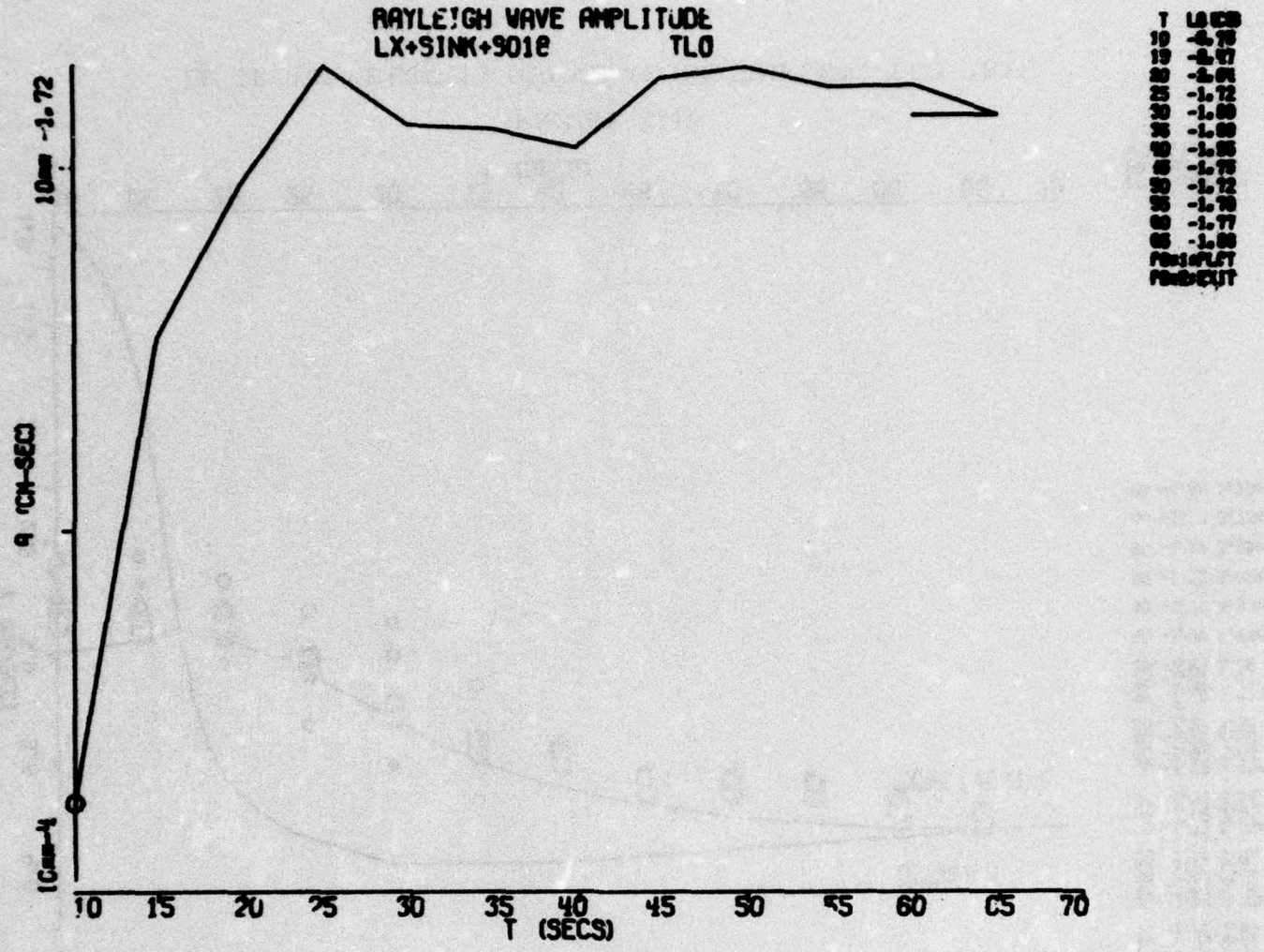

FIGURE A-1c

UNCORRECTED RAYLEIGH WAVE SPECTRUM: TLO

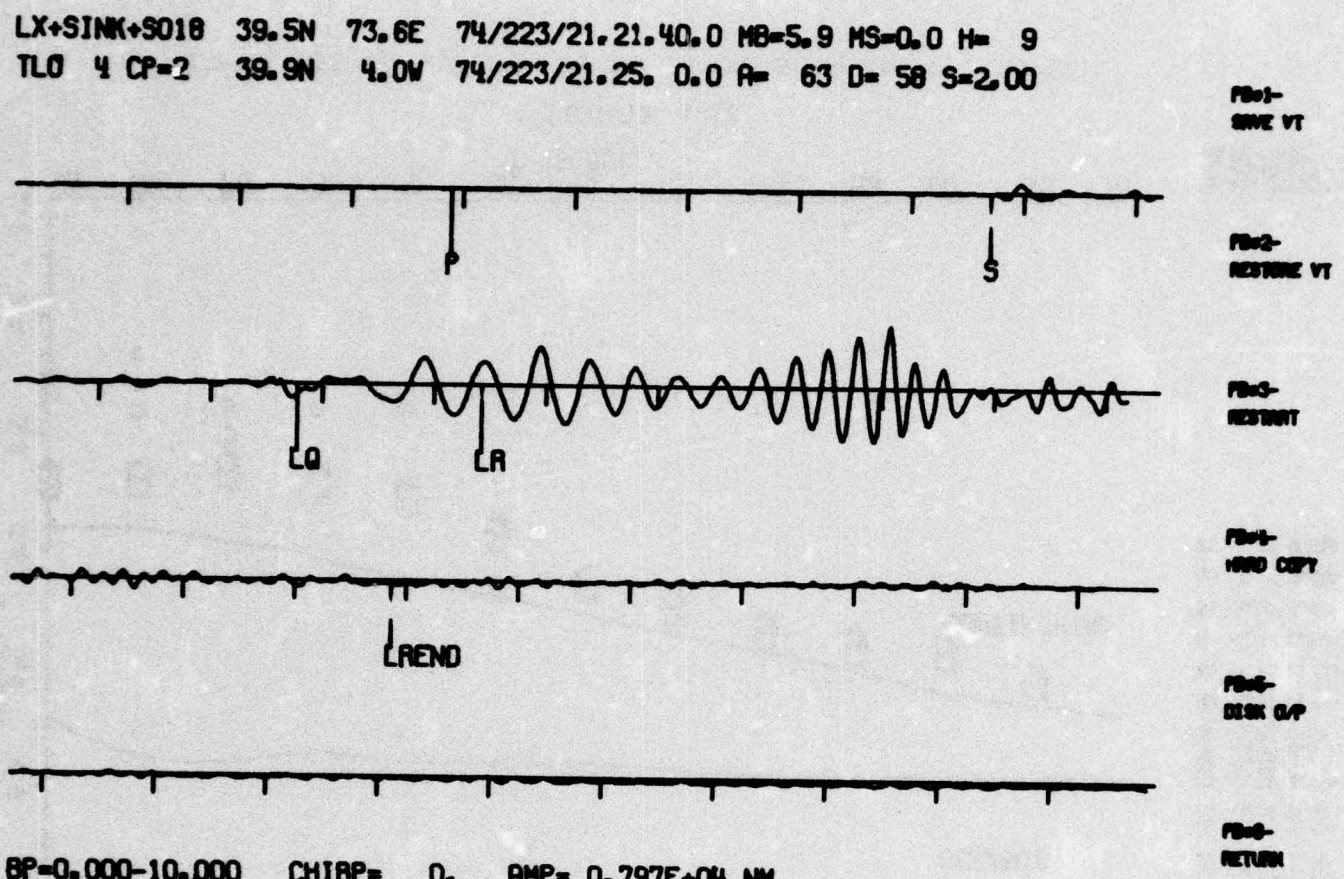

FIGURE A-1d

LOVE WAVE TRACE: RECORDED AT TLO

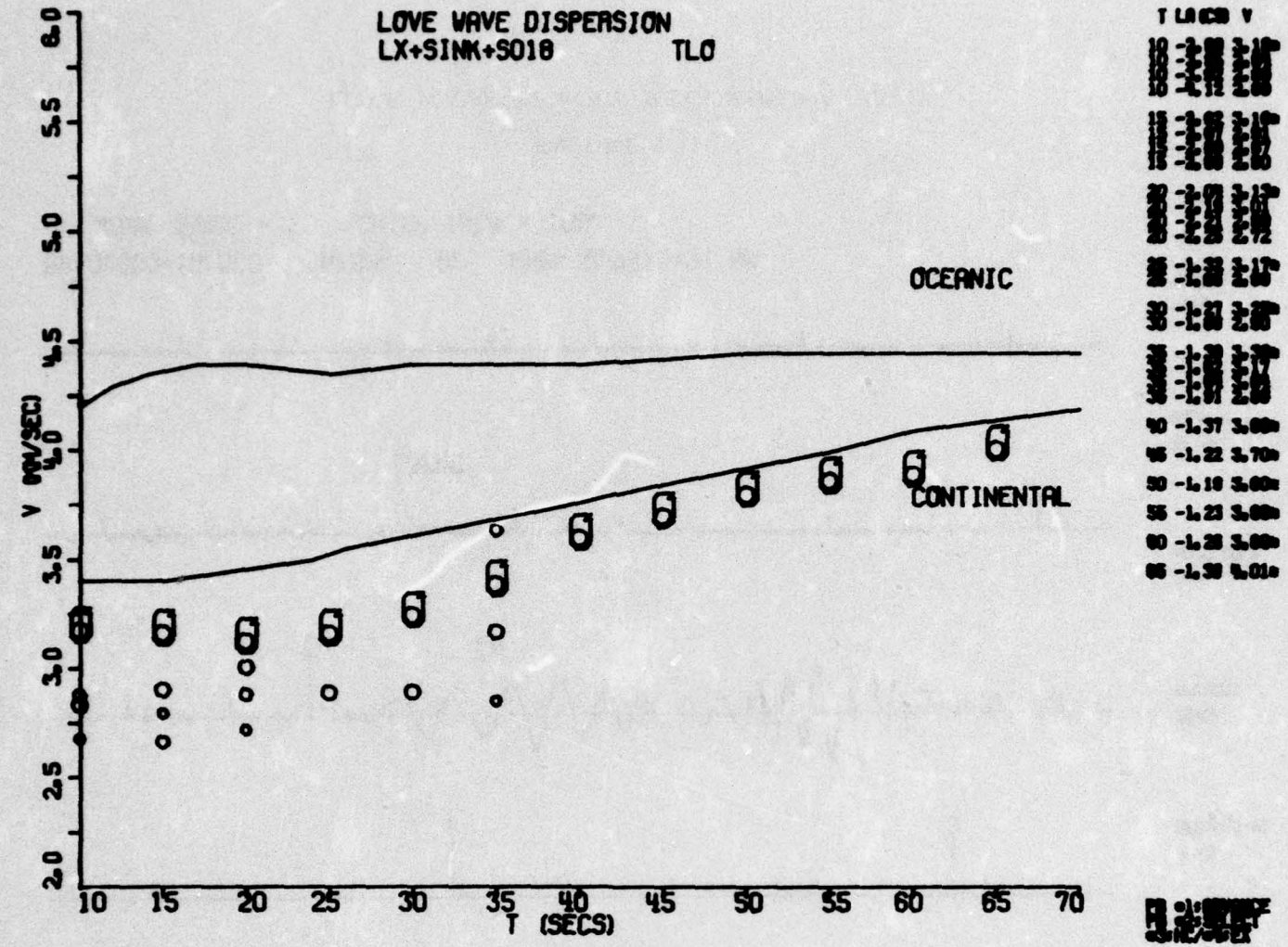

FIGURE A-1e

LQ GROUP VELOCITY CURVE ALONG SINKIANG-TLO PATH

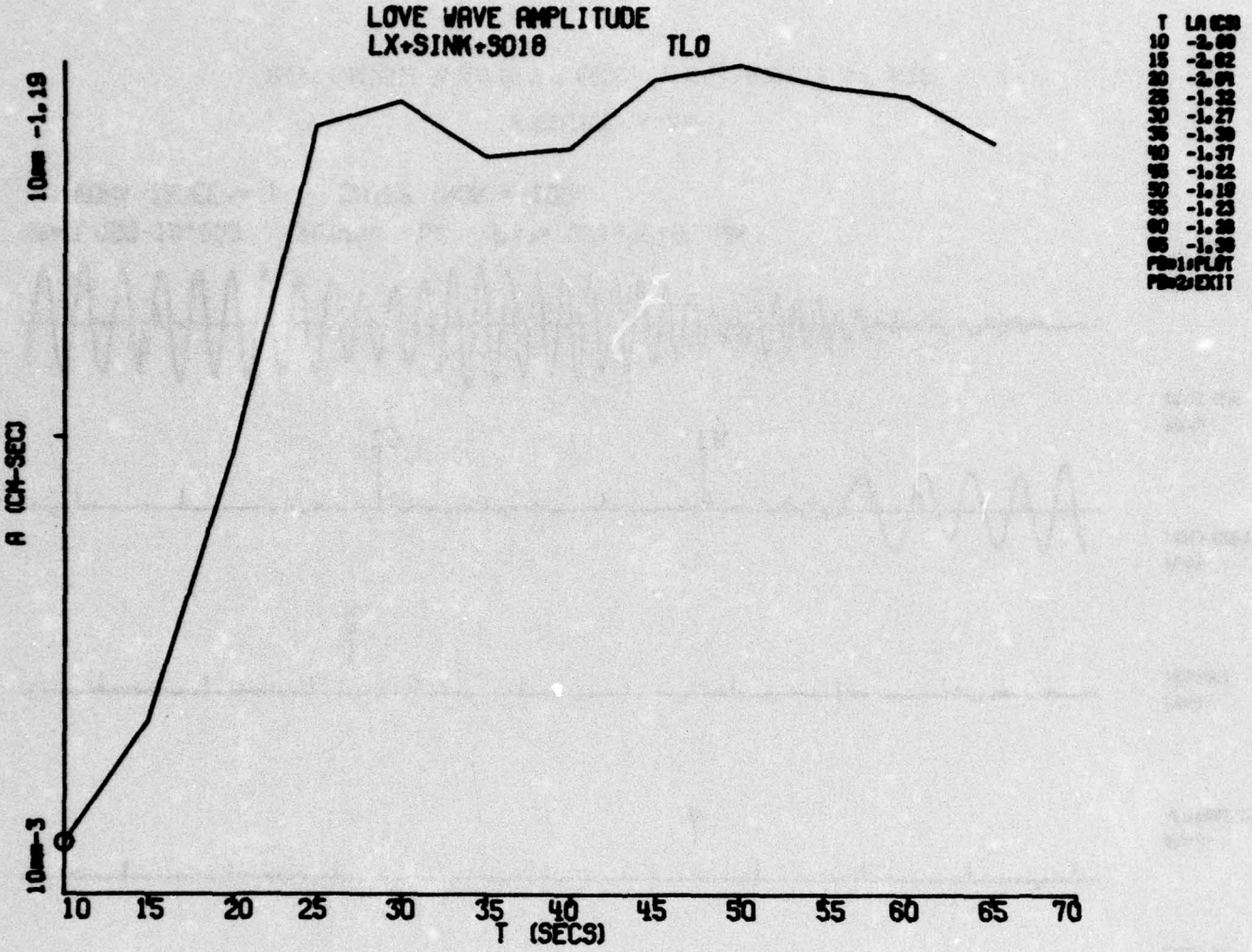

FIGURE A-1f

UNCORRECTED LOVE WAVE SPECTRUM: TLO

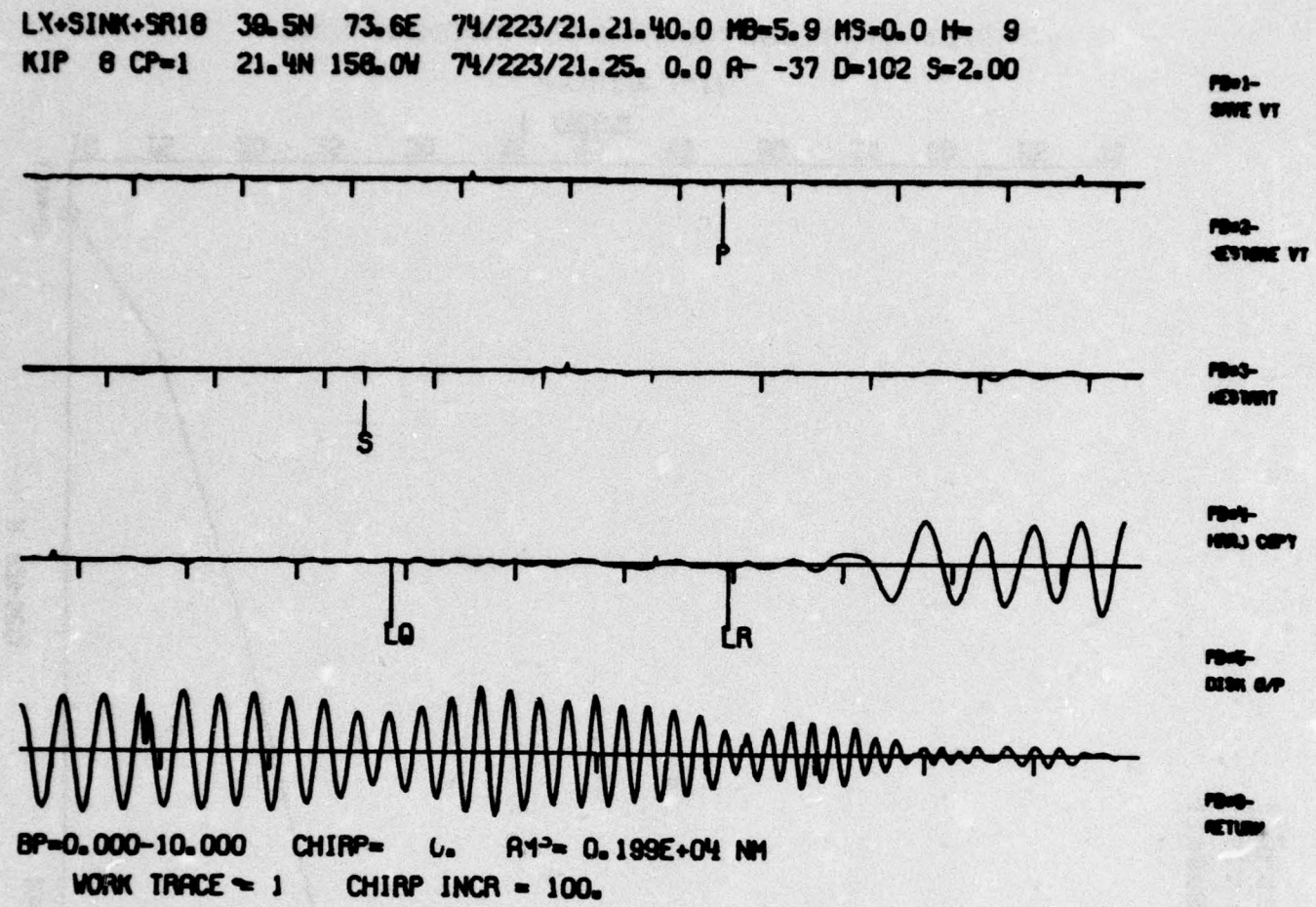

FIGURE A-2a

RAYLEIGH WAVE TRACE: RECORDED AT KIP

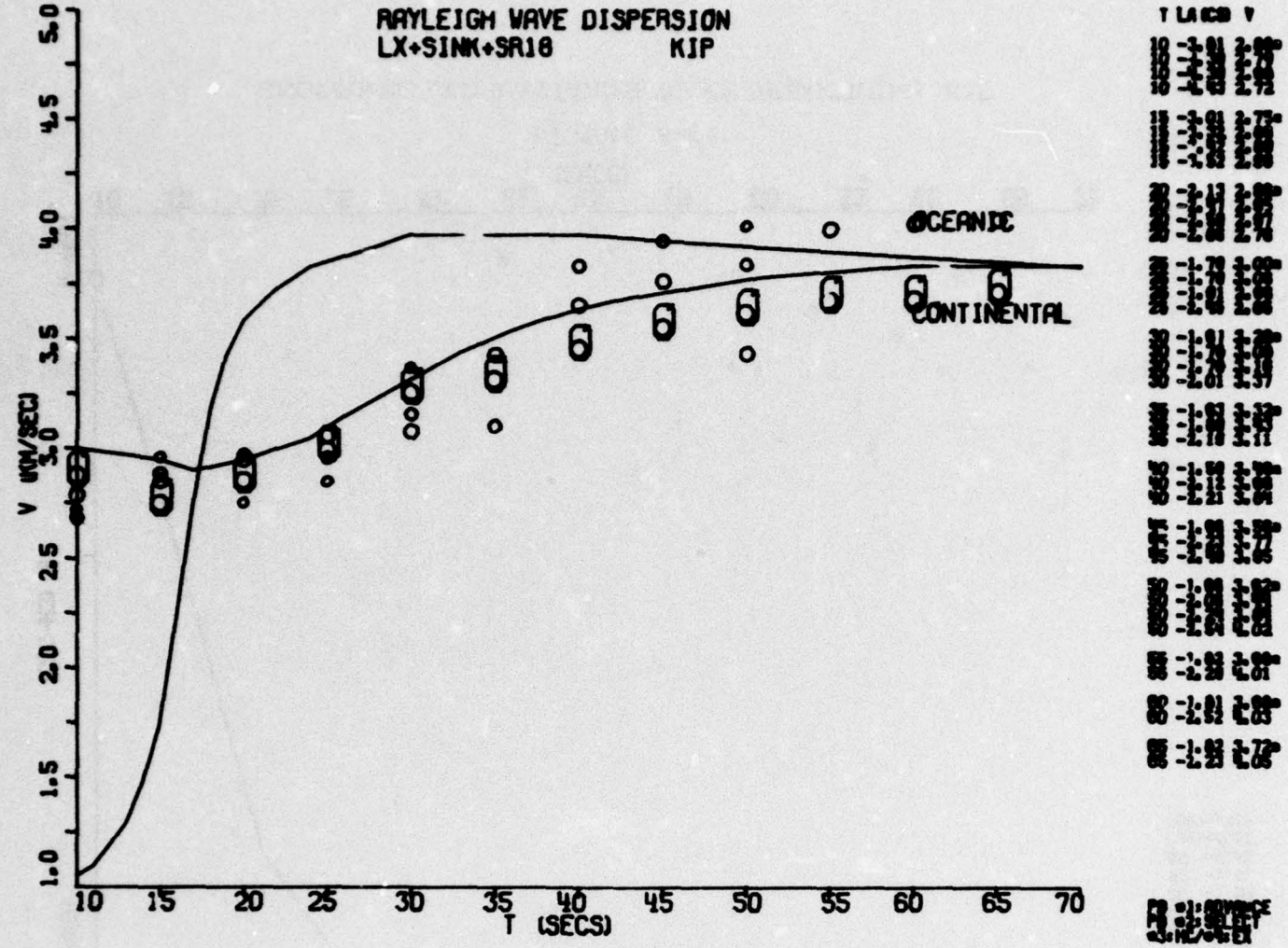

FIGURE A-2b

LR GROUP VELOCITY CURVE ALONG SINKIANG-KIP PATH

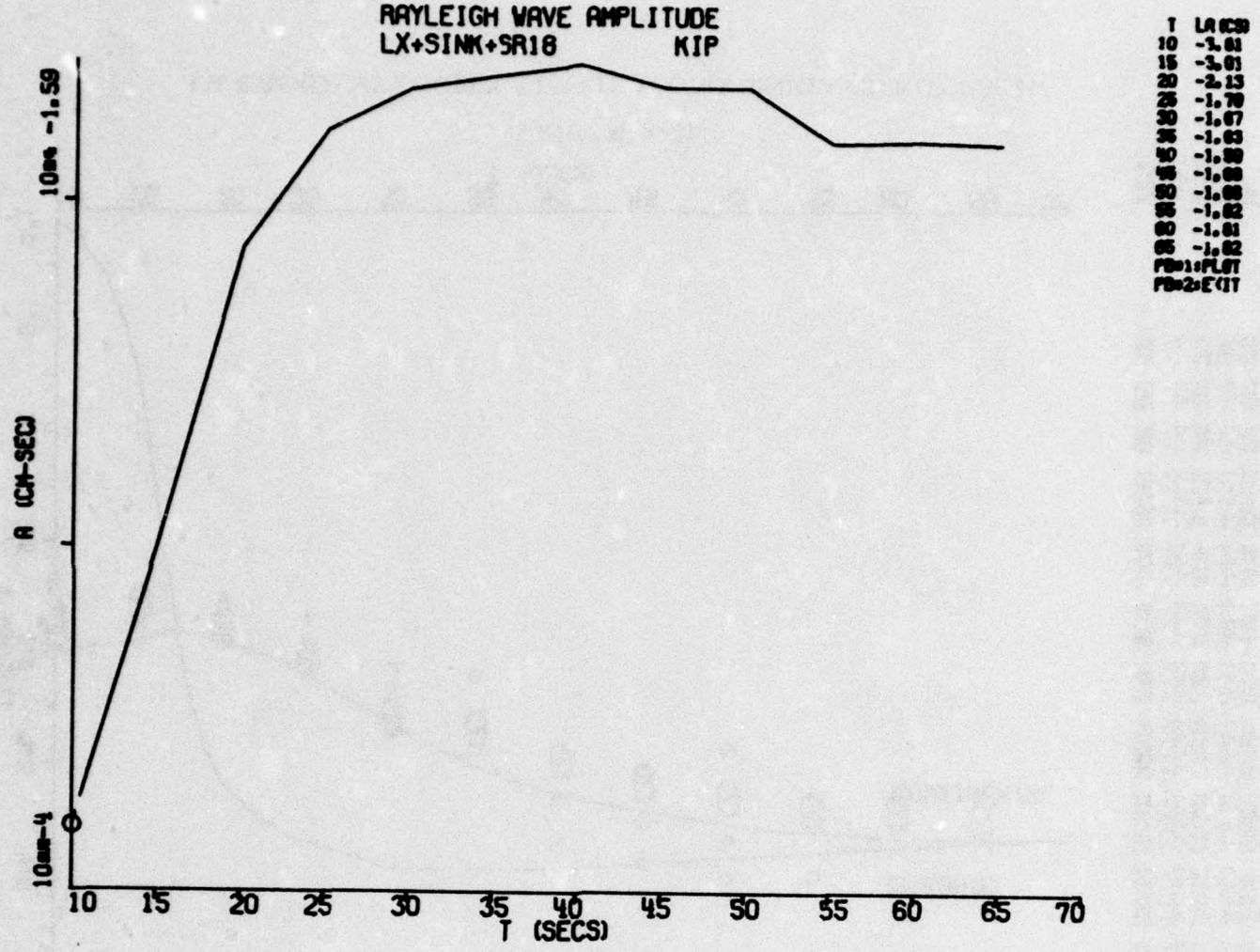

FIGURE A-2c

UNCORRECTED RAYLEIGH WAVE SPECTRUM: KIP

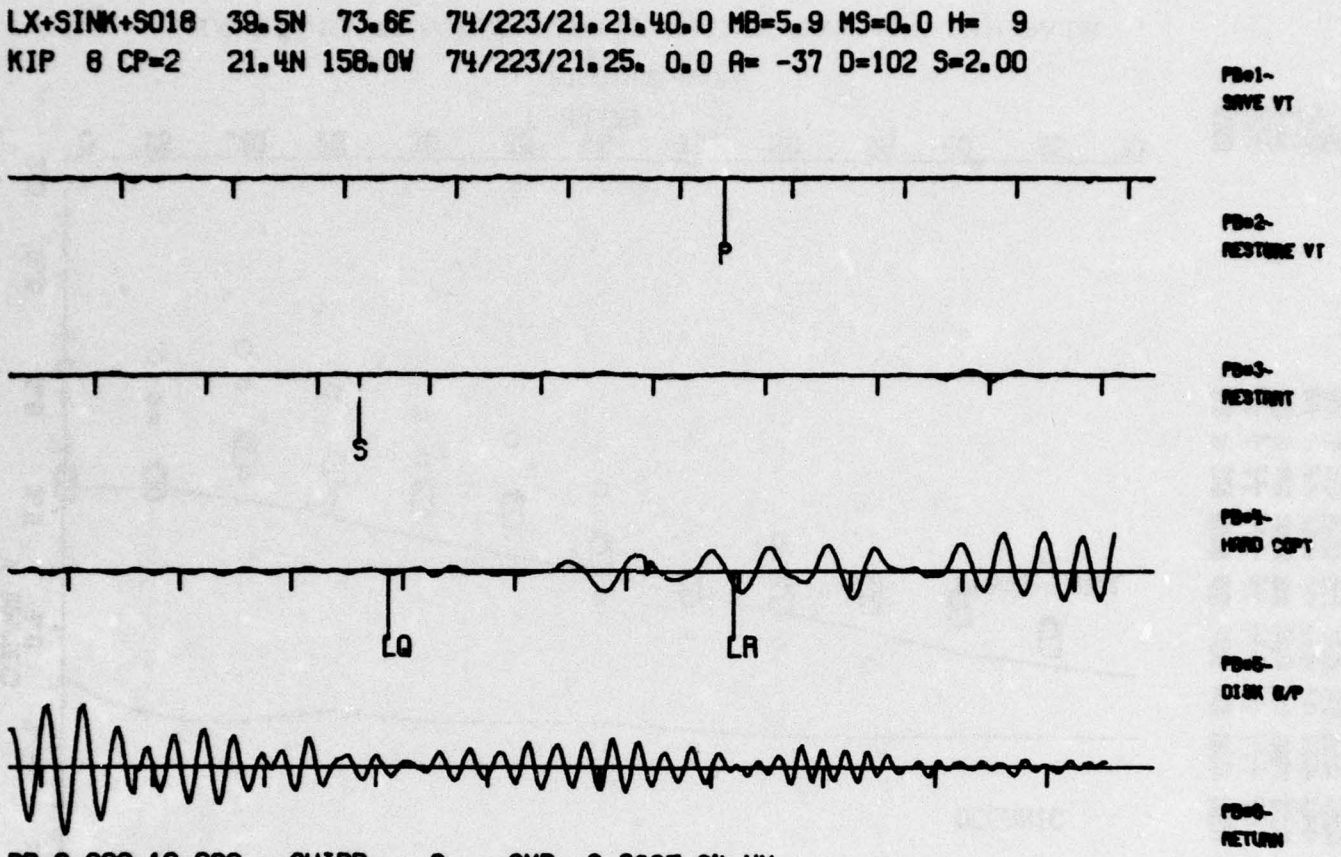

FIGURE A-2d

LOVE WAVE TRACE: RECORDED AT KIP

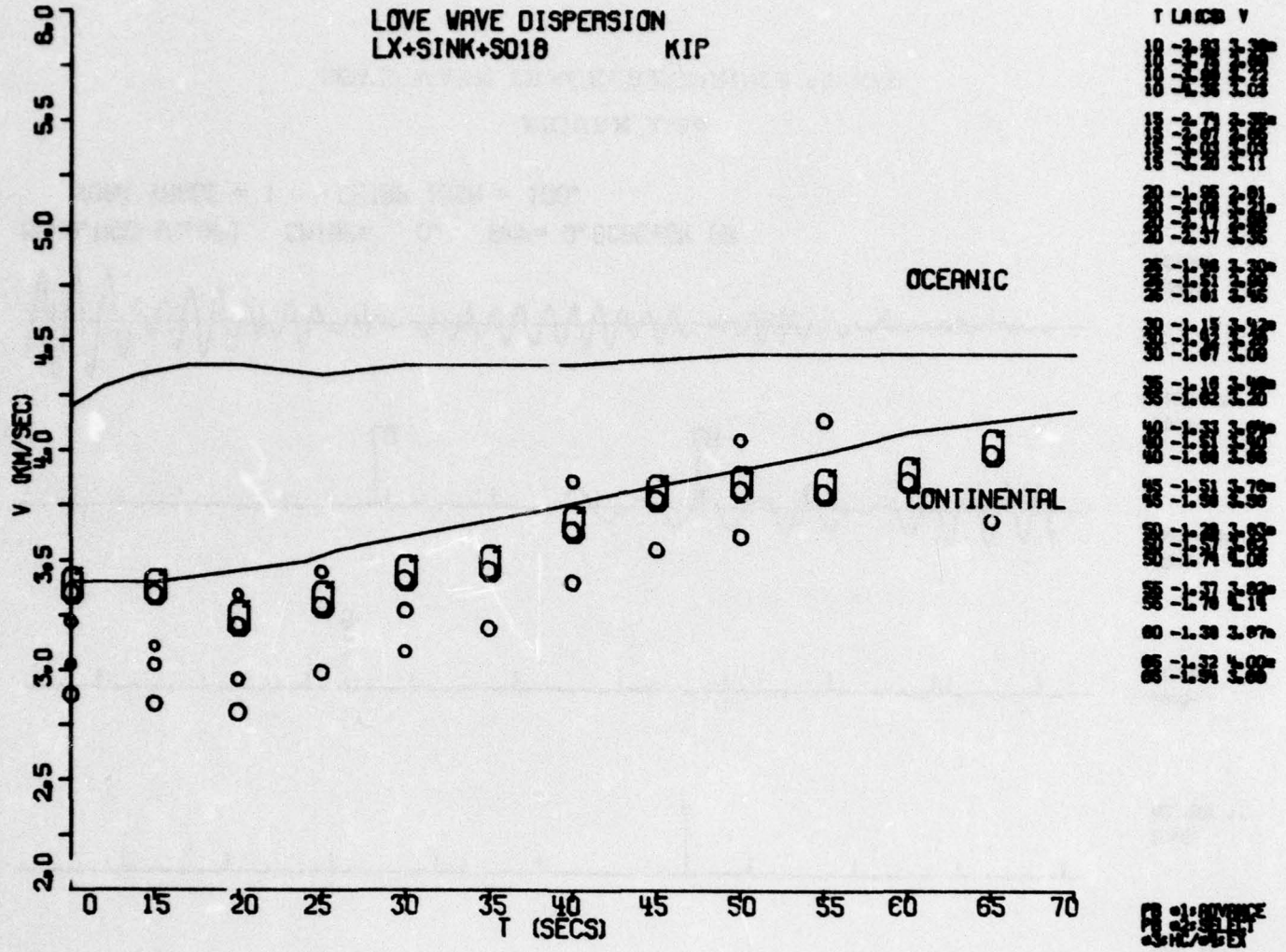

FIGURE A-2e

LQ GROUP VELOCITY CURVE ALONG SINKIANG-KIP PATH

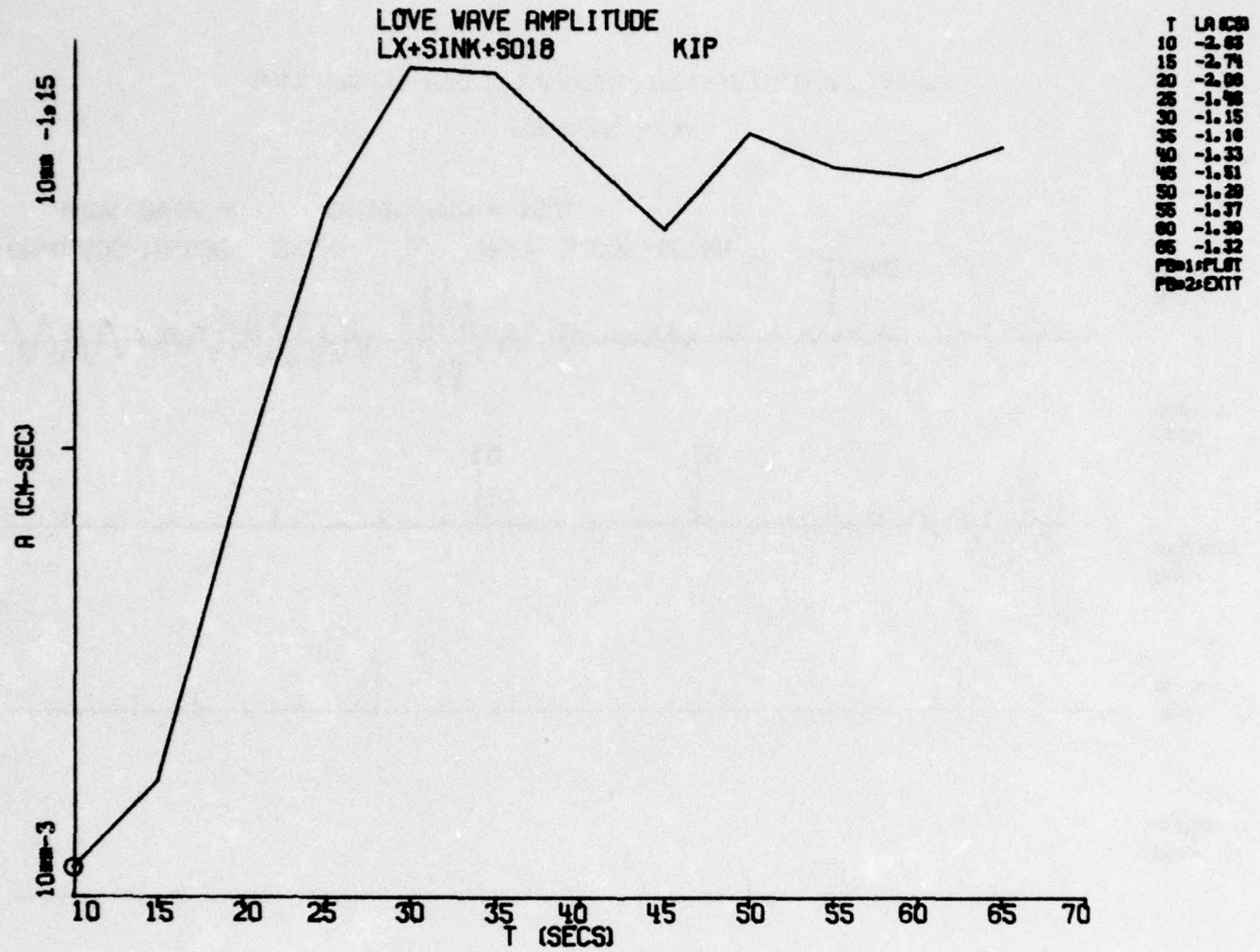

FIGURE A-2f

UNCORRECTED LOVE WAVE SPECTRUM: KIP

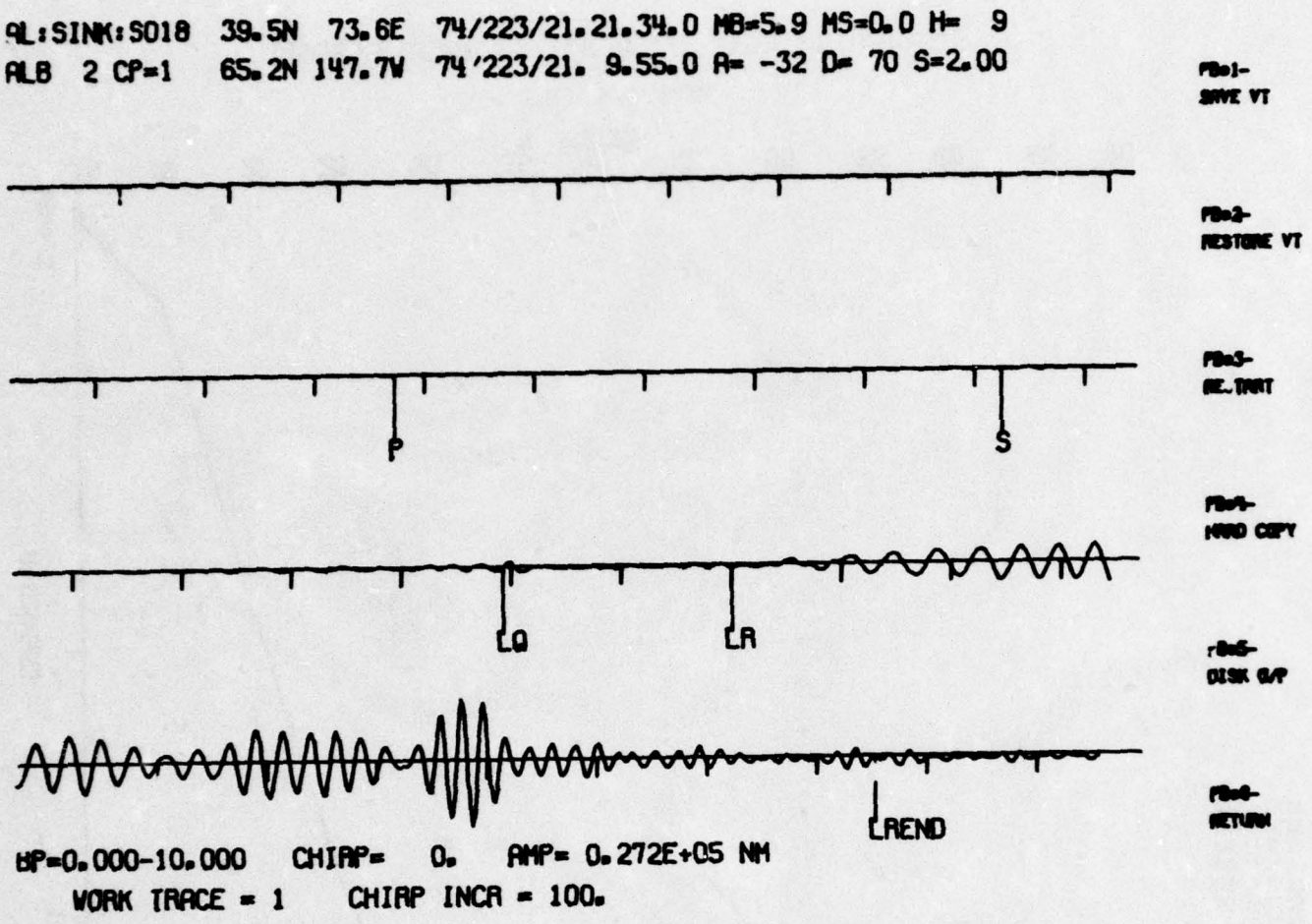

FIGURE A-3a

RAYLEIGH WAVE TRACE: RECORDED AT ALPA

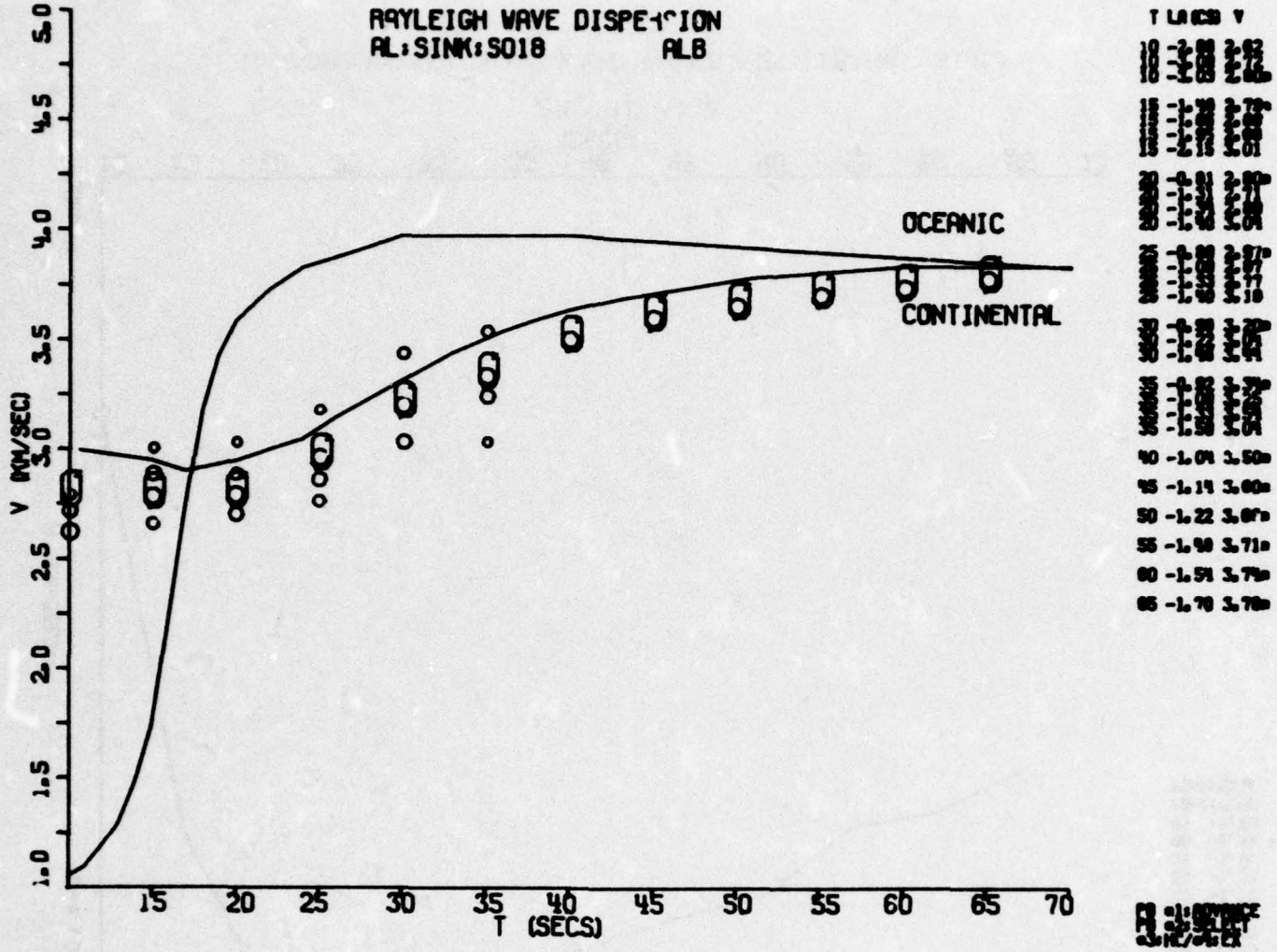

FIGURE A-3b

LR GROUP VELOCITY CURVE ALONG SINKIANG-ALPA PATH

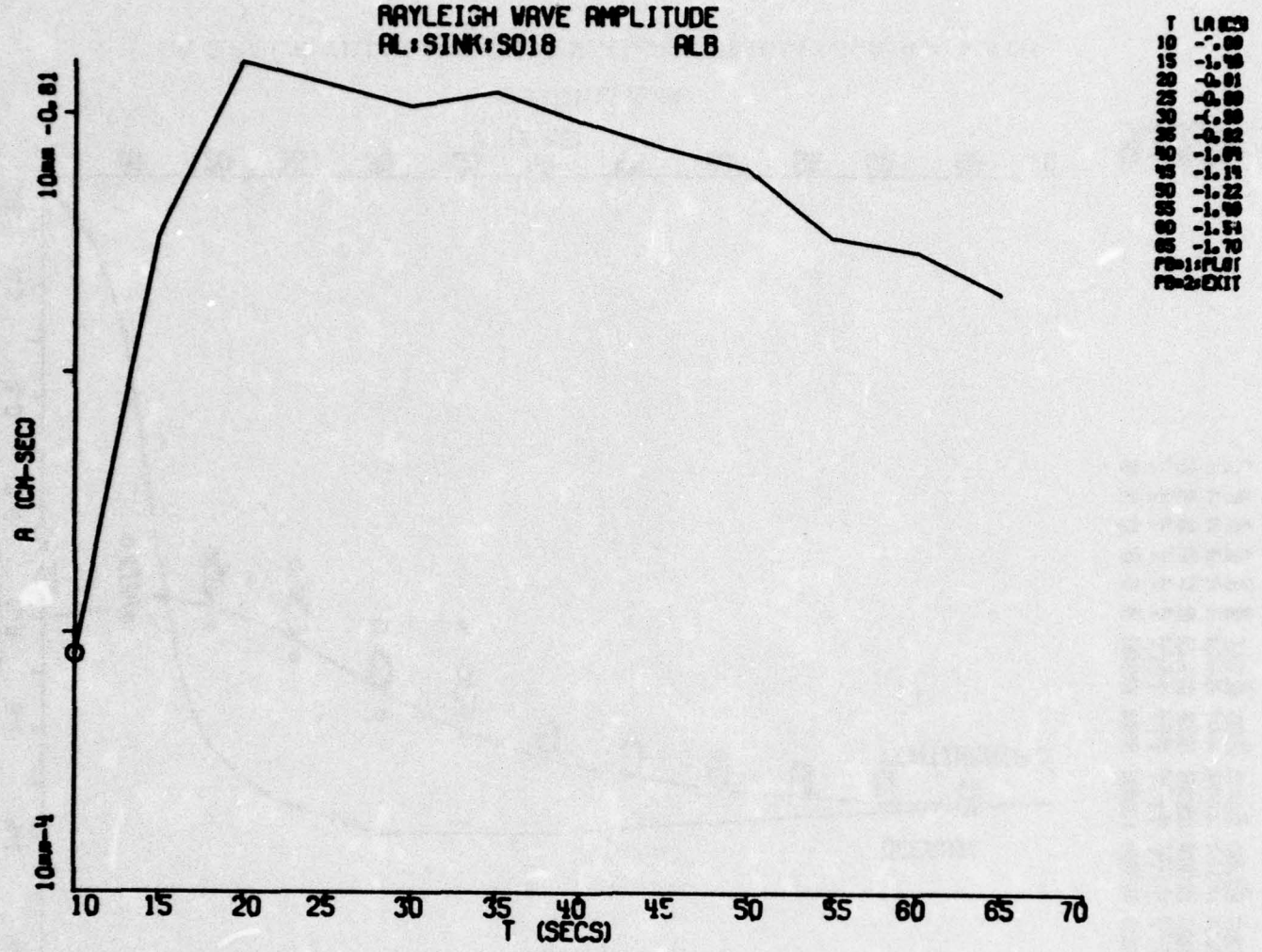

FIGURE A-3c

UNCORRECTED RAYLEIGH WAVE SPECTRUM: ALPA

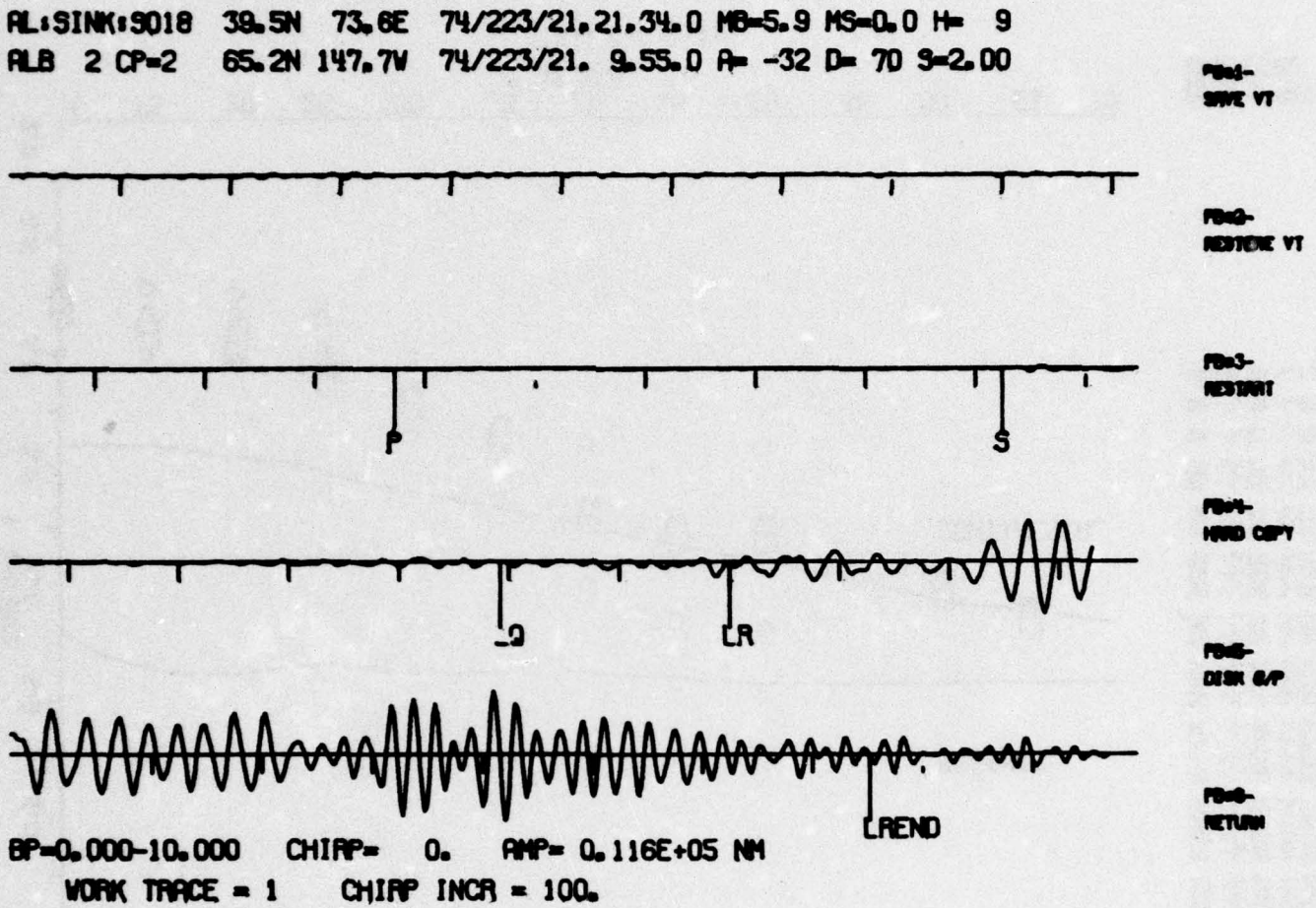

FIGURE A-3d

LOVE WAVE TRACE: RECORDED AT ALPA

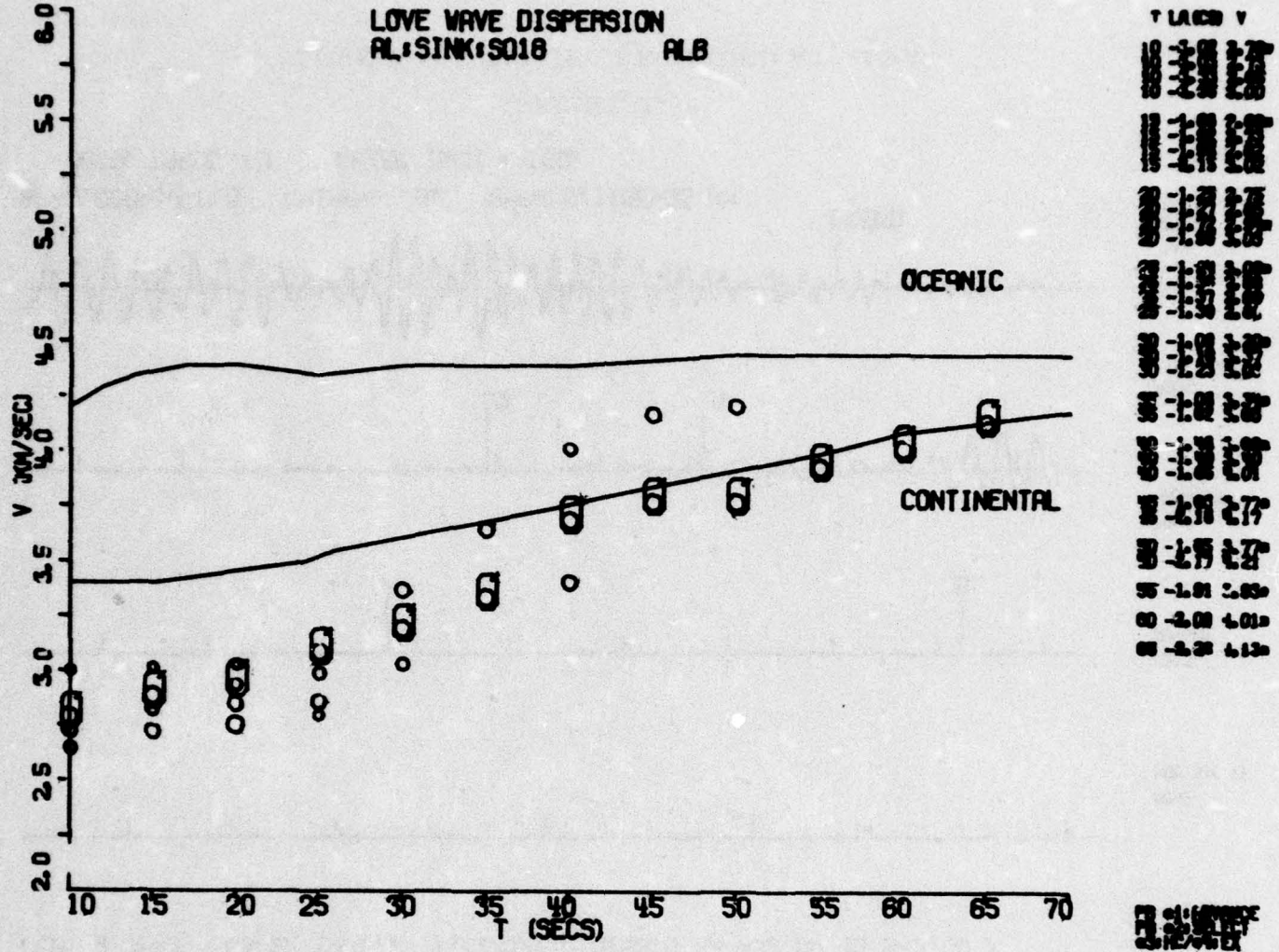

FIGURE A-3e

LQ GROUP VELOCITY CURVE ALONG SINKIANG-ALPA PATH

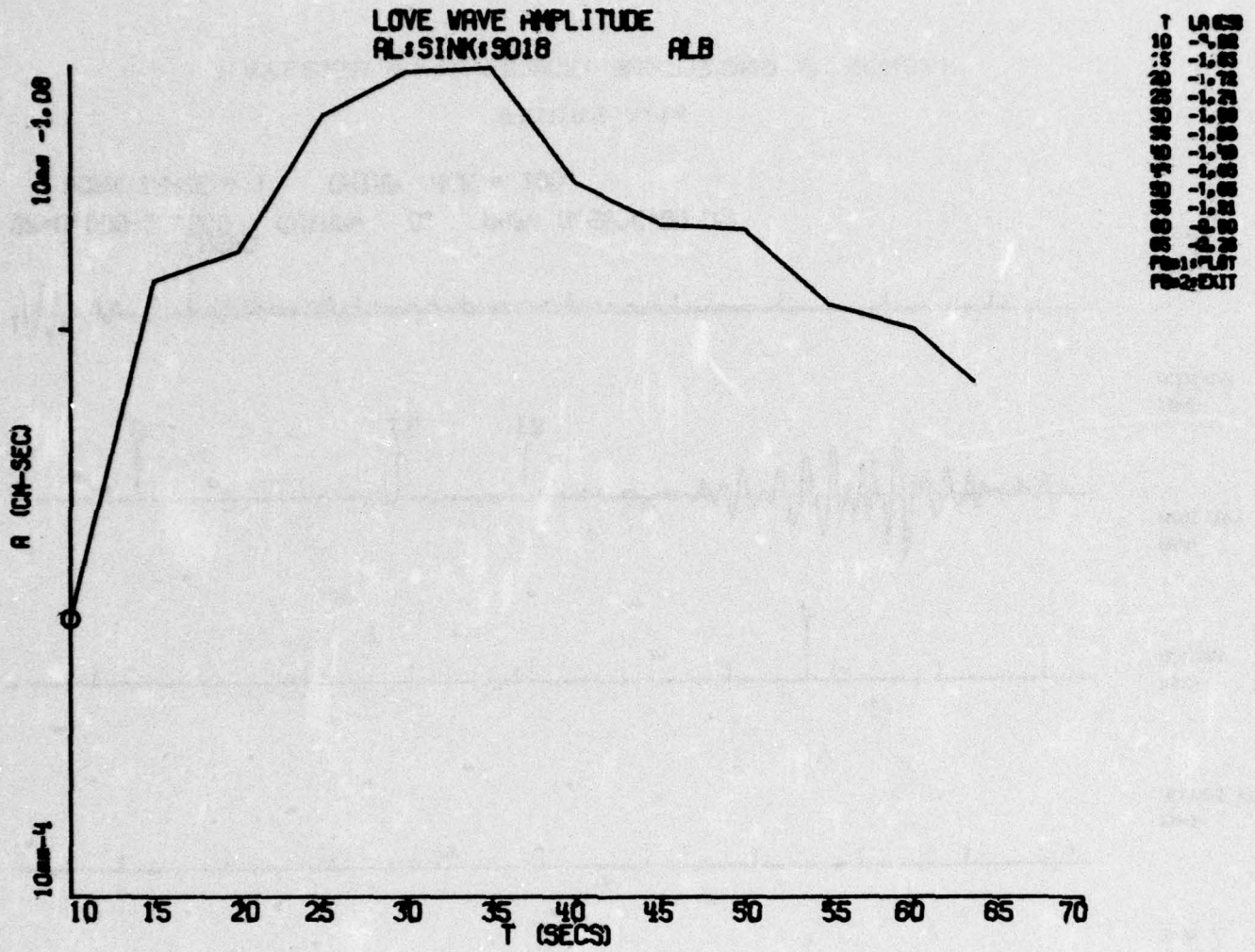

FIGURE A-3f

UNCORRECTED LOVE WAVE SPECTRUM: ALPA

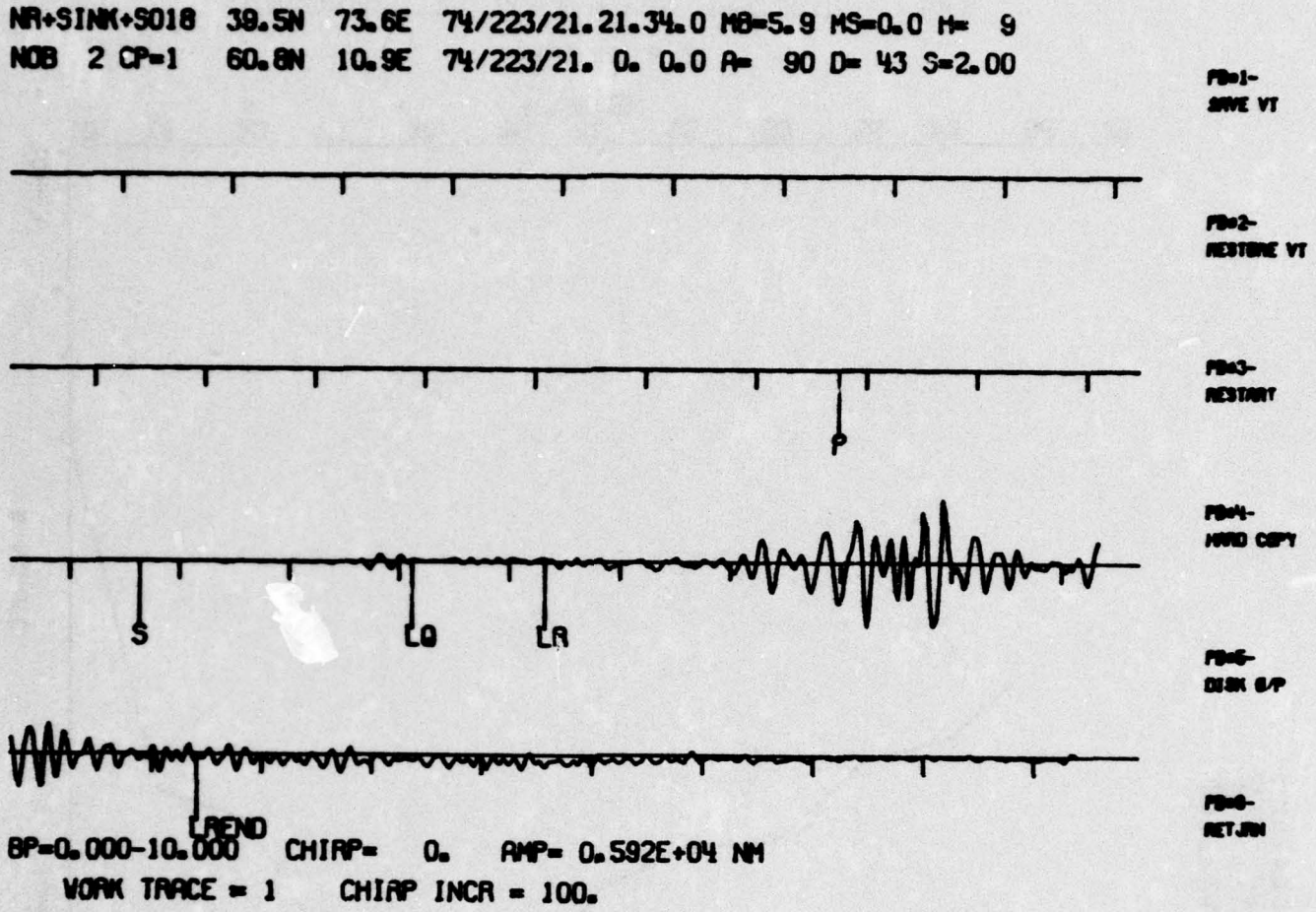

FIGURE A-4a

RAYLEIGH WAVE TRACE: RECORDED AT NORSAR

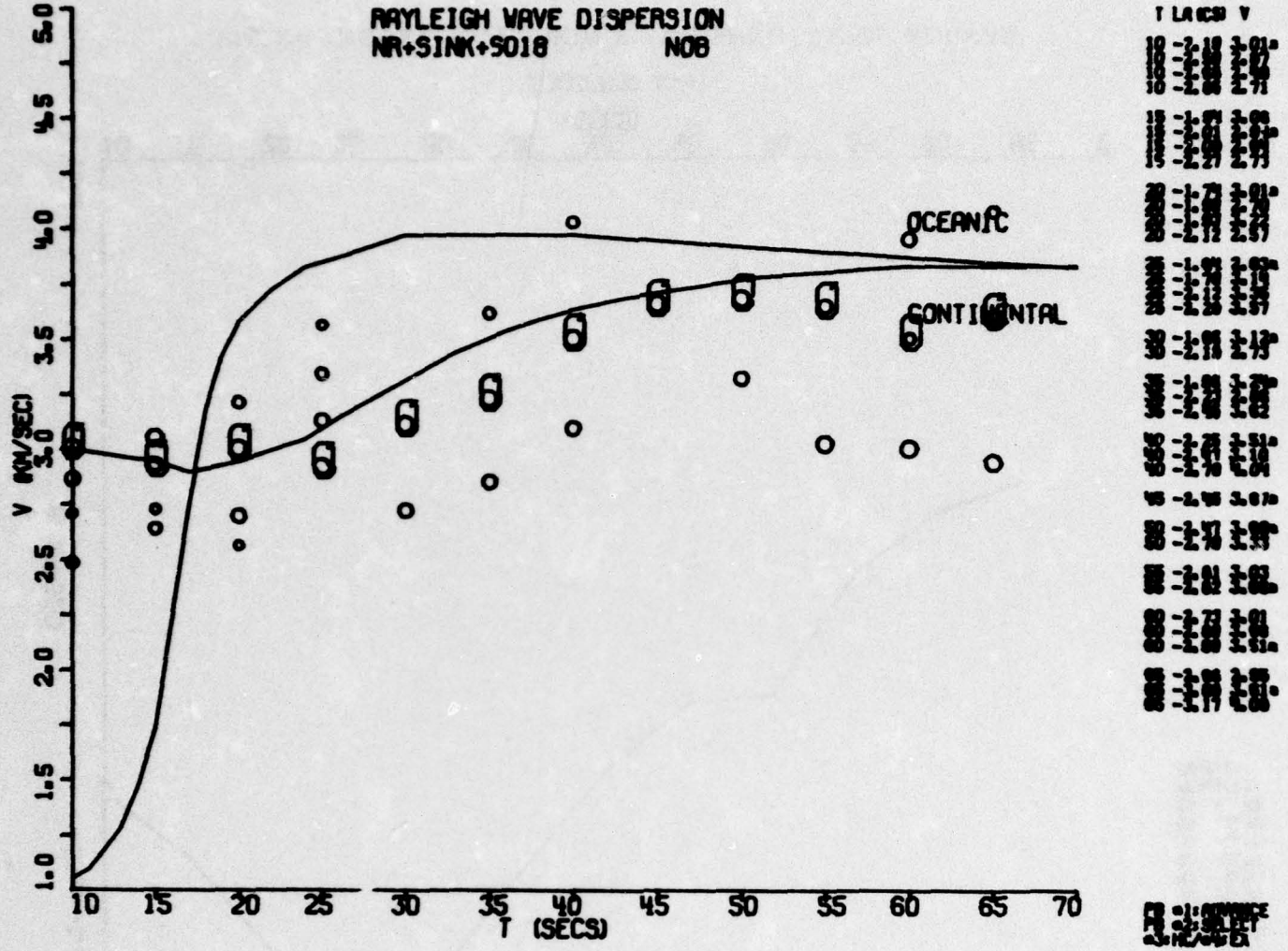

FIGURE A-4b

LR GROUP VELOCITY CURVE ALONG SINKIANG-NORSAR PATH

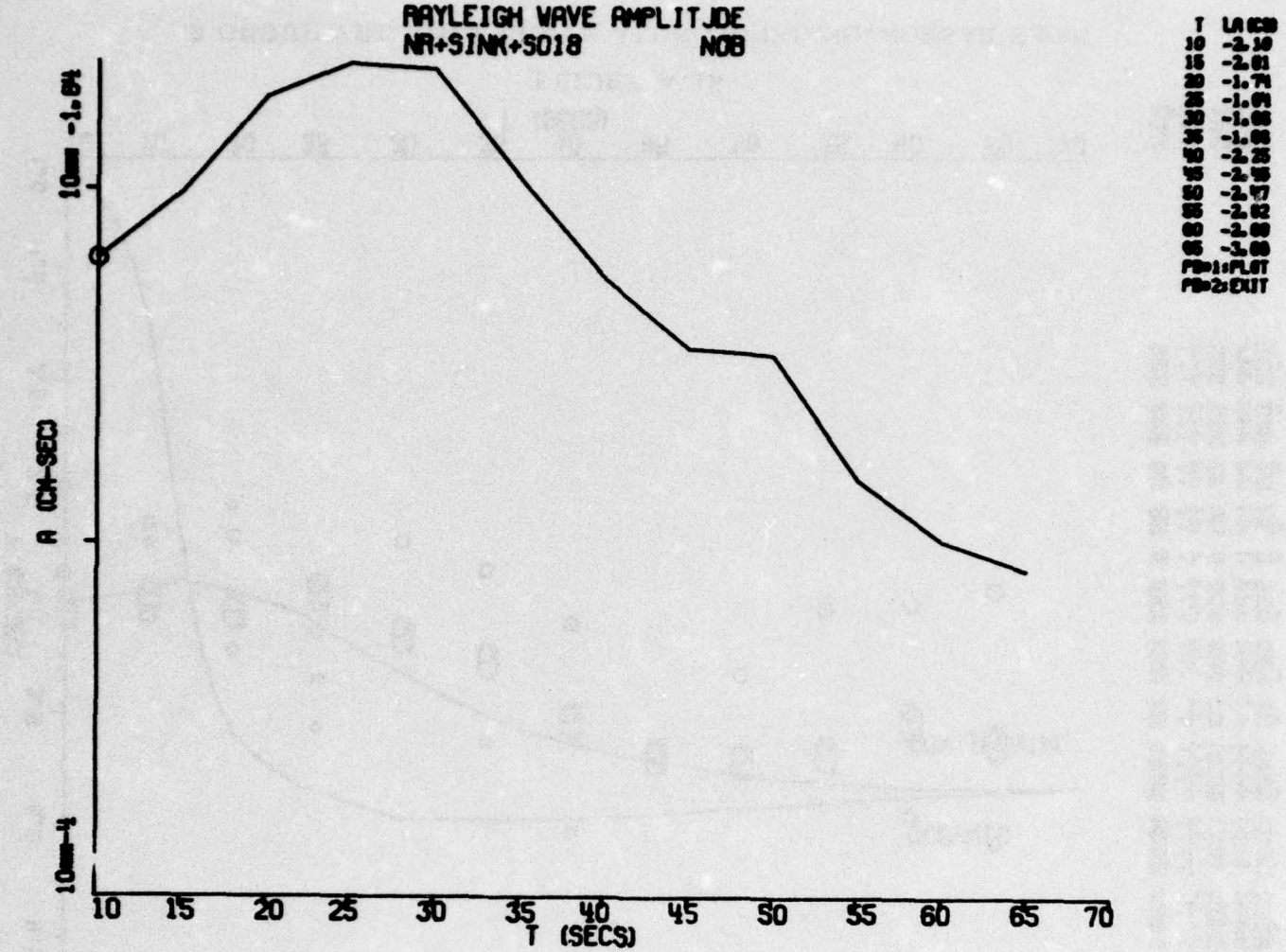

FIGURE A-4c

UNCORRECTED RAYLEIGH WAVE SPECTRUM: NORSAR

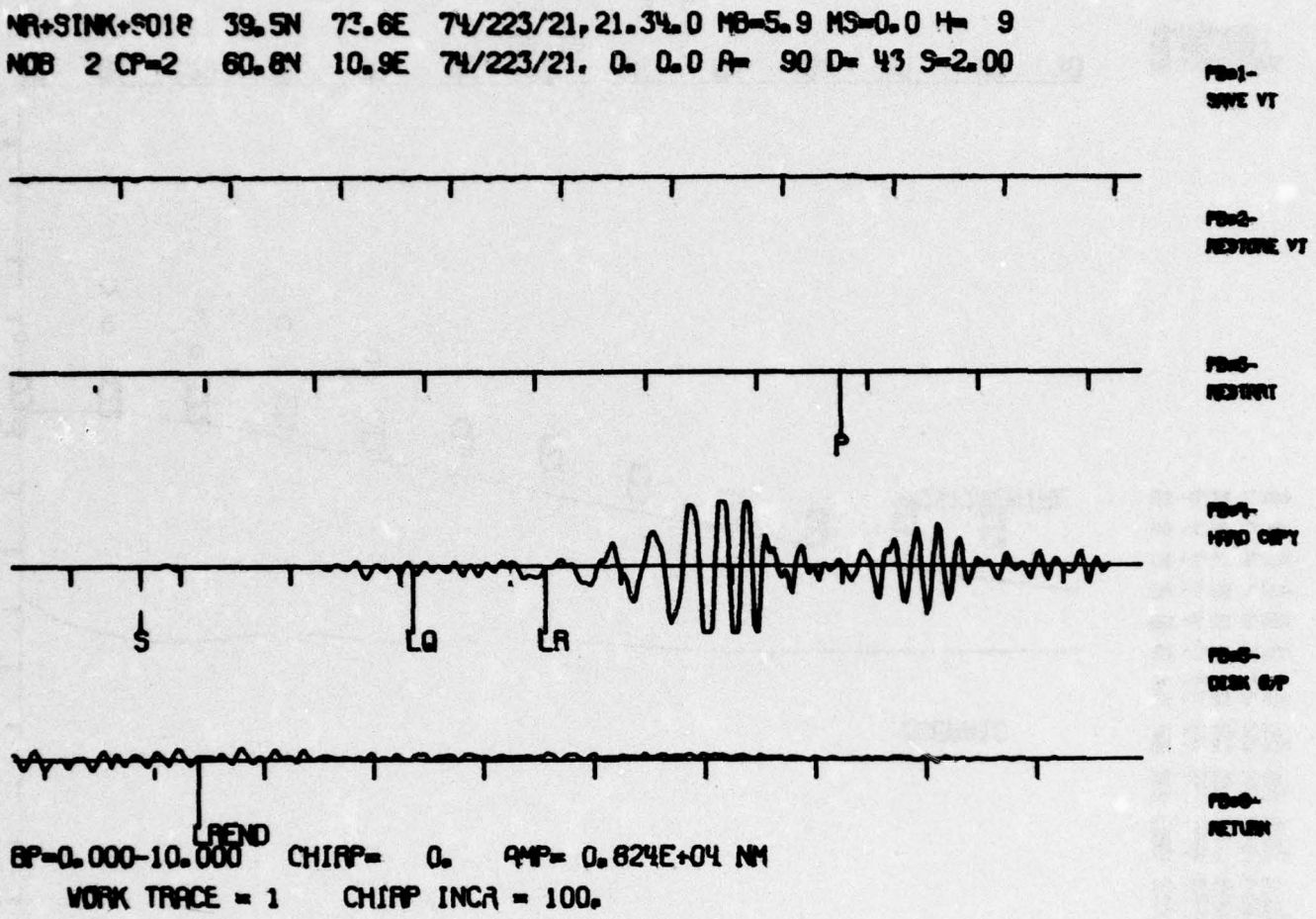

FIGURE A-4d

LOVE WAVE TRACE: RECORDED AT NORSAR

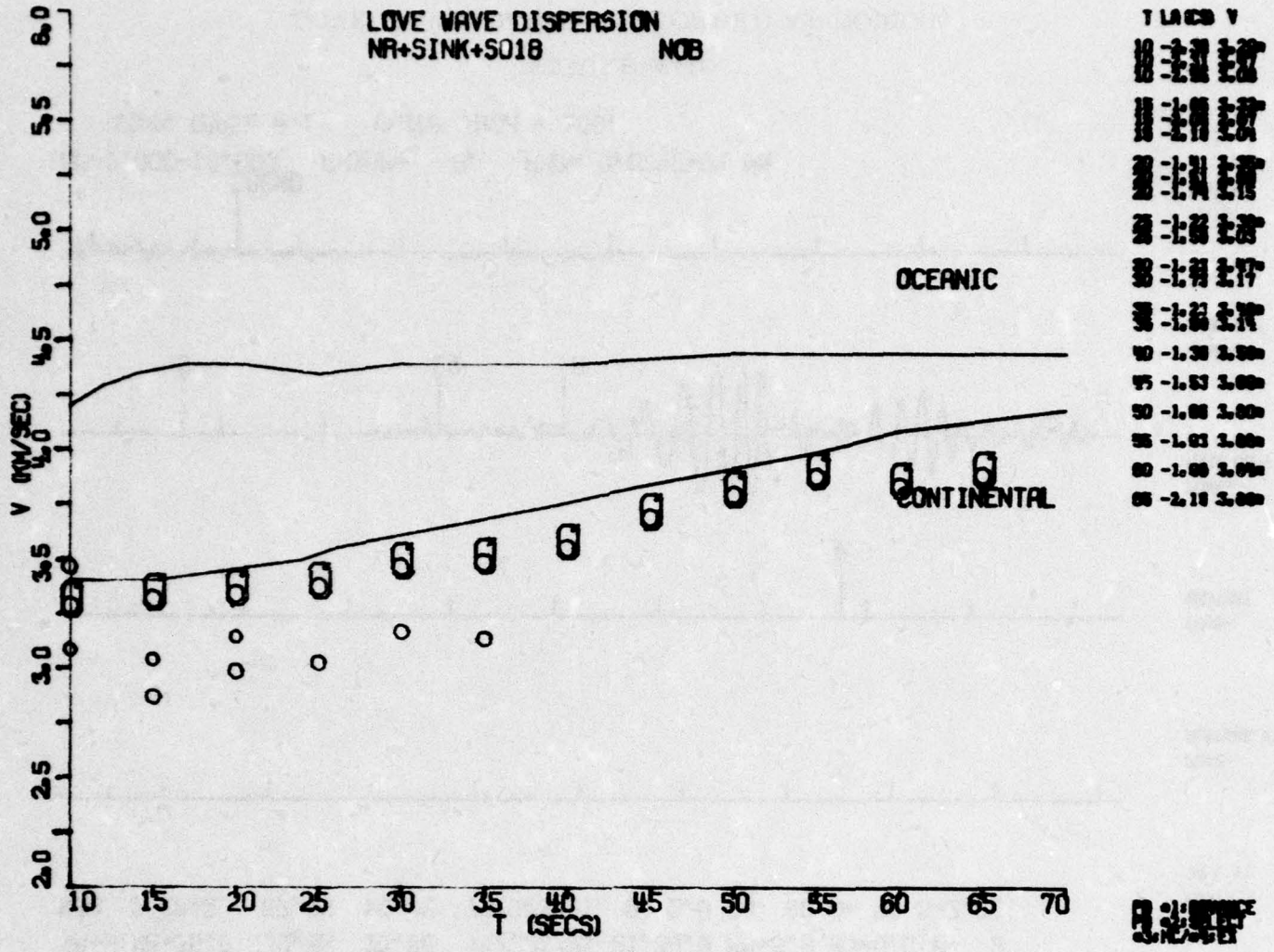

FIGURE A-4e

LQ GROUP VELOCITY CURVE ALONG SINKIANG-NORSAR PATH

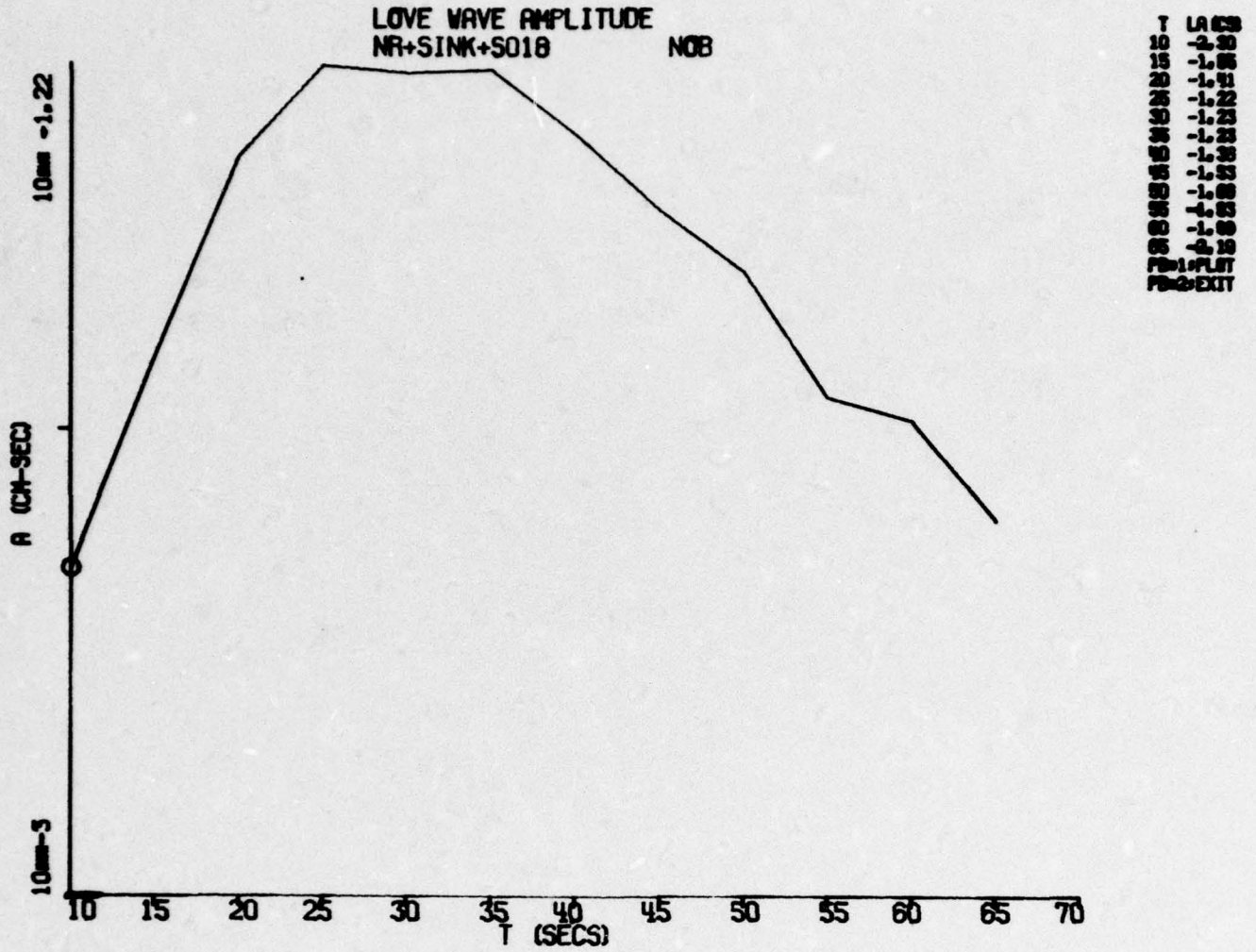

FIGURE A-4f

UNCORRECTED LOVE WAVE SPECTRUM: NORSAR

APPENDIX B

The following figures present the distribution of the minimum residuals of each source parameter for the second group of events discussed in Subsection II-C with their spatial fits.

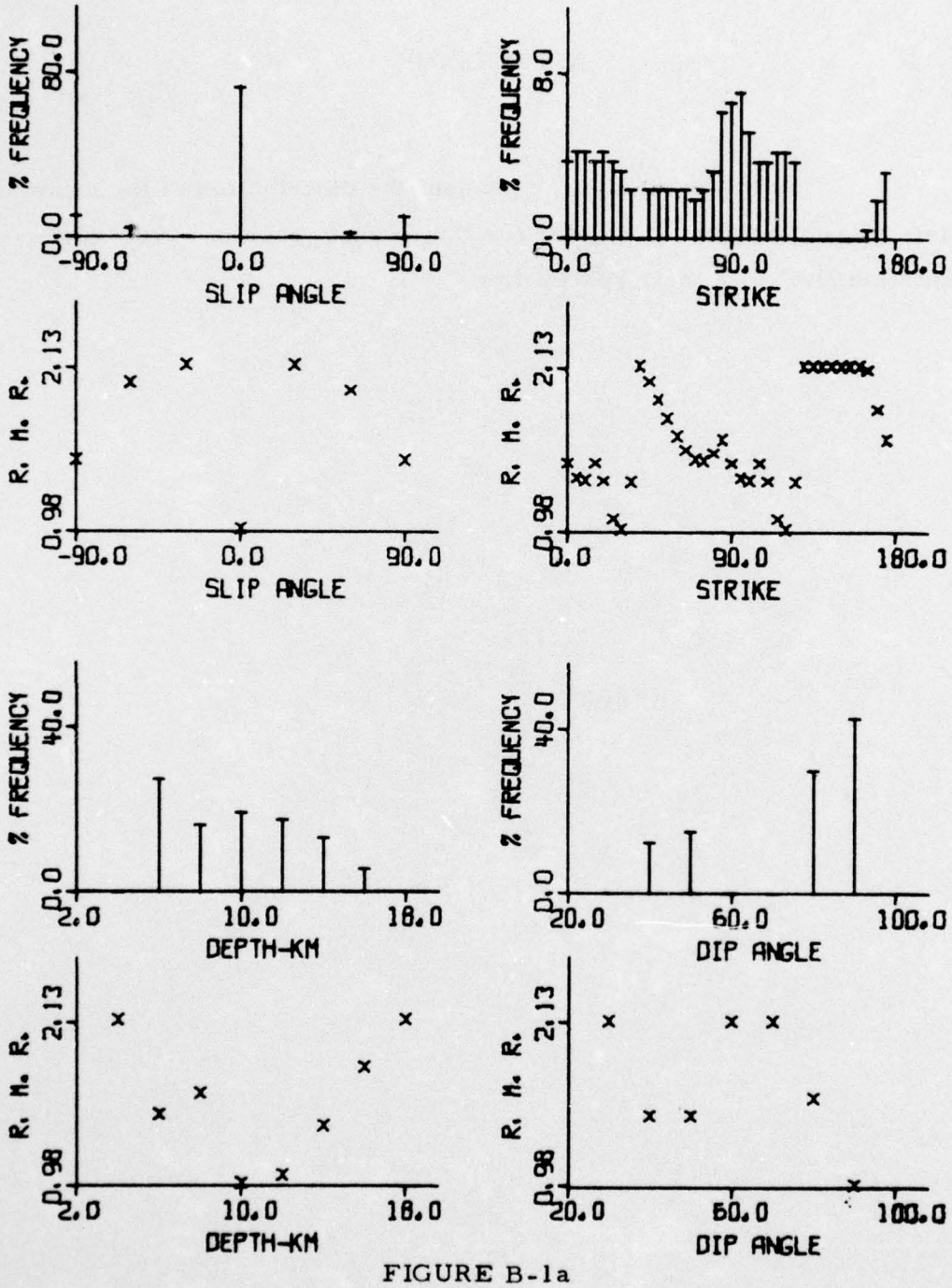

FIGURE B-1a

SOURCE PARAMETER DISTRIBUTIONS: LX+SINK+S004

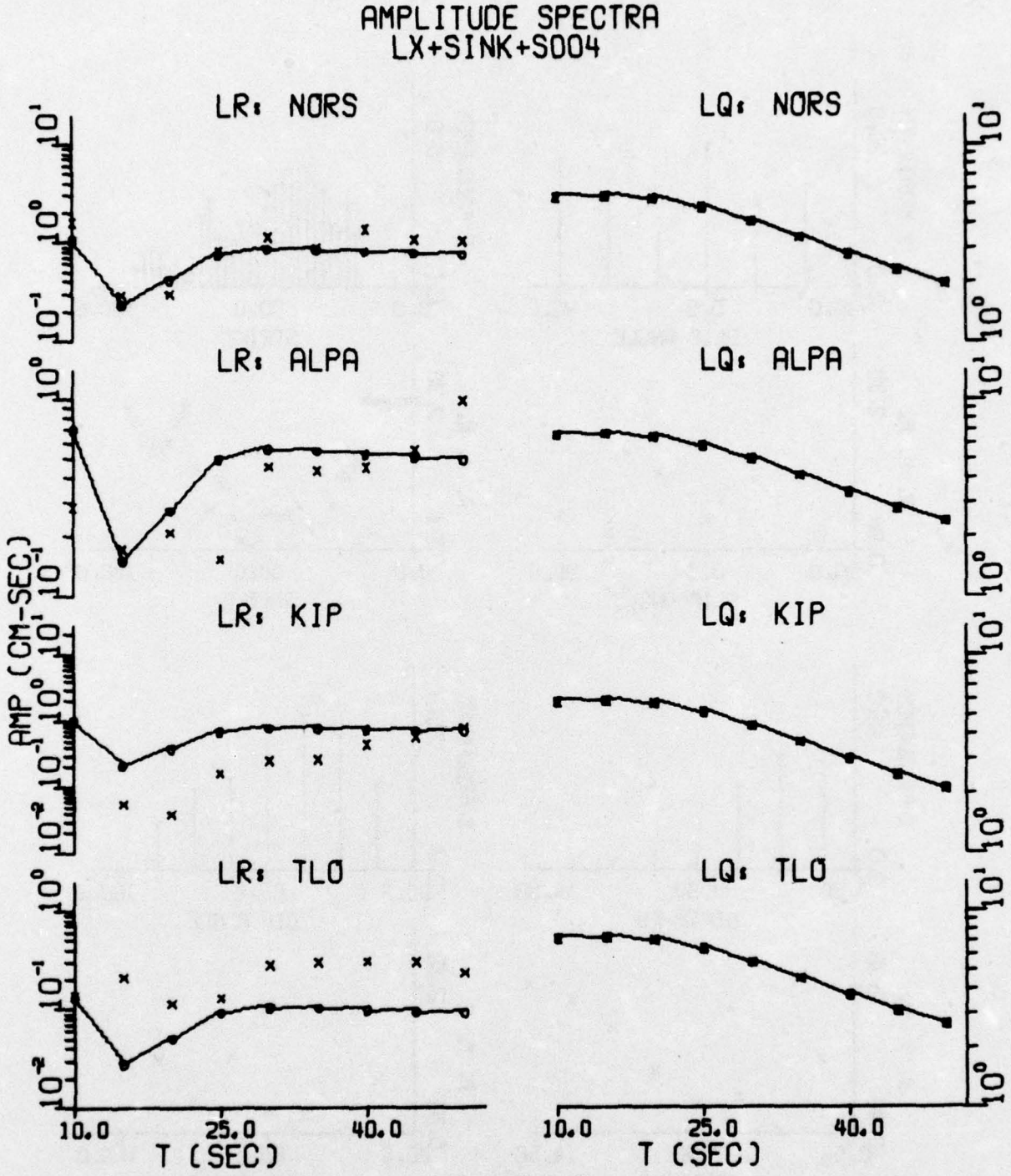

FIGURE B-1b

SPECTRAL FIT: LX+SINK+S004

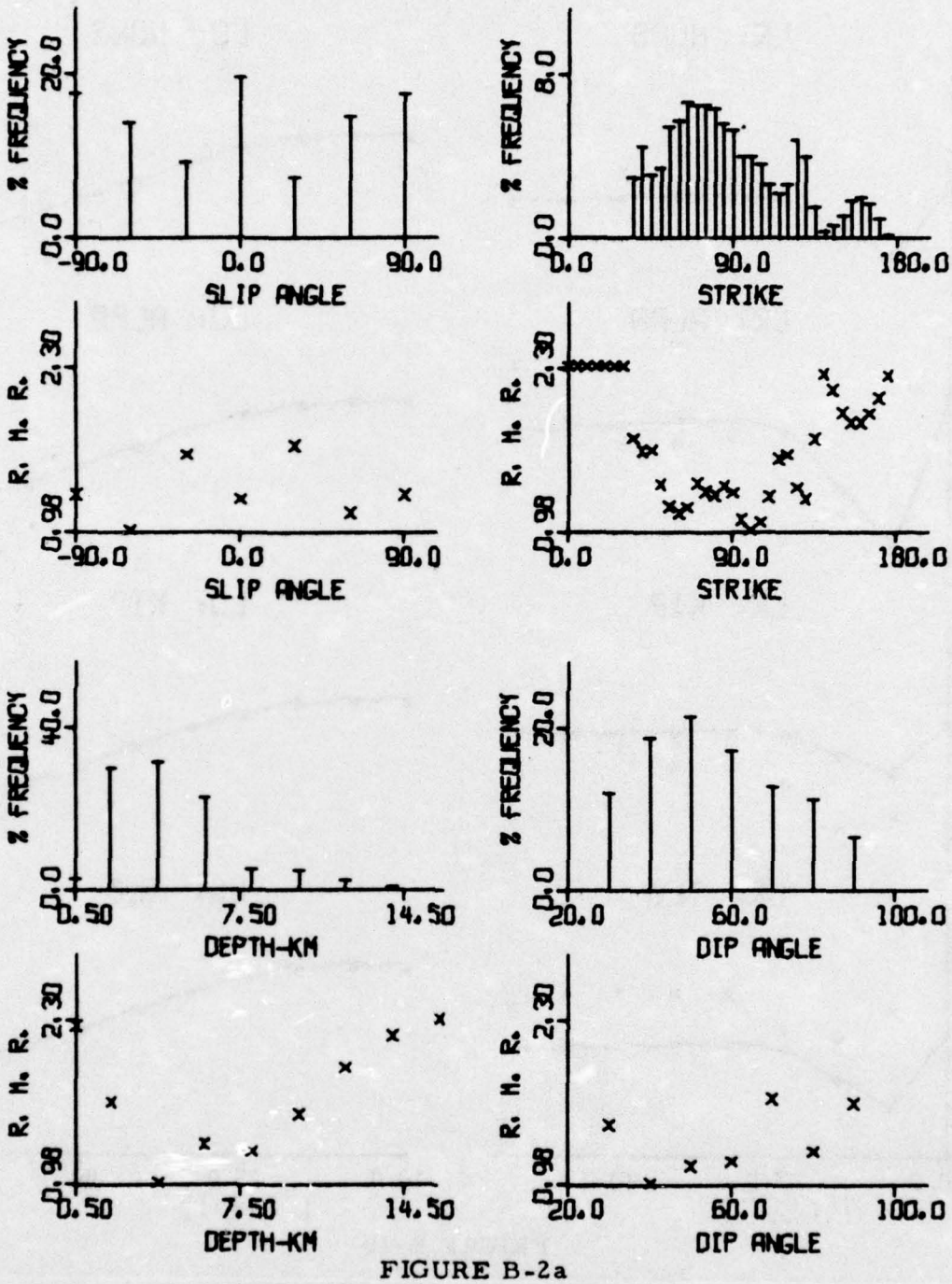

FIGURE B-2a

SOURCE PARAMETER DISTRIBUTIONS: LX+SINK+S005

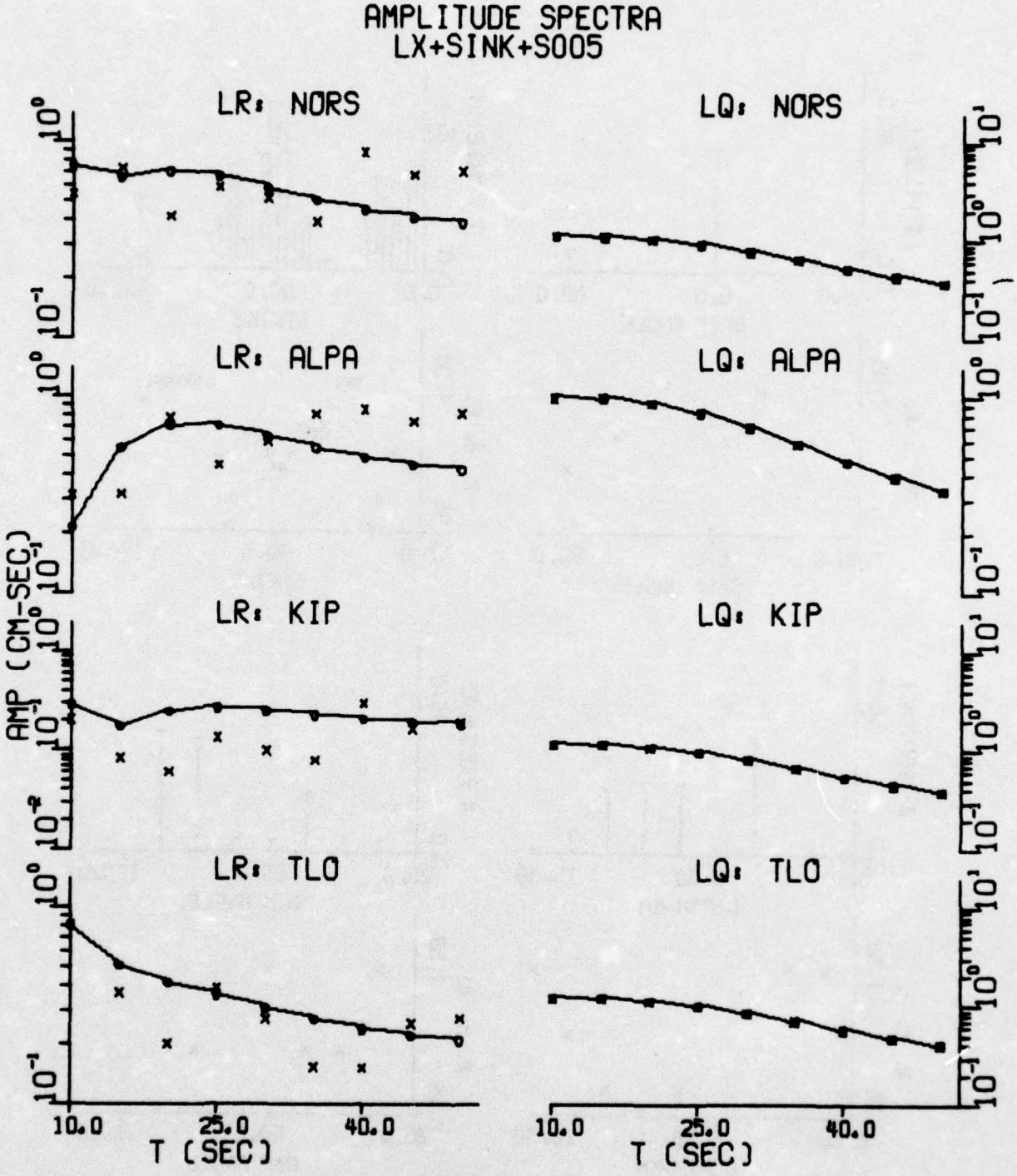

FIGURE B-2b

SPECTRAL FIT: LX+SINK+S005

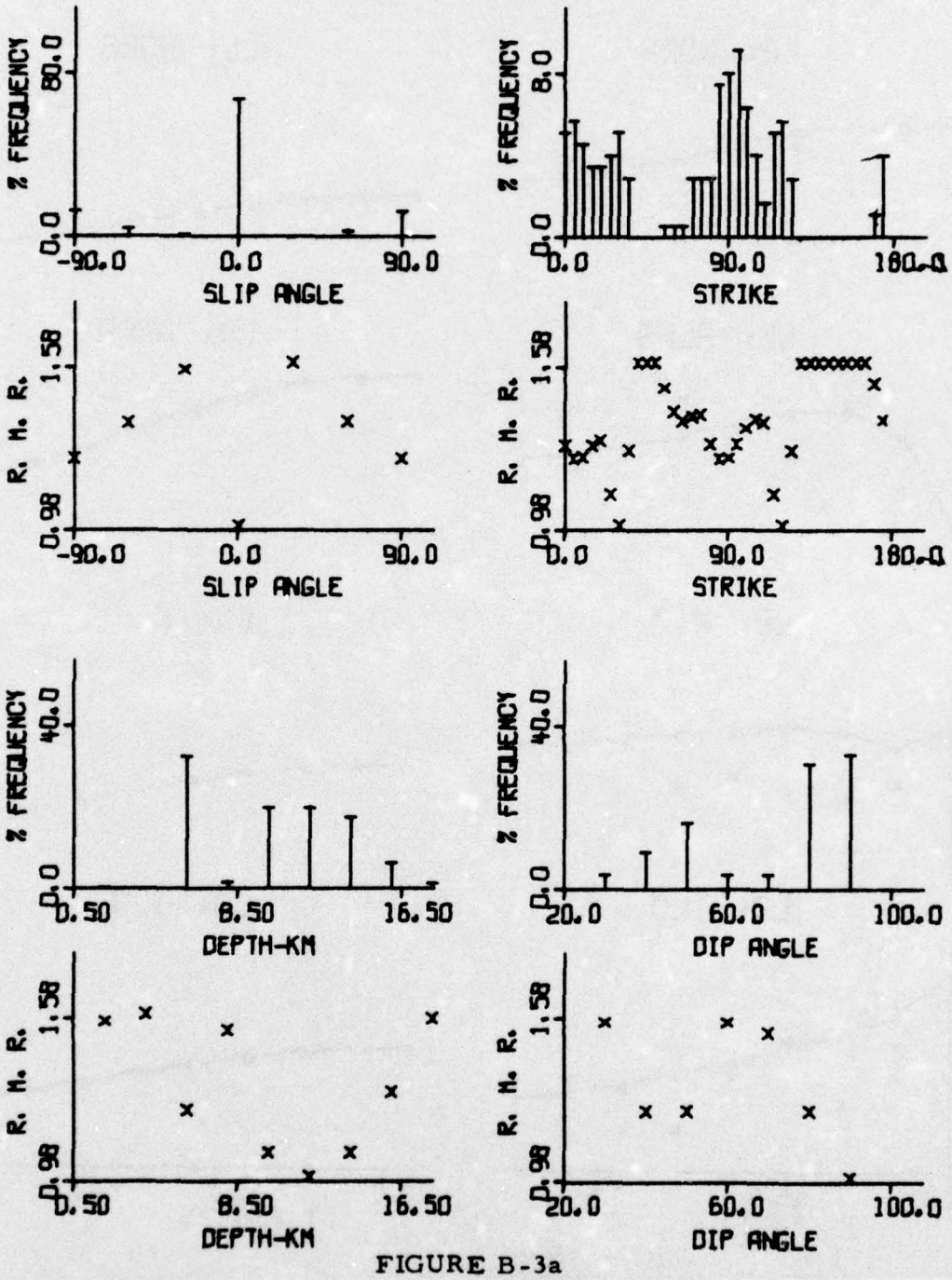

FIGURE B-3a

SOURCE PARAMETER DISTRIBUTIONS: LX+SINK+S006

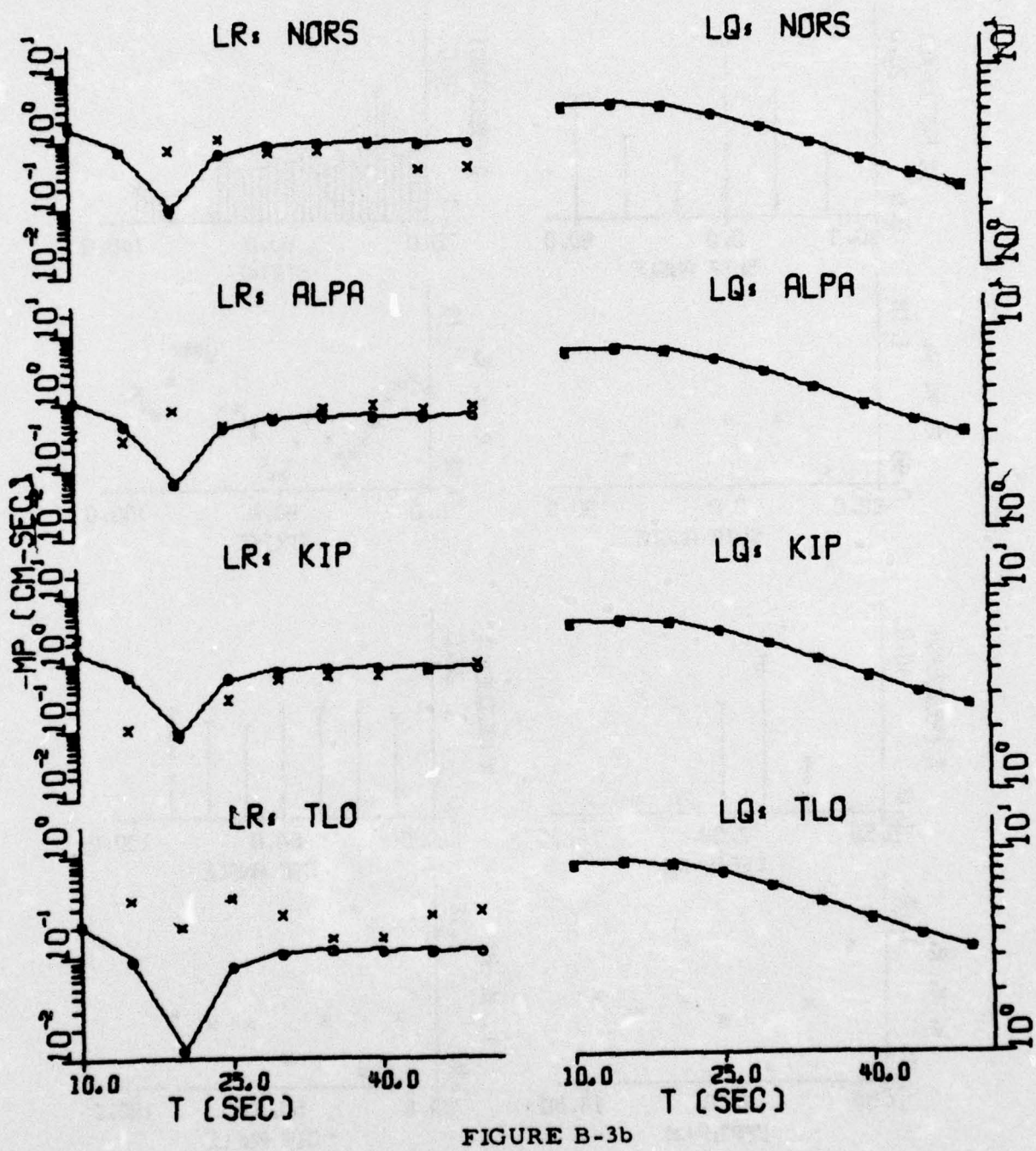

FIGURE B-3b

SPECTRAL FIT: LX+SINK+S006

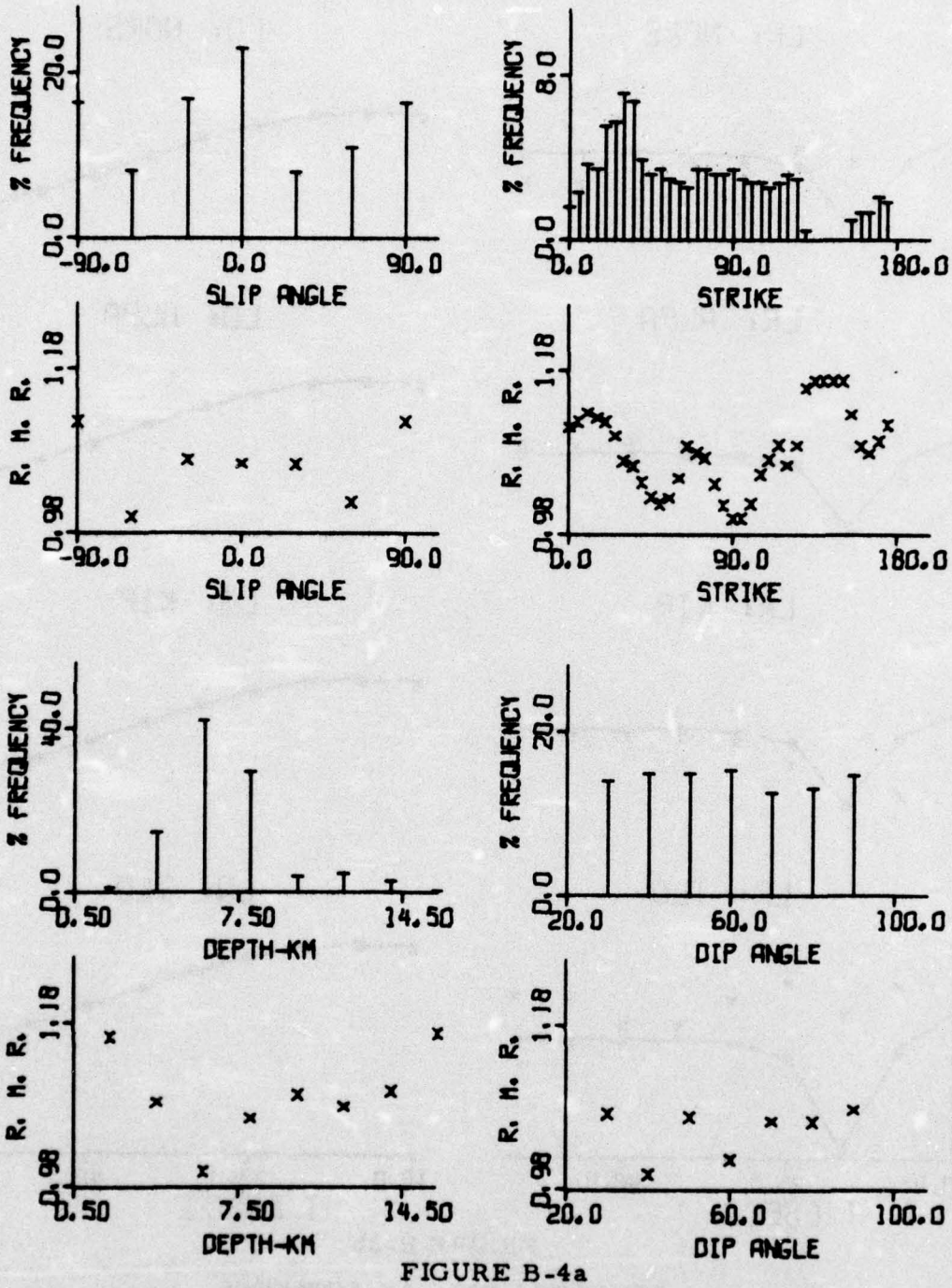

FIGURE B-4a

SOURCE PARAMETER DISTRIBUTIONS: LX+SINK+S008

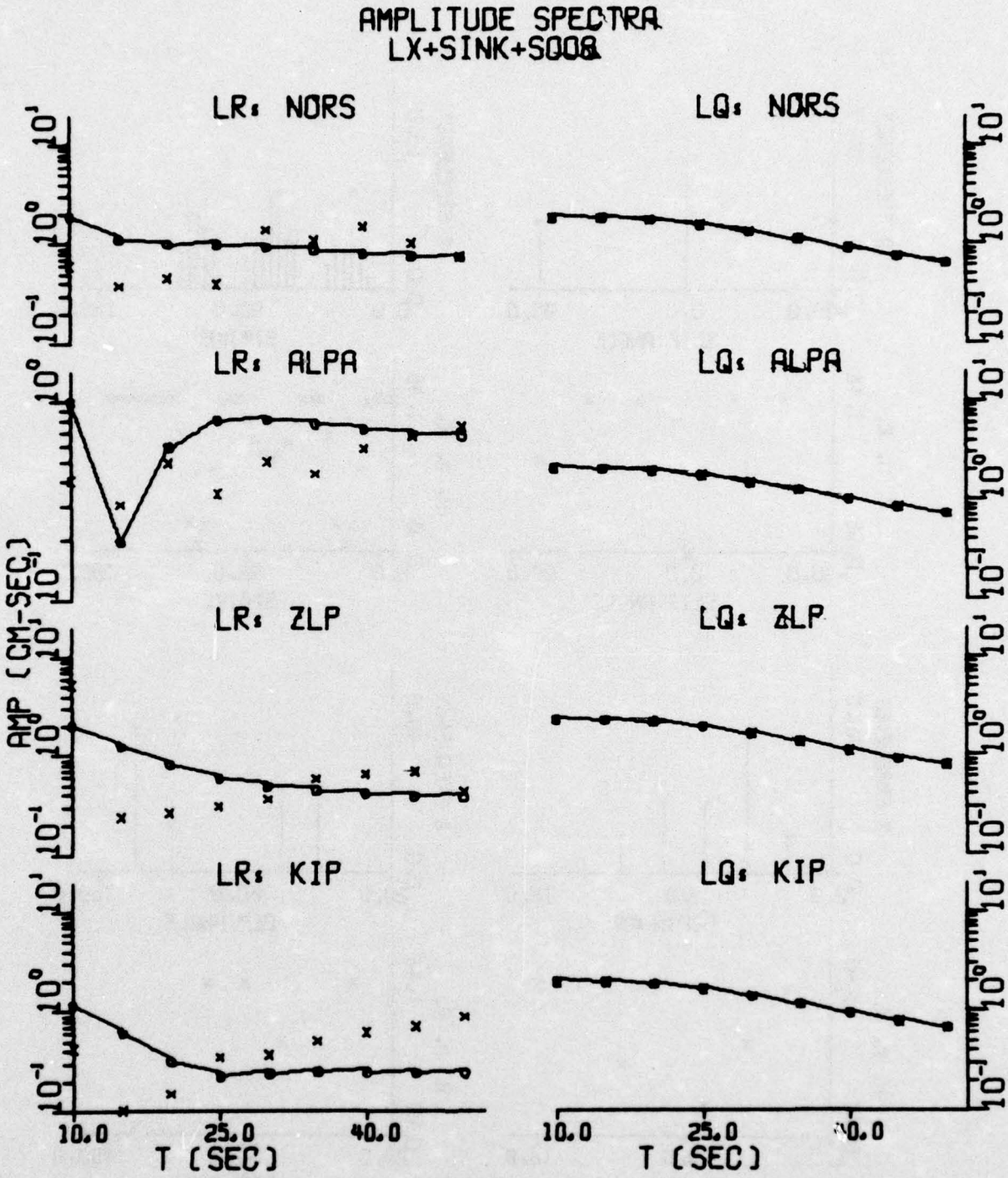

FIGURE B-4b

SPECTRAL FIT: LX+SINK+S008

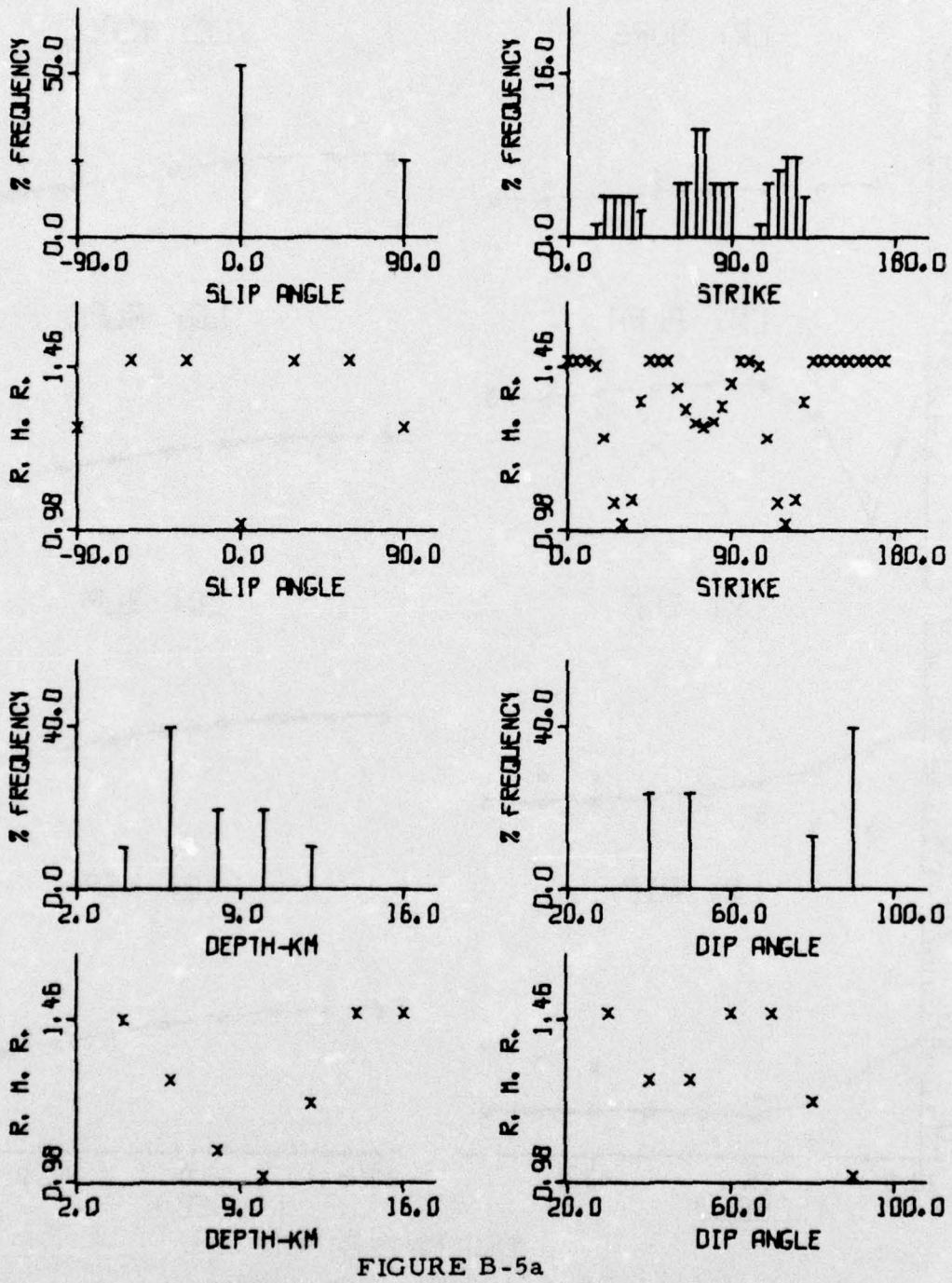

FIGURE B-5a

SOURCE PARAMETER DISTRIBUTIONS: LX+SINK+S010
(PAGE 1 OF 3)

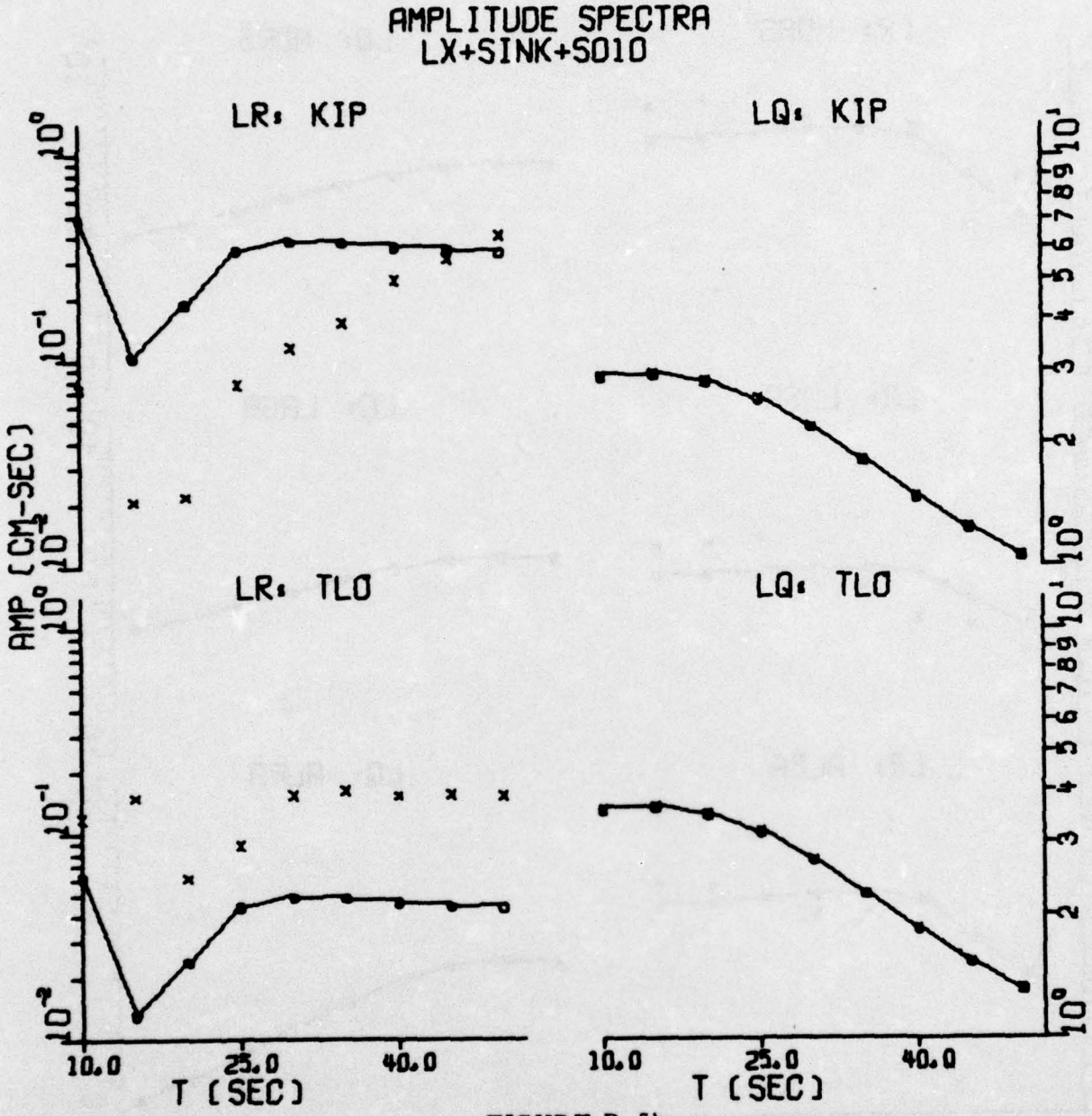

FIGURE B-5b

SPECTRAL FIT: LX+SINK+S010
(PAGE 2 OF 3)

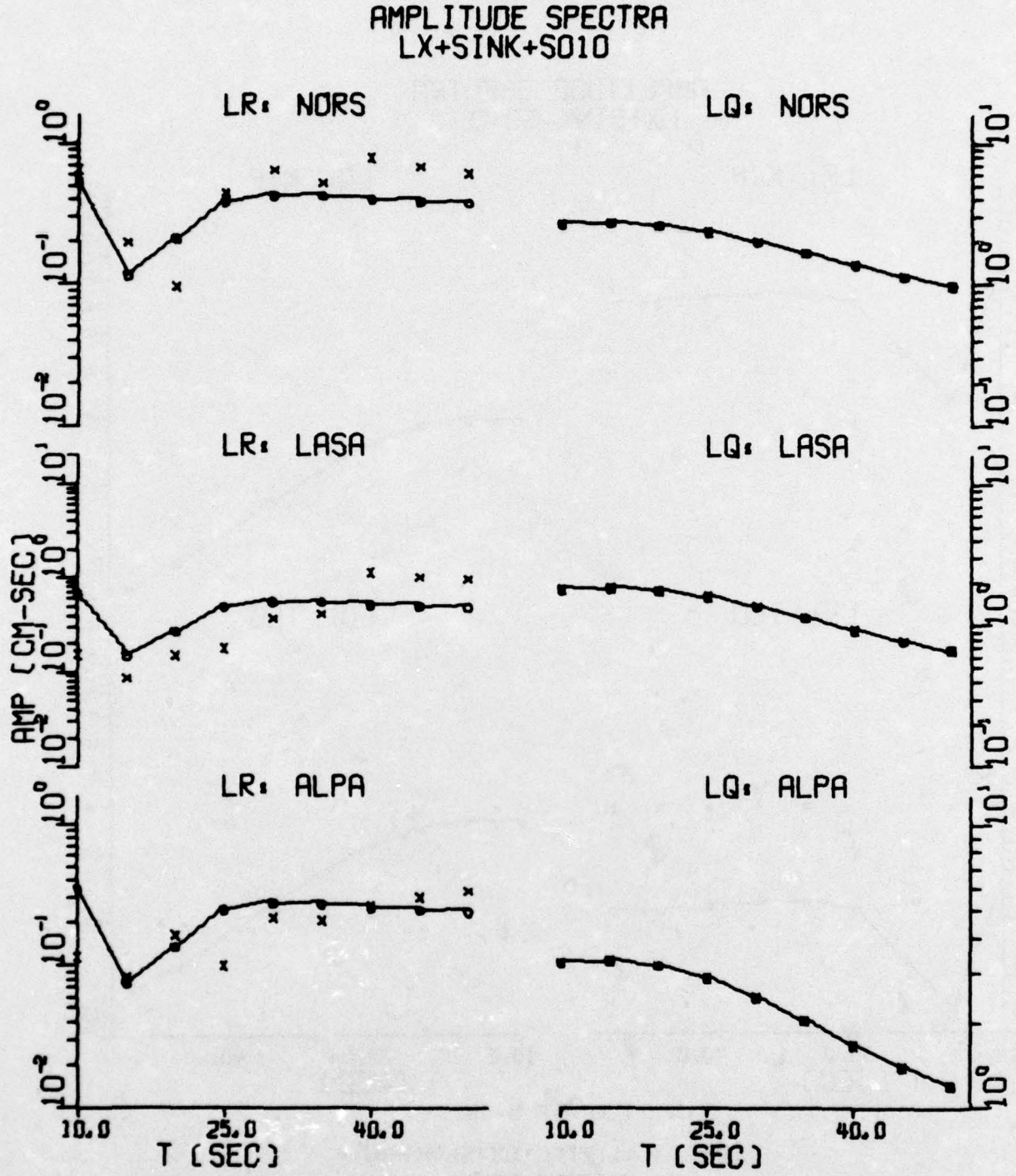

FIGURE B-5b

SPECTRAL FIT: LX+SINK+S010
(PAGE 3 OF 3)

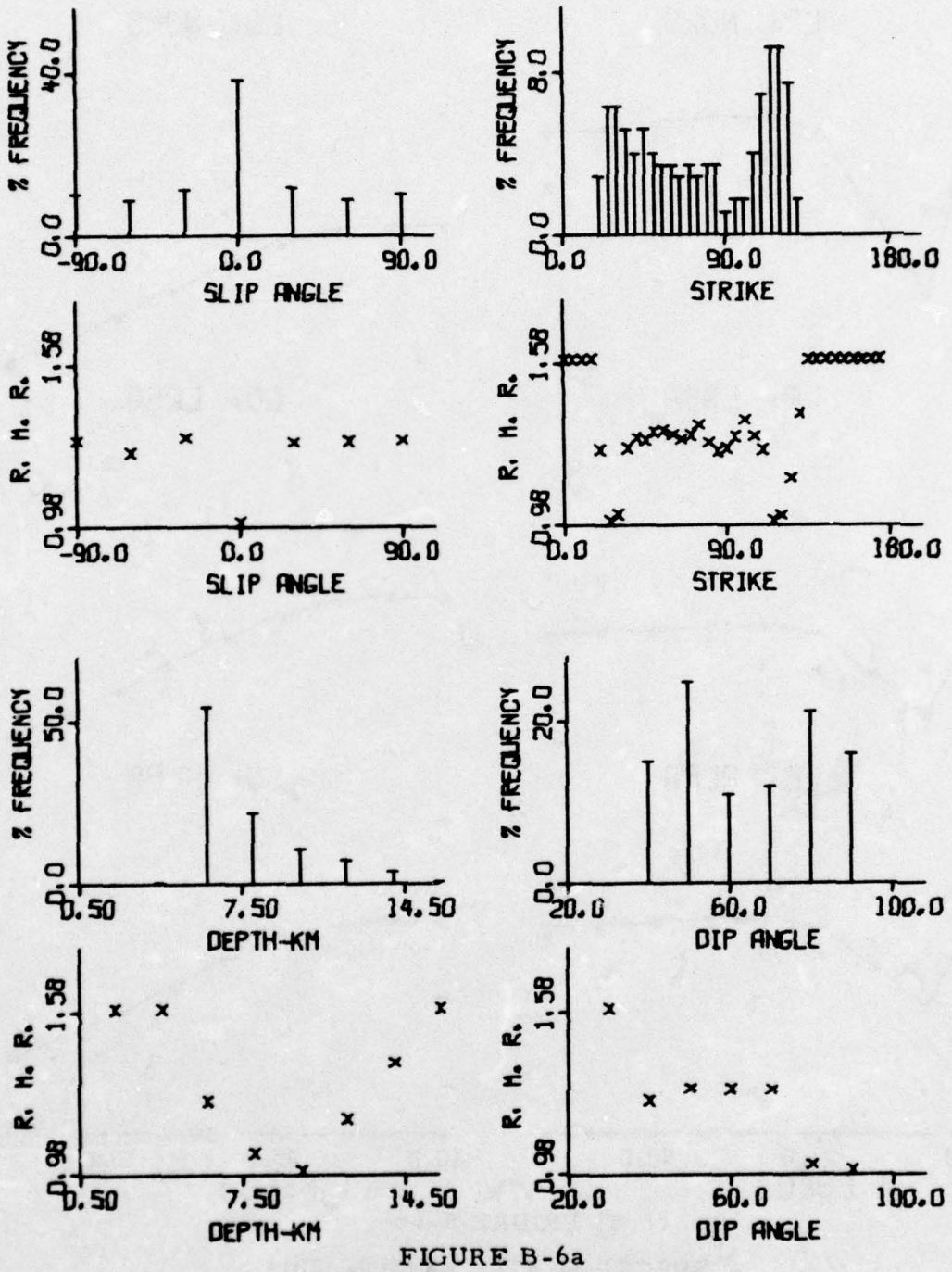

FIGURE B-6a

SOURCE PARAMETER DISTRIBUTIONS: LX+SINK+S011

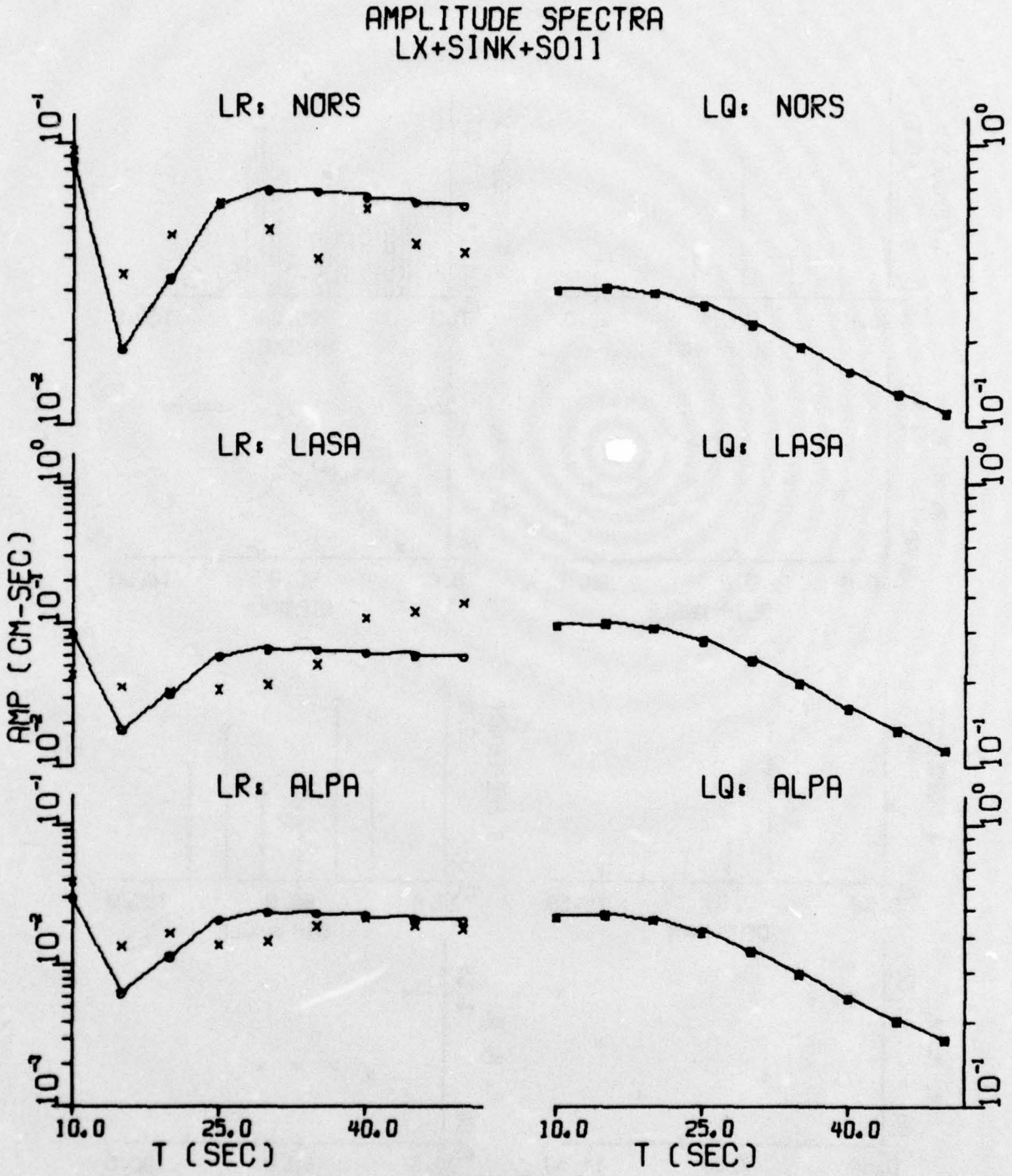

FIGURE B-6b

SPECTRAL FIT: LX+SINK+S011

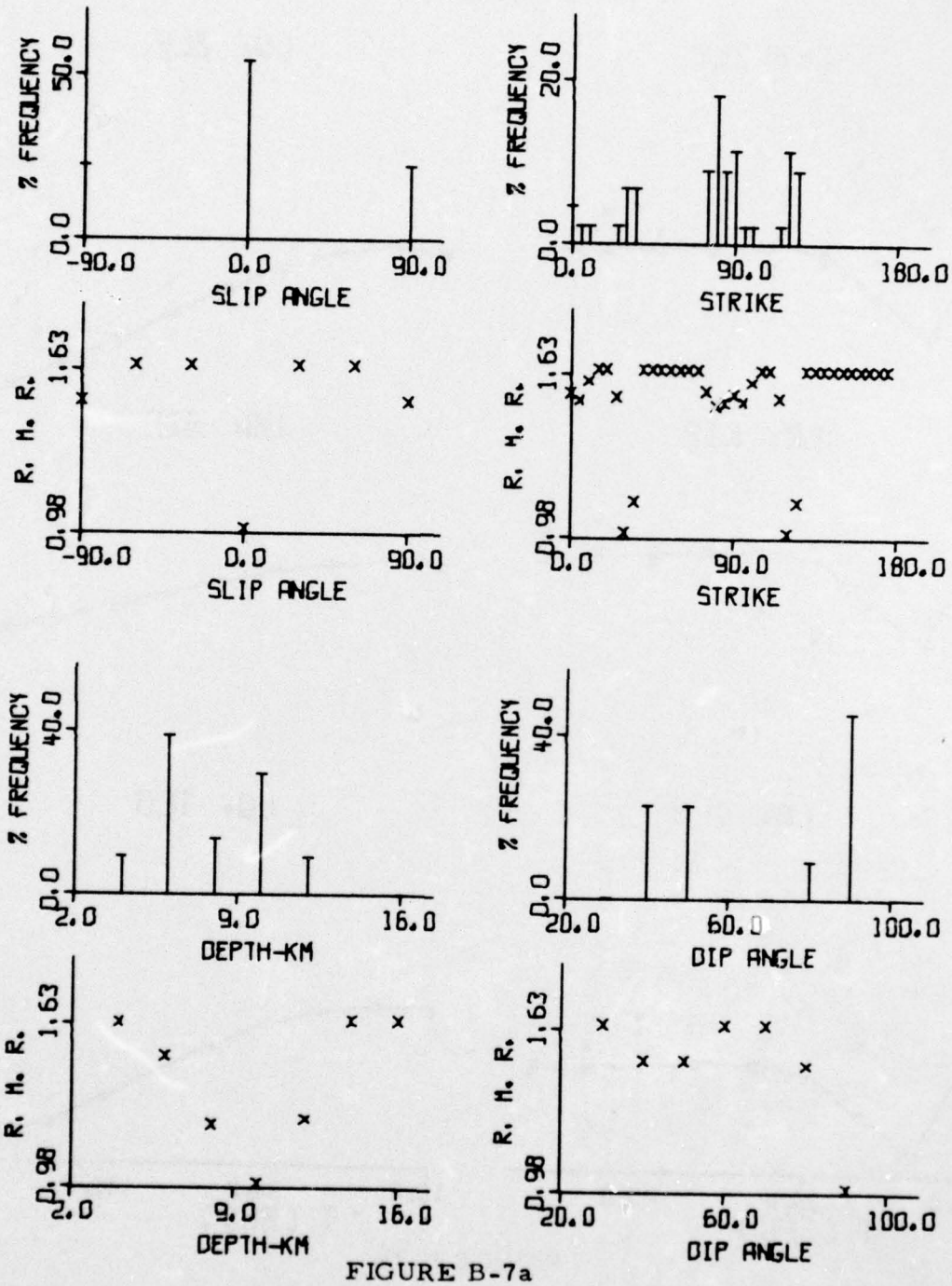

FIGURE B-7a

SOURCE PARAMETER DISTRIBUTIONS: LX+SINK+S017
(PAGE 1 OF 3)

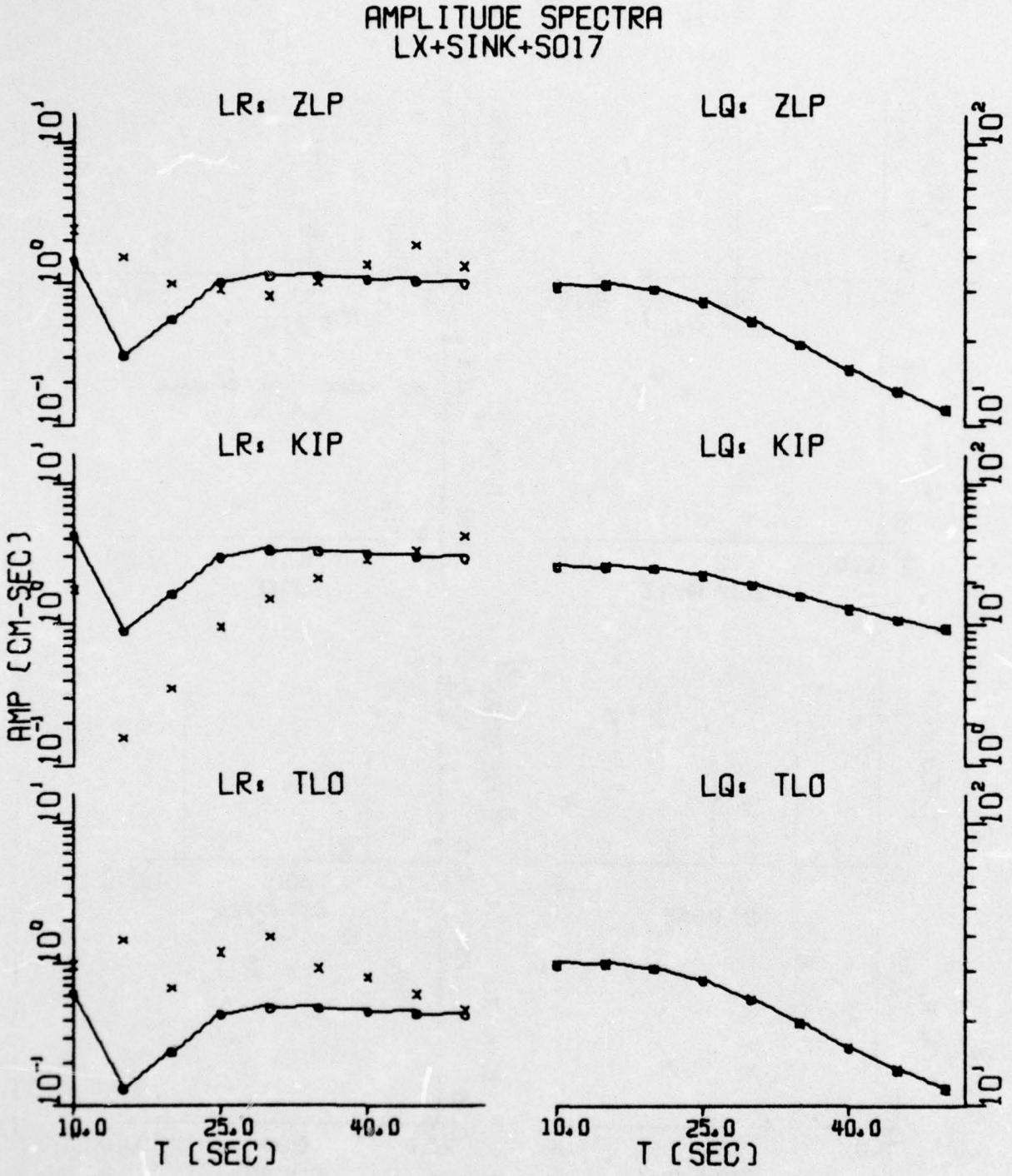

FIGURE B-7b

SPECTRAL FIT: LX+SINK+S017
(PAGE 2 OF 3)

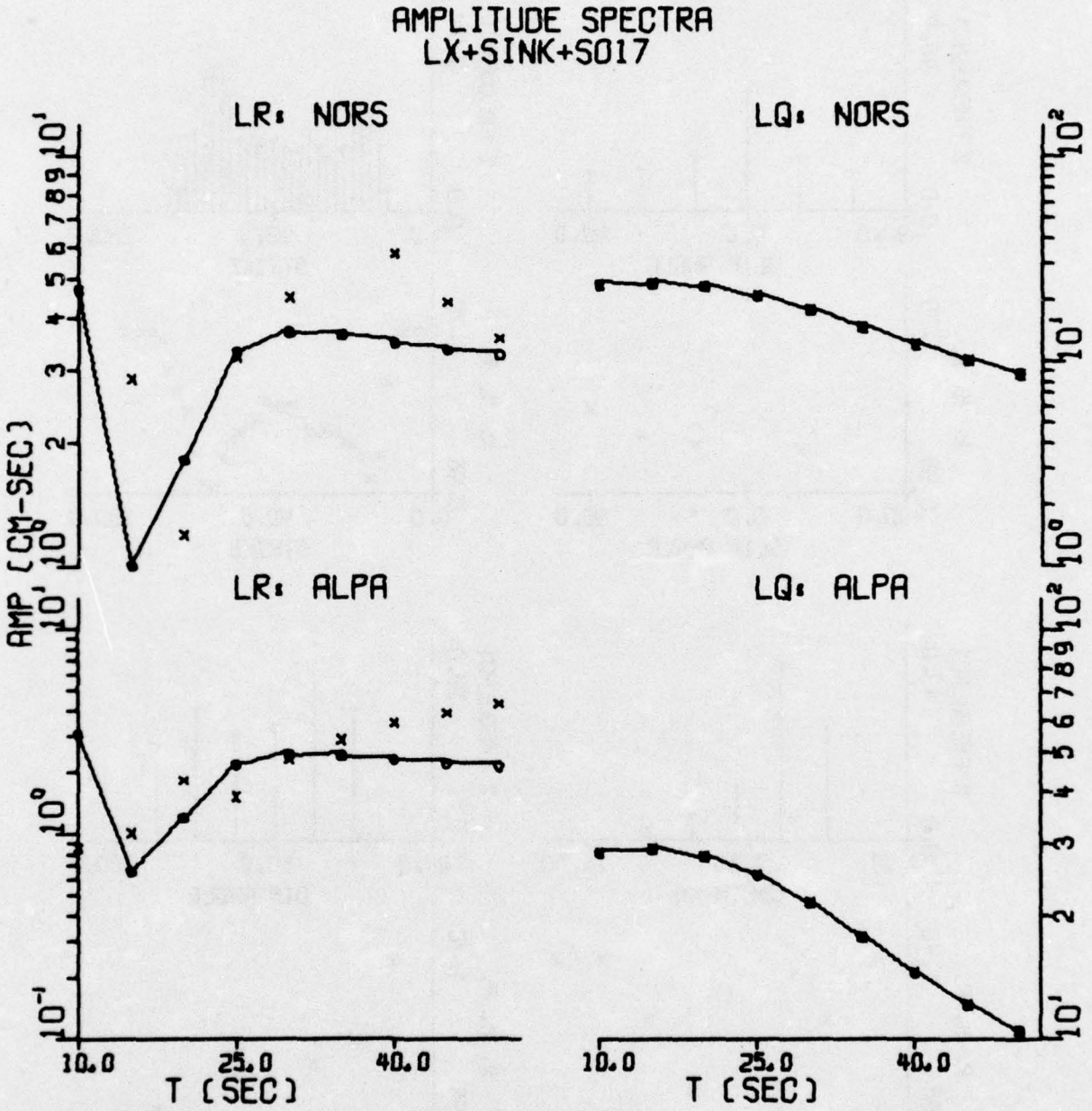

FIGURE B-7b

SPECTRAL FIT: LX+SINK+S017
(PAGE 3 OF 3)

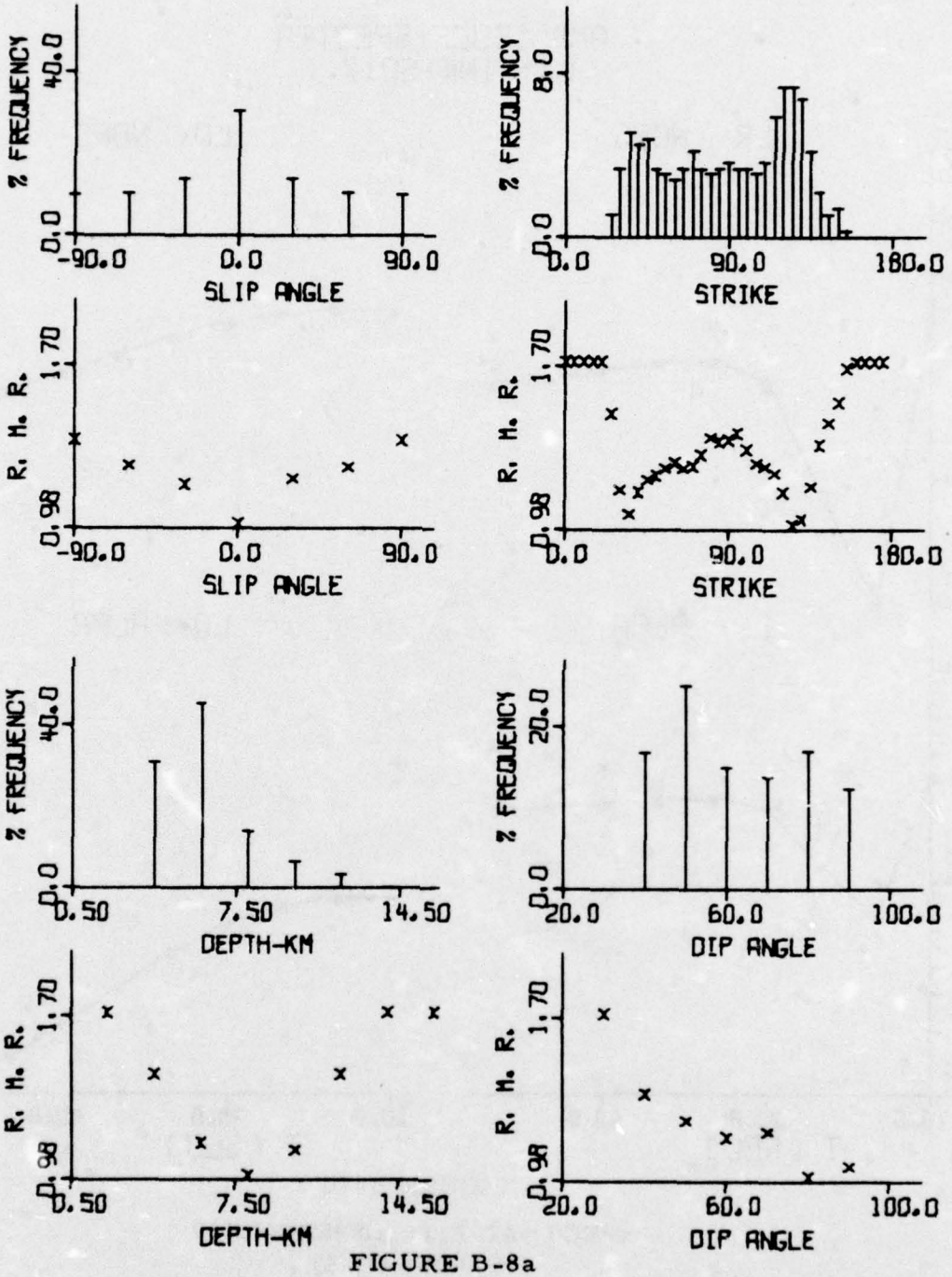

FIGURE B-8a

SOURCE PARAMETER DISTRIBUTIONS: LX+SINK+S023

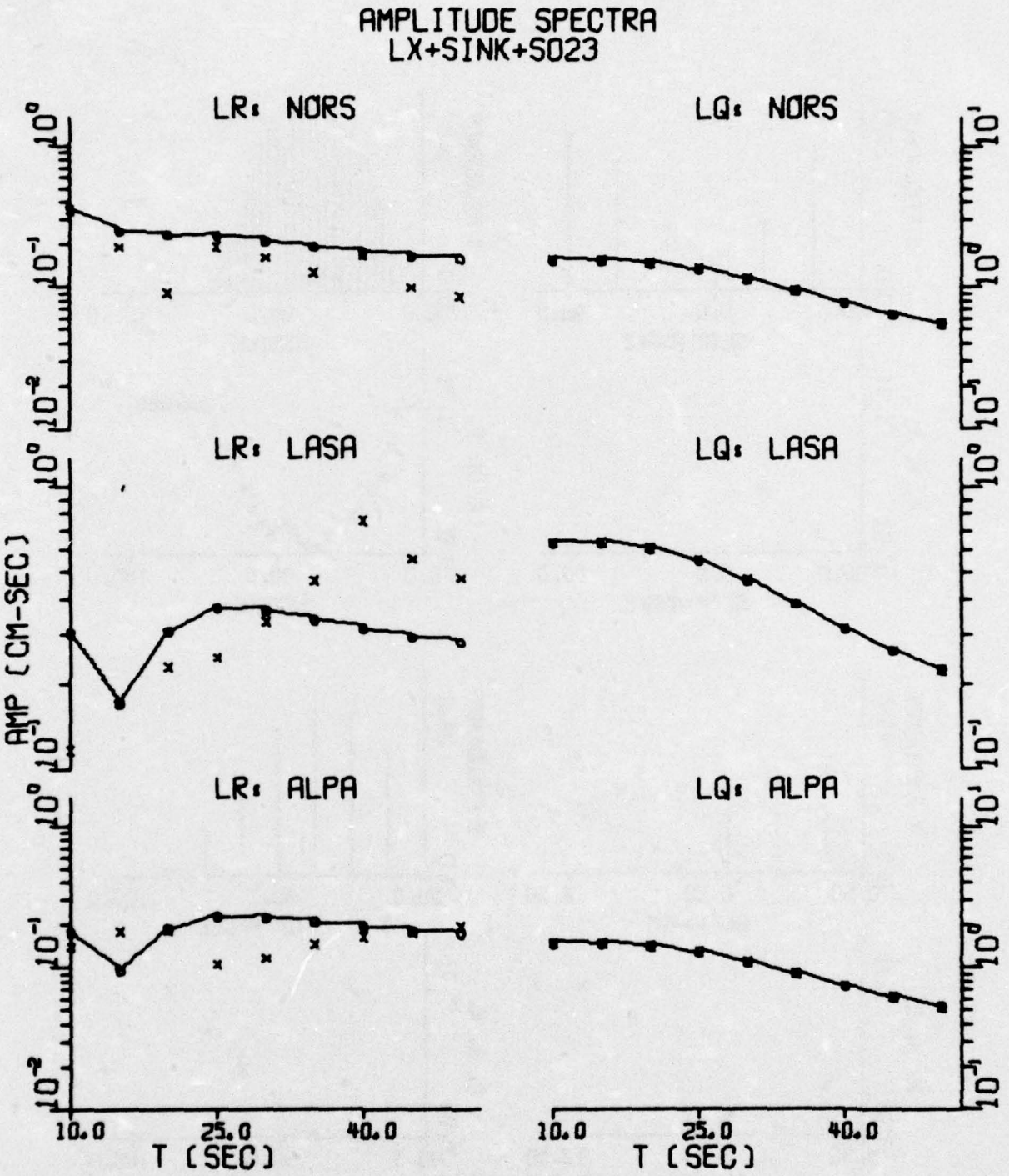

FIGURE B-8b

SPECTRAL FIT: LX+SINK+S023

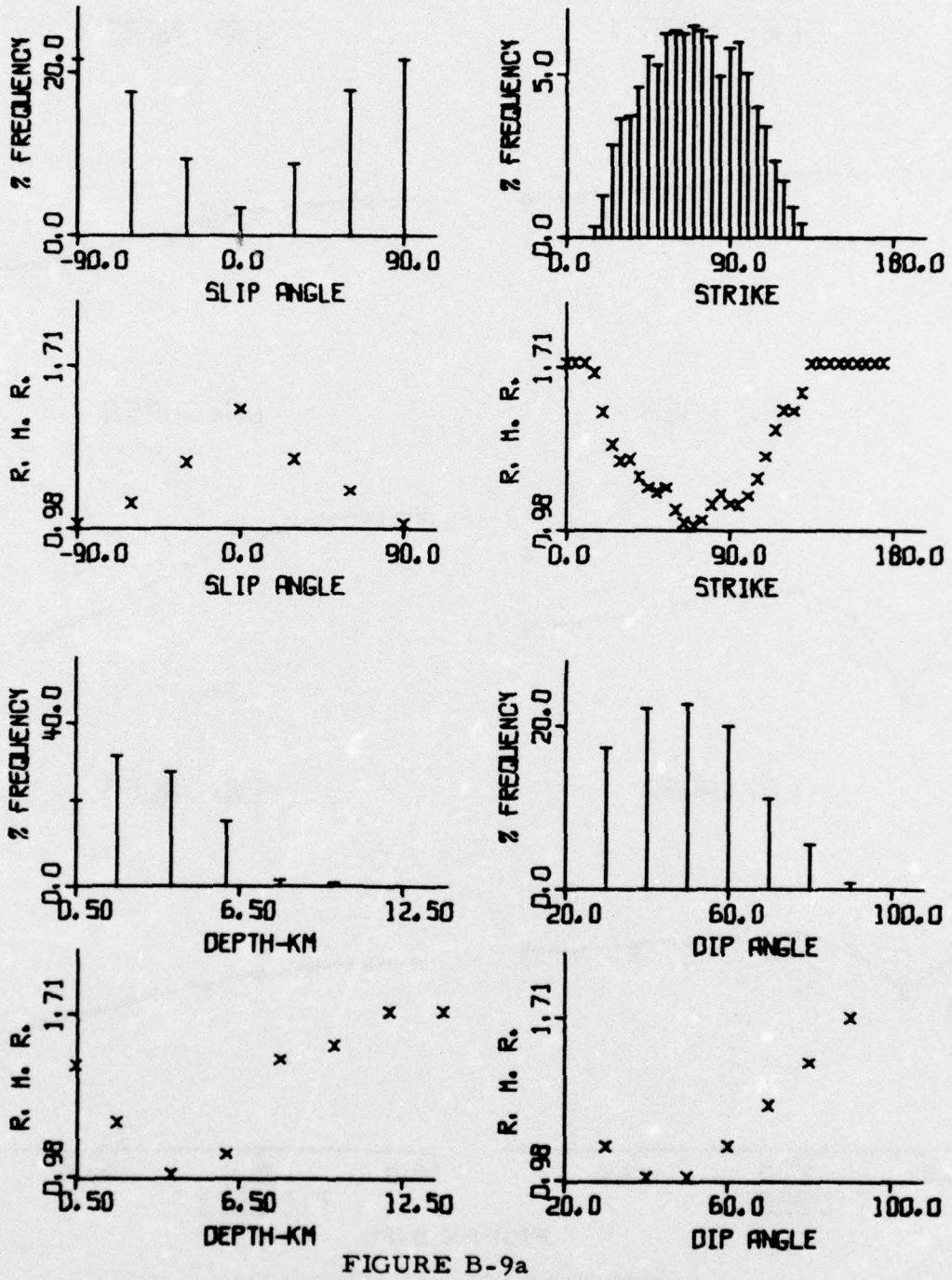

FIGURE B-9a

SOURCE PARAMETER DISTRIBUTIONS: LX+SINK+S025

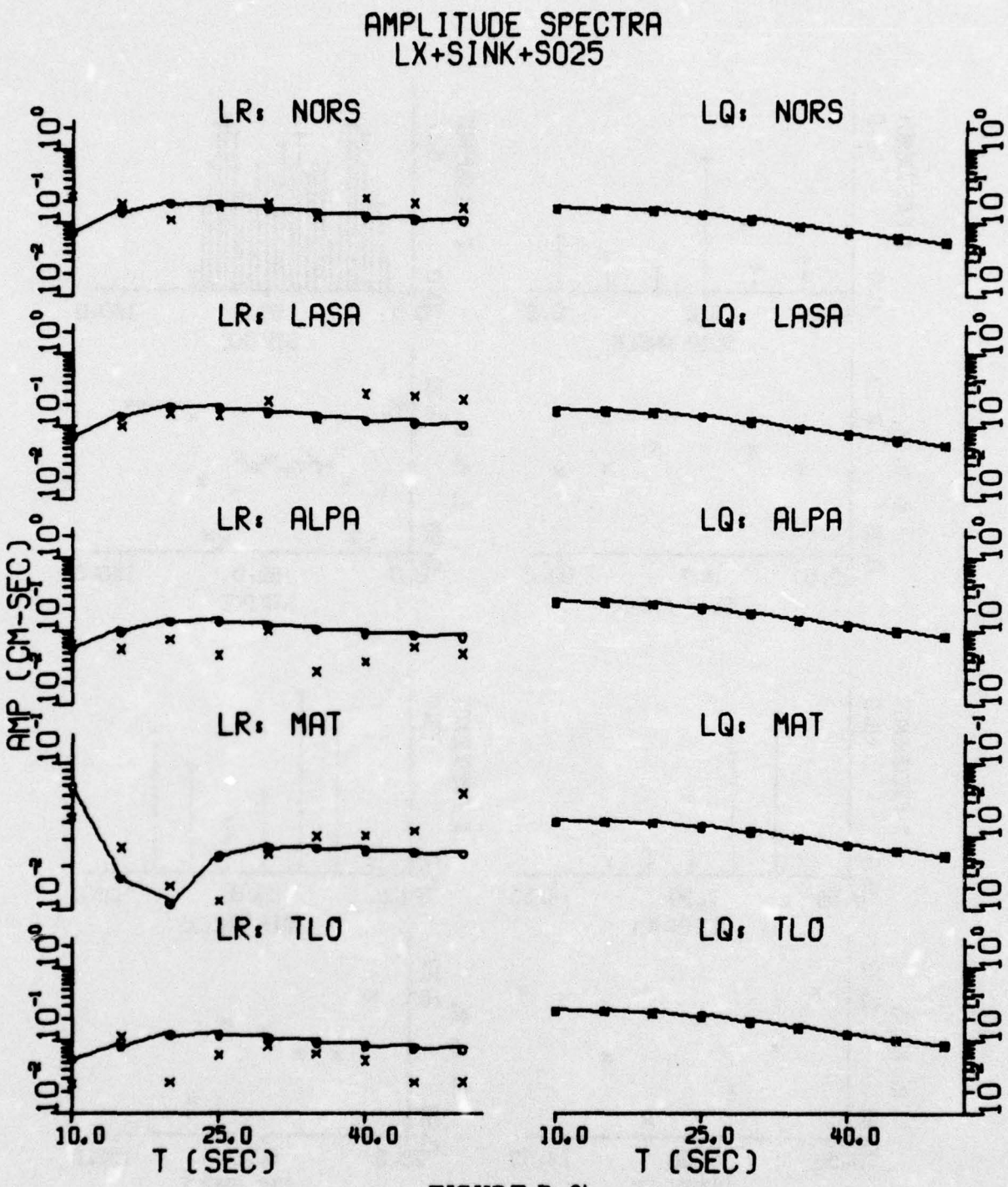

FIGURE B-9b

SPECTRAL FIT: LX+SINK+S025

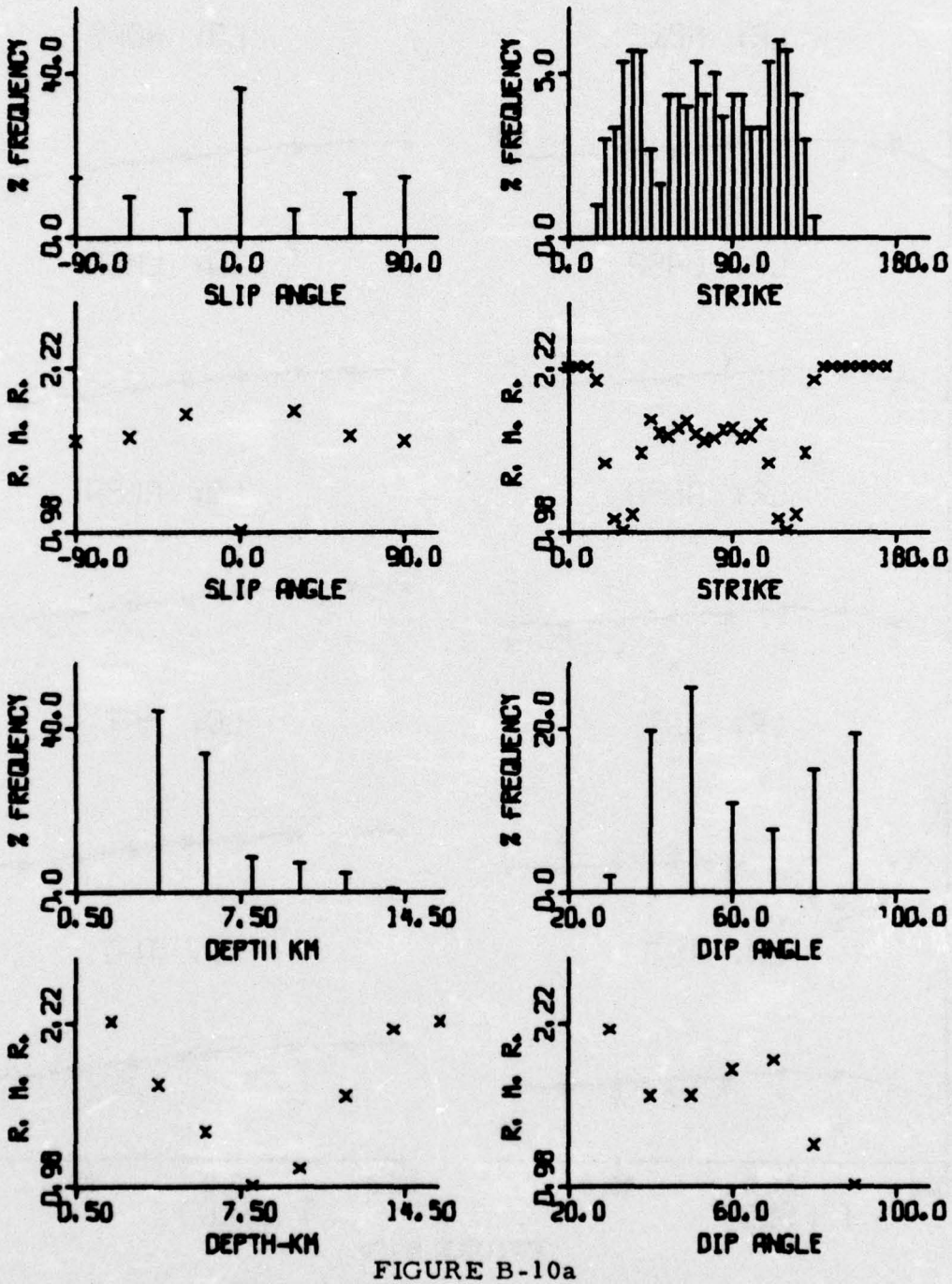

FIGURE B-10a

SOURCE PARAMETER DISTRIBUTIONS: LX+SINK+S031

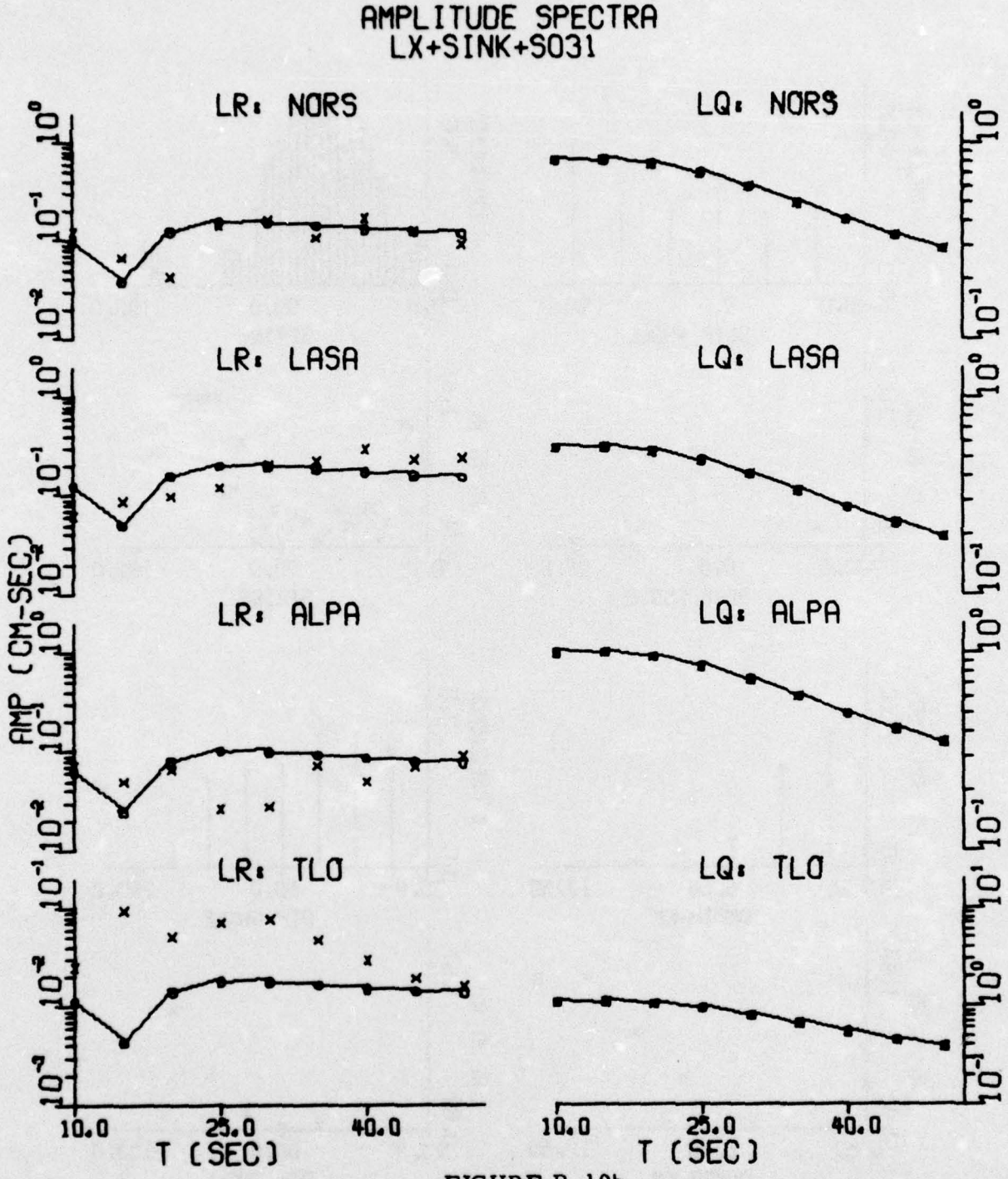

FIGURE B-10b

SPECTRAL FIT: LX+SINK+S031

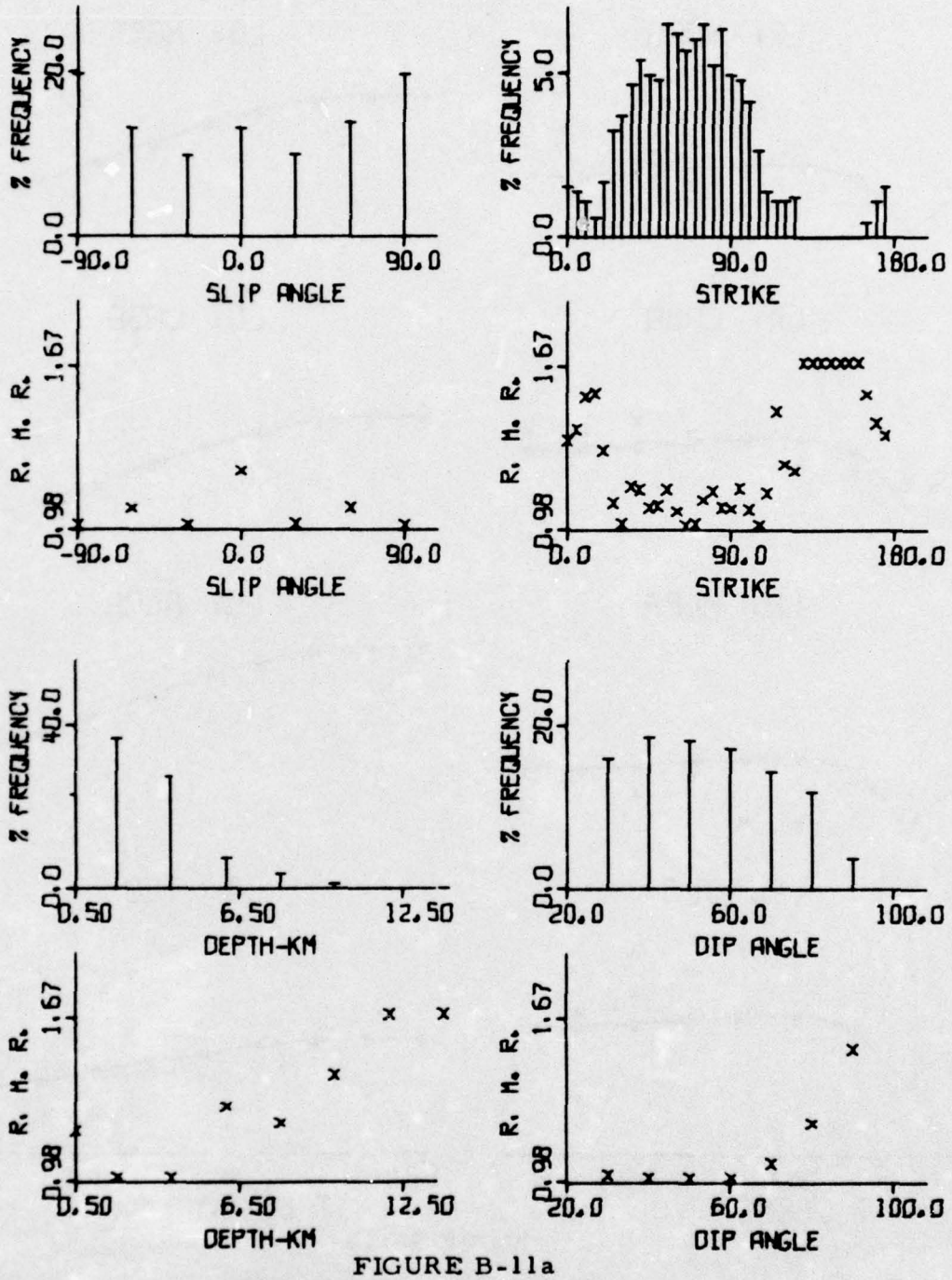

FIGURE B-11a

SOURCE PARAMETER DISTRIBUTIONS: LX+SINK+S036

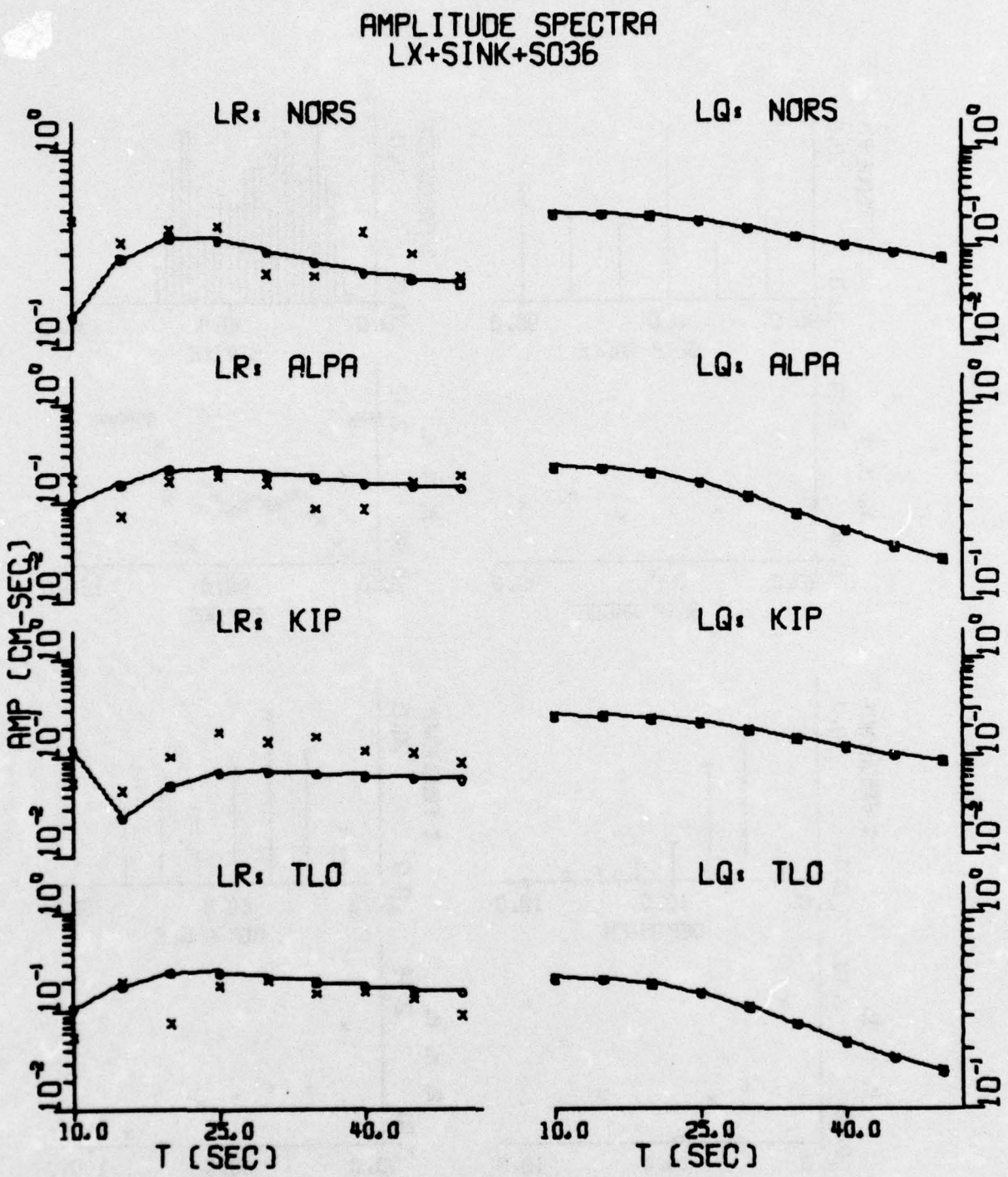

FIGURE B-11b

SPECTRAL FIT: LX+SINK+S036

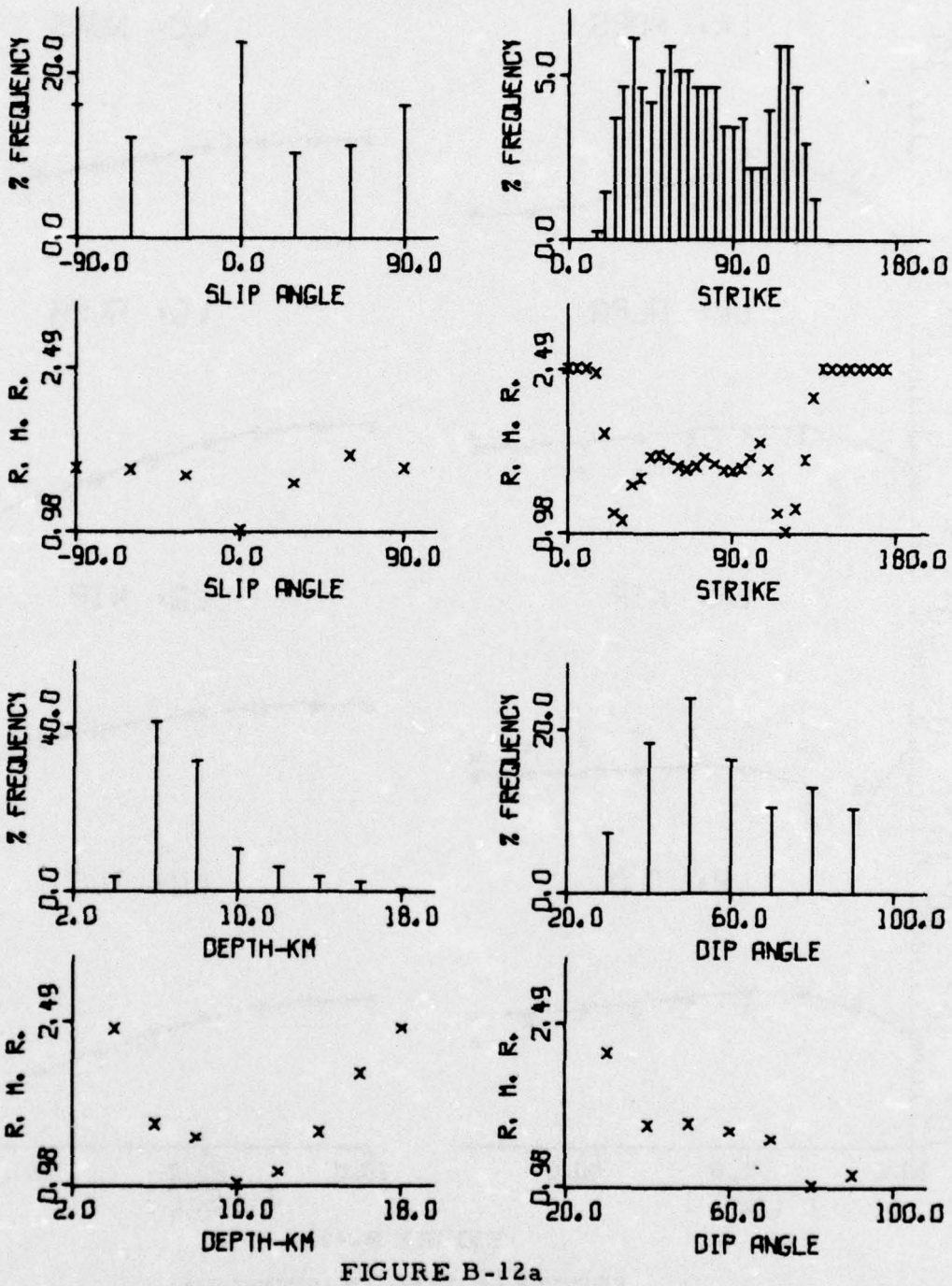

FIGURE B-12a

SOURCE PARAMETER DISTRIBUTIONS: LX+SINK+S043

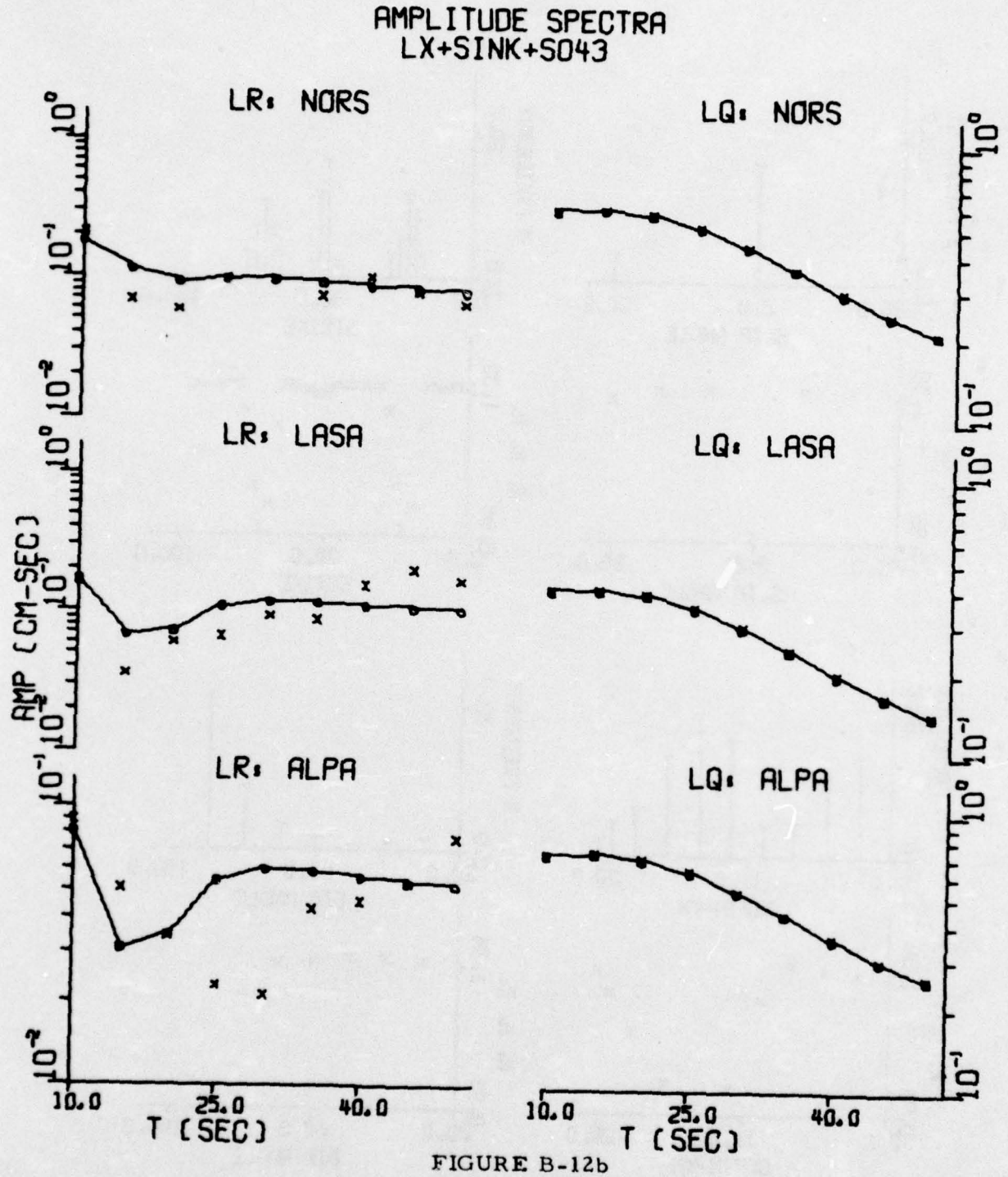

FIGURE B-12b

SPECTRAL FIT: LX+SINK+S043

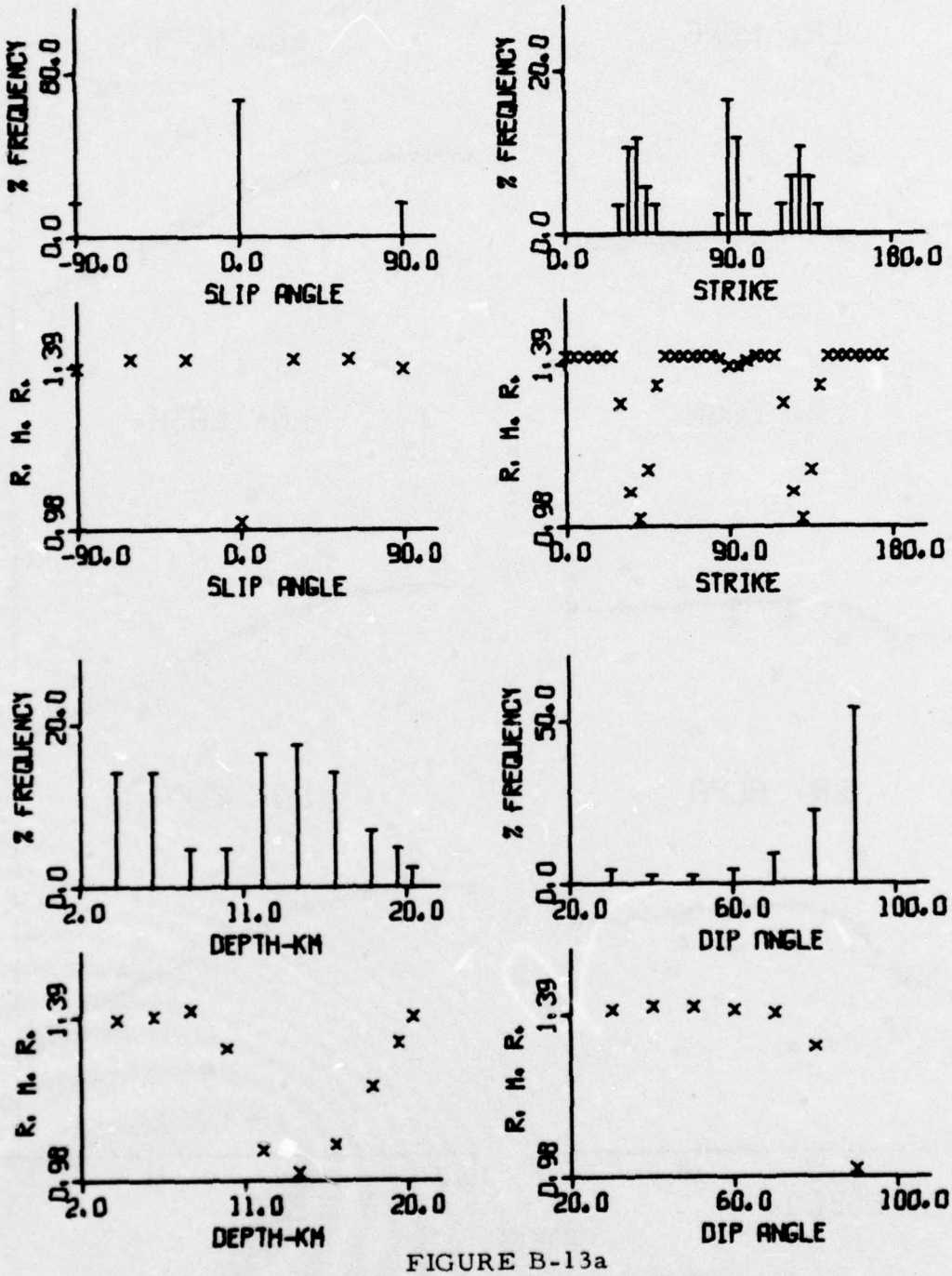

FIGURE B-13a

SOURCE PARAMETER DISTRIBUTIONS: I.X+SINK+S056

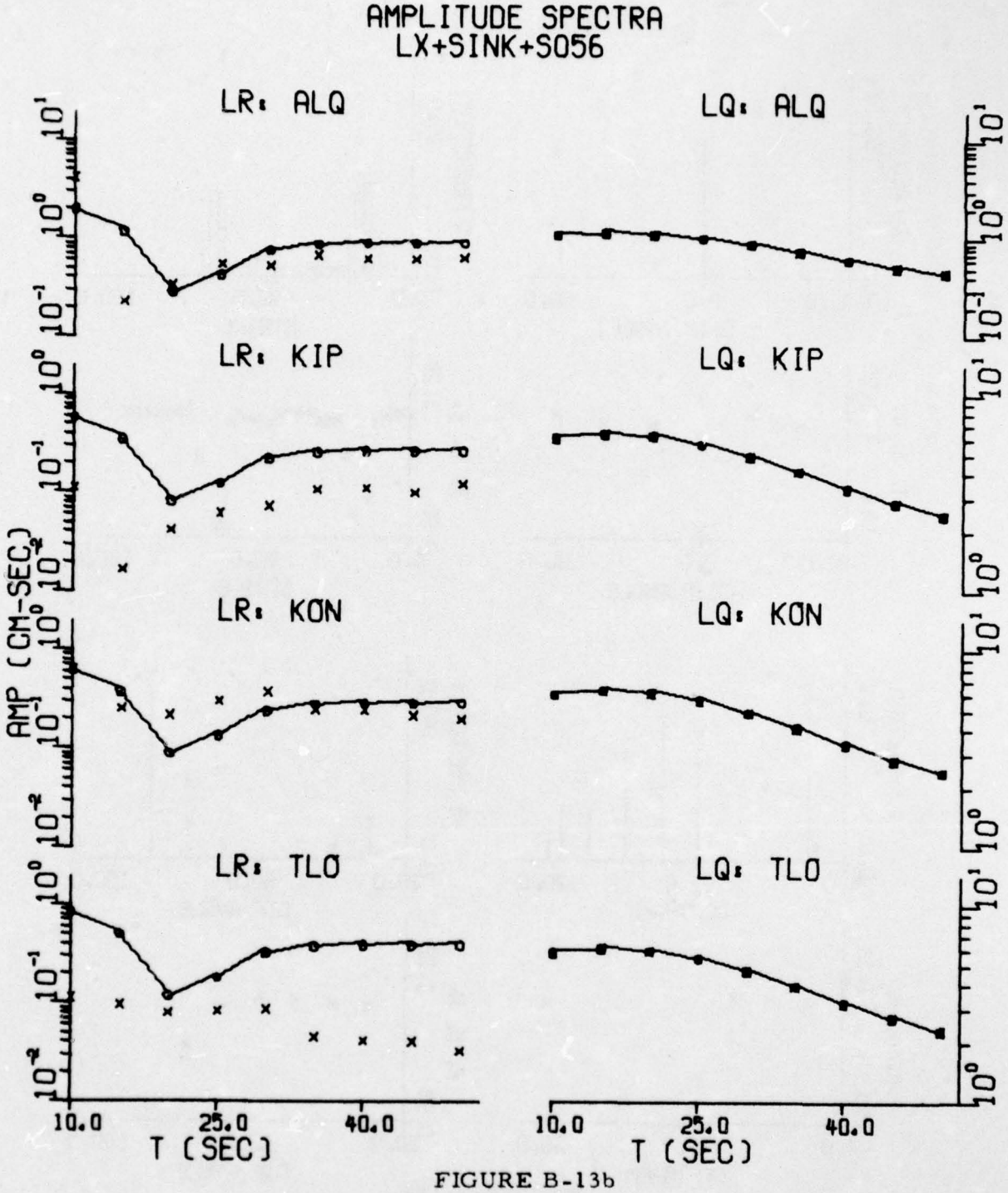

FIGURE B-13b

SPECTRAL FIT: LX+SINK+S056

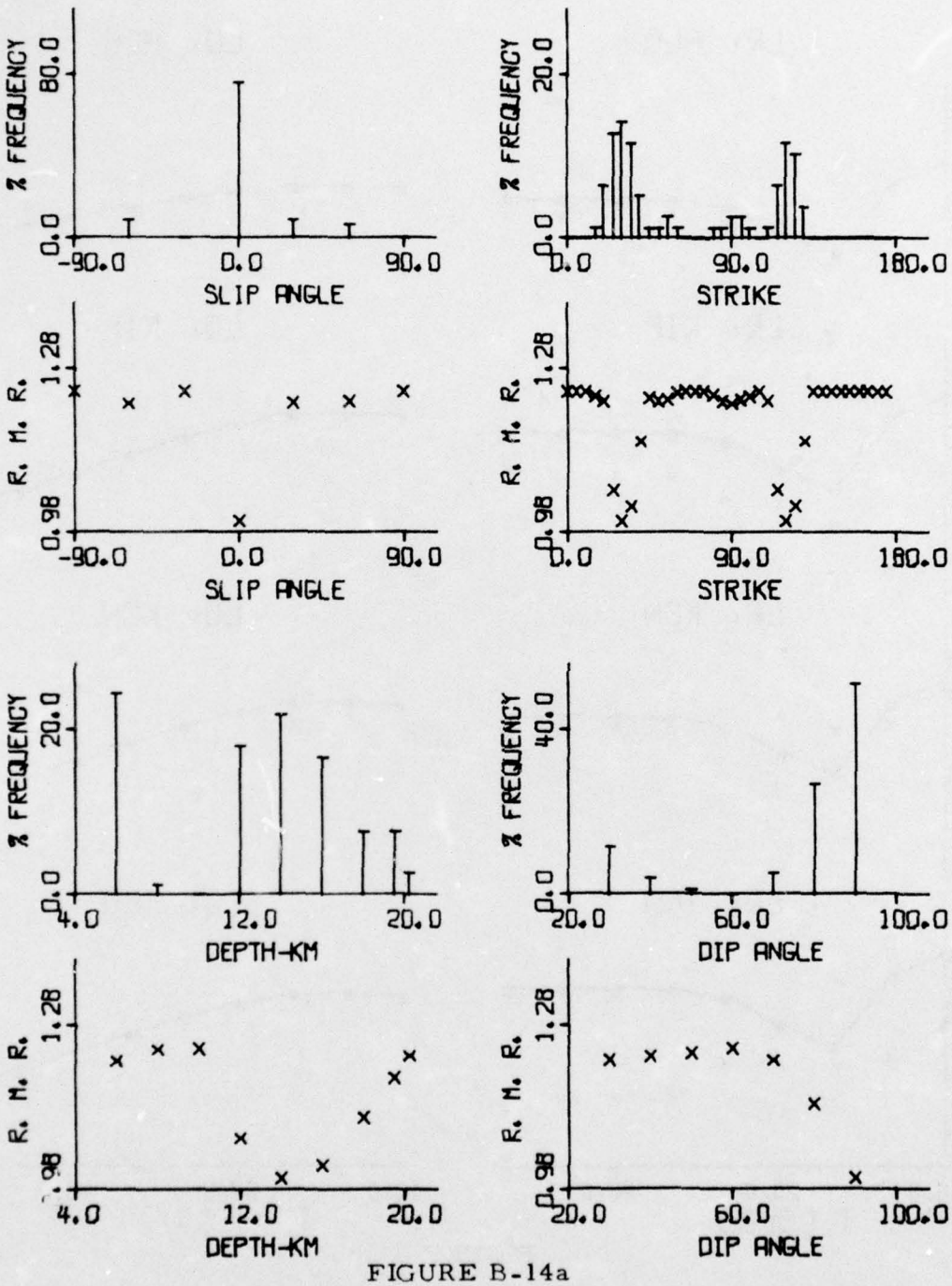

FIGURE B-14a

SOURCE PARAMETER DISTRIBUTIONS: LX+SINK+S059

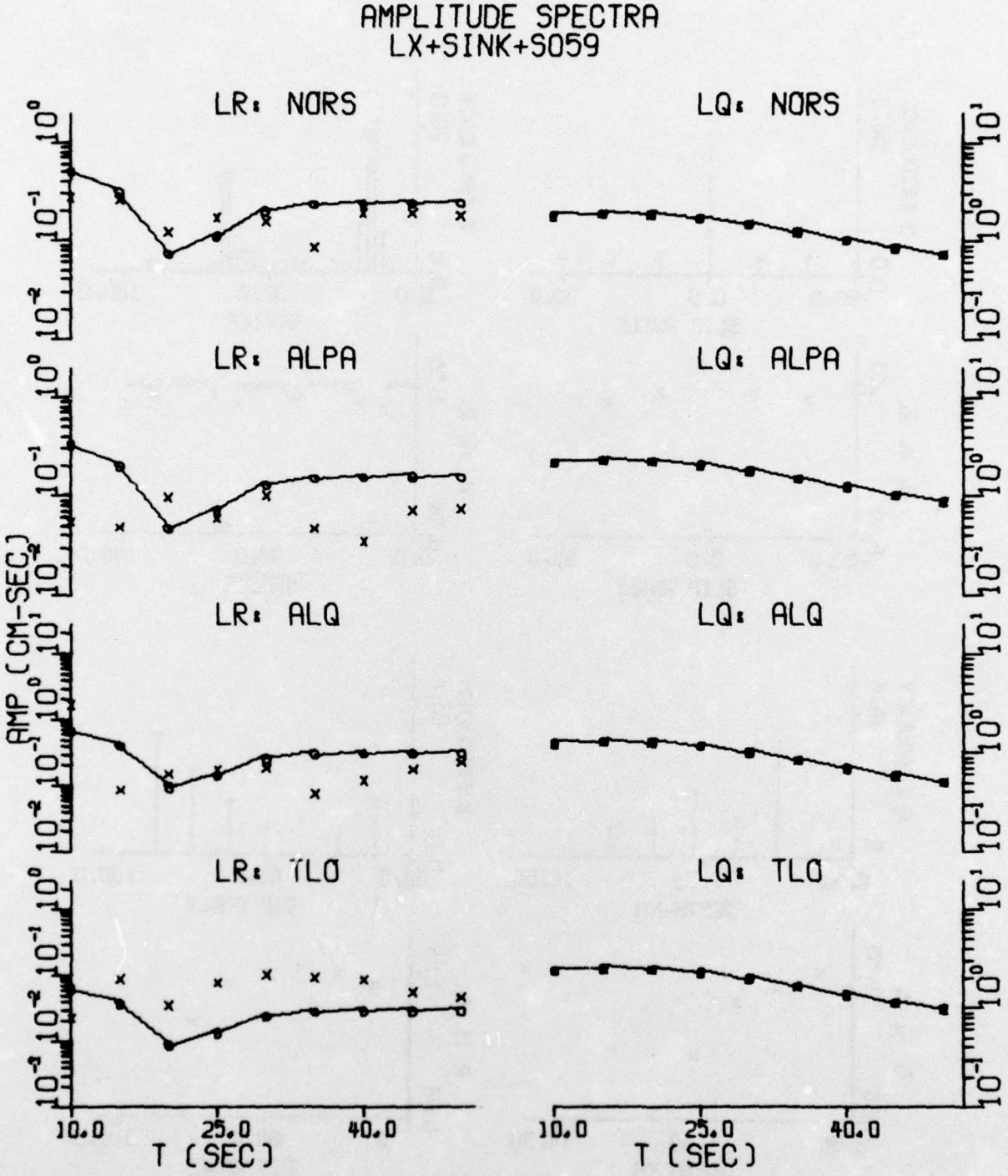

FIGURE B-14b

SPECTRAL FIT: LX+SINK+S059

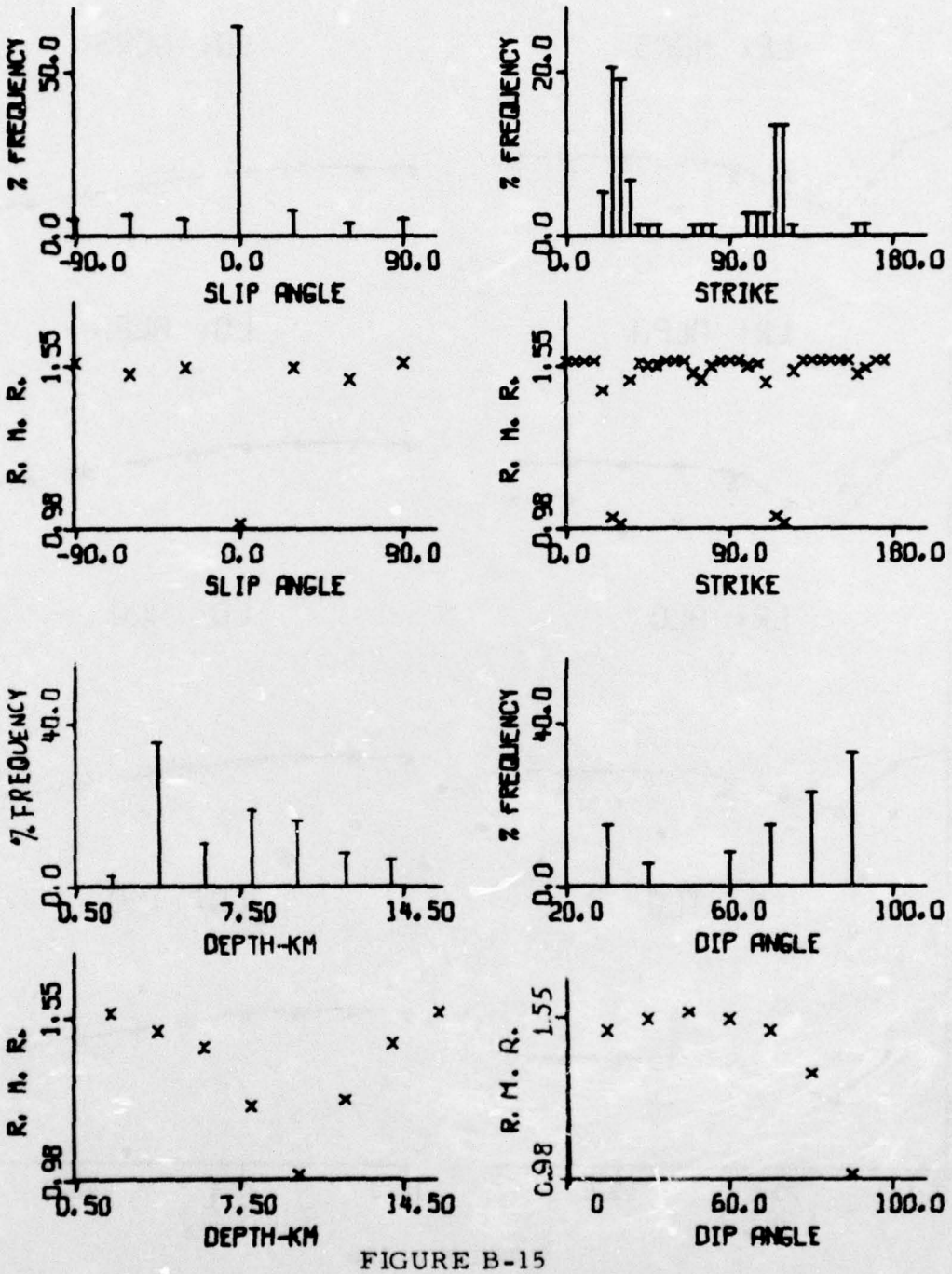

FIGURE B-15

SOURCE PARAMETER DISTRIBUTION BY RATIO-OF-EVENTS:
LX+SINK+S004

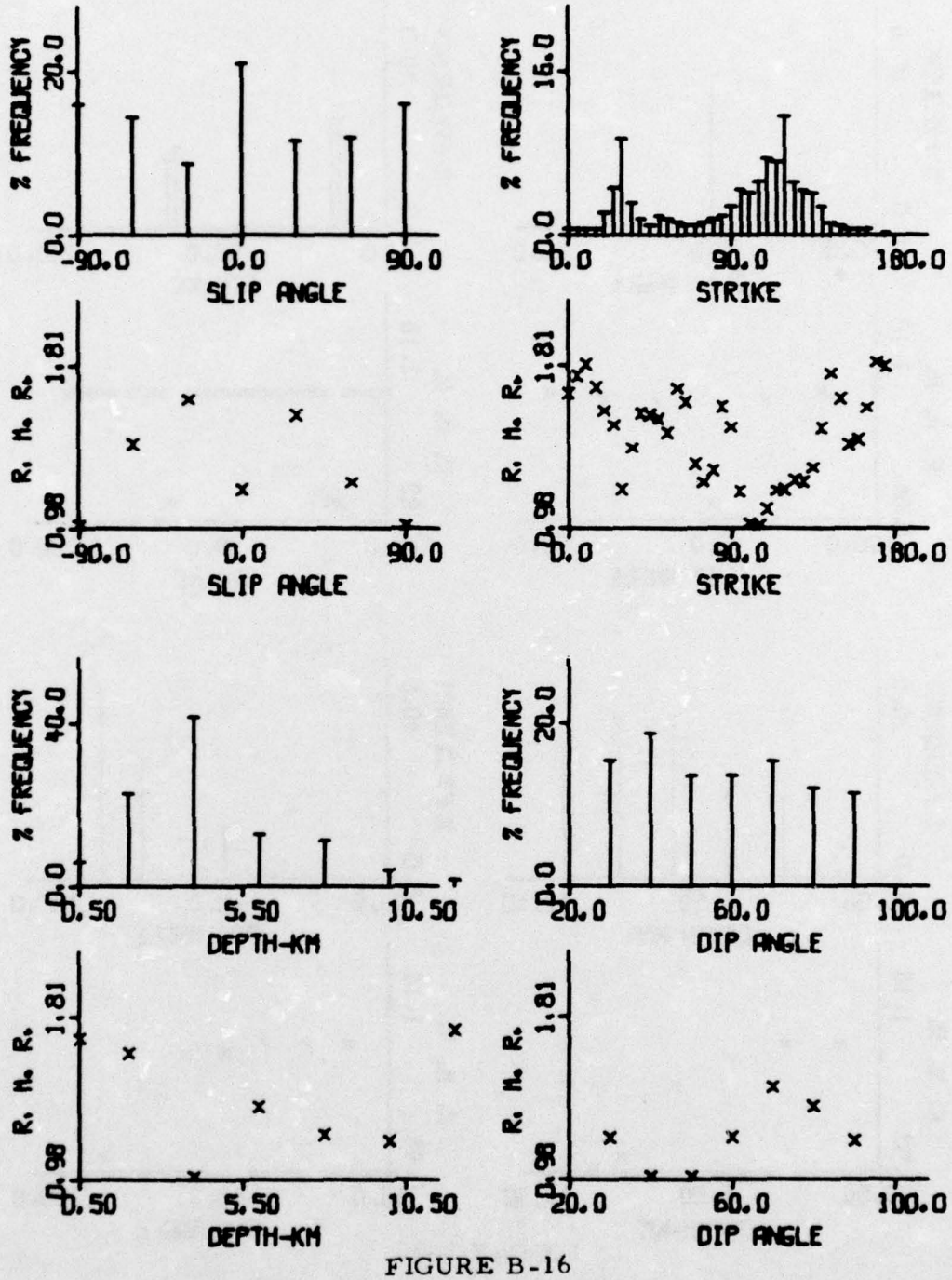

FIGURE B-16

SOURCE PARAMETER DISTRIBUTION BY RATIO-OF-EVENTS:
LX+SINK+S005

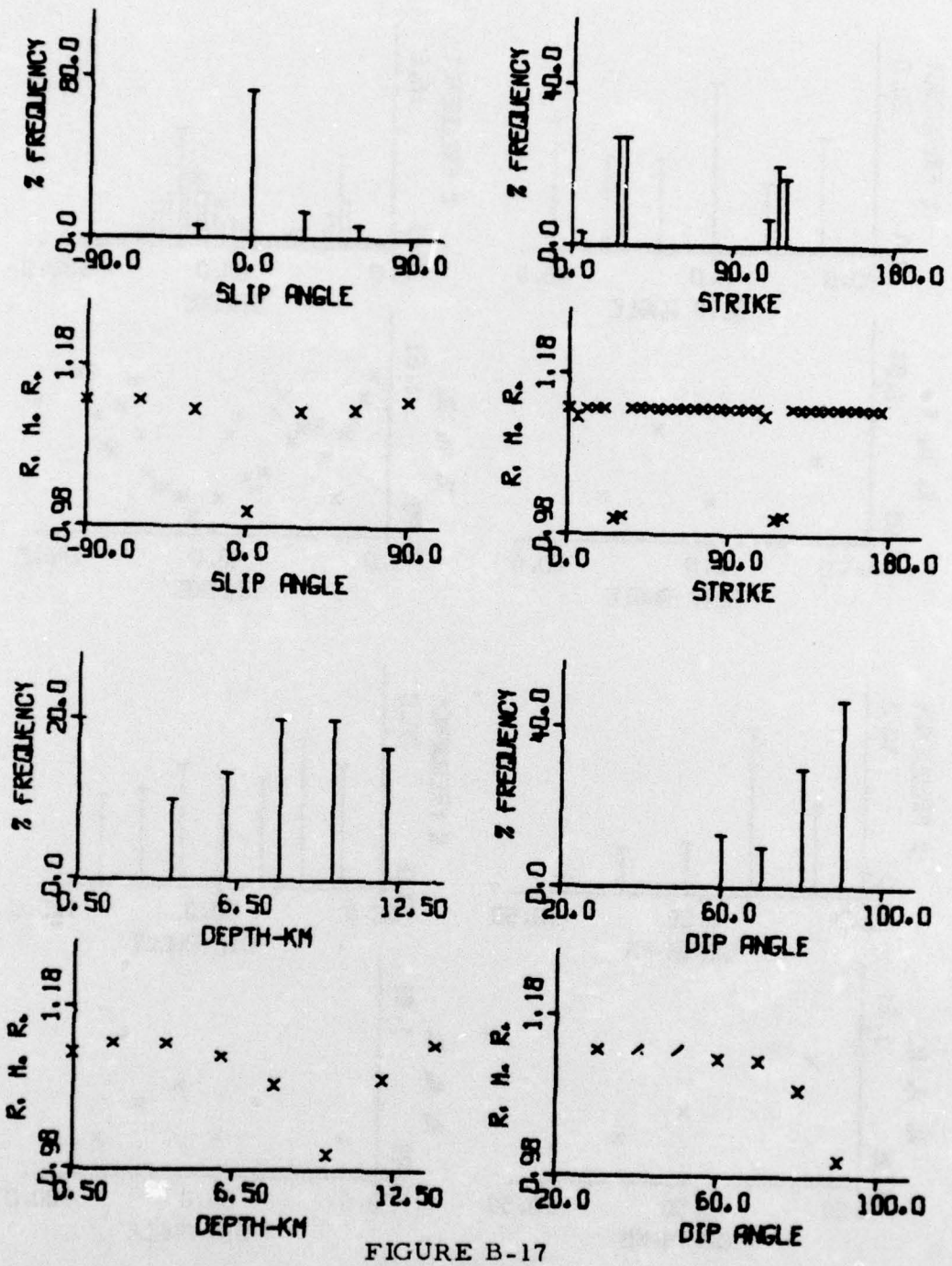

FIGURE B-17

SOURCE PARAMETER DISTRIBUTION BY RATIO-OF-EVENTS:
LX+SINK+S006

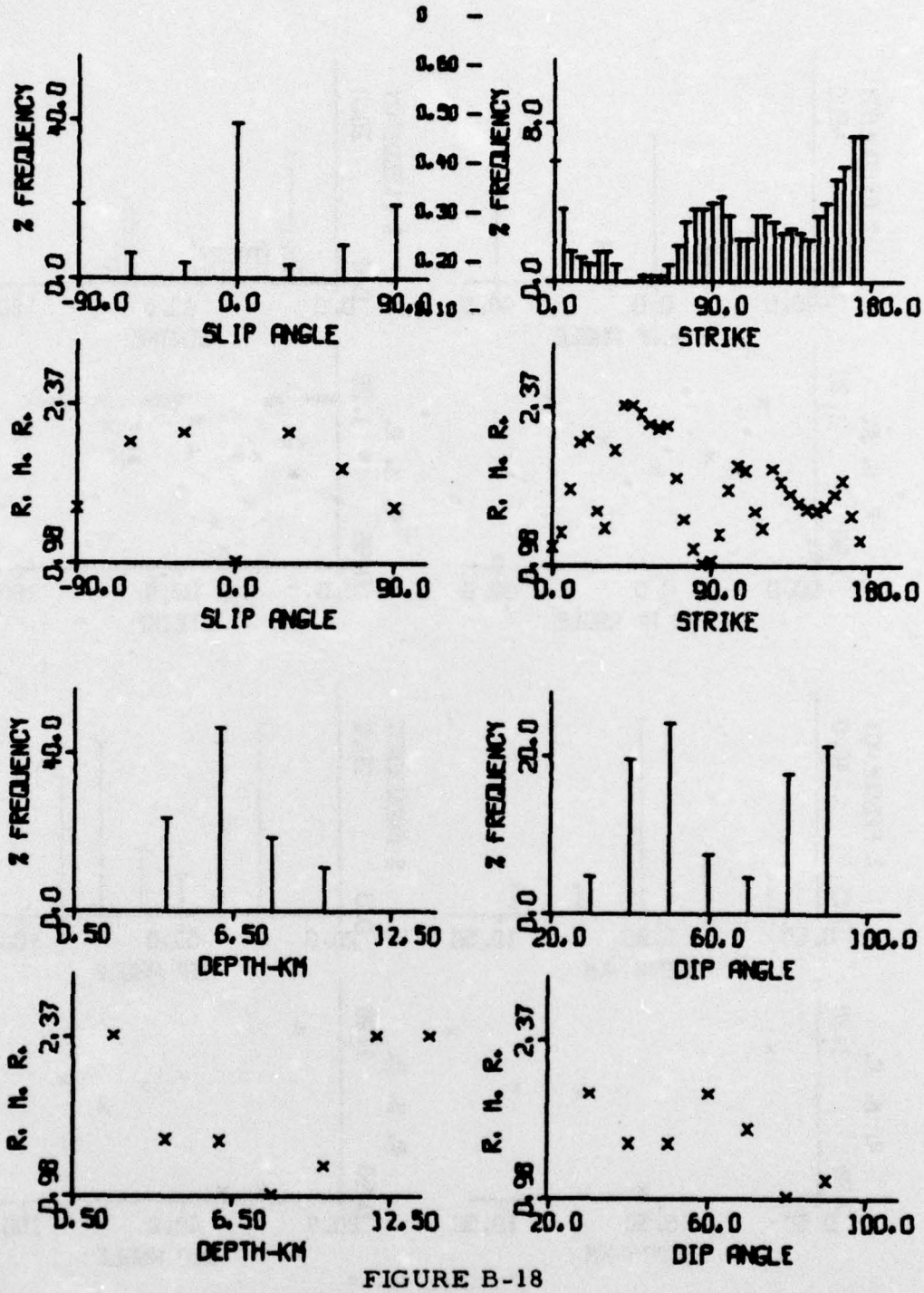

FIGURE B-18

SOURCE PARAMETER DISTRIBUTION BY RATIO-OF-EVENTS:
LX+SINK+S008

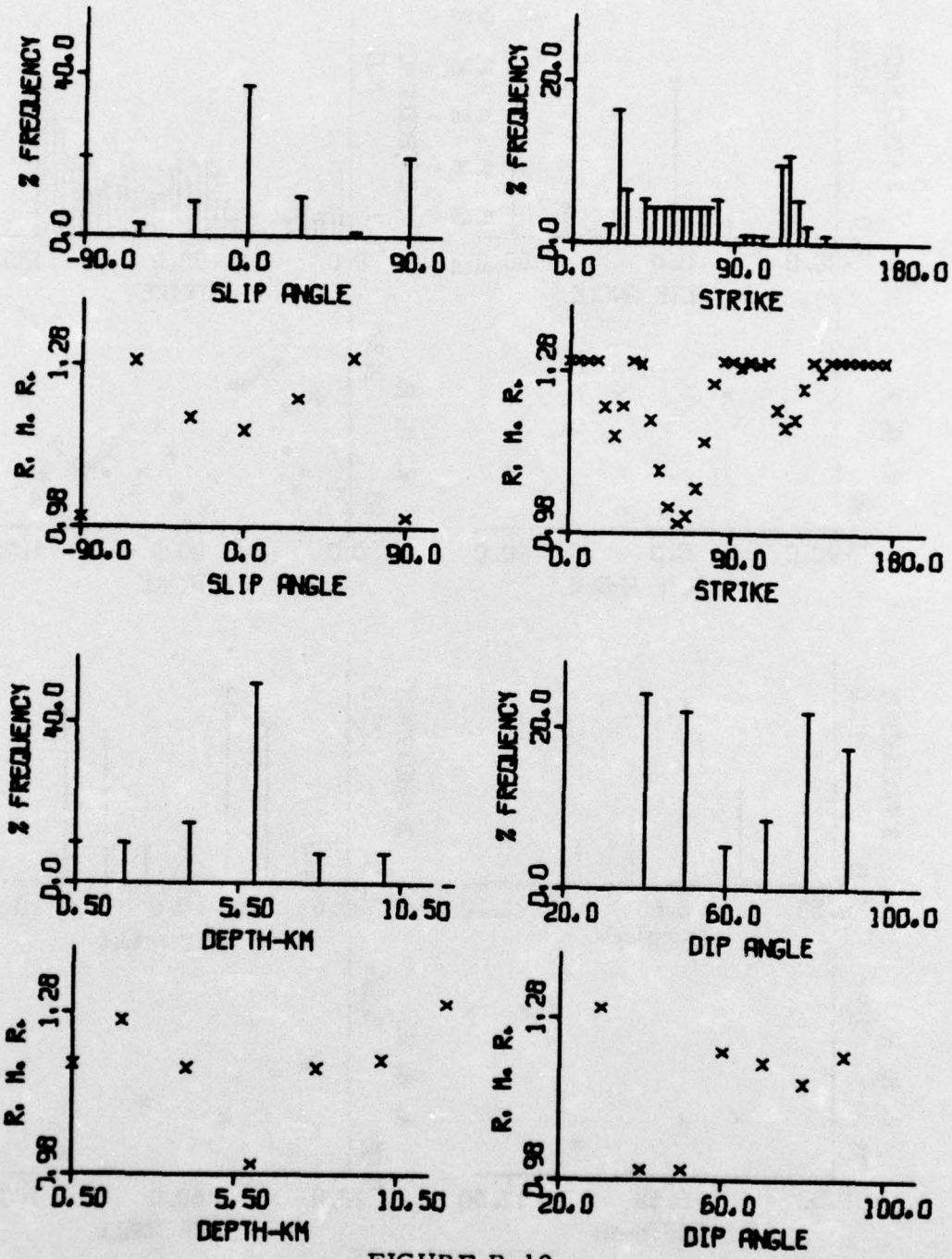

FIGURE B-19

SOURCE PARAMETER DISTRIBUTION BY RATIO-OF-EVENTS:
LX+SINK+S011

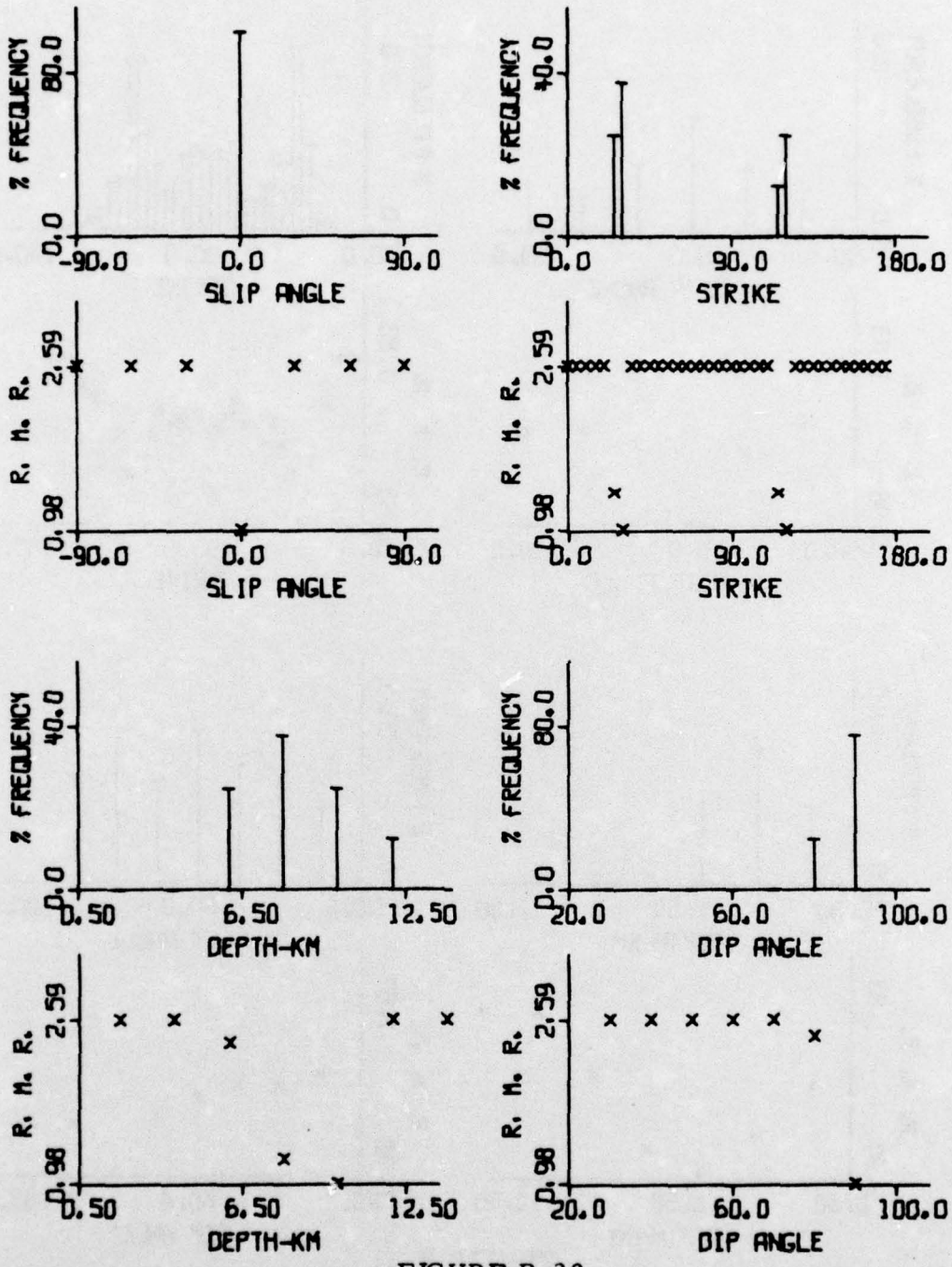

FIGURE B-20

SOURCE PARAMETER DISTRIBUTION BY RATIO-OF-EVENTS:
LX+SINK+S017

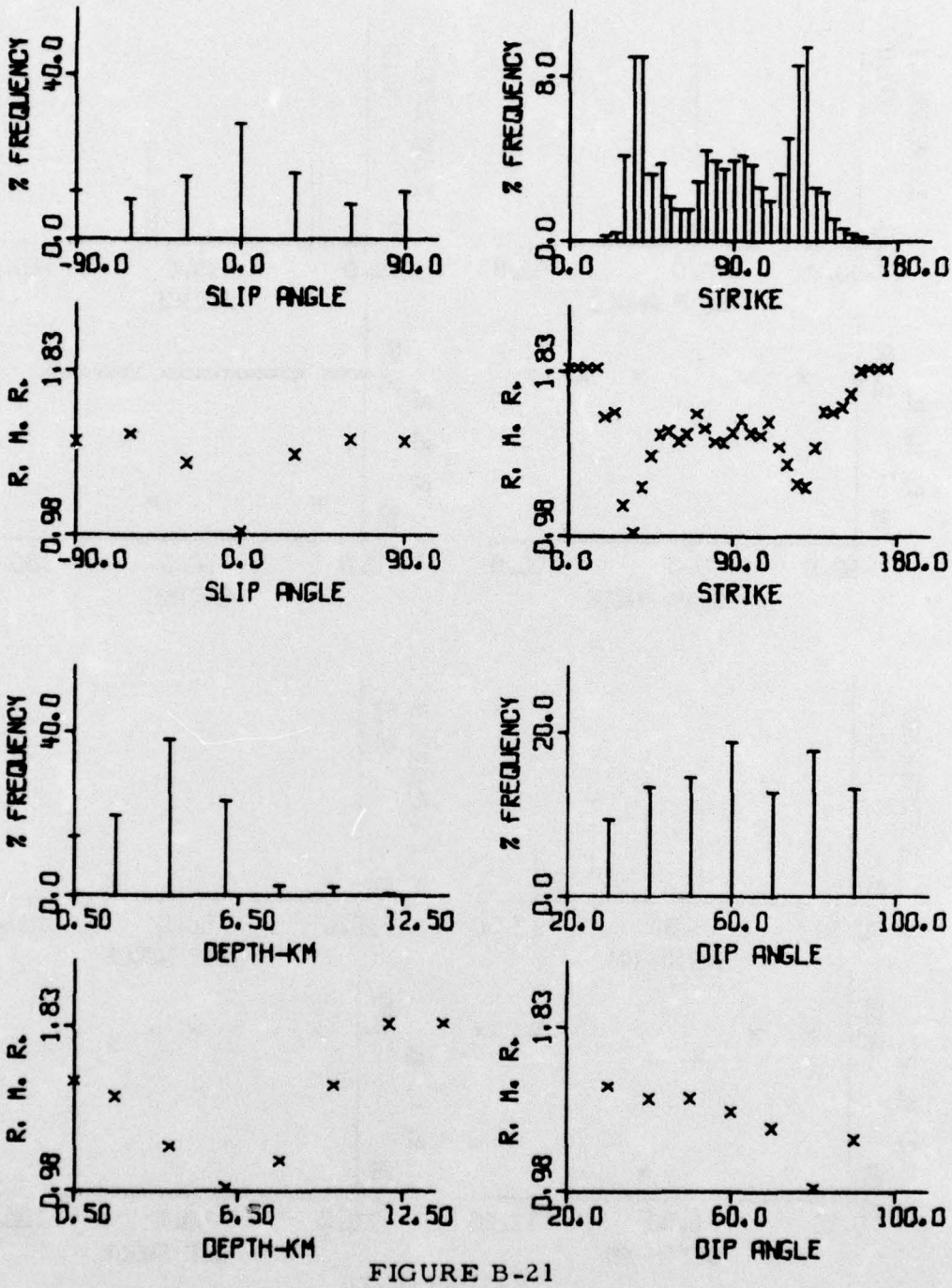

FIGURE B-21

SOURCE PARAMETER DISTRIBUTION BY RATIO-OF-EVENTS:
LX+SINK+S023

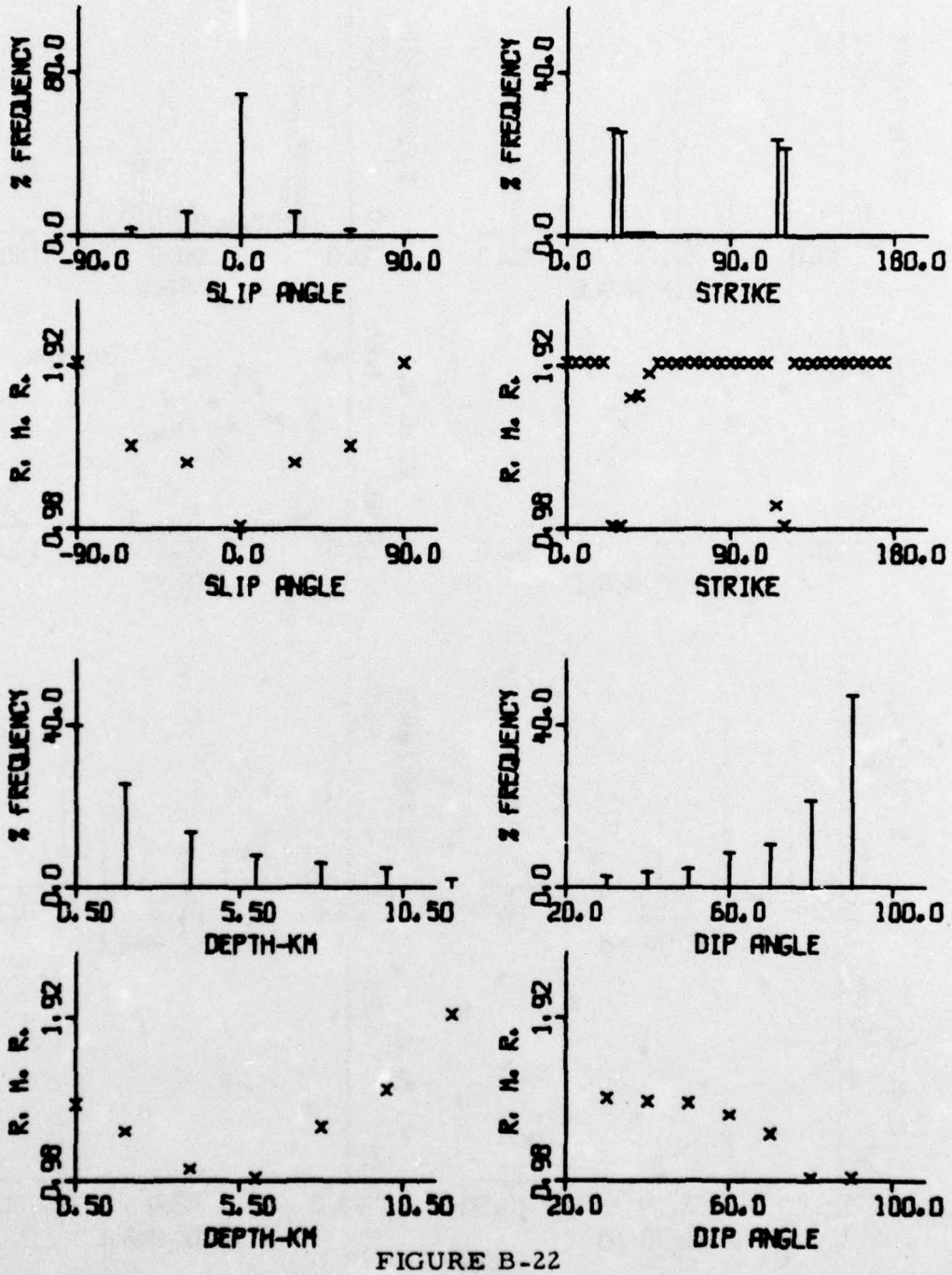

FIGURE B-22

SOURCE PARAMETER DISTRIBUTION BY RATIO-OF-EVENTS:
LX+SINK+S025

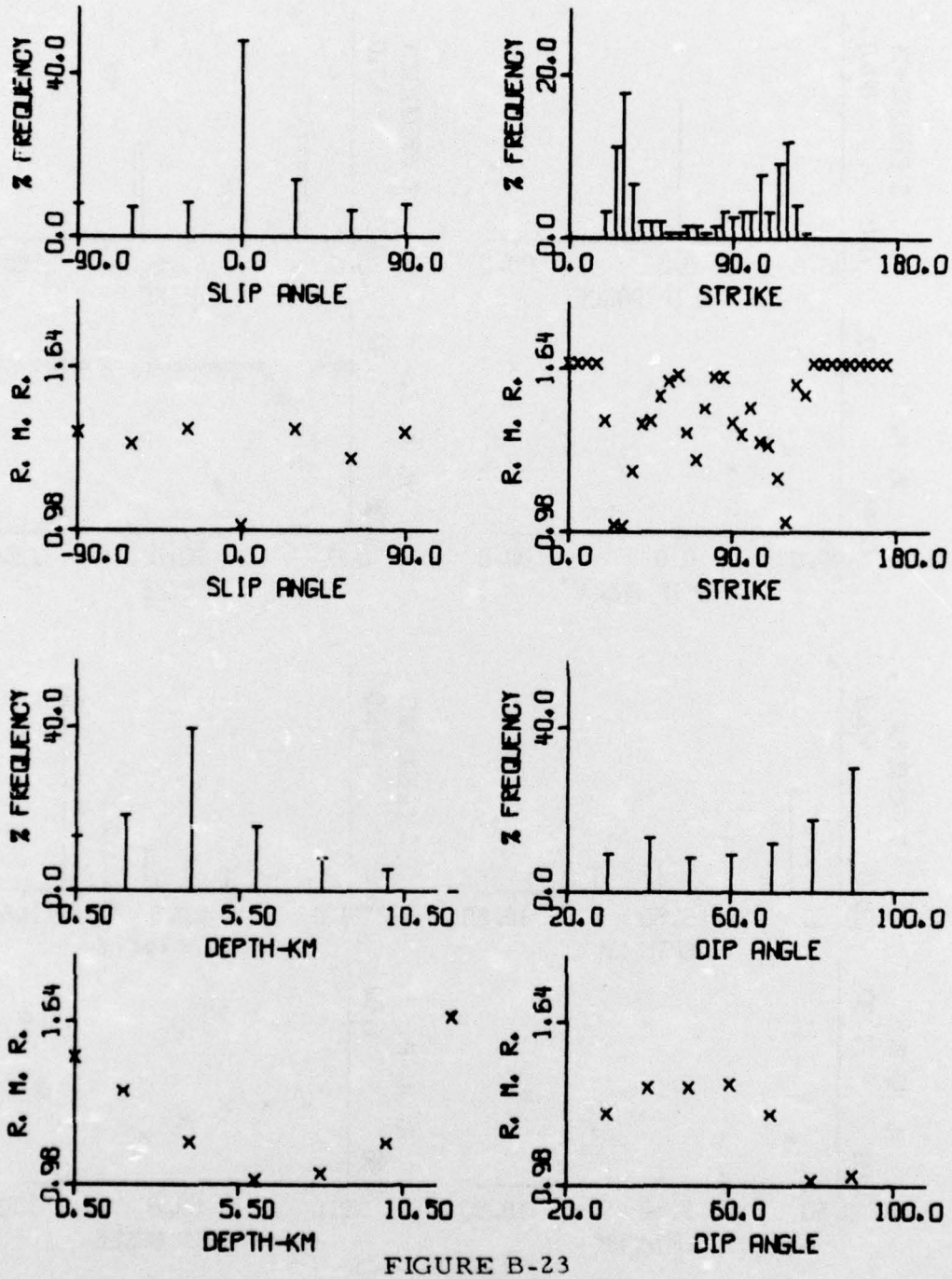

FIGURE B-23

SOURCE PARAMETER DISTRIBUTION BY RATIO-OF-EVENTS:
LX+SINK+S031

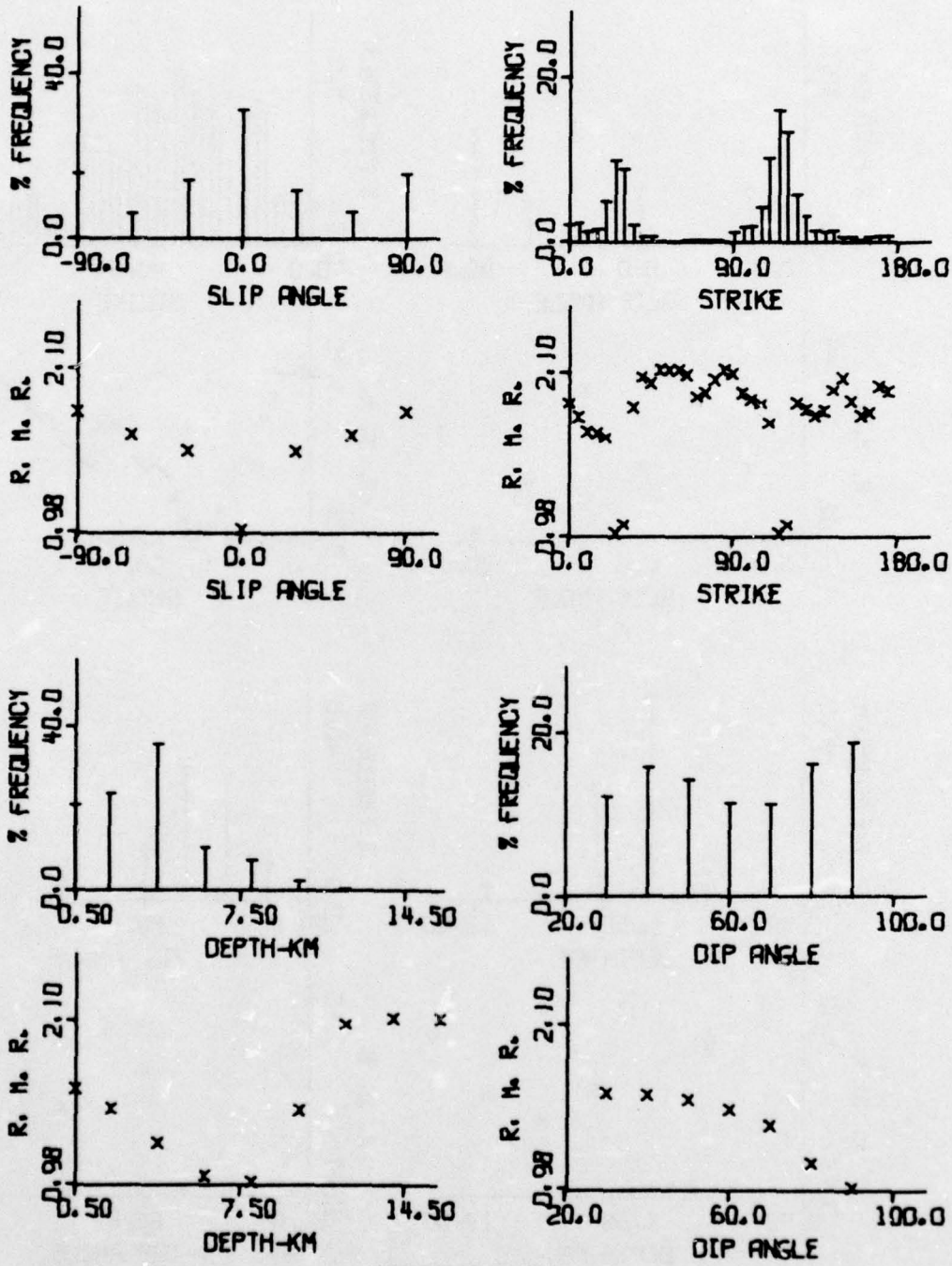

FIGURE B-24

SOURCE PARAMETER DISTRIBUTION BY RATIO-OF-EVENTS:
LX+SINK+S036

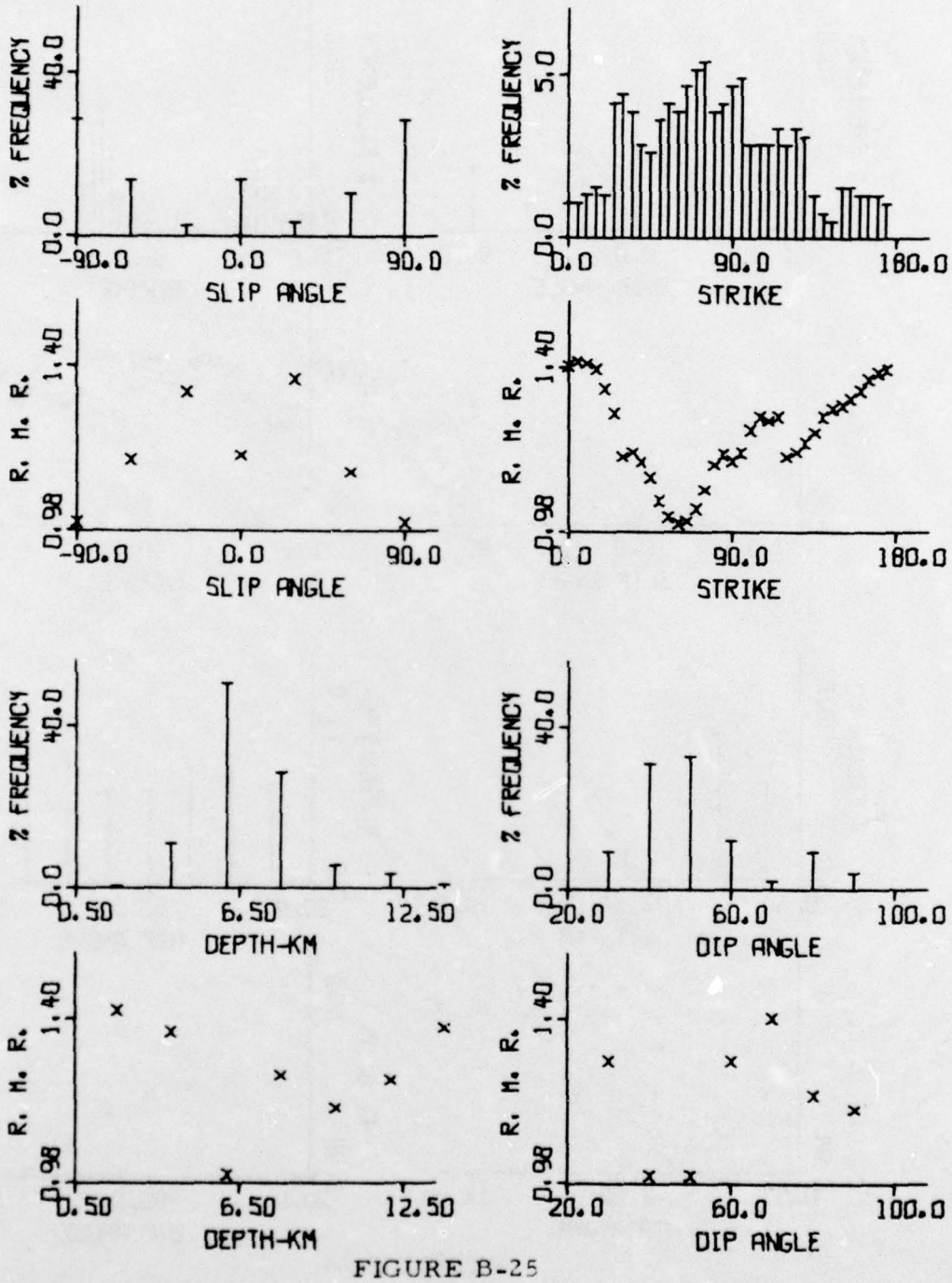

FIGURE B-25

SOURCE PARAMETER DISTRIBUTION BY RATIO-OF-EVENTS:
LX+SINK+S043

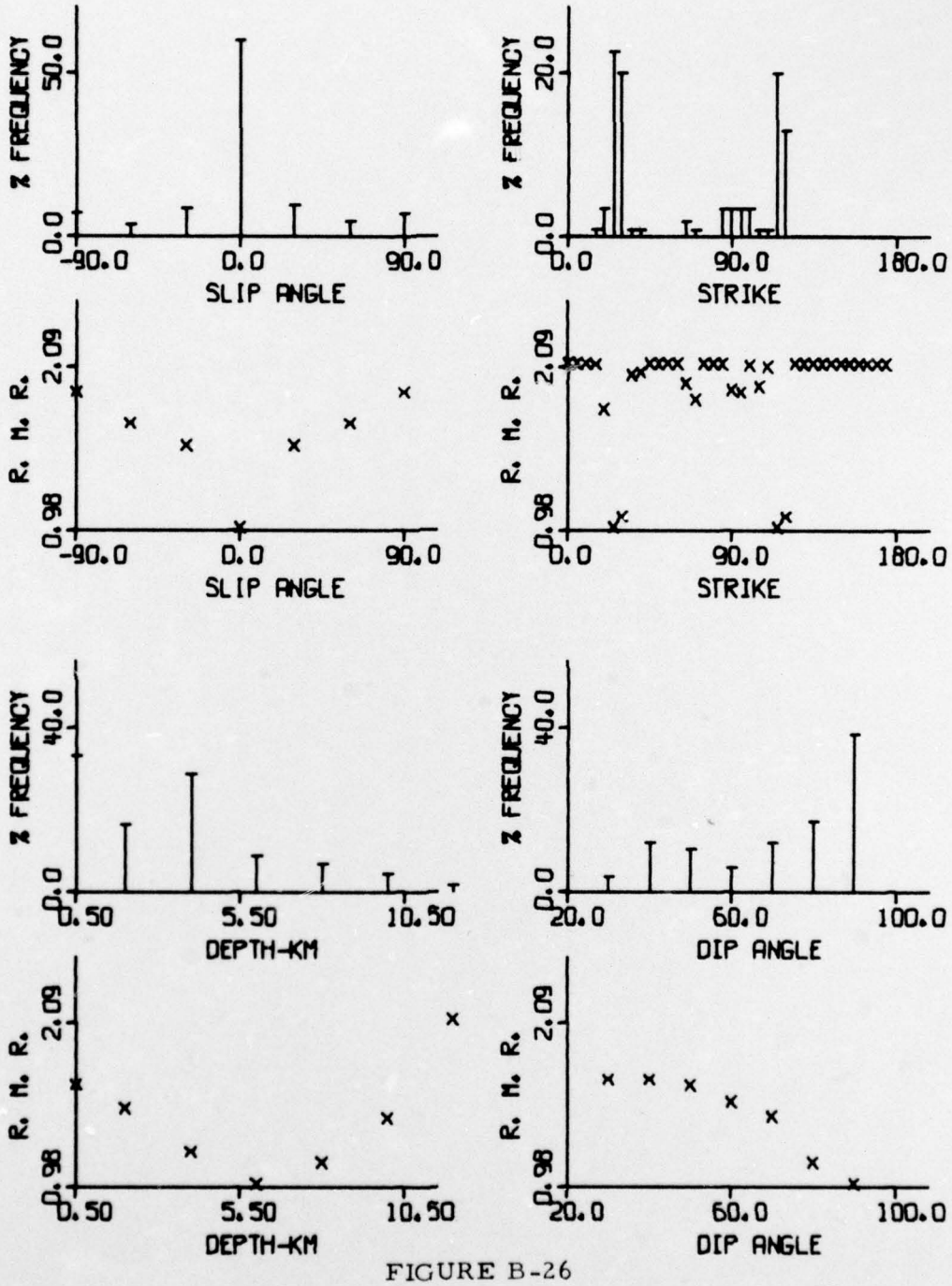

FIGURE B-26

SOURCE PARAMETER DISTRIBUTION BY RATIO-OF-EVENTS:
LX+SINK+S059